Interfacial Properties
on the Submicrometer Scale

About the Cover

The background design is an atomic force microscopy image of an organosilane polymer film exposed to an oxygen plasma. The etching was performed through a mask, resulting in highly reticulated silicon oxide surfaces, smooth unexposed planes, and the gradient between the two featured in this image. The interface between reacted and unreacted areas displays anisotropic texture oriented perpendicular to the mask edge. The interfacial morphology is believed to result from a destabilization and pinning of the film during the conversion from nonpolar organosilane to polar silicon oxide. Image dimensions are approximately 30×40 micrometers in x and y, and 50 nanometers in z.

Collaborators contributing to this work include Gabriela Hernandez, Monika Balk, Martha Harbison, Vanessa Chan, Edwin Thomas, Victor Lee, Robert Miller, and Jane Frommer (*Chem. Mater.* **1998**, *10*, 3895). Assistance from Digital Instruments, Veeco Metrology Group in image processing is gratefully acknowledged.

Interfacial Properties
on the Submicrometer Scale

Jane Frommer, EDITOR
IBM Research Division

René M. Overney, EDITOR
University of Washington

American Chemical Society, Washington, DC

The paper used in this publication meets the minimum requirements of American National Standard for Information Sciences—Permanence of Paper for Printed Library Materials, ANSI Z39.48–1984.

Foreword

The ACS Symposium Series was first published in 1974 to provide a mechanism for publishing symposia quickly in book form. The purpose of the series is to publish timely, comprehensive books developed from ACS sponsored symposia based on current scientific research. Occasionally, books are developed from symposia sponsored by other organizations when the topic is of keen interest to the chemistry audience.

Before agreeing to publish a book, the proposed table of contents is reviewed for appropriate and comprehensive coverage and for interest to the audience. Some papers may be excluded to better focus the book; others may be added to provide comprehensiveness. When appropriate, overview or introductory chapters are added. Drafts of chapters are peer-reviewed prior to final acceptance or rejection, and manuscripts are prepared in camera-ready format.

As a rule, only original research papers and original review papers are included in the volumes. Verbatim reproductions of previously published papers are not accepted.

ACS Books Department

Preface

The goal of the symposium from which this book evolved was to bring an interdisciplinary group of researchers together to address material properties that arise at interfaces. Why is this particular juncture of such great interest? Material confinement that often takes place at interfaces is not satisfactorily described by current phenomenological theories. Many material processes are influenced by the limitations of very small numbers (dimensions and populations) or by intimate interaction with the neighboring component at an interface. Processes that are affected by interfacial constraints or size limitations include wetting, diffusion, friction, lubrication, phase transitions, catalytic reactions, and chemical reactivity. Modern device technologies, such as microelectronics and biotechnology, demand precision and control in material processes. It is increasingly important for today's technological processes to be based on a fundamental understanding of material properties of solids and fluids in submicrometer boundary regime at interfaces: the increasingly "diminishing" interfaces as device dimensions scale down.

In composing this book, we strive to support a dialog between researchers in different disciplines with backgrounds in chemistry, physics, biology, materials, and surface sciences. This diversity is reflected in the chapters that the reader will find in this book, addressing the topics of interfacial properties from the angles of microscopic and spectroscopic techniques, liquid and solid states, surfaces and thin films, and empirical and computational convergence. Articles in this volume describe nanomechanical properties and structure of thin films in contrast to their bulk counterparts, from both experimental and theoretical perspectives. Recognition of the influence of the interface on material properties drives the development of methods described here to address properties such as viscoelasticity, microroughness, and friction, particularly in polymers. Advances in instrumentation include scanning probes (thermal, harmonically driven, and chemically modified), X-ray scattering, sum frequency generation spectroscopy, and nanorheometers. The origin of film properties is investigated via tailored molecular modification of film components. Examples are given in selective fluorination and its effect on wetting, correlation of chromatographic performance with the conformation of the stationary phase in chromatographic media, and direct observation of the initiation of hydrolysis at defect sites in organic coatings. Empirical studies are complemented with molecular dynamics simulations and modeling of interfaces, including indentation of monolayers with nanotubes, frictional dependence on chain length, and

the effect of substrate geometry on wetting. Included are articles that address issues of instrument design, property measurement, and the molecular origin of materials found in ever-increasing confined spaces. In the structuring of the book, we strive to organize and blend the diversity of disciplines to offer a product of comparative and integrated research obtained by complementary techniques from various research areas.

The introductory chapter provides the reader with an overview of the field by discussing interfacial constraints in materials from both a simple geometrical angle and a structural perspective. It would be desirable to offer a classification in terms of steady-state and transient thermodynamics. This would enable classification of mesoscale observations as thermally equilibrated novel material properties or as transient transport processes with critical time scales. However, current scientific development still lacks the necessary information on the mesoscale to distinguish between equilibrated properties and transient apparent properties. This lack of information often leads to misinterpretation of observations, adding to the difficulty in combining our efforts to develop the fundamentals of mesoscale science. We urge the reader to reflect on this emerging awareness when reading the introductory chapter and the subsequent contributed chapters with their diverse examples of interfacial material properties.

JANE FROMMER
Almaden Research Center
IBM Research Division
650 Harry Road
San Jose, CA 95120–6099

RENÉ M. OVERNEY
Department of Chemical Engineering
University of Washington
Seattle, WA 98195–1750

Chapter 1

Constrained Systems: Caught between Dimensions

René M. Overney and Scott E. Sills

Department of Chemical Engineering, University of Washington, Seattle, WA 98195–1750

This chapter discusses the problematic nature of interfacial sciences when constrained to the mesoscale. Interfacial sciences are trapped between the atomistic and the three-dimensional bulk regimes – the mesoscale. We experience a breakdown of phenomenological descriptions used to characterize macrosystems. Furthermore, submicrometer systems with their fractal-like dimension cannot be adequately described with quantum or molecular interaction theories. The challenge of describing the mesoscale for the various scientific fields is to find a common denominator. By suggesting a possible classification of the field and by discussing examples in each category, this chapter attempts to illuminate the similarities of mesoscale properties obtained in different research and engineering disciplines.

Since mathematicians have introduced us to many dimensions, it has been our desire to strive for more degrees of freedom while seemingly unsatisfied with the three dimensions we live in. Our pursuit of entertaining ourselves with fictions that escape our common senses is documented as early as 1884 in the satire "Flatland - A Romance of Many Dimensions" by Edwin A. Abbott.[1] While Abbott's work tries to introduce the reader to the concept of the multi-dimensional space, it chooses fewer dimensions than three as starting point. By doing so, Abbott came up with imaginary laws of nature that apply in one and two dimensions. Although these laws, which for instance explain how rain is experienced in two dimensions, are unrealistic, they impressively illustrate the mystery of lower dimensionalities.

Indeed, the laws of nature, or more appropriately, the perception of them in the form of material and transport properties, are challenged if a three dimensional bulk

© 2001 American Chemical Society

material is reduced to a two dimension plane. This becomes apparent in many interfacial applications, such as thin film technologies. Structural, material, and transport properties are increasingly dominated by interfacial, interactive, and dimensional constraints. Statistical properties are altered in small ensemble systems, and interfacial properties become dominant on the so-called *mesoscale*.

This introductory chapter is intended to provide an overview of the field, and Table 1 will be utilized as a guide to classify the various aspects of interfacial sub-microscale properties. An alternate system classification would have been in terms of steady-state and transient thermodynamics. Unfortunately, many available interpretations of experimental data obtained on the mesoscale are disputable regarding their distinction between equilibrated properties and apparent transient properties.

Table 1: Classification of Various Aspects of Interfacial Sub-microscale Properties.

Structural, Material, and Transport Properties			
Dimensional Effects on Properties	Small Ensemble Systems	Constrained Systems	Critical Length Scales, Kinematics, and Dissipation
Property equations solved in 1D, 2D or 3D lead to different solutions.	Statistical mechanics fails to predict exotic properties.	Properties are affected by internal or interfacial constraints.	Processes are affected by dimensional limitations.
e.g., Rayleigh surface waves vs. Huygen's body wave	e.g., exciton annihilation in ultrathin films	e.g., interfacial constraints in ultrathin films	e.g., friction as an interfacial process

The Reader will find each category of Table 1 discussed in the following sections of this chapter. The first section provides some brief general remarks about properties supported by an illustrative example that would have fit well into Abbott's satirical novel on how the perception of properties are characterized by the dimensionality of the governing equation. Small ensembles and size effects are discussed in the succeeding section. Particularly emphasized in the second section are optoelectronic properties and quantum confinement. The third section deals with interfacially constrained systems and discusses structural changes at interfaces and their effect on viscoelastic and thermal material properties. Specific emphasis is placed on thin polymeric and interfacially trapped fluidic systems. Finally, the fourth section introduces the terminology of critical time and length scales, and discusses the effect of dimensional limitations on processes such as friction.

Remarks about Material and Transport Properties

Material properties, either physical or chemical in nature, are distinctive attributes of a steady-state condensed system. It is imposed that such *intrinsic* properties are time independent, i.e., they describe thermodynamically equilibrated material characteristics.

An experimentally determined value is referred to as an *apparent property value* if it depends on system parameters, for instance, the rate at which the experiment is performed. An example of a rate dependent property is viscosity. By definition, the intrinsic value of a rate dependent property is the extrapolated value in regards of an infinite time period over which the property is obtained. There are properties that are combinations of truly independent properties, e.g., the material density as the mass per unit volume. The properties of foremost interest are *intensive* properties, i.e., properties that are independent of the size of a system.

Transport properties such as wave propagation, diffusion, and conduction are known to depend strongly on material properties, but also on geometrical constraints and dimensional confinement. It is very challenging, especially in mesoscopic systems like ultrathin films, to determine the origin for exotic, not bulk-like, transport properties.

Let us consider a well-known example where transport properties are significantly dissimilar for different dimensionalities; that is the energy transport described by the wave equation, i.e.:

$$\Delta_N u = c^2 \frac{\partial^2 u}{\partial t^2}; \quad u = u(\vec{x}, t); \quad \vec{x} = (x_1, x \ldots, x_N).\tag{1}$$

It is well known that the qualitative time behavior of the solution, u, of the wave equation is significantly different for a three dimensional wave propagation, N=3, compared to a one or two dimensional system, N = 1 or 2. For N=3, a spatially localized initial disturbance gives rise to a time limited disturbance only, at any accessible location away from the source of the disturbance. This is different for N=1 or 2, where the disturbance is for all times noticeable at any accessible location if there are no dissipative effects.

The moving wave propagations in three dimensions have well defined tailing and front border wave fronts that we experience daily by speaking with each other or by listening to radio transmissions. We would not be able to communicate in the same manner in a two dimensional world with surface waves. Lord Rayleigh discovered that waves propagating over the surface of a body with a small penetration distance into the interior of the body, travel with a velocity independent of the wavelength and slightly smaller than the velocity of equivoluminal waves propagating through the body.[2] It has been found that the so-called Rayleigh waves, which diverge in two-dimensions only, acquire a continually increasing preponderance at great distances from the source. This two dimensional effect of wave propagation has been found to be very important in the study of seismic phenomena.[3]

Small Ensembles and Size Effects

Quantum Confinement

   Phenomenological theories fail to describe transport and material properties of small ensemble systems, i.e., systems in which the number of molecules is smaller than Avogadro's number. Within the last century, it has been theoretically predicted and experimentally confirmed that small ensemble systems generate some sort of quantum confinement, in which optoelectronic, electronic, and magnetic wave propagation experience quantized nanoscale size effects.

   It has been found that size limited materials such as particles, films, and composites, synthesized with nanometer dimensions can exhibit exotic quantized properties. For instance, altered phenomena in emission lifetime, luminescence quantum efficiency, and concentration quenching have been reported with nanoparticle-doped systems.[4-9] In various doped nanocrystalline (DNC) phosphors, ZnS:Mn and ZnS:Tb, quantum confinement effects were found for doping particles with critical dimensions below 5 nm resulting in shortening of the luminescence lifetime by several orders of magnitude.[10] The origin of these quantum confinement effects is postulated to arise from mixing of s-p and d-f electrons from the host with the valence band of the activator leading to forbidden d-d and f-f transitions.[10] Theoretical predictions are still sparse due to the inadequate experimental database. One of the few theoretical predictions suggests that the electron-phonon interactions are modified on the nanometer scale.[11] This is supported by experiments in semiconducting nanoparticles which claim growth rates inversely proportional to the square of particle diameter $(\sim 1/d^2)$.[12,13] With site-selective optical spectroscopy, where lanthanide emitters serve as sensitive probes of nanostructured materials, quantum confinement effects are utilized to determine material properties such as the degree of disorder or crystallinity, phase transformations and distributions, phonon spectra, and defect chemistry.[4,14,15].

Interfacially induced Pseudo-Quantum Confinement in Optoelectronic Devices

   Outside the quantum-well distance of about 10 nm or even less, it is expected that the materials exhibit bulk-like properties. However, in a recent study by Jenekhe and coworkers, it has been shown that the electroluminescence (EL) wave length of a binary ultrathin polymer film exhibits very unique properties that could be attributed to an unexpected quantum effect.[9]

   The origin of the EL emission is provided by the formation of excitons, or electron-hole pairs, which are formed at defect sites, i.e. donor/acceptor sites, in the material and at the interface of a heterojunction of two semiconducting polymer layers. Little is known at this time about the mobility of the electrons, holes, and excitons at the interface of heterojunctions. Limited exciton diffusion lengths in the materials and the interfacial nature of the photogeneration process could explain these exotic transport properties in terms of topological constraints.
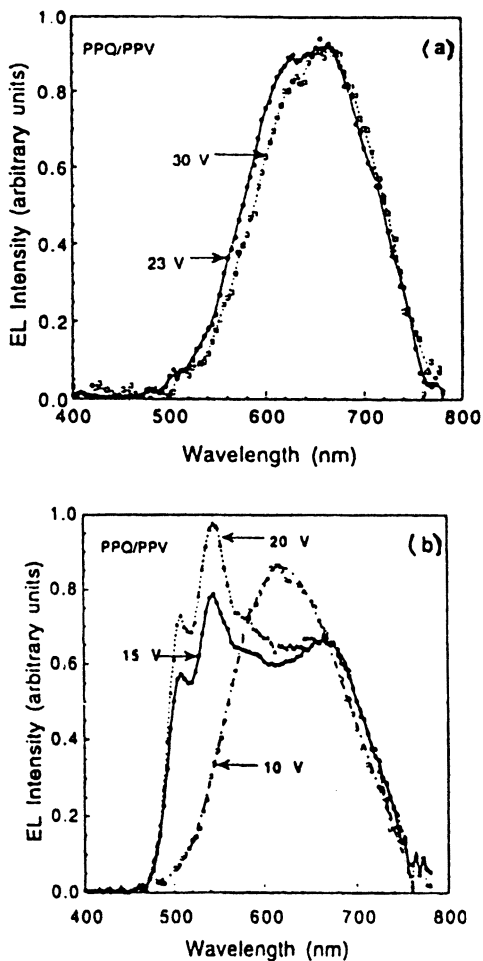
Figure 1. EL spectra of PPQ/PPV heterojunction devices with constant PPV thickness of 25 nm. (a) Voltage independent spectra for a PPQ film thickness of 67 nm. (b) Voltage dependent spectra for a PPQ film thickness of 40 nm. Adapted from Ref. 9

The experiment by Jenekhe and coworkers demonstrated that below a critical thickness of the semiconducting polymer structure, the optoelectronic device exhibits a three-fold enhancement in the photoconductivity and allows for voltage-tunable reversible color changes, Figure 1.[9] These interfacially induced pseudo-quantum confinement effects have been observed for critical sizes (i.e., film thicknesses) up to at least 40 nm.

The optoelectronic experiment is briefly described as follows: Two semiconducting films, n-type and p-type, were sandwiched between aluminum and indium-tin oxide (ITO) electrodes as illustrated in Figure 2.
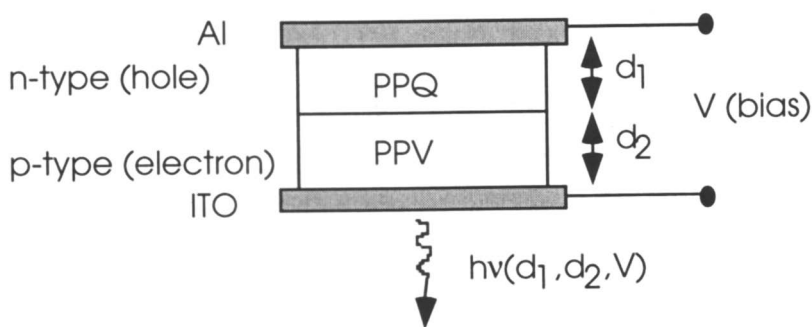

Figure 2: EL junction of two semiconducting polymer films. The frequency, v, of the luminescence is found to be dependent on the bias voltage, V, for films with critical thickness d_1=40 nm and d_2=20 nm, respectively (see Figure 1). Note that the finite size distance is outside the expected quantum-well dimension (~10 nm) asking for mesoscale interpretations.

The n-type, electron transporting polymer layer consisted of polyquinolines (PPQ), and the p-type, hole transporting polymer layer consisted of p-phenylenes (PPV). The luminescence was measured as function of the film thickness of the polymers, and the applied voltage, Figure 1. The electroluminscent (EL) spectra were found dependent on the thickness of the PPQ n-type polymer layer. For 67 nm thick PPQ films and 25 nm PPV p-type layer, the photoluminescence was found to be voltage independent over the range of 10-30 V and identical to a single-layer ITO-PPQ-AL device (orange/red), Figure 1(a). Significantly altered spectra were obtained for a reduced film thickness of PPQ from 67 nm to 40 nm, Figure 1(b). At low bias voltages ranging from 8-10 V, a unipolar hole transfer was observed leading to an orange emission that is characteristic of PPQ. At a higher voltage range of 13-20 V, a broadband spectra was obtained caused by a bipolar electron-hole transfer of both layers leading to a green color. The emission intensity could also be influenced for a PPQ film of constant thickness of 40 nm by varying the thickness of the p-type layer of PPV. In such a system, the intensity of the hole transport is controlled by the film thickness of PPV, and the electron transport is controlled with the voltage.[9]

Structurally Constrained Systems

Interfacially Confined Polymer Films

The "large" size effect that has been found in polymeric optoelectronic devices (see above) is not unique in polymer science. While materials such as ceramics, metals, oxides, exhibit size limitations only noticeable below 10 nm, quantum-well effects, it was found that in polymer systems, interfacial effects could be noticeable over distances of tens to hundreds of nanometers. Over the last few years, various groups reported bulk-deviating structural and dynamic properties for polymers at interfaces. [16-22] For instance, increased molecular mobility was observed at the free surface for thick films.[16] Reduced molecular mobility at the film surface of ultrathin films was reported based on forward recoil spectroscopy measurements.[17] In secondary ion mass spectrometry (SIMS) and scanning force microscopy (SFM) studies of graft-copolymers, it was found that the degree of molecular ordering significantly affects dynamic processes at interfaces.[18] Self-organization of graft and block-copolymers at surfaces and interfaces were found with transmission electron microscopy (TEM) and neutron reflectivity (NR).[19-22]

Application of mean-field theories to interfacially constrained and size-limited polymer systems failed to describe the rather unexpected mesoscale behavior observed experimentally. The extension of the interfacial boundary far into the bulk is *unexpected* because many amorphous polymer systems are theoretically well treated as van der Waals liquids with an interaction length on the order of the radius of gyration, i.e., the effective molecular size. At solid interfaces the radius of gyration is further compressed, like a pancake, and thus, any memory effects of the solid are expected to be even more reduced to a pinning regime of only 0.5 to 2 nm[23]. Within the pinning regime, it is commonly accepted that the material is structurally altered and exotic properties are expected. Outside the pinning regime, the polymer is expected to behave bulk-like. Experiments show however, that such scaling theories, i.e., mean-field theories, fail in describing the observed unique mesoscale properties because they do not consider effects that occur during the film coating process, e.g., rapid solvent evaporation. For instance, recent SFM experiments revealed that the spin coating process altered the structural properties of polyethylene-copropylene (PEP) at silicon interfaces due to anisotropic molecular diffusion that is caused by process-induced structural anisotropy.[24] The polymer structure at the interface affects properties such as the entanglement strength, illustrated in Figure 3, and thermal properties such as the glass transition temperature (see also Buenviaje et al. in *Kinetics of Constrained Systems*).[25]
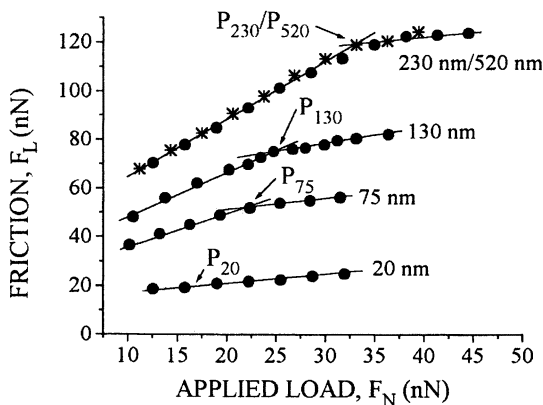
Figure 3. The transition point P_x (x = thickness of polymer film) corresponding to the discontinuity in the friction vs. loading curve is a measure of the entanglement strength of the polymer (polyethylene-copropylene). The bulk value is reached for films thicker than 230 nm. Films thinner than 230 nm are partially disentangled due to the spin coating process, and thus, the transition point occurs earlier. Within a 20 nm boundary regime, the film is entirely disentangled (gel-like). Reproduced with permission from reference 24. American Chemical Society, 1999.

Thermal annealing has been found inadequate to relax process-induced structural anisotropy for interfacially constrained PEP systems because of insufficient "mixing" at the interface [24] (see also below fractal kinetics at interfaces).

Interfacially Confined Liquids - above the critical threshold

Note that complex liquids like polymer solutions are different from thin polymer films. Interfacial effects have been found to exceed the molecular dimension by more than one order of magnitude.[26-28] Rheological properties of submicrometer thick liquids have been studied in the past quite successfully with surface force apparatus (SFA).[26-43] Montfort and Hadziioannou, for instance, confined nanometer thick films of long chain molecules between mica sheets and measured the static forces as the two SFA surfaces engaged each other[28]. As illustrated in Figure 4, repulsive forces were found to extend beyond separation distances of 10 times the radius of gyration, R_g, determined for the bulk. The steep repulsive slope in the force at small separation distances is due to a hard wall effect. The authors conclude, based on the high wetability of perfluorinated polyether used to clean mica surfaces, that the formation of surface films on each face plus unattached chains in between are causing the measured long-range repulsive forces.
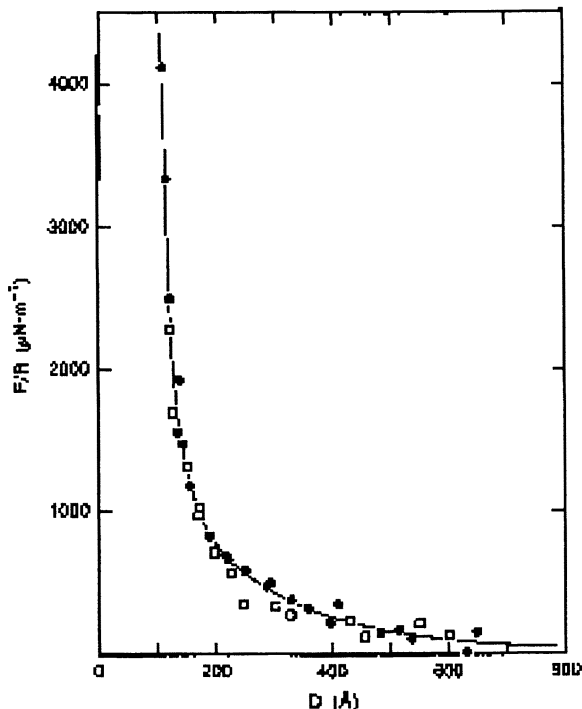
Figure 4. Logarithmic force/(radius of curvature) vs. distance, d, of perfluorinated polyether liquid at 25 °C (• droplet between the surfaces) (immersed surfaces in the liquid). Reprinted with permission from reference 28. American Institute of Physics, 1988.

Montfort and Hadziioannou also studied the effect of interfacial interactions, ie., surface forces, on the rheological response of films as thin as 200 nm with sinusoidal modulated perturbation. They considered the following forces:

(a) the inertial force, $F_I = m \dfrac{d^2 x}{dt}$,

(b) the restoring force of the spring, $F_R = -kx$,

(c) the surface forces, F_S,

(d) the hydrodynamic forces, F_H.

The surface forces were approximated from sinusoidal perturbation as:

$$F_S(D) = F_S(\overline{D}) + k_{eff} \times (D - \overline{D}),$$ (2)

with the perturbation distance, D, around the mean distance, $\overline{D}$, and the effective spring constant, k_{eff}, that is determined from static force-distance measurements. k_{eff} is a measure of the effective stiffness of the systems including the sample liquid and

the surface force apparatus. Repulsive forces are provided by $k_{eff} < 0$. The hydrodynamic force, F_H, of the confined liquid has been treated by *Montfort* and *Hadziioannou* as a first-order linear, viscoelastic fluid by combining the continuity equation and the equation of motion for incompressible liquids with the Maxwell model. Based on this model, they obtained the following functional relationship between the relative response amplitude A' and k_{eff} (and k_{eff}/k) for a constant modulation frequency, ω, and a fixed geometry:

$$\frac{1}{A'} = \frac{\left[\dfrac{\omega \eta_o}{\alpha \left(1 + \omega^2 t_o^2\right)}\right]^{-1}}{\sqrt{1 + \left[\omega t_o + \alpha \left(1 - \dfrac{k_{eff}}{k}\right)\dfrac{1 + \omega^2 t_o^2}{\omega \eta_o}\right]^2}} \ ; \quad \alpha = \frac{k\overline{D}}{6\pi R^2} \ , \quad (3)$$

where the system relaxation time is t_o. Equation 3, illustrated in Figure 5, indicates that repulsive surface forces show a comparable and qualitatively similar response behavior to systems where no surface forces are present. For attractive surface forces, the qualitative behavior of A' strongly depends on the stiffness relationships between the system, both the spring and the liquid.

Montfort and *Hadziioannou* experimentally confirmed their macroscopic theory for perfluorinated polyether beyond a mean separation distance of approximately 200 nm.[28] Thus, phenomenological theories are found to predict well the viscoelastic behavior of semidilute polymer solutions up to a critical thickness where interfacial interactions become dominant.

Interfacially Confined Liquids - below the critical threshold

Below a critical thickness of interfacially confined liquids, macroscopic phenomenological theories have to be adjusted. Simple nonpolar liquids such as hexadecane exhibit oscillarory solvation forces if compressed to a remaining film thickness of less than 4 nm.[26] This phenomena had been described as freezing-melting transition and layering.[44] Grand canonical Monte Carlo and Molecular Dynamic (MD) simulations discussed the oscillatory solvation forces in terms of phase transitions and recrystallization.[45] Such interfacial "structuring" has been observed in linear alkanes and spherical shaped molecules, such as octamethylcyclotetrasiloxane (OMCTS) under extreme compression down to the few remaining molecular layers between the surfaces.[26,46]
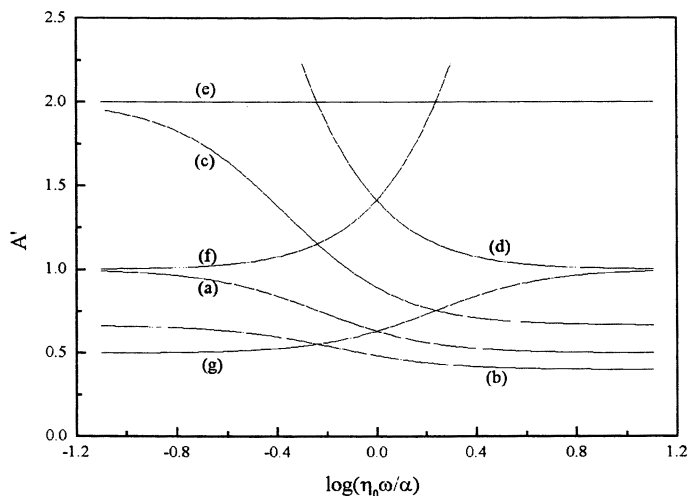
Figure 5. Amplitude of oscillations for a Maxwell fluid in the presence of surface forces: (a) $k_{eff}<0$, (b) no surface forces: $k_{eff}=0$, (c) $0<k_{eff}/k<1$, (d) $k_{eff}/k=1$, (e) $k_{eff}/k=1+G_o/\alpha$, (f) $k_{eff}/k>1+G_o/\alpha$; for $G_o/\alpha=1$. Reprinted with permission from reference 28. American Institute of Physics, 1988.

To date there is no conclusive experimental evidence that the solvation forces in nonpolar liquids are indeed crystallization processes. *Gao* and *Landman* suggest with their MD simulation that the molecular surface corrugations are "imprinted" into the nanoconfined and highly pressured (MPa) liquid. Their simulation predicts that if the commensurability of the molecular surface corrugation of the two solid surfaces around the confined liquid of spherical shaped molecules is altered, e.g., incommensurable, the amplitude of the oscillatory solvation forces are reduced.[47] The theory of imprinted commensurable structures implies that the solvation forces of surface confined liquids should be drastically reduced for amorphous surfaces and for adjacent surfaces on the molecular dimension. O'Shea and Welland partially confirm this hypothesis with their SFM study on OMCTS in which they observe oscillatory solvation forces only for very large blunt tips, 700 nm in diameter.

In general, the regime in which the solvation forces appear could be described as an entropically cooled boundary regime. The question arises if this boundary regime also exist without external pressure forces, i.e., solely because of surface interactions and a reduction in dimensionality. Winkler et al. predict with a MD simulation that hexadecane is well ordered, in crystalline like monolayers for strongly attractive surfaces.[48] In a very recent experimental study by Szuchmacher, He and Overney it was found by SFM shear modulation without applying external normal pressures, that there is an entropic cooling effect for hexadecane, illustrated in Figure 6, and for OMCTS at amorphous silicon-oxide surfaces.[49] A lateral modulation was chosen to avoid surface tapping and hydrodynamical damping in normal direction.

The cantilever tip radius of curvature was estimated to be about 10-20 nm. A lateral modulation amplitude of 2 nm was chosen and an approach velocity of 0.5 nm/s was used. These small values guarantee a steady state approach.

In summary, we have discussed how interfacial effects can influence the viscoelastic properties of polymer coatings, polymer melts and solutes, and even simple nonpolar liquids within an interfacial boundary regime. In high molecular weight polymer systems, the interfacial boundary regime can reach up to hundreds of nanometers. The interfacial boundary layer of simple nonpolar fluids is restricted to a few nanometers. While outside the critical interfacial boundary layer interfacial effects on properties can be approached with phenomenological theories, modified or new theories are in demand within the structurally - or entropically cooled interfacial boundary layer. The modern theoretical approach of the fractal dimensionality will be discussed next.
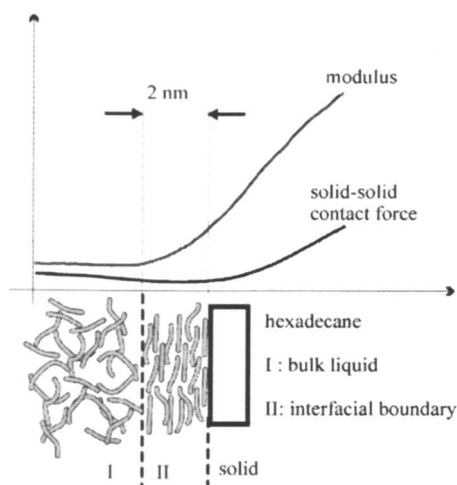
Figure 6. Interfacially confined hexadecane measured by SFM shear modulation spectroscopy. The shear response is measured simultaneously with the normal force deflection of the cantilever as function of the cantilever-siicon sample distance. The difference in the bending onset of the two curves defines the interfacially confined boundary layer thickness.

Critical Length Scales, Kinematics, and Dissipation

Dimensional and topological constraints

Critical length scales, kinematics and dissipation are primarily problems of distributions, probabilities, and cutoff limits.

Moving from two dimensional systems or nanoscale small ensembles to three dimensional systems, we will find ourselves in a fractional dimensionality. Material transport and reaction properties are known to be strongly affected by the so-called

fractal dimension. For instance, for decades it is common knowledge that bulk kinetics and the kinetics at surfaces are significantly different processes. While bulk kinetics are described by time-independent rate constants, kinetics at surfaces reveal time dependent rate coefficients, also termed apparent coefficients [50]. Chemical and non-chemical, e.g., exciton-exciton recombination, reactions that take place at interfaces of different phases, are called *heterogeneous* reactions. Already in the late 1950s, the diffusion and the kinetics, for instance of the adsorption of alcohols at water-air interfaces, has been discussed in terms of barrier-limited adsorption [51] and diffusion-limited [52] processes with time-dependent reaction coefficients. The difference between a three-dimensional vs. a two-dimensional process is the degree of freedom. The degree of freedom limits the diffusive fluxes and hence, any kinetics in the absence of a convective process such as stirring. For chemical synthesis, this entropic cooling effect can be pictured as a constraint in the natural self-stirring process by diffusion.

Thus, dimensional constraints of surface reactions or topological constraints of solid-state reactions affect the nature and the strength of the transport mechanisms. It is important to note that underlying structural properties of the material might not be affected by these constraints. For chemical reactions the material properties will change over time if the products are incorporated in the interface. In that regard, the apparent material properties are favorably discussed in terms of transient thermodynamics.

Bulk processes which are not governed by a simple diffusion equation were found to yield time-dependent reaction coefficients. Briefly, diffusion controlled reactions between small molecules lead for two reactants to the following classical second order rate equation, Smoluchowski equation: [53]

$$\frac{\partial n_A}{\partial t} = \frac{\partial n_B}{\partial t} = -k n_A n_B; \qquad k = 4\pi (D_A + D_B) b \qquad (4)$$

where the two species number densities are n_A and n_B, the two diffusion coefficients of the reactants are D_A and D_B, the capture or reaction radius is b, and the reaction rate constant is k. This equation is applicable to small molecule diffusion provided that the time $t \ll b^2/D_{AB}$, i.e., the diffusion length $(D_{AB}t)^{1/2}$ exceeds the capture radius. However, macromolecules in melts or in concentrated solutions with attached flexible reacting groups show, for system relaxation times, or memory function, exceeding the process rates, a different rate equation of the form: [54]

$$\frac{\partial n_A}{\partial t} = \frac{\partial n_B}{\partial t} = -k(t) n_A n_B; \qquad k(t) = \frac{x^d(t)}{t} \frac{\sin(\pi u d)}{\sigma \pi} \qquad (5)$$

with a time dependent rate coefficient, where x(t) is the rms displacement of one monomer during a time *t*, *d* is the fractal dimension (for bulk d=3, for an ultrathin film, 2<d<3), *u* is the exponent of the memory function S(t) in form of a power law

(u=1/2 for simple diffusion, i.e., S(t)~$t^{3/2}$ in three dimensions, and x(t)~$t^{1/2}$), and σ is the transport coefficient of the memory function (σ=$2^{-3}\pi^{-3/2}$ for a Rouse chain with a reaction time smaller than the Rouse relaxation time of the chain). It is striking that besides the time dependence of the reaction rate coefficient in Eq. (5), k becomes essentially independent of the capture radius b for 0<b<x(t). This last statement also holds for noncompact explorations (fast decaying memory function) although the rate coefficient is again time independent.

Properties and critical time scales

Underlying material properties that were in the past predominantly determined by macroscopic experiments are microscopic transfer properties of momentum and energy. Microscopic transport mechanisms are governed by couplings between atoms or molecules, intra- and intermolecular degrees of freedom, and external forces. While for example, the dimensionality of the system, e.g., a two-dimensional surface vs. a three-dimensional body, significantly affects the intermolecular degrees of freedom of molecules. The intramolecular degrees of freedom are influenced by chemical groups and the stiffness of intramolecular chemical bonds.

Associated with couplings is a spectrum of intrinsic characteristic times, τ_i, and extrinsic characteristic times, τ_e, also called the operational "drive" time. With intrinsic characteristic times, it is referred to structural relaxation, energy distribution and dissipation times, and with extrinsic characteristic times it is pointed to operational dependent times that are connected to the rate of the applied external forces. The relationship between the two relaxation times (the ratio is called the Deborah number, D_e [55]) is critical for many processes.

In mechanical systems of confined rheological films with drive velocities that are comparable to material relaxation times, i.e., $D_e \sim 1$, new strategies have to be developed to avoid energy consuming resonance effects. In experiments that were concerned with modern *boundary* lubrication, where the lubricant film thickness is on the molecular length scale, the rate dependence of dissipative forces such as friction was illustratively documented.

Israelachvili and co-workers found that thin lubricant films can exhibit solid-like properties, including a critical yield stress and a dynamic shear melting transition, which can lead to stick-slip motions [34,35,56,57]. The generic shape of an overdamped stick-slip behavior is illustrated in Figure 7, which has been observed with SFA measurements as sketched in Figure 8 [57]. The spring force, F=-k(u-vt), results from the difference of the relative displacement of the block to the stationary lower surface, u, and the drive distance, vt, in conjunction with the spring constant k.

Yoshizawa and *Israelachvili* interpreted the stick-slip behavior at lower velocity as some sort of melting-freezing transition [57]. More accurately one could describe these two pseudo-states during a stick-slip cycle as transition phases in a dynamic process with high and low degrees of order, respectively. The less ordered or fluidized state was found to be increasingly important at higher velocities [58,59]. As it is illustrated in Figure 7, above a critical velocity, v_c, steady sliding is observed. Experimentally, *Yoshizawa, Chen* and *Israelachvili* [58], and theoretically, *Gao,*

Luedtke and *Landman* [59], observed that at velocities even higher than v_c, eventually a state of ultralow kinetic friction occurs. *Landman* et al. observed this ultra-low friction regime also by lateral sinusoidal perturbation with small amplitudes (~1 Å) and high frequencies, which are related to the relaxation times in the material [59]. They found that at Deborah numbers of 0.75 and 7.5, stick-slip behavior and superkinetic sliding, respectively, dominated.
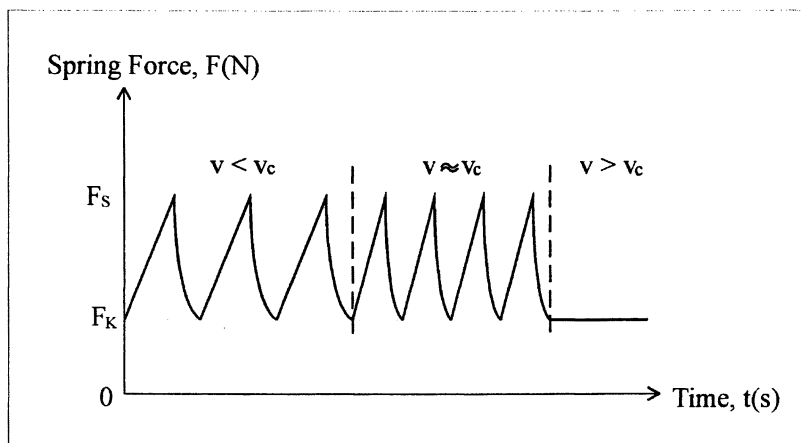

Figure 7. Illustration of a generic stick-slip motion of an overdamped spring system for increasing pulling velocities. Below the critical values for temperature, T_c, and shear rate, v_c, dominant stick-slip motions have been observed for hexadecane films [57]. The stick-slip spikes disappear as the velocity is increased above v_c. Reprinted with permission from reference 27. World Scientific, 1998.
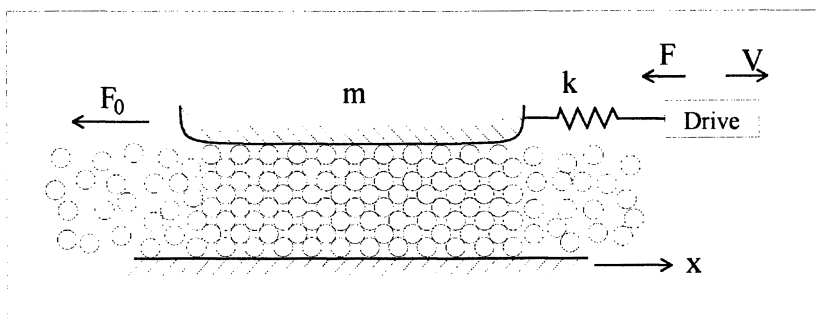
Figure 8: Mechanical analog of the SFA experimental setup used for measurements of friction forces F_o. A block of mass m which is confining a thin liquid film of hexadecane between atomically smooth mica is pulled laterally at velocity v. The lateral forces, F, are measured with an elastic spring of spring constant k [57]. Reprinted with permission from reference 27. World Scientific, 1998.

"Stick-slip" and dissipation

The stick-slip behavior discussed above, originates from dynamic order transitions of mechanically confined fluids. It should not be confused with the true molecular stick-slip behavior as theoretically predicted by Prandtl [60] and Tomlinson [61] at the beginning of the last century and experimentally confirmed towards the end of the century by scanning force microscopy [62].

Molecular or atomistic stick-slip was found to be the microscopic origin of dry friction where a single molecule or atom is dragged in contact over a molecularly structured surface. Briefly, the surface structure defines a corrugation potential along which the dragged atom moves, or more accurately, sticks and slips. The potential shape has to be considered relative to the position of the dragged atom, and is distorted if one considers surface elastic components. Thus, the potential stiffness, k_{pot} (second spatial derivative of the potential) has to be compared to the drag force stiffness, k_{drag} (first spatial derivative of the drag force). As long as $k_{pot} > k_{drag}$, the molecule or atom will "stick" to the surface. Its relative lateral motion is restricted to very small elastic distortions of the surface beneath. With increasing relative distortion of the potential, the potential stiffness is decreasing until at $k_{pot} = k_{drag}$, a sudden transition from sticking to slipping occurs. At this instability point, the dragged atom (molecule) will pop off the surface and slip until it dissipated enough energy so that it can be capture again by the surface beneath. Note that there is always a positive load applied between the dragged atom or molecule and the "sliding" surface. During the slip process, there is enough energy available to overcome the normal load component, and the dragged atom or molecule temporarily looses contact. Thus, the applied load is a crucial parameter for the stick-slip motion. Further, the qualitative behavior of the stick-slip motion, i.e., the slip distance, was found to depend on the drag velocity [62]. At very low drag velocities (~1nm/s), the slip distance was found to correspond to the lattice distance of the structured surface, Figure 9. At higher but still very slow drag velocities (~100 nm/s), the slip distance increased and changed its regular pattern to become more erratic.

During the slip-process, energy is dissipated in the form of vibrations. The terminology of "dissipative vibrations" implies an entropically driven atomistic or molecular uncoordinated process (stochastic, chaotic). In other words, the dissipation is a form of energy transformation from a lower dimensionality to a higher dimensionality, i.e., a 2D frictional interface to a 3D bulk material. The slip-process is irreversible because the probability for reverse-energy-transfer is unlikely; i.e., a reversed energy transfer would require a highly improbable collective process of all vibrating molecules leading to a reduced entropy state. The unlikeness of the reversed process is illustrated with the following *Gedanken*-experiment:

A non-moving solid, which is connected to a spring, on a horizontal plane is heated up from an initial temperature T_i to an elevated temperature T_f. It is assumed that the structural integrity is maintained and that, with adiabatic boundary conditions, all energy due to a constant heat rate is stored as vibrational energy in the solid. If molecular friction as described above were reversible, there would be a high probability that the solid starts moving in a particular direction as if pulled, and thus would exert a force on the spring. Hence, frictional reversibility would imply that
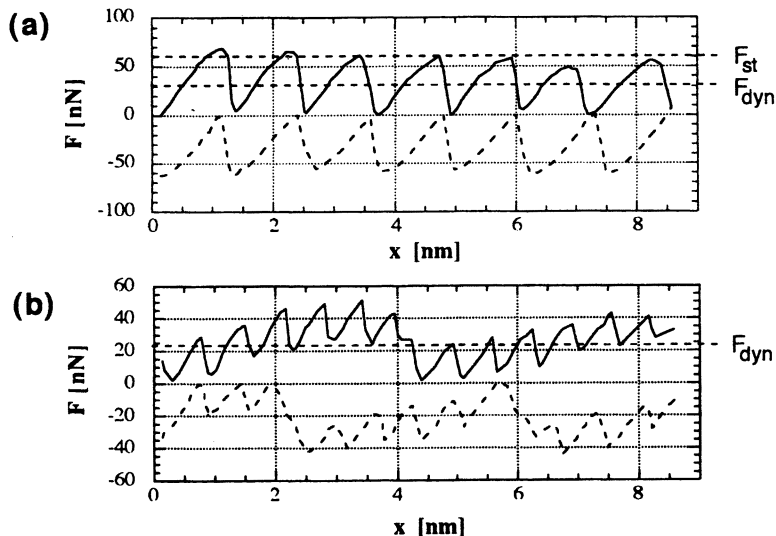
Figure 9. Molecular stick-slip behavior measured on anisotropic, row-like, surface lattice of a lipid film at a drag velocity of 1 nm/s. (a) Sliding direction perpendicular to the row-like structure, (b) sliding direction 60°to the row-like structure. Reprinted with permission from reference 62. The American Physical Society, 1994.

thermal energy can be reversibly transformed into mechanical energy, which contradicts the second law of thermodynamics. There is an interesting aspect to this *Gedanken*-experiment, if one considers the sliding direction. Frictional sliding is well directed in one dimension. The sliding process in the *Gedanken*-experiment could however occur in any direction on the two-dimensional (2D) plane over any time interval, i.e., it could resemble Brownian motion on a plane. Let us discuss what would happen if vibrational motion in two-dimensions could be transformed into 2D Brownian motion. If we collapse the solid to a single atom, the degree of vibrational freedom would not be three, but two because we would have to deduct one degree of freedom for the constraining surface. Thus, for a single molecule, the vibrational motion is like the 2D Brownian motion. If we consider a molecularly thick planar horizontal sheet as our solid, the observed 2D Brownian motion results from the weighted average of the 2D-constrained vibrating sheet-molecules. Thus as long as the vibrating molecules do not vibrate in registry, the thermal energy stored could not be extracted by the attached spring.

At that point, the question arises if it is desirable to intentionally activate vibrational modes in the solid that show a high degree of coordination. It is not because it opens up other gateways for energy dissipation, e.g., acoustic activation due to frictional sliding. Thus, as discussed above for lubricated sliding or dry sliding, the stick-slip phenomena has to be depressed to reduce dissipation. A way to depress the stick-slip behavior is to control either, chemical interactions by embedding surface inhomogeneities, or one of the most crucial parameters, the

applied load. This topic is further discussed in *Finite Size Systems*. Porto, Urbakh and Klafter introduce novel modes of friction that are based on modifying imaginary shear modes; the *shearons*.

Closing Remarks

Reduced dimensionality paired with interfacial interactions were discussed as the major source for constraints in mesoscale systems. Material constraints leading to the observation of exotic properties were documented and illustrated from various fields. Although on first sight, the findings from the different disciplines appeared to be unrelated, they can be interpreted on a similar basis with the proposed classification of interfacial sciences.

To develop a unifying theory of Interfacial Mesoscale Sciences, it is necessary, as a combined effort, to classify the field. The classification presented here represents a first step. We urge the reader to reflect on this when reading the subsequent contributed chapters.

References

(1) Abbott, E. A. *Flatland - A Romance of Many Dimensions*; Dover Publ.: New York, 1992.
(2) Love, A. E. H. *A treatise on the mathematical theory of elasticity*; 4 ed.; Dover Publ.: New York, 1927.
(3) Jeans, J. H. *Roy. Soc. Proc. (Ser.A)* **1923**, *102*, 554.
(4) Tissue, B. M. *Chem. Mater.* **1998**, *10*, 2837.
(5) Goldburt, E. T.; Kulkarni, B.; Bhargava, R. N.; Taylor, J.; Libera, M. *J. Lumin.* **1997**, *72/74*, 190.
(6) Chen, X. L.; Jenekhe, S. A. *Macromolecules* **1996**, *29*, 6189-6192.
(7) Jenekhe, S. A.; Zhang, X.; Chen, X. L. *Chem. Mater.* **1997**, *9*, 409-412.
(8) Osaheni, J. A.; Jenekhe, S. A.; Perlstein, J. *J. Phys. Chem.* **1994**, *98*, 12727-12736.
(9) Zhang, X.; Jenekhe, S.; Perlstein, J. *Chem. Mater.* **1996**, *8*, 1571-1574.
(10) Bhargava, R. N. *J. Lumin.* **1996**, *70*, 85.
(11) Wolf, D.; Wang, J.; Phillpot, S. R.; Gleiter, H. *Phys. Rev. Lett.* **1995**, *74*, 4686.
(12) Itoh, T.; Furumiya, M. *J. Lumin.* **1991**, 704.
(13) Takagahara, T. *J. Lumin.* **1996**, *70*, 129.
(14) Wright, J. C. *Amorph. Mater.* **1985**, *12*, 505.
(15) G.A., W.; Beeson, K. W. *J. Mater. Res.* **1990**, *5*, 1573.
(16) Liu, Y.; Russell, T. P.; Samant, M. G.; Stohr, J.; Brown, H. R.; CossyFavre, A.; Diaz, J. *Macromolecules* **1997**, *30*, 7768-7771.
(17) Frank, B.; Gast, A. P.; Russel, T. P.; Brown, H. R.; Hawker, C. *Macromolecules* **1996**, *29*, 6531-6534.
(18) Overney, R. M.; Guo, L.; Totsuka, H.; Rafailovich, M.; Sokolov, J.; Schwarz, S. A. *Interfacially confined polymeric systems studied by atomic force microscopy*; Material Research Society:, 1997.

(19) Rabeony, M.; Pfeiffer, D. G.; Behal, S. K.; Disko, M.; Dozier, W. D.; Thiyagarajan, P.; Lin, M. Y. *J. Che. Soc. Faraday Trans.* **1995**, *91*, 2855-61.

(20) Green, P. F.; Christensen, T. M.; Russel, T. P.; Jérôme, J. J. *J. Chem. Phys.* **1990**, *92*, 1478.

(21) Russel, T. P.; Menelle, A.; Anastasiadis, S. H.; Satija, S. K.; Majkrzak, C. F. *Macromolecules* **1991**, *24*, 6263.

(22) Zheng, X.; Rafailovich, M. H.; Sokolov, J.; Strzhemechny, Y.; Schwarz, S. A.; Sauer, B. B.; Rubinstein, M. *Phys. Rev. Lett.* **1997**, *79*, 241-244.

(23) Brogley, M.; Bistac, S.; J., S. *Macromol. Theor. Simul.* **1998**, *7*, 65-68.

(24) Buenviaje, C.; Ge, S.; Rafailovich, M.; Sokolov, J.; Drake, J. M.; Overney, R. M. *Langmuir* **1999**, in press.

(25) Overney, R. M.; Buenviaje, C.; Luginbuehl, R.; Dinelli, F. *J. Thermal Anal. and Cal.* **2000**, in press.

(26) Israelachvili, J. N. *Intermolecular and Surface Forces, 2nd Ed.*; Academic Press:, 1992.

(27) Meyer, E.; Overney, R. M.; Dransfeld, K.; Gyalog, T. *Nanoscience, Friction and Rheology on the Nanometer Scale*; World Scientific: Singapore, 1998.

(28) Montfort, J. P.; Hadziioannou, G. *J. Chem. Phys.* **1988**, *88*, 7187-7196.

(29) Israelachvili, J. N. *Pure & App. Chem.* **1988**, *60*, 1473.

(30) Israelachvili, J. N.; Kott, S. J.; Fetters, L. J. *J. Polym. Sci., Phys. Ed.* **1989**, *27*, 489.

(31) Klein, J.; Kamiyama, Y.; Yoshizawa, H.; Israelachvili, J. N.; Fredrickson, G. H.; Pincus, P.; Fetters, L. J. *Macromolecules* **1993**, *26*, 5552.

(32) Luengo, G.; Schmitt, F.-J.; Israelachvili, J. *Macromolecules* **1997**, *30*, 2482-2494.

(33) Thompson, P. A.; Robbins, M. O.; Grest, G. S. *Israel J. Chem.* **1995**, *35*, 93.

(34) Yoshizawa, H.; McGuiggan, P.; Israelachvili, J. N. *Science* **1993**, *259*, 1305.

(35) Gee, M. L.; McGuiggan, P. M.; Israelachvili, J. N.; Homola, A. M. *J. Chem. Phys.* **1990**, *93*, 1895.

(36) Christenson, H. K.; Gruen, D. W. R.; Horn, R. G.; Israelachvili, J. N. *J. Chem. Phys.* **1987**, *87*, 1834-41.

(37) Cho, Y. K.; Dhinojwala, A.; Granick, S. *J. Polymer Sci. Part B - Polymer Physics* **1997**, *35*, 2961-2968.

(38) Granick, S. *Science* **1991**, *253*, 1374.

(39) Granick, S.; Hu, H.-W. *Langmuir* **1994**, *9*, 1983.

(40) Granick, S. *MRS Bulletin* **1996**, *21*, 33-6.

(41) Hu, H.-W.; Carson, G. A.; Granick, S. *Phys. Rev. Lett.* **1991**, *66*, 2758.

(42) Hu, H.-W.; Granick, S. *Science* **1992**, *258*, 1339.

(43) Reiten, G.; Demirel, A. L.; Peanasky, J.; Cai, L. L.; Granick, S. **199**.

(44) Israelachvili, J.; McGuiggan, P.; Gee, M.; Homola, A.; Robbins, M.; Thompson, P. *J. Phys.-Cond. Matter* **1990**, *2*, SA89.

(45) Bordarier, P.; Rousseau, B.; A.H., F. *Molecular Simulation* **1996**, *17*, 199.

(46) O'Shea, S. J.; Welland, M. E. *Langmuir* **1998**, *14*, 4186.

(47) Gao, J. P.; Landman, U. *Phys. Rev. Lett.* **1997**, *79*, 705.

(48) Winkler, R. G.; Schmid, R. H.; Gerstmair, A.; Reineker, P. *J. Chem. Phys.* **1996**, *104*, 8103.

(49) He, M.; Szuchmacher, A.; Overney, R. M. *in preparation* **2000**.

(50) Kopelman, R. *Science* **1988**, *241*, 1620.
(51) Hansen, R. S.; Wallace, T. C. *J. Phys. Chem.* **1959**, *63*, 1085.
(52) Defay, R.; Hommelen, J. R. *J. Colloid. Sci.* **1959**, *14*, 411.
(53) Von Smoloushowski, M. *Z. Phys. Chem.* **1917**, *92*, 192.
(54) de Gennes, P. G. *J. Chem. Phys.* **1981**, *76*, 3316.
(55) Reiner, M. *Phys. Today* **1964**, *January*, 62.
(56) Israelachvili, J. N. *Science* **1988**, *240*, 189.
(57) Yoshizawa, H.; Israelachvili, J. N. *J. Phys. Chem.* **1993**, *97*, 11300.
(58) Yoshizawa, H.; Chen, Y.-L.; Israelachvili, J. N. *Weat* **1993**, *168*, 161.
(59) Gao, J.; Luedtke, W. D.; Landman, U. *J. Phys. Chem. B* **1998**, *102*, 5033.
(60) Prandtl, L. *Z. Angew. Math. Mechanik* **1928**, *8*, 85.
(61) Tomlinson, G. A. *Phil. Mag.* **1929**, *7*, 905.
(62) Overney, R. M.; Takano, H.; Fujihira, M.; Paulus, W.; Ringsdorf, H. *Phys. Rev. Lett.* **1994**, *72*, 3546-49.

Chapter 2

Is There an Optimal Substrate Geometry for Wetting (at the Microscopic Scale)?

J. De Coninck

Université de Mons-Hainaut, Center for Research in Molecular Modeling, 20, Place du Parc, 7000 Mons, Belgium (tel.: +32.65.37.80.80; fax: +32.65.37.38.81; email: joel.de.coninck@galileo.umh.ac.be)

The Young's equation is the well-known relationship used to describe a sessile drop at equilibrium on top of a solid surface. This relationship has been discussed thermodynamically and microscopically for purely flat surfaces in the literature. To characterize the non-flatness of a surface, one may introduce the Wenzel's roughness r defined as the area of the wall surface devided by the area of its projection onto the horizontal plane. Obviously, r is equal to 1 once the surface is flat. For r>1, it is known that Young's equation has to be modified to take into account the increase of surface. The generalization of Young's relation is the so-called Wenzel's law. In this presentation, we will study this relation within microscopic models. We will in particular show that the roughness may enhance the wetting of the substrate even at the microscopic scale.

1. Introduction

Wetting and spreading are two very active domains of research, not only for academic reasons. Consider a drop of liquid B in coexistence with a gas phase A which is put on top of a substrate W. The key equation describing this situation is the famous Young's equation [1,2]

$$\tau_{AB} \cos\theta = \tau_{AW} - \tau_{BW} \qquad (1)$$

where τ_{ij} refers to the interfacial tension between the media i and j, θ is the equilibrium contact angle represented in fig. 1

24   © 2001 American Chemical Society

This equation (1) describes the relationship between macroscopic interfacial quantities such as the surface tension τ_{AB} and the wall free energy τ_{AW} - τ_{BW}. At this point, it should be pointed out that this relation only makes sense for purely flat and chemically homogeneous substrates. When the solid surface becomes disordered, we then have to consider advancing and receding angles as defined in fig.2 by considering a drop in which we put or from which we take some quantity of liquid.

The difference between θ_A and θ_R measures somehow the quality of a substrate.

Suppose now that the substrate W is rough. It is then natural to wonder what equation (1) becomes and at which scale will roughness play a role in wetting. This is precisely the aim of that paper. It is organized in the following way: section 2 is devoted to the presentation of the problem, the new results are given in section 3; concluding remarks end the contribution.

2. Position of the problem

The first problem lies in the definition itself of roughness. There are indeed several ways, non-equivalent, to define this quantity. Consider to fix the ideas a surface z(x,y) such as represented in fig. 3.
The simplest way to introduce the roughness r is by computing the dispersion of the surface around its mean position $\overline{z}$, i.e.

$$r = \frac{1}{N} \sum_{(x,y)\in \, surface} \left| z(x, y) - \overline{z} \right| \qquad (2)$$

This quantity is widely used in atomic force microscopy techniques to give an example. Now, for wetting, it does not really describe the area of the solid surface, which may be in contact with the liquid. More conveniently, we use in this context the so-called Wenzel's variable r defined as

$$r_{Wenzel} = \frac{\text{Area of the surface}}{\text{Area of the projected surface on the tangential plane}} \qquad (3)$$

Many other possibilities may still be considered, but we will here, for the sake of clarity, concentrate on the last one.

In [3,4], Wenzel suggests that the relation between the wall free energy $\Delta\tau(r) = \tau_{AW} - \tau_{BW}$ of a rough substrate, with roughness r, and the wall free energy $\Delta\tau$ (1) of a purely flat substrate, for which r = 1, is simply linear
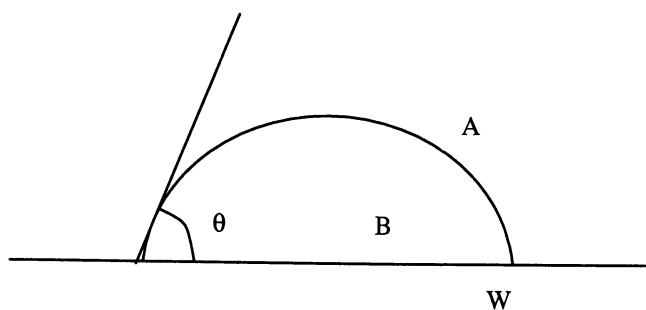
Figure 1. Young's contact angle θ
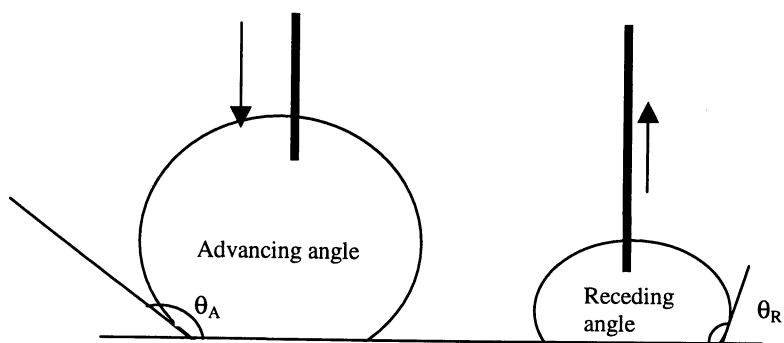
Figure 2. The advancing θ_A and the receding θ_R angles.
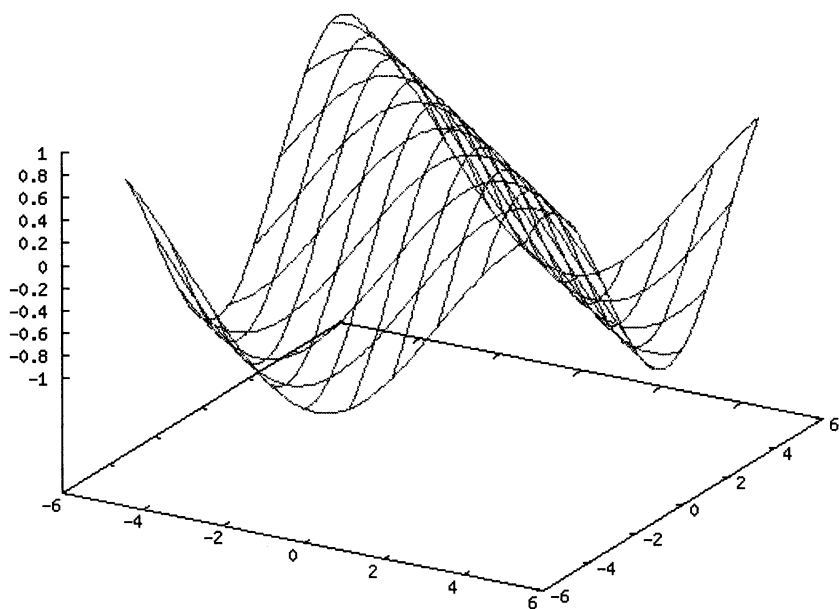
Figure 3. A rough surface z (x, y)

$$\Delta\tau(r) = r_{Wenzel} \cdot \Delta\tau(1) \tag{4}$$

Recent rigorous results [5, 6] based on lattice gas models have shown that there are in fact corrections to that relation which are function of the temperature T

$$\Delta\tau(r) = r_{Wenzel} \cdot \Delta\tau(1) + O\left(e^{-J/kT}\right) \tag{5}$$

where K is the Boltzmann's constant and J is some appropriate coupling constant.

Now, for a given temperature and for two dimensional lattice gas models, it has been shown that different substrate geometries with a fixed Wenzel's roughness r_{Wenzel} lead to different wall free energies $\Delta\tau(r)$ [7]. Indeed, it is easy to show that different geometrical structures of a substrate can yield the same r_{Wenzel} value. For example, a surface decorated by several raised features (hills) will exhibit the same r_{Wenzel} value as a substrate supporting depressions (holes of similar size and density as those of the hills).

These results were obtained via some numerical simulation techniques (Monte Carlo). In this reference [7], different geometries were examined in detail, ranging from elementary deformation of the flat surface, including pores, to more realistic substrates generated randomly with a given roughness. Evidences were given that complex geometries lead to wall tensions that are bounded by those associated with two simple well-characterized substrates, protusion and pits.

These results have been improved recently by a rigorous analysis [8] showing that

$$\Delta\tau^{\inf}(r) \le \Delta\tau(r) \le \Delta\tau^{\sup}(r) \tag{6}$$

where $\Delta\tau^{\inf}(r)$ refers to the single protusion case and $\Delta\tau^{\sup}(r)$ is almost the equipartition protusion-pits case which means that the wall free energy of a substrate for any type of geometry with a fixed roughness r can be bounded approximately by appropriate limits.

Now, the problem with respect to the physics of the phenomenon is the following.

What is the relevant scale at which roughness plays a significant role?

Indeed, one weakness of the developed arguments is that they all refer to lattice gas models. Those models have to be viewed in a coarse graining sense, as renormalization of real systems. The characteristic length scale is therefore hidden in the approximation model itself.

Let us then try to model systems directly at the atomic scale and study the effect of roughness on wetting. We will use molecular dynamics techniques for that.

3. New results

In our simulations, all potentials between atoms, solid as well as liquid, are described by the standard pair-wise Lennard-Jones 12-6 interactions:

$$V_{ij}(r) = 4\varepsilon_{ij}\left(\left(\frac{\sigma_{ij}}{r}\right)^{12} - \left(\frac{\sigma_{ij}}{r}\right)^{6}\right) \tag{7}$$

where r is the distance between any pair of atoms i and j. The parameters ε_{ij} and σ_{ij} are in the usual manner related respectively to the depth of the potential well and the effective molecular diameter [9]. Translated into reduced (dimensionless) units (r.u.), eq. (7) becomes

$$V_{ij}*(r*) = 4\left(\frac{C_{ij}}{r*^{12}} - \frac{D_{ij}}{r*^{6}}\right) \tag{8}$$

where the asterisk stands for reduced units [9]. For simplicity, C_{ij} and D_{ij} are chosen constant for each type of atom. We chose $C_{ff} = D_{ff} = 1.0$, $C_{SS} = 35.0$, $D_{SS} = 5.0$ and $D_{Sf} = D_{Sf} = 0.4$, where the subscripts stand for fluid-fluid (ff), solid-solid (ss) and solid-fluid (sf) interactions. The intrafluid coefficients are standard and the solid-solid coefficients are chosen to produce a stable lattice structure at the temperature of interest. The choice of the solid-fluid interactions ensures that the liquid partially wets the solid. The theoretical range of the Lennard-Jones 12-6 interactions extends to infinity. To be correct, one should therefore evaluate the interactions between all possible pairs in the system. For the system considered here this would add up to about $2.0\ 10^{+10}$ evaluations per time step. Fortunately, the interaction potentials decrease rapidly as the distance becomes large. We therefore apply a spherical cutoff at 2.5, so that the pair potential is set to zero if $r* \geq 2.5$. As a result, we only consider short-range interactions in these simulations. We simulate a molecular structure for the liquid by including a strong elastic bond between adjacent atoms within a molecule, of the form $V_{conf} = D_{conf}\ r^{6}$ with $D_{conf} = 1.0$. The liquid molecules are always 16 atoms long. This extra interaction forces the atoms within one molecule to stay together and reduces evaporation considerably.

We apply a harmonic potential on the solid atoms, so that they are strongly pinned on their initial fcc lattice configuration, in order to give a realistic atomic representation of the solid surface. To give comparable time scales between solid and liquid, we choose $m_{solid} \sim 50 \times m_{liquid}$. To avoid edge effects, we apply periodic

boundary conditions for the solid atoms, in the plane of the solid. The cubic box containing all the atoms is set to be large enough so that the liquid atoms never reach the edges during the simulation.

We are thus considering a very simple chain like liquid system, made by 16 monomers with spherical symmetry, on top of a few layers of a fcc solid lattice.

To compute the associated contact angle, we proceed as follows. First, we subdivide the liquid droplet into several horizontal layers of arbitrary thickness. The constraint on the number of layers is provided by the need to maximize the number of layers whilst ensuring that each layer contains enough molecules to give a uniform density. For each layer, we locate its center by symmetry and compute the density of particles as a function of the distance where the density falls below some cutoff value, usually 0.5, as shown in figure 1. To check the consistency of the method, different layer thicknesses and cutoff values were considered; these gave almost identical results. This method enables us to construct the complete profile of the drop and to determine how it evolves with time. The best circular fits through the profiles were always situated within the region where the density dropped from 0.75 to 0.25, except in the first few layers above the substrate. This indicates that the simulated drops always retain their spherical form during spreading, except very close to the solid surface. Indeed, we expect the profile to be perturbed in the vicinity of the solid for energetic and entropic reasons. To avoid this problem, we investigated the profile as a function of the number of layers used, from top to bottom. Evidently, to reproduce the macroscopic thermodynamics of the drop, we need to consider enough layers and to stay sufficiently far from the substrate. The circular fit using all the experimental points except the last ten above the substrate leads to stable results for drops with more than 20 000 atoms.

Thus, we are able to measure the contact angle θ as a function of the number of time steps during our simulations. Typical results are presented in figure 4 for three different interactions, $C_{sf} = D_{sf} = 0.3$, 0.4 and 0.5, where for the sake of clarity we have translated the curves to the same starting time, 0, at which the drop is just touching the wall in each of the three simulations. If we arbitrarily choose the unit distance to be 5 Å, the unit mass to be 10 times the mass of hydrogen, and the temperature of the solid to be 300 K, then the time unit in the figure is 5 ps. Clearly, the equilibrium contact angle depends strongly on the solid-liquid interactions and decreases with increasing interaction, as expected.

To introduce some roughness on the surface, we have removed regular stripes of atoms (one layer thick) from the perfectly flat case. Typical cases are presented in fig. 5.

A typical series of representative sideview snapshots of our simulations is given in fig. 6 where we have fixed $C_{sf} = D_{sf} = 0.4$.
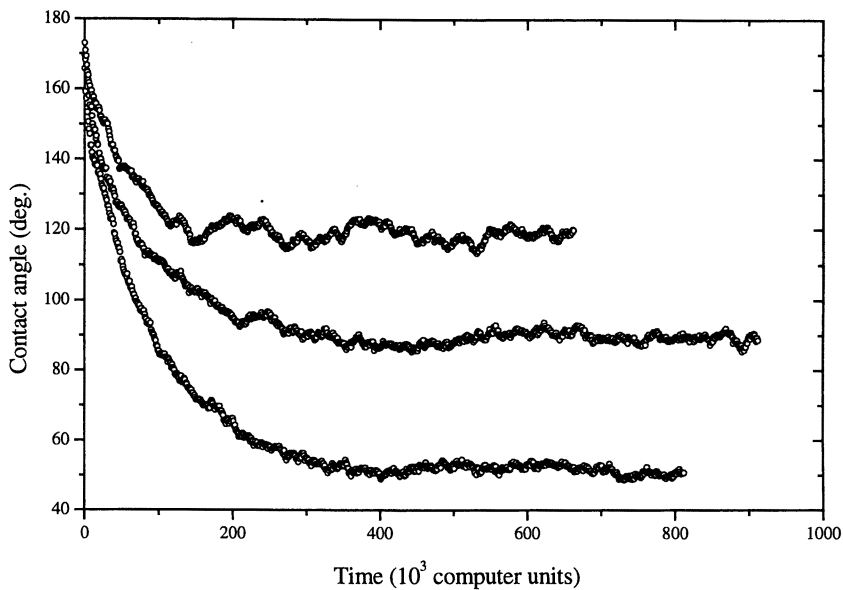
Figure 4. The dependence of contact angle relaxation on the solid-liquid interactions. From top to bottom $C_{sf} = D_{sf} = 0.3, 0.4, 0.5$.
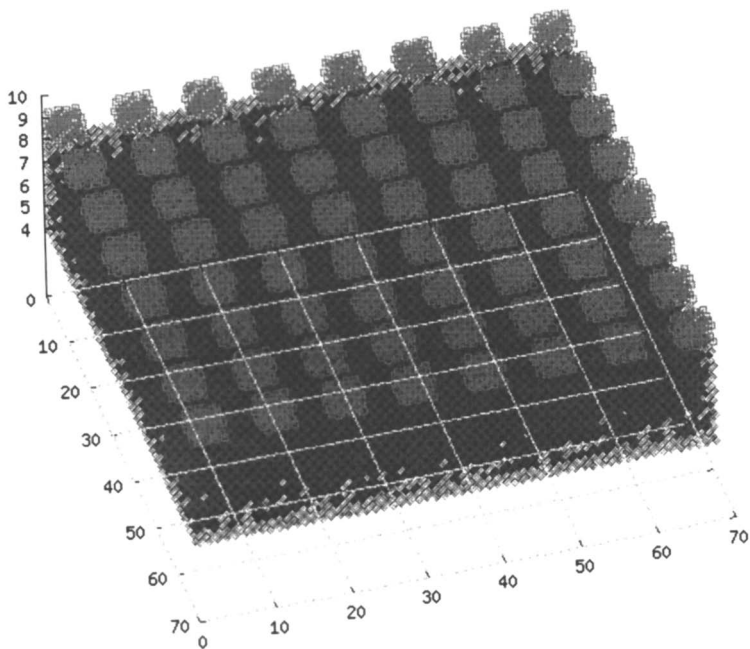
Figure 5. Side view of the solid substrate with regular squares on top of the flat surface to generate different roughness
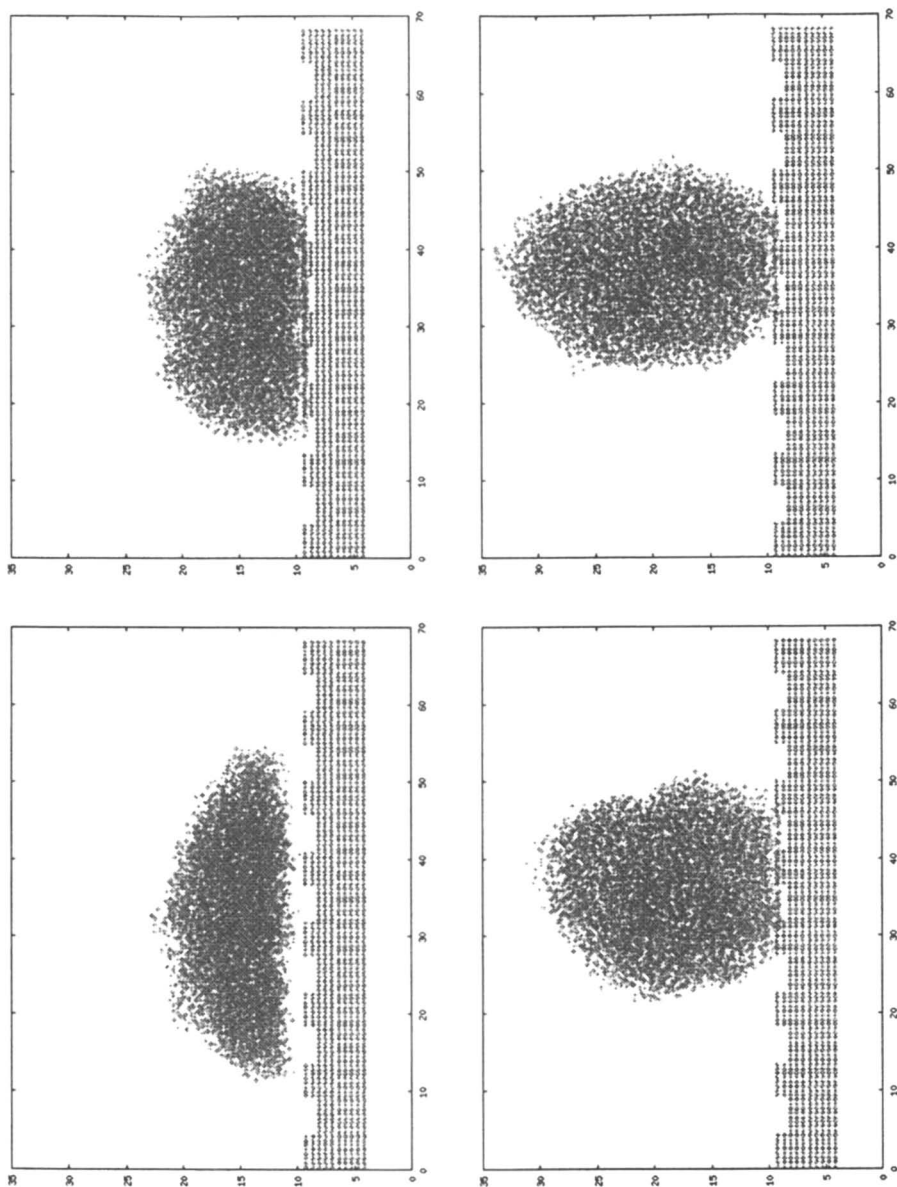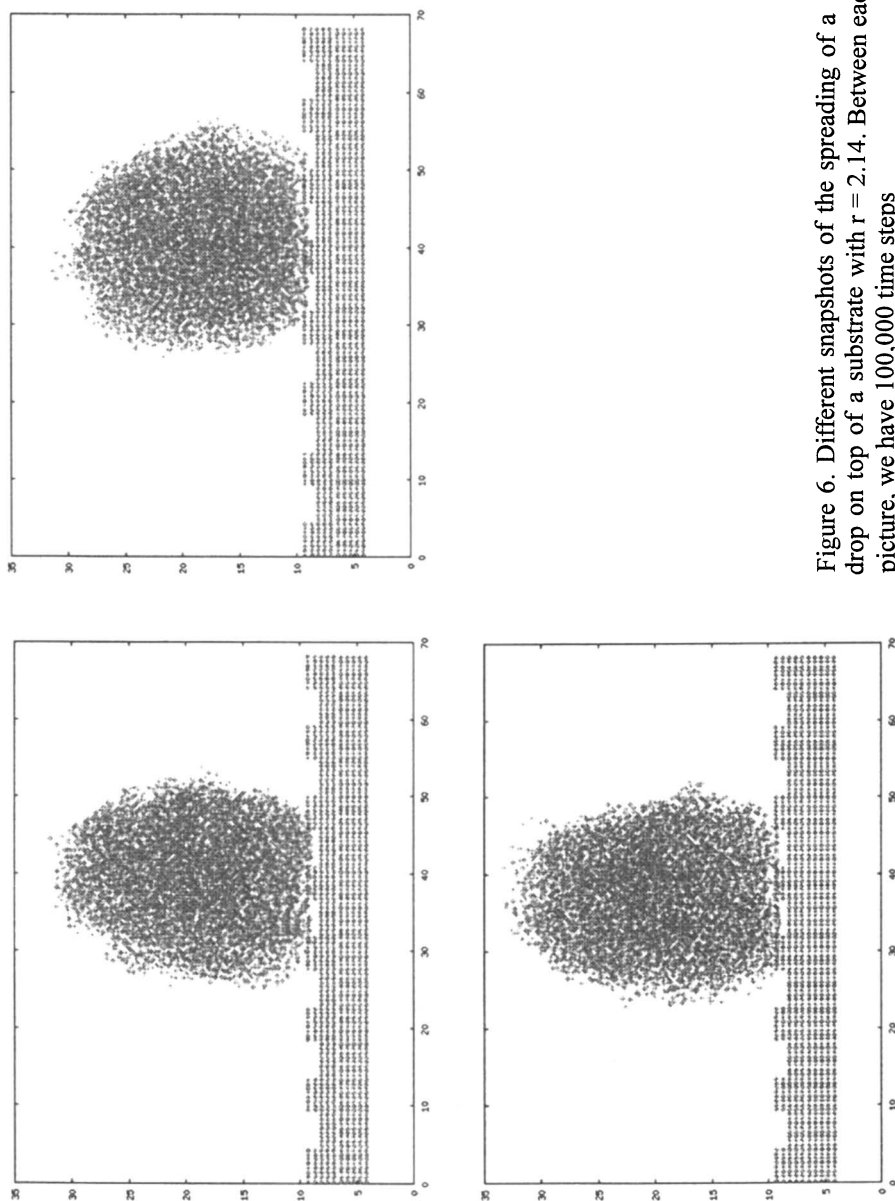
Figure 6. Different snapshots of the spreading of a drop on top of a substrate with r = 2.14. Between each picture, we have 100,000 time steps

After almost 500,000 time steps, we observe stable values for the contact angles of the drops. We plot in fig. 7 the average values over the last 200,000 time steps with statistical deviations. The only variable which has been modified over the simulations is the geometry of the substrate, i.e. its roughness. All the other variables such as the couplings, the temperature ... were kept constant.

Clearly, we observe that the trend is consistent with the Wenzel's law since the considered wall tension is proportional to cos θ as represented in fig. 7.

This result is interesting since it shows that the effect of roughness affects wetting even at the nanoscale.

4. Concluding remarks

We have shown for model systems using molecular dynamics techniques that the roughness of the solid surface plays an important role even at the nanoscale. This shows that the pertinent variable to describe wetting even at that scale certainly has to refer to the Wenzel's variable. To enhance (de) wettability, it is therefore enough to incorporate protusions and pits at the solid surface for cos θ > 0 (cos θ < 0) at least for low enough temperatures. More simulations with more atoms are still needed to discriminate between different geometries for a fixed roughness. This is under current investigations.

Acknowledgements

References

[1] Adamson, A.W. *Physical Chemistry of Surfaces*, 5th Ed.; Wiley & Sons: New York, 1990.

[2] de Gennes, P.G., *Rev. Mod. Phys.*, **1985**, *57*, 827.

[3] Wenzel, R.N., *Ing. Eng. Chem.*, **1936**, *28*, 988.

[4] Wenzel, R.N., *J. Phys. Coll. Chem.*, **1949**, 53, 1466.

[5] C. Borgs, J. De Coninck, R. Kotecky and M. Zinque, *Phys. Rev. Lett.*, **1995**, *74*, 2292-2294.

[6] C. Borgs, J. De Coninck and R. Kotecky, *J. Stat. Phys.*, **1999**, *94*, 299.
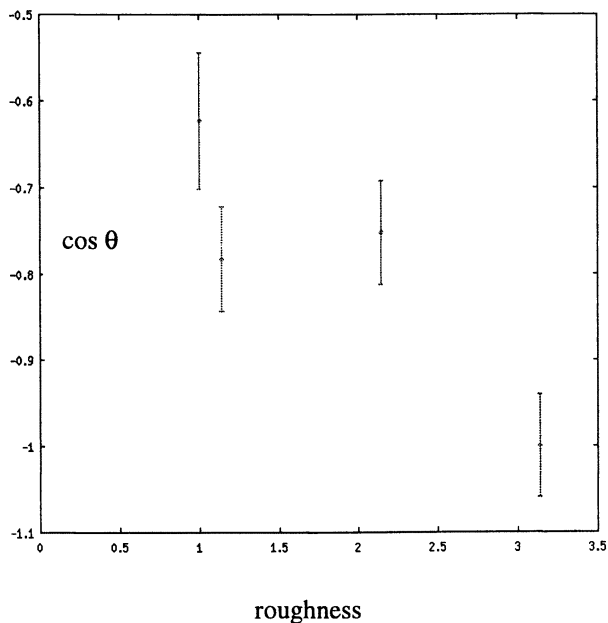
Figure 7. The cosine of the contact angle versus the Wenzel's roughness for C_{sf} = 0.4

[7] K. Topolski, D. Urban, S. Brandon and J. De Coninck, *Phys. Rev. E.*, **1997**, *56*, 3353 – 3357.

[8] J. De Coninck, S. Miracle-Solé and J. Ruiz, submitted for publication to *J. Stat. Phys.*

[9] Allen, M.P. and Tildesley, D.J., *Computer Simulations of Liquids*; **1987**, Oxford University Press.

Chapter 3

Kinetics and Domain Formation in Surface Reactions by Inverted Chemical Force Microscopy and FTIR Spectroscopy

Holger Schönherr[1], Victor Chechik[2,3], Charles J. M. Stirling[2,4], and G. Julius Vancso[1,4]

[1]MESA$^+$ Research Institute and Faculty of Chemical Technology, University of Twente, Materials Science and Technology of Polymers, P.O. Box 217, 7500 AE Enschede, The Netherlands
[2]Department of Chemistry and Center for Molecular Materials, University of Sheffield, Sheffield S3 7HF, United Kingdom

Reaction kinetics of the alkaline hydrolysis of ester groups at the surface of self-assembled monolayers was monitored by a combination of atomic force microscopy (AFM) and FT-IR spectroscopy. In a novel approach, which we termed „inverted" chemical force microscopy (CFM), reactions are studied which take place at the surface of the tip coated with the reactants. The course of the reaction is followed in situ on a scale of less than 100 molecules, corresponding to the contact area between AFM tip and the sample surface at pull-off, by recording force-distance curves. Reactivity differences related to the structure of the monolayers, observed by inverted CFM on the nanometer scale, agree well with average behavior observed by FT-IR. The combined results, together with additional force microscopy data, support the conclusion that for closely packed ester groups, the reaction spreads from defect sites, causing separation of the homogeneous surface into domains of reacted and unreacted molecules.

Self-assembled monolayers (SAMs) of organic molecules on solid substrates offer unique opportunities to enhance fundamental understanding of interfacial phenomena. The high degree of order of the assemblies and the ease of their

---

[3]Current address: Department of Chemistry, University of York, Heslington, York YO10 5DD, United Kingdom.
[4]Corresponding authors.

© 2001 American Chemical Society

preparation make them attractive for fundamental studies on *e.g.* wettability [1], tribology or lubrication [2]. As shown in this paper, SAMs can be useful also as model systems for surface reactions [3].

The confinement of functional groups can result in a markedly different reactivity. For example, Töllner et al. reported significantly enhanced catalysis of acetone hydrogenation probably because of an enforced (favorable) orientation of a rhodium complex incorporated in corresponding Langmuir-Blodgett films [4]. Penetration of external reagents to functional groups buried in well-packed monolayers is usually restricted, and reactivity is thus reduced [5,6].

In situ molecular level studies of chemical reactions have largely eluded surface scientists until recently. However, the recent developments in the field of scanning probe techniques promise to give novel insights in processes at surfaces or interfaces, as surface studies with nanometer resolution can be carried out in different media or in different environments. It is therefore not surprising that surface processes have already been studied with high resolution scanning probe microscopies [7]. For instance, *ex situ* AFM using chemically modified tips provides information about surface energy changes related to interfacial reactions [8]. Previously, *in situ* AFM was applied predominantly to monitor topographical changes, *e.g.* in crystal growth or dissolution, in crystallization of polymers from the melt, and in solid state isomerization reactions [9].

All the aforementioned observations are, in general, limited by the finite contact area between AFM tip and the sample surface. Depending on the radius of curvature of the AFM tips, on the materials properties, and on the imaging force, the radius of the contact area can be estimated to be between 2 and 5 nm [10]. As a consequence, the *true* resolution is often *much* lower than the nominal accuracy of positioning the specimen and the sensitivity of height or lateral force data [11]. Strictly speaking, the "high" molecular resolution obtained with conventional contact mode AFM (*e.g.* for periodic lattice structures found for SAMs) [12] corresponds to a "lattice resolution". As shown recently [13], lattice resolution can be considered as an average over the periodic electron density distribution of the actual contact area. In any case, the true resolution of AFM in imaging of surface reactions in liquid can be assumed to be no better than several nm.

In addition, thermal and instrumental drift make high resolution imaging of chemical reactions very difficult or often impossible. Since the area imaged is changing constantly, and furthermore "reference points" such as topographical features might change as well as a consequence of the reaction, the lateral resolution is practically below the true physical resolution briefly discussed above.

As described here, these problems can be circumvented by "inverted" chemical force microscopy (CFM) [14]. In inverted CFM, pull-off forces [15] between the tip coated with the reactant and an inert surface are monitored as a function of time (Figure 1). The contact area of the tip at pull-off in such experiments using non-reactive SAMs (as inert samples) deposited on Au(111) varies between approximately 10 - 100 effectively interacting molecular pairs [16,17].

Depending on the changes in the pull-off forces with the extent of the reaction, the effective force per interacting molecular pair, as well as the number of interacting pairs, can vary [16]. Thus, one can, in principle, monitor chemical reactions with a resolution of the number of contacting pairs of molecules in AFM force measurements provided that the conversion of the reactants to products is
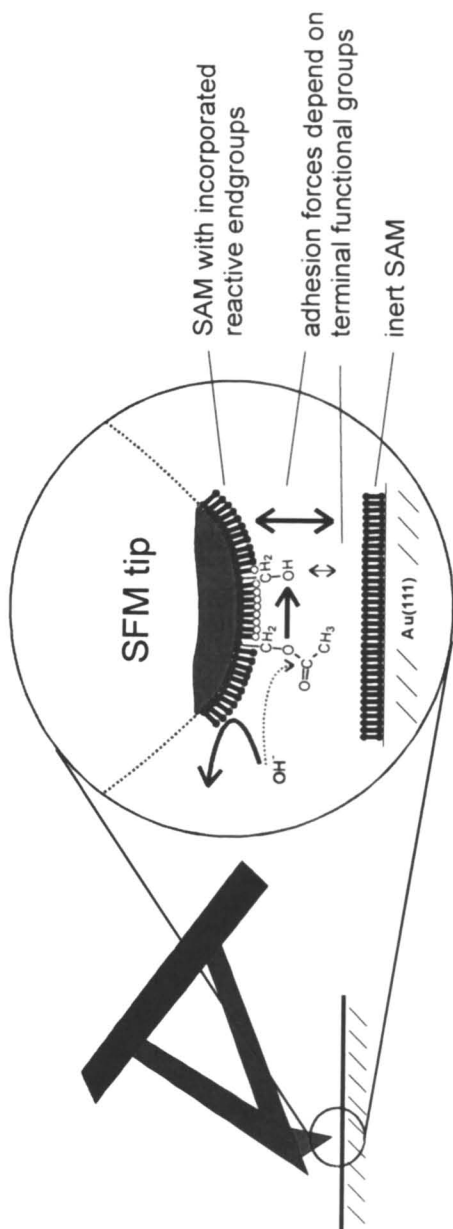
Figure 1. In "inverted" chemical force microscopy the pull-off forces of a reactant-covered AFM tip are measured in situ during the conversion of the reactive groups. The interaction between tip and inert surface varies with the extent of the reaction. The approach is depicted schematically for the reaction of ester groups to hydroxyl groups in aqueous NaOH. (Adapted with permission from reference 14. Copyright 2000 American Chemical Society.)

accompanied by changes in the pull-off forces. As demonstrated here, the kinetics of surface reactions can be followed *in situ* on a *non-continuum* level (10 - 100 molecules) by this technique. In combination with FT-IR spectroscopy and additional AFM data interfacial reaction mechanisms were successfully elucidated [14].

Experimental

Materials. Compounds **1 - 3** were synthesized as described elsewhere [14]. The crude products were isolated by flash chromatography and characterized by ^{1}H, ^{13}C NMR, IR spectroscopy, mass spectrometry, and elemental analysis. HPLC grade dichloromethane and ethanol were purchased from Aldrich and used as such. Millipore Milli-Q water was used in all experiments.

Preparation of SAMs. SAMs for FT-IR analysis were self-assembled from 1 mM solutions of compounds **1, 2,** or **3** in dichloromethane for 16 h onto evaporated gold as described in reference 18. SAMs for AFM experiments were prepared similarly at RT on annealed Au(111) substrates as described in reference 19.

Instrumentation. IR spectra of monolayers were determined with a Perkin-Elmer 1725 X instrument fitted with an MCT detector and a grazing angle accessory (Spectra-Tech Inc.). Freshly cleaned (conc. HNO_3, 10 min) bare gold slides were used as background. The sample compartment of the spectrometer was purged with nitrogen.

AFM and Tip Modification. Triangular shaped silicon nitride cantilevers and tips (Digital Instruments (DI), Santa Barbara, CA, USA) were covered with 50 - 70 nm of gold in a Balzers SCD 040 sputtering machine at an argon pressure of 0.1 mbar or alternatively with ca. 2 nm Ti and ca. 75 nm Au in high vacuum (Balzers). The gold covered tips were then functionalized with SAMs of **1, 2,** or **3** following the procedures described in references 8b, 8c, and 18. The AFM measurements were carried out with a NanoScope II and a NanoScope III multimode AFM (DI) utilizing a liquid cell. The force measurements were performed with modified tips, and the imaging with unmodified silicon nitride tips, respectively. Cantilever spring constants were calibrated as described in reference 20. Tapping mode AFM images of the Au(111) substrate were acquired as described in references 8b and 8c.

Inverted CFM. The functionalized AFM tip was placed in the liquid cell. After a brief equilibration period in ultrapure water the tip was engaged on an octadecanethiol SAM on Au(111) and a set of force-distance curves was recorded. After withdrawal of the tip the cell was flushed with more than 20 times the cell volume of aqueous NaOH. After a stable photodiode reading the tip was engaged again on the octadecanethiol SAM. Immediately after engaging force-distance curves were recorded in intervals of 30 (60) seconds. The mean of 10 individual pull-off events, measured after each 30 seconds (60 seconds for slow reactions), was calculated. The conversion x, of ester groups to hydroxyl groups was calculated from:

$$x = [F_0 - F_t]/[F_0 - F_\infty] \tag{1}$$

where F_0, F_t and F_∞ denote the measured average pull-off force at t = 0, at t = t and t = ∞, respectively [8a] . This equation is based on the JKR theory, which states that on a flat surface the pull-off force F of a sphere with radius R changes linearly with the work of adhesion W_{ad} [28].

$$F = -3/2 \, \pi \, R \, W_{ad} \qquad (2)$$

The surface free energy of the tip γ_{tip} and the interfacial free energy $\gamma_{tip-substrate}$ are assumed to be only influenced by changes in the endgroup while the surface free energy of the inert substrate $\gamma_{substrate}$ is assumed to be constant [8a].

$$W_{ad} = \gamma_{tip} + \gamma_{substrate} - \gamma_{tip-substrate} \qquad (3)$$

Results and Discussion

In this paper we will first discuss the characterization of the SAMs studied, followed by the determination of reaction kinetics using FT-IR spectroscopy. After presenting the results of the new approach, namely inverted CFM, applied to in situ studies of the reaction kinetics of an ester hydrolysis, additional in situ AFM friction images will be shown.

SAM Characterization

The structure of the SAMs of compounds 1 - 3 (Figure 2) was investigated in detail using contact angle, FT-IR spectroscopy, and surface plasmon resonance spectroscopy. The data was consistent with the formation of tightly-packed SAMs, which exposed the corresponding ω-functional groups at the SAM-air interface.

The FT-IR data fully agreed with literature data on similar films [21]. The asymmetric stretching vibrations $v_a(CH_2)$ at 2919-2920 cm^{-1} are typical of alkane chains in an all-*trans* conformation [22] and the $v(C-O)$ vibration at 1259-1262 cm^{-1} was shifted to higher frequencies as compared with bulk spectra (1240-1242 cm^{-1}), which is indicative for strong lateral interactions between adjacent carbonyl groups in ordered quasi-crystalline environments [23]. SAMs of 3 showed a higher frequency $v_a(CH_2)$ vibration (2922 cm^{-1}) and the water contact angle of SAMs of 3 was lower than those of 1 and 2, indicating partial exposure of hydroxyl groups at the monolayer surface [24,25].

Ester Hydrolysis Studied Ex Situ by FT-IR

The ester hydrolysis was carried out in 1.0 M aqueous sodium hydroxide at room temperature. Average "macroscopic" kinetics were determined by FT-IR spectroscopy following the decrease of the integrated intensity of the $v(C=O)$, $v(C-O)$, and $\delta_s(CH_3)$ vibrations *ex situ*. SAMs of thiol 1 (and disulfide 2) reacted much more slowly than SAMs of the mixed disulfide 3 (Figure 3). The kinetics of the mixed disulfide 3 was exponential while 1 and 2 showed sigmoid behavior.
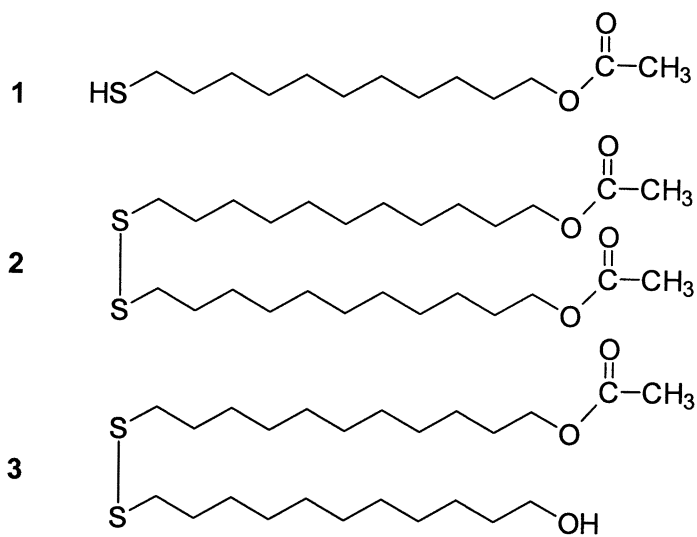
Figure 2. Compounds used for the formation of self-assembled monolayers. (Reproduced with permission from reference 14. Copyright 2000 American Chemical Society.)
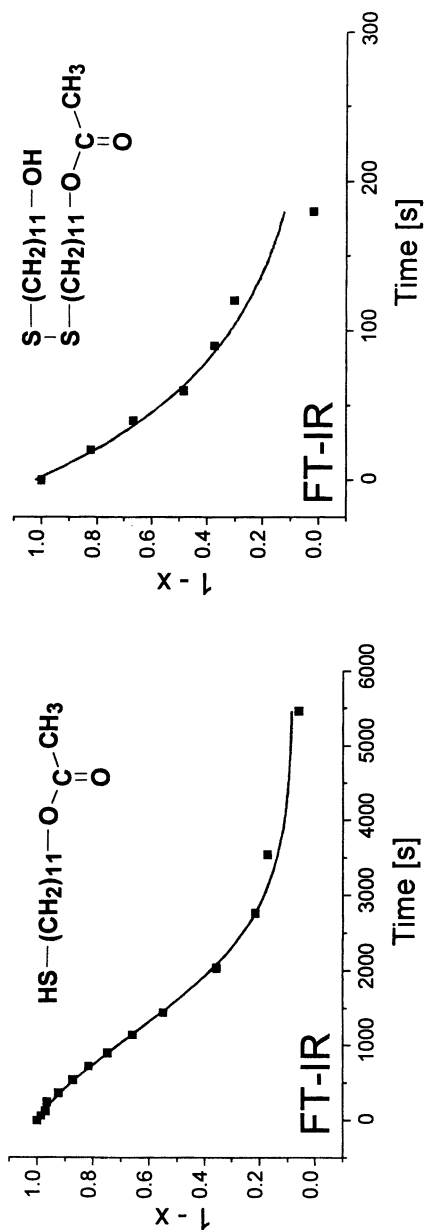
Figure 3. Hydrolysis ([1-x] as a function of reaction time t; with extent of reaction x) in 1 M NaOH as determined by FT-IR for thiol 1 (left) and disulfide 3 (right). (Adapted with permission from reference 14. Copyright 2000 American Chemical Society.)

The half reaction times are listed in Table I. For **3**, the pseudo first order rate constant k_{FT-IR} was 1.00×10^{-2} s^{-1}.

Table I. Half-reaction times $\tau_{1/2}$ as determined by FT-IR (ex situ hydrolysis in 1.0 M NaOH)

SAM	$\tau_{1/2}$
1	1644 s
2	684 s
3	72 s

In monolayers **1** and **2**, which possess a close-packed surface of ester groups, the access of hydroxide ions to the carboxyl groups appears to be hindered although the carboxyl groups are very near to the surface. A similar, initially low reactivity and sigmoid kinetic behavior is known for perfect crystals [26]. SAMs of esters **1** and **2** at 50% conversion would at first sight appear to be equivalent to SAMs of the mixed disulfide **3**. The reaction of esters **1** and **2** at 50% conversion is however, *ca.* 10-20 times slower than that of ester **3** [27].

Ester Hydrolysis Studied In Situ by Inverted CFM

The origin of the differences in reactivity mentioned above must lie in the structure of the surface of the SAMs. *In situ* information on the composition of the reacting monolayers was obtained by the "inverted" chemical force microscopy approach described in the introduction. In these experiments, the force required to pull the AFM tip coated with **1**, **2**, or **3** away from contact with an inert octadecanethiol SAM on flat Au(111) was followed in real time *in situ* during the hydrolysis. The Au(111) substrates are atomically smooth over distances of several hundred nanometers with only occasional steps and depressions present (Figure 4). With highly ordered octadecanethiol SAMs on top of these substrates it is ensured that the interaction between tip and surface takes place between exactly the same functional groups at the tip apex and a homogeneous inert substrate.

The *individual* reaction profiles for thiol **1** and disulfide **2** showed significant induction periods (Figure 5). These periods were found to depend on the hydroxide concentration (Table II). For SAMs of the mixed disulfide **3** no induction periods were observed. Test experiments with (inert) octadecanethiol-coated tips showed that SAM damage does not occur and that the SAM / gold assembly stays intact over the typical experiment times. The AFM results are summarized in Table II.

The change in surface composition could be measured accurately because the adhesive force between ester (the reactant) and alkyl-terminated surfaces is large. Average pull-off forces measured between *neat* ester-SAMs and methyl-terminated tips were found to be 9 ± 2 nN, whereas neat hydroxyl-terminated SAMs and methyl-terminated tips show an average pull-off force of 0.4 ± 0.3 nN.
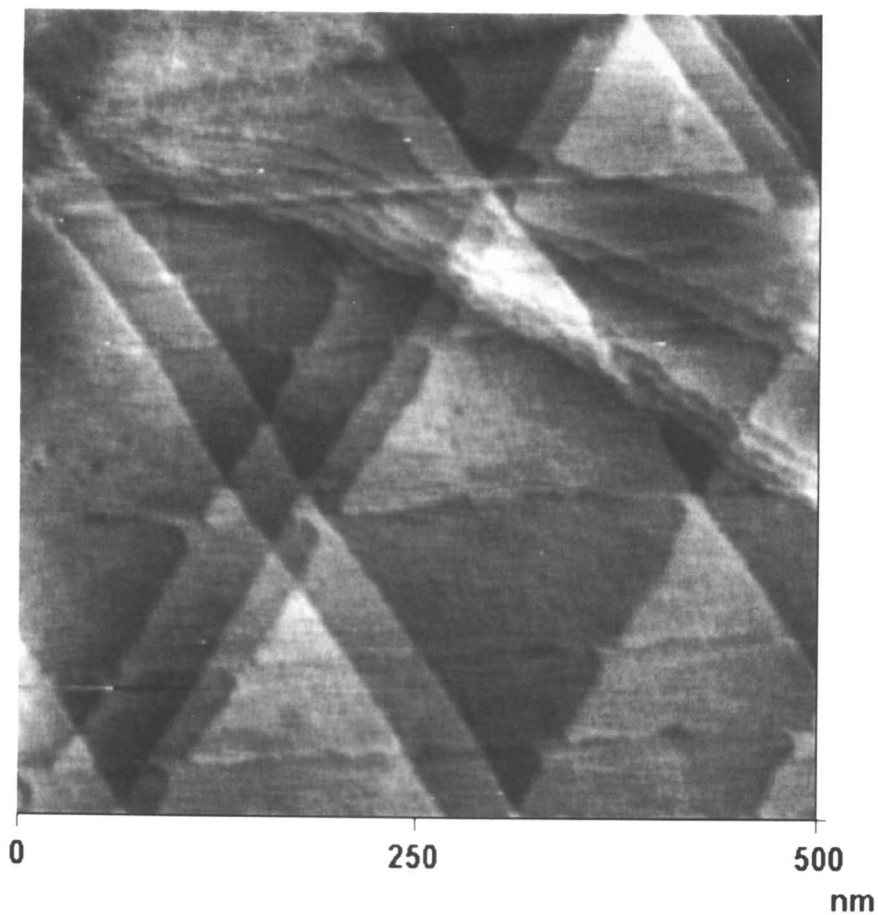
Figure 4. Tapping mode AFM height image of Au(111) substrate covered with inert octadecanethiol SAM (z-scale from black to white 5.0 nm). (Adapted with permission from reference 14. Copyright 2000 American Chemical Society.)

These forces follow the trend predicted by the Johnson-Kendall-Roberts theory of contact mechanics [16,28].

In Figure 6, the results of four individual experimental curves for thiol **1** recorded under identical conditions are shown. These *individual* reaction profiles showed a wide distribution of induction periods, indicated here by the arrows.

The contact area between the tip and the surface at pull-off is smaller than the typical domain size in SAMs [29]. If the reaction starts at defect sites, the variable induction periods can be attributed to the time elapsed before a defect is formed in the contact area between ester-modified tip and alkyl-terminated inert surface. If a defect is already present in the contact area, the observation of the reaction starts instantaneously, and consistently the induction period is small or non-existent. If there are no defects in the contact area, the reaction cannot be observed before a defect is formed, or alternatively, the reaction front reaches the contact area. This interpretation is corroborated by an estimate of the domain size based on the observed induction times and reaction kinetics [30]. From the data summarized in Table II a maximum domain size of 3.2 ± 0.2 nm for thiol **1**, and 2.6 ± 1.2 nm for the symmetric disulfide **2** can be estimated. These values are in agreement with literature data [31].

The observed distribution of induction periods is a strong indication for separation of reacted (-OH) and unreacted (-O-CO-CH$_3$) terminal groups during the hydrolysis. Thus, the profiles of the different experiments shown in Figure 6 differ because inverted CFM follows the reaction with very high lateral resolution.

Table II.   Kinetics of *in situ* hydrolysis of SAMs on gold-covered AFM tips.

SAM	Concentration NaOH (mol/l)	Average half reaction time $\tau_{1/2}$ (s)	Range of induction periods (s)
1	1.00	365	0 - 560
2	1.00	-	-
3	1.00	28	0
1	0.10	965	0 - 1100
2	0.10	630	150 - 435
3	0.10	220	0
1	0.01	2298	1305 - 1677
2	0.01	1655	100 - 1267
3	0.01	889	0

The macro-kinetic profiles can be obtained by averaging many AFM experiments. These profiles were found to be very similar to the FT-IR profiles. The reaction of SAMs of half-ester disulfide **3** (Figure 8C) gives an *average* second order rate constant $k_{AFM} = 2.4 \times 10^{-2}$ 1 mol^{-1} s^{-1} which is in good agreement with the value obtained by FT-IR (Figures 7 and 8) [32]. By contrast, the SAMs of both thiol **1** and symmetrical disulfide **2** showed sigmoid profiles for the average kinetics (Figure 8). Macro-scale kinetics determined by FT-IR can thus be reproduced by averaging snapshots of the reaction of 10-100 molecules from the AFM experiments.
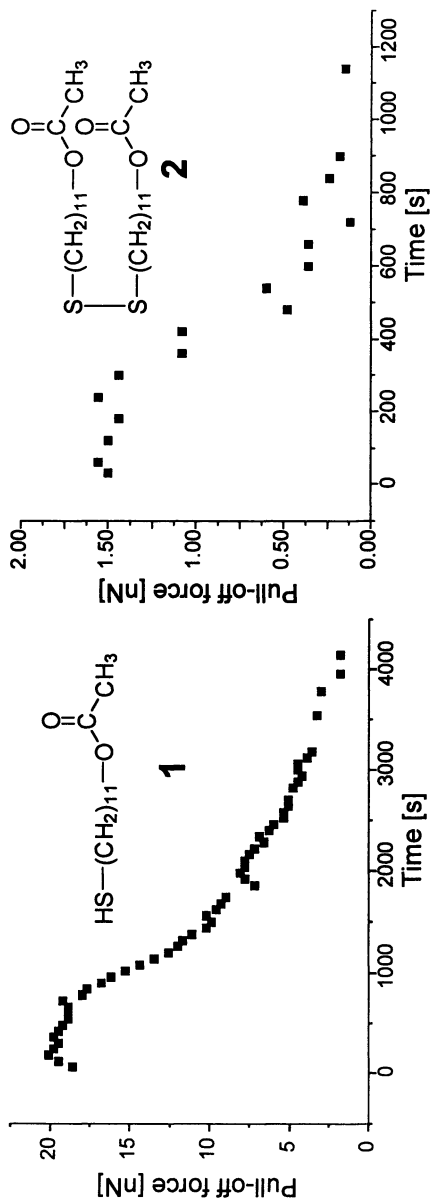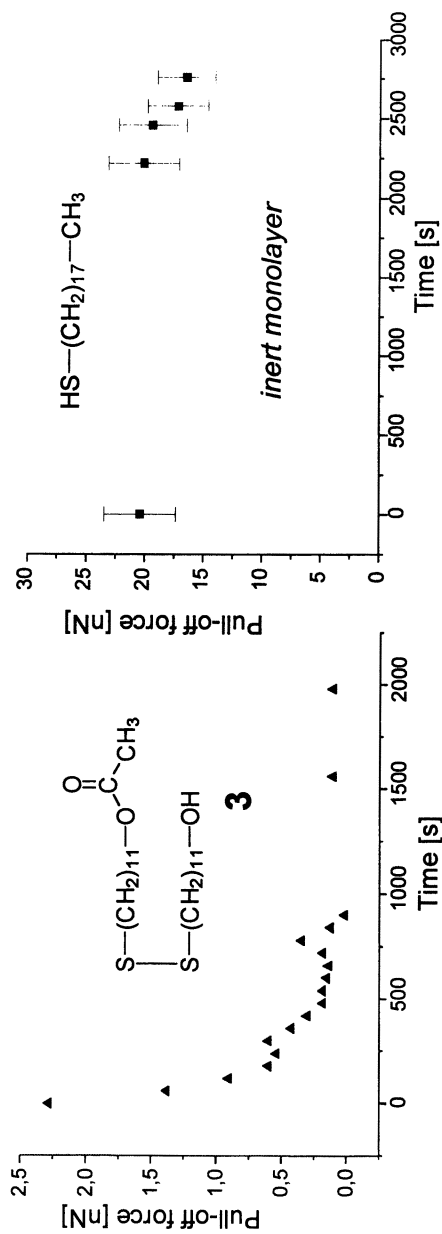
Figure 5. Pull-off forces measured during hydrolysis as a function of reaction time of SAMs of 1, 2, 3, and octadecanethiol in 0.1 M NaOH followed by inverted CFM. Results of representative individual experiments are shown. (Adapted with permission from reference 14. Copyright 2000 American Chemical Society.)
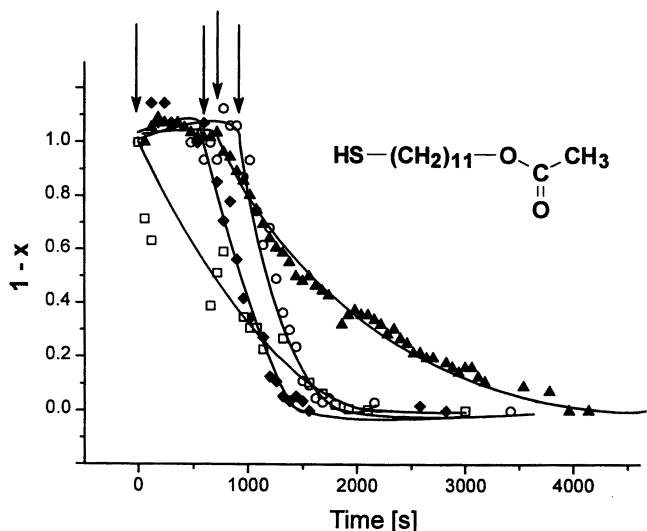
Figure 6. Hydrolysis ([1-x] as a function of reaction time t; with extent of reaction x) of SAMs of 1 in 0.1 M NaOH followed by inverted CFM. Results of four individual experiments are shown. Induction periods (as indicated by arrows) vary between 0 and 1000 seconds. Following the induction periods the reactions proceed at similar rates. The lines have been added to guide the eyes. (Adapted with permission from reference 14. Copyright 2000 American Chemical Society.)
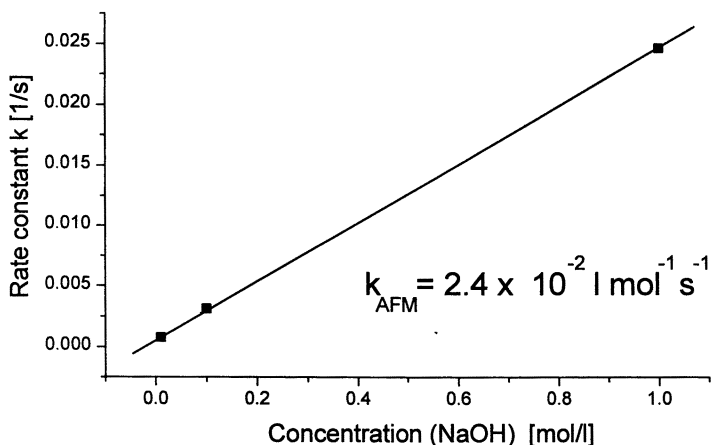
Figure 7. The pseudo first order rate constants for the hydrolysis reaction observed for 3 by inverted CFM depend linearly on the concentration of NaOH. An average second order rate constant $k_{AFM} = 2.4 \times 10^{-2}$ l mol^{-1} s^{-1} can be calculated. (Adapted with permission from reference 14. Copyright 2000 American Chemical Society.)

In Situ AFM Imaging of Hydrolysis

Further indication for the formation of domains of reacted and unreacted molecules during the hydrolysis reaction is obtained from *in situ* contact mode AFM experiments with uncoated tips on SAMs of **1** and **3** on flat Au(111) substrates. As shown in Figure 9, the friction force measured on SAMs of **1** changes significantly during hydrolysis. After ca. 4 minutes the smooth image which shows only the step edges of the Au surface began to change to an image exhibiting a „rippled" appearance. The inhomogeneous friction producing the ripples increased and then disappeared during the course of the reaction. We postulate that the observed „ripples" are related to inhomogeneous adhesion, and hence friction [16], because of the formation of domains of reacted and unreacted molecules during the course of reaction [33].

The inhomogeneous friction producing the ripples can be evaluated by analyzing the deviation of the friction for each pixel from the mean value similar to a roughness analysis [14]. The friction contrast peaks after ca. 15 minutes for thiol **1**, while there is no contrast change for mixed disulfide **3**. These observations are in agreement with the FT-IR and inverted CFM results.

The lattice of the SAMs could be imaged by AFM with molecular (lattice) resolution prior to and after the hydrolysis on the Au(111) terraces shown in Figure 9. In Figure 10 the corresponding high resolution lattice images are shown. The fact that lattice imaging was possible prior to and after the hydrolysis demonstrates that SAM damage can be excluded as origin for the disappearing inhomogeneity of the friction images of **1**. The true resolution of the friction measurements can be assumed to be in the order of 2 - 5 nm which is a typical size for domains in SAMs [29,33]. As the friction contrast did not change significantly in SAMs of the mixed disulfide **3**, the inhomogeneous friction observed for thiol **1** strongly suggests that the reaction proceeds inhomogeneously.

The scenario proposed for the reaction in well-packed SAMs is depicted schematically in Figure 11. The mechanism shown is consistent with the AFM and FT-IR data and accounts for the reactivity differences between half-reacted monolayers of **1** and **2** on the one hand and the monolayers of **3** on the other hand. The macro-compositions are the same, but while the layer of **3** remains homogeneous, **1** and **2** separate into domains during the hydrolysis.

Conclusions

We have demonstrated for the first time that average macroscopic kinetics of reactions in SAMs can be correlated and explained by nanometer level force (adhesion) measurements in the confined environment of the monolayer studied. Using a modified CFM approach, which we termed "inverted chemical force microscopy", reactions of as few as 10 to 100 molecules could be followed *in situ*. Structure-reactivity differences, arising from differences in monolayer structure, as observed on the nanometer scale, on average agree well with macroscopic behavior observed by FT-IR. The studies show that reagents penetrate functionalized monolayers at specific defect sites or at domain boundaries.
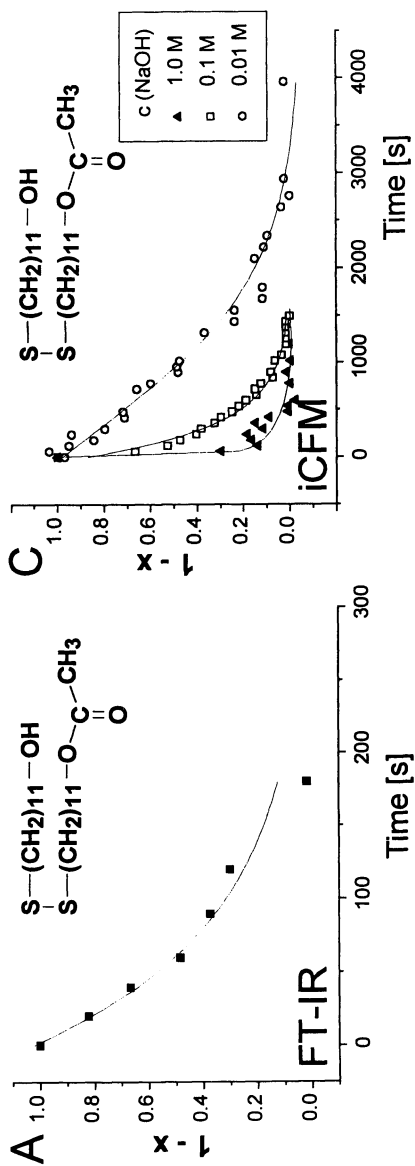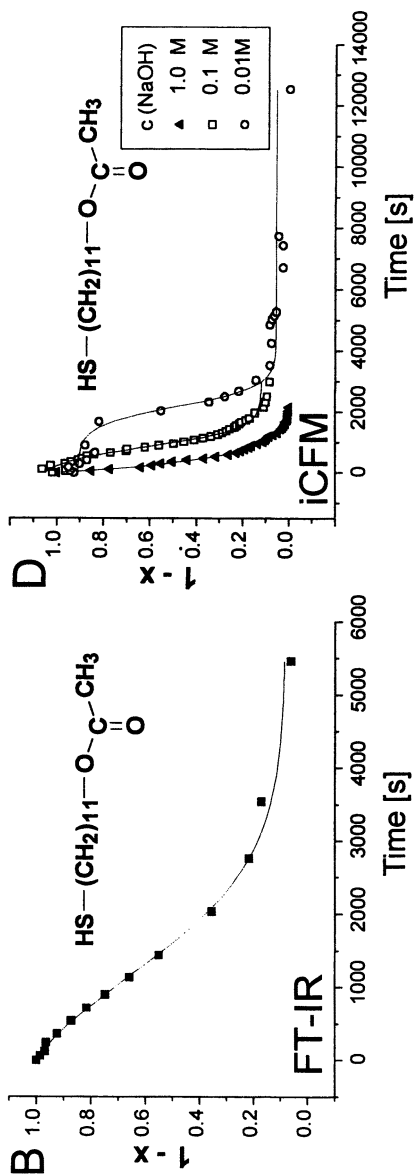
Figure 8. Course of the hydrolysis ([1-x] as a function of reaction time t; x denotes the extent of the reaction) as measured by FT-IR (A, B) for 1 M NaOH and measured by inverted CFM (C, D) for various concentrations. The CFM data was obtained by averaging over many individual experiments. Note the different time scales. The lines correspond to exponential or sigmoid fits, for details see text. (Adapted with permission from reference 14. Copyright 2000 American Chemical Society.)
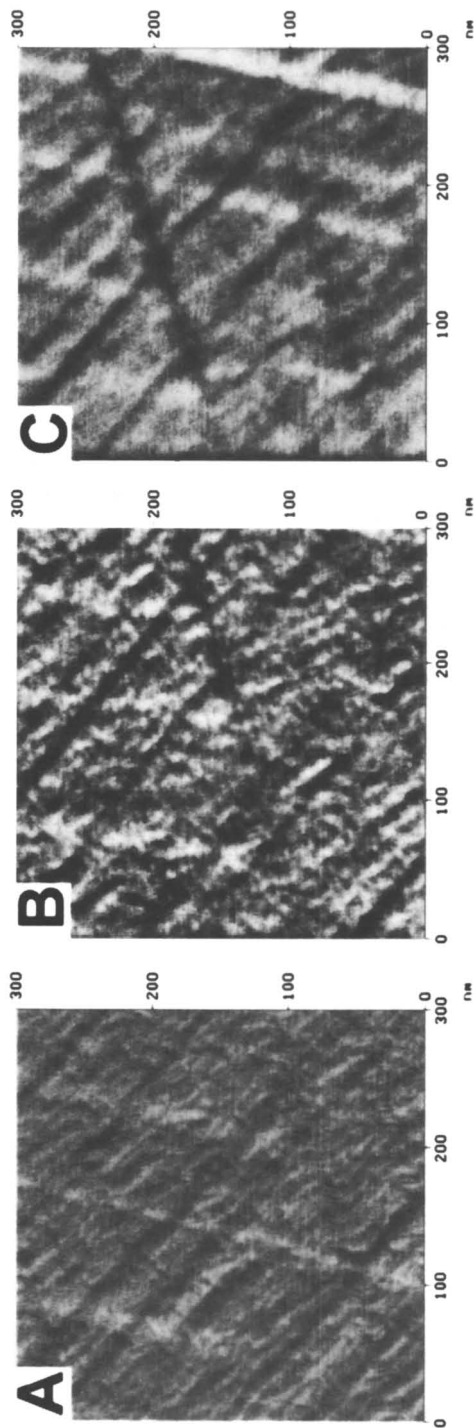
Figure 9. In situ AFM (friction mode with unmodified tip) of hydrolysis of a SAM of 1 on Au(111) in 1 M NaOH (bright color corresponds to high friction; z-scale from black to white: 0.05 V). The images were captured after 4 minutes (A), 13 minutes (B), and 24 minutes (C), respectively. (Adapted with permission from reference 14. Copyright 2000 American Chemical Society.)
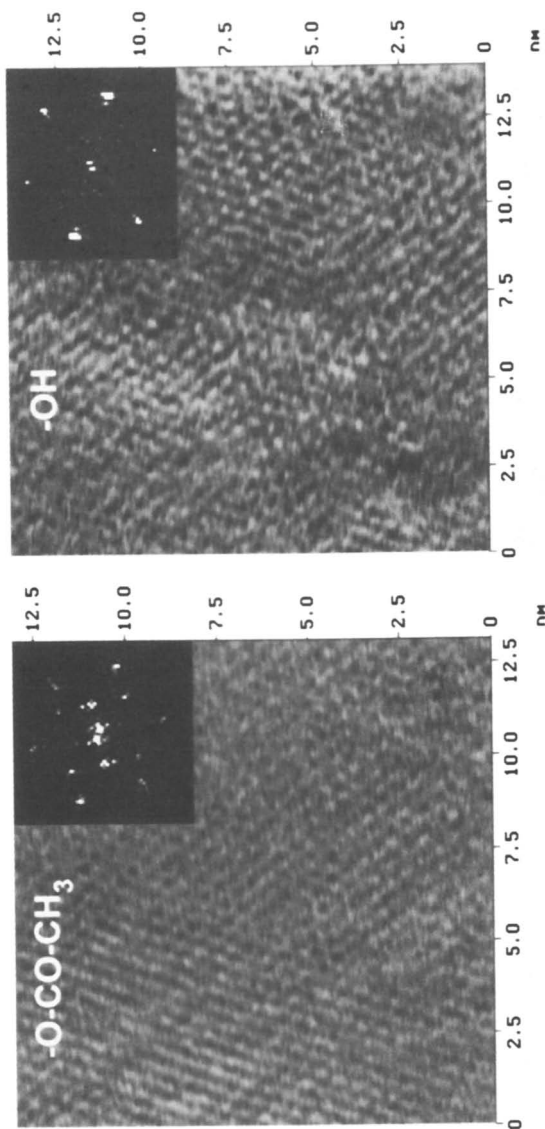
Figure 10. Unprocessed AFM images of SAM of 1 prior to (left) and after (right) hydrolysis in 1 M NaOH (inset: 2-D fast Fourier transform). The lattice constant of the hexagonal lattice was found to be 5.2 ± 0.2 Å. (Adapted with permission from reference 14. Copyright 2000 American Chemical Society.)
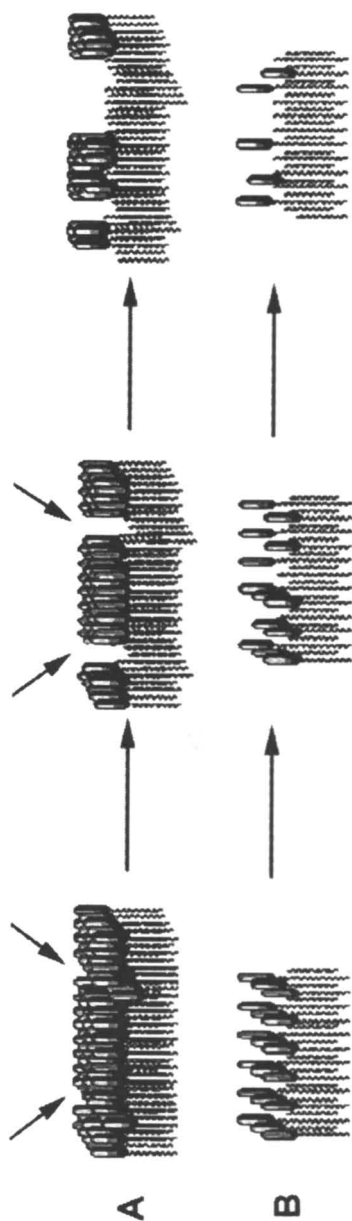
Figure 11. Schematic representation of (A) inhomogeneous reactions for SAMs of thiol **1** and disulfide **2** and (B) the homogeneous reaction of mixed disulfide **3**. The reaction of **1** starts at defect sites (indicated by arrows) and creates domains of reacted and unreacted molecules. The reaction then proceeds at these domain boundaries until all molecules have reacted, while for **3** the reaction occurs homogeneously. (Adapted with permission from reference 14. Copyright 2000 American Chemical Society.)

Acknowledgment

References

1. (a) Ulman, A. *An Introduction to Ultrathin Organic Films: From Langmuir-Blodgett to Self-Assembly*, Academic Press: New York, 1991; (b) Bishop, A. R.; Nuzzo, R. G. *Curr. Opinion Coll. Interface Sci.* **1996**, *1*, 127; (c) Dubois, L. H.; Nuzzo, R. G. *Ann. Rev. Phys. Chem.* **1992**, 43, 437; (d) Ulman, A. *Chem. Rev.* **1996**, 96, 1533;

2. (a) Carpick, R. W.; Salmeron, M. *Chem. Rev.* **1997**, *97*, 1163; (b) Lio, A.; Charych, D. H.; Salmeron, M. *J. Phys. Chem. B* **1997**, *101*, 380.

3. For a recent study on the hydrolysis of monolayers of succinimide ester with AFM see: Wang, J.; Kenseth, J. R.; Jones, V. W.; Green, J.-B. D.; McDermott, M. T.; Porter, M. D. *J. Am. Chem. Soc.* **1997**, *119*, 12796.

4. Töllner, K.; Popovitz-Biro, R.; Lahav, M.; Milstein, D. *Science* **1997**, *278*, 2100.

5. Neogi, P.; Neogi, S.; Stirling, C. J. M. *J. Chem. Soc., Chem. Commun.* **1993**, 1134.

6. van Ryswyk, H.; Turtle, E. D.; Watson-Clark, R.; Tanzer, T. A.; Herman, T. K.; Chong, P. Y.; Waller, P. J.; Taurog, A. L.; Wagner, C. E. *Langmuir*, **1996**, *12*, 6143.

7. Scanning tunneling microscopy (STM) is in general limited to conducting samples. For a recent review see *e.g.*: Somorjai, G. A. *Chem. Rev.* **1996**, *96*, 1223 and references herein. In addition, the STM tip can induce changes in the surface when it contacts the surface (Touzov, I.; Gorman, C. B. *J. Phys. Chem.* **1997**, *101*, 5263). In case of a thick layer of adsorbate, the feedback loop, which keeps a constant tunneling current while scanning, will cause the tip to penetrate into the material resulting in high shear forces.

8. (a) Werts, M. P. L.; van der Vegte, E. W.; Hadziioannou, G. *Langmuir* **1997**, *13*, 4939; (b) Schönherr, H.; Hruska, Z.; Vancso, G. J. *Macromolecules* **1998**, *31*, 3679; (c) Schönherr, G. J. Vancso *J. Polym. Sci. B, Polym. Phys.* **1998**, *36*, 2486.

9. (a) Gidalewitz, D.; Feidenhans'l, R.; Matlis, S.; Smilgies, D.-M.; Christensen, M. J.; Leiserowitz, L. *Angew. Chem. Int. Ed. Engl.* **1997**, *36*, 955; (b) Pearce R.; Vancso, G. J. *Macromolecules* **1997**, *30*, 5843; (c) Kaupp, G.; Haak, M. *Angew. Chem. Int. Ed. Engl.* **1996**, *35*, 2774; (d) Kautek, W.; Dieluweit, S.; Sahre, M. *J. Phys. Chem. B* **1997**, *101*, 2709; (e) Wall, J. T.; Grieser, F.; Zukoski, C. F. *J. Chem. Soc., Faraday Trans.* **1997**, *93*, 4017.

10. The estimation is based on the Hertz theory as described in reference 13. For a normal force of 2 nN and a tip radius of 5 nm a contact radius of 1.8 nm can be estimated. However, typical tip *radii* of modified AFM tips are of the

order of 50 - 75 nm. This leads to a radius of the contact area of 4.0 to 4.5 nm.

11. True atomic resolution has been reported for experiments with custom made force microscopes which operate in UHV conditions, see e.g. Giessibl, F. J. *Science* **1995**, *267*, 68.

12. SAMs were subject to numerous studies by AFM, see *e.g.*: (a) Alves, C. A.; Smith, E. L.; Porter, M. D. *J. Am. Chem. Soc.* **1992**, *114*, 1222; (b) Pan, J.; Tao, N.; Lindsay, S. M. *Langmuir* **1993**, *9*, 1556; (c) Jaschke, M.; Schönherr, H.; Wolf, H.; Butt, H.-J.; Bamberg, E.; Besocke, M. K.; Ringsdorf, H. *J. Phys. Chem.* **1996**, *100*, 2290; (d) Schönherr, H.; Vancso, G. J.; Huisman, B.-H.; van Veggel, F. C. J. M.; Reinhoudt, D. N. *Langmuir* **1997**, *13*, 1567.

13. (a) Nelles, G.; Schönherr, H.; Vancso, G. J.; Butt, H.-J. *Appl. Phys. A* **1998**, *66*, S1261; (b) Nelles, G.; Schönherr, H.; Jaschke, M.; Wolf, H.; Schaub, M.; Küther, J.; Tremel, W.; Bamberg, E.; Ringsdorf, H.; Butt, H.-J. *Langmuir* **1998**, *14*, 808.

14 Schönherr, H.; Chechik, V.; Stirling, C. J. M.: Vancso, G. J. *J. Am. Chem. Soc.* **2000**, *122,* 3679.

15. Weisenhorn, A. L.; Maivald, P.; Butt, H.-J.; Hansma, P. K. *Phys. Rev. B* **1992**, *45*, 11226.

16. (a) Noy, A.; Frisbie, C. D.; Rozsnyai, L. F.; Wrighton, M. S.; Lieber, C. M. *J. Am. Chem. Soc.* **1995**, *117*, 7943; (b) Vezenov, D. V.; Noy, A.; Rozsnyai, L. F.; Lieber, C. M. *J. Am. Chem. Soc.* **1997**, *119*, 2006; (c) Noy, A.; Vezenov, D. V.; Lieber, C. M. *Annu. Rev. Mater. Sci.* **1997**, *27*, 381.

17. In recent reports on functionalized carbon nanotubes used as AFM tips it was demonstrated that smaller tip *radii* and thus contact areas are, in principle, accessible: (a) Wong, S. S.; Joselevich, E.; Woolley, A. T.; Cheung, C. L.; Lieber, C. M. *Nature* **1998**, *394*, 52; (b) Wong, S. S.; Woolley, A. T.; Joselevich, E.; Cheung, C. L.; Lieber, C. M. *J. Am. Chem. Soc.* **1998**, *120*, 8557. The tip chemistry, degree of functionalization and lateral confinement of reactive groups are, however, better controlled using self-assembled monolayers.

18. Chechik, V.; Schönherr, H.; Vancso, G. J.; Stirling, C. J. M. *Langmuir* **1998**, *14*, 3003.

19. Schönherr, H.; Vancso, G. J.; Huisman, B.-H.; van Veggel, F. C. J. M.; Reinhoudt, D. N. *Langmuir* **1999**, *15,* 5541.

20. Tortonese, M.; Kirk, M. *Proc. SPIE* **1997**, *3009*, 53.

21. (a) Nuzzo, R. G.; Dubois, L. H.; Allara, D. L. *J. Am. Chem. Soc.* **1990**, *112*, 558; (b) Engquist, I.; Lestelius, M.; Liedberg, B. *Langmuir* **1997**, *13*, 4003.

22. Porter, M. D.; Bright, T. B.; Allara, D. L.; Chidsey, C. E. D. *J. Am. Chem. Soc.* **1987**, *109*, 3559.

23. Sondag, A. H. M.; Tol, A. J. W.; Touwslager, F. J. *Langmuir* **1992**, *8*, 1127.

24. Takami, T.; Delamarche, E.; Michel, B.; Gerber, Ch.; Wolf, H.; Ringsdorf, H. *Langmuir* **1995**, *11*, 3876.

25. There is ample evidence that mixed disulfides do not phase separate at room temperature.(a) reference 24; (b) Schönherr, H.; Ringsdorf, H.; Jaschke, M.; Butt, H.-J.; Bamberg, E.; Allinson, H.; Evans, S. D. *Langmuir* **1996**, *12,* 3898; (c) Tsao, M.-W.; Rabolt, J. F.; Schönherr, H.; Castner, D. G. *Langmuir* **2000**, *16,* 1734.

26. Harrison, L. G. in *Comprehensive Chemical Kinetics; Vol. 2.; The Theory of Kinetics;* Bamford, C. H.; Tipper, C. F. H. (Eds.), Elsevier, Amsterdam, 1969, pp. 377-462.

27. Intramolecular general base catalysis [which could be responsible for the autocatalytic (sigmoid) behavior] can be excluded on the basis of control experiments with mixed disulfides in which one arm carries a terminal ester group and the other a terminal methyl group.

28. Johnson, K. L.; Kendall, K.; Roberts, A. D. *Proc. R. Soc. London A* **1971**, *324*, 301.

29. Typical domain size of SAMs on gold, which has not been heat-treated during or after the assembly, is in the order of 5 nm (Delamarche, E.; Michel, B.; Gerber, Ch.; Anselmetti, D.; Güntherodt, H.-J.; Wolf, H.; Ringsdorf, H. *Langmuir* **1994**, *10*, 2869).

30. For this rough estimate a circular domain shape was assumed. The longest induction period was assigned to the idealized situation that the circular contact area (with radius r_0) is centered on this domain. Based on JKR theory the original contact area was calculated ($K = 4.7 \times 10^{10}$ Pa; W_{12} (t = 0) = 50 mN/m). A reaction rate was defined as ratio of r_0 and reaction time t_R. Using this rate the original domain size can be calculated based on the observed induction time.

31. It is reasonable to assume that the domain sizes on sputtered or evaporated gold are smaller than on flat Au(111) [29]. Experimental evidence for small crystalline patches further supports this assumption, see: Schönherr, H.; Vancso, G. J. *Langmuir* **1997**, *13*, 3769.

32. Discrepancies between the AFM and FT-IR results can be explained by the fact that the sampling area for AFM is more than ca. 10^{12} times smaller than for FT-IR and that reactions *e.g.* at grain boundaries of gold grains on the tip would not affect the AFM results.

33. The true resolution of the AFM is not sufficiently high to unequivocally enable one to image sub-domain details. In addition, it is not *a priori* clear how the friction measured on a few molecules can be related to exposed functional groups.

Interfacial Properties of Specifically Fluorinated Self-Assembled Monolayer Films

**Ramon Colorado, Jr., Michael Graupe, Hyun I. Kim,
Mitsuru Takenaga, Olugbenga Oloba, Seunghwan Lee,
Scott S. Perry,* and T. Randall Lee***

**Department of Chemistry, University of Houston,
Houston, TX 77204–5641**

This report describes a systematic exploration of the molecular basis for friction and wettability in organic thin films. The experimental approach relies on the construction of specifically fluorinated self-assembled monolayers (SAMs) generated by the adsorption of terminally fluorinated alkanethiols onto the surface of gold. Analysis of the SAMs by atomic force microscopy (AFM) reveals that the size of the terminal group strongly influences the frictional properties of the monolayers but fails to influence their lattice periodicity. Characterization of the films by polarization modulation infrared reflection absorption spectroscopy (PM-IRRAS) shows that the conformational order of the hydrocarbon chains in adsorbates having equivalent numbers of methylene groups are independent of the size of the terminal group. Contact angle measurements reveal the strong influence of oriented surface dipoles on the wettabilities of the films. The indistinguishable frictional response of mixed CF_3- and CH_3-terminated films of varying composition, however, suggests that the surface dipoles exert little, if any, influence upon the frictional properties of the films. Frictional studies of i-Pr-terminated SAMs are consistent with a model in which the size of the terminal group influences the frictional properties.

The widespread commercial use of fluorinated organic films is largely due to their unique interfacial properties [1]. These films have proven to be both chemically and biologically inert, to exhibit high thermal and mechanical stabilities, and to resist oxidation and corrosion. Furthermore, their hydrophobicity and anti-adhesive nature have led to their use in a diverse range of applications. Recently, much interest has focused on understanding the frictional properties of fluorinated films [2-6]. These

studies demonstrated that fluorocarbon films exhibit higher friction than hydrocarbon films. Given the well-known lubricating properties of fluorinated materials such as Teflon, these results might be considered surprising. The enhanced frictional properties of fluorocarbon films have been attributed to a number of phenomena, including differences in the packing energy of hydrocarbons and fluorocarbons, differences in packing density, greater stiffness of fluorocarbons, greater elasticity of hydrocarbons, and the resistance to deformation and rupture of fluorocarbons [2-8]. The widely differing and sometimes conflicting rationalizations suggest that further insight into the physical and chemical contributions to friction in organic films is needed to advance a hypothesis that is both plausible and comprehensive. To this end, we have employed atomic force microscopy (AFM) to explore the frictional response of a series of self-assembled monolayers (SAMs) on Au(111) generated from alkanethiols that possess chemically distinct terminal groups $\omega(CH_2)_nSH$, where $\omega = CF_3$ and CH_3 (n = 12,13,15) and $CH(CH_3)_2$ (n = 13) [9-14]. Despite the presence of strong interfacial dipole effects in the CF_3-terminated films, we were able to correlate the observed trends in frictional response to the presence of correlated steric interactions among these terminal groups.

Experimental

Generation of SAMs. The SAMs were generated on gold substrates containing (111) terraces by adsorption from 1 mM ethanolic solutions of the appropriate alkanethiol. The gold substrates used for ellipsometry, contact angle goniometry, and PM-IRRAS analyses were prepared by evaporating 2000 Å of gold onto chromium-primed silicon wafers. The gold substrates used for AFM measurements were microballs prepared by annealing a gold wire in a hydrogen/oxygen flame. All substrates were incubated in solution for 24 h. The synthesis of the alkanethiols has been described elsewhere [14].

Contact Angle Wettabilities. A ramé-hart model 100 contact angle goniometer was used to measure the advancing contact angles of contacting liquids on the films. A Matrix Technologies Electrapette 25 operated at the slowest possible speed (*ca.* 1 µL sec^{-1}) was used to dispense the liquids. For a given sample, the data were collected with the pipette tip in contact with the drop and averaged over three separate slides.

Infrared Spectroscopy. A Nicolet MAGNA-IR 860 Fourier transform spectrometer equipped with a liquid nitrogen-cooled mercury-cadmium-telluride (MCT) detector and a Hinds Instruments PEM-90 photoelastic modulator (37 kHz) was used to acquire the polarization modulation infrared reflection absorption spectroscopy (PM-IRRAS) data. The spectra were collected using p-polarized light incident at 80° for 1000 scans at a spectral resolution of 4 cm^{-1}.

Atomic Force Microscopy. A homemade beam deflection atomic force microscope equipped with a single tube scanner, an optical deflection scheme, Si_3N_4 tip-cantilever assemblies (Digital Instruments, CA), and RHK AFM 100 and RHK STM 100 electronics was used to measure the lattice constants and frictional properties of

the SAMs under ambient atmospheric conditions (24° C and 40% humidity). Additional experimental details are provided in reference 13.

X-ray Photoelectron Spectroscopy. A PHI 5700 X-ray photoelectron spectrometer equipped with an monochromatic Al Kα X-ray source (hv = 1486.7 eV) incident at 90° relative to axis of a hemispherical energy analyzer was used to obtain X-ray photoelectron spectra of the films at a photoelectron takeoff angle of 45° from the surface and a pass energy of 23.5 eV. The surface concentration of CF_3 groups in the mixed monolayers was determined by integrating the F 1s and Au 4f photoelectron peaks. Additional experimental details are provided in reference 13.

Results and Discussion

Our initial comparison of the frictional properties of fluorocarbon and hydrocarbon films involved the study of SAMs generated from CF_3- and CH_3-terminated tridecanethiols (Figure 1) on gold [9]. Figure 2 shows the frictional response of the films versus the applied load measured by AFM. As the load increases, the frictional response of the CF_3-terminated film exhibits a larger increase than that of the CH_3-terminated film. To rationalize this phenomenon, we considered the following list of possible causes for the frictional difference: (1) differences in the packing density of the two films, (2) differences in film order, (3) differences in the packing energies of the two films, (4) differences in the stiffness or elasticity of the two films, (5) differences in the chemical composition of the terminal groups, and (6) the presence of surface dipoles in the films [15-17]. We then systematically evaluated the influence of each of these factors upon the frictional properties.

First, we probed the structural features of the films by collecting lateral force images using AFM (Figure 3). The lattice structure of both SAMs were hexagonal and exhibited indistinguishable periodicities (~4.9 Å), even though the CF_3 groups are substantially larger than the CH_3 groups (Figure 1) [9,18]. In light of this result, it seems unlikely that differences in either packing density or interfacial order are responsible for the observed differences in friction [19]. Next, we analyzed the band position of the antisymmetric methylene C-H stretch ($v_a^{CH_2}$) by PM-IRRAS to evaluate the conformational order of the chemically identical backbones of the CH_3- and CF_3-terminated adsorbates [13,20]. This band position shifts to higher wavenumbers as the conformational order of the methylene backbones in SAMs decreases (i.e., decreased interchain interactions and increased intrachain gauche defects) [21]. Figure 4 shows that the $v_a^{CH_2}$ band positions of CF_3-terminated and CH_3-terminated films are the same, which suggests that the methylene backbones in both films possess similar degrees of conformational order. Because the two SAMs exhibit indistinguishable degrees of conformational order, the observed difference in frictional properties of the films must arise from factors other than differences in packing energy or film elasticity.

Since the difference in the chemical composition of the terminal groups might be solely responsible for the increased frictional response [22-27], we considered exactly how this difference might influence the frictional response. First, differences in the
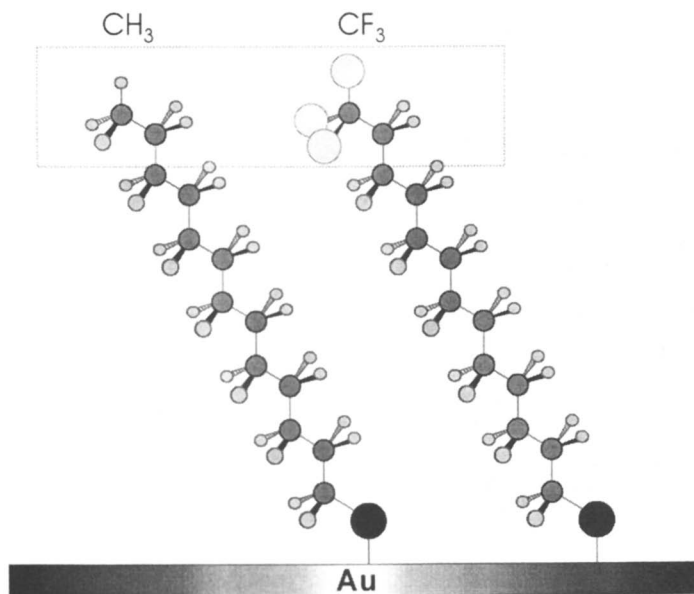
Figure 1. Schematic representation of CH_3-terminated and CF_3-terminated SAMs derived from $\omega(CH_2)_{12}SH$, where $\omega = CH_3$ and CF_3.
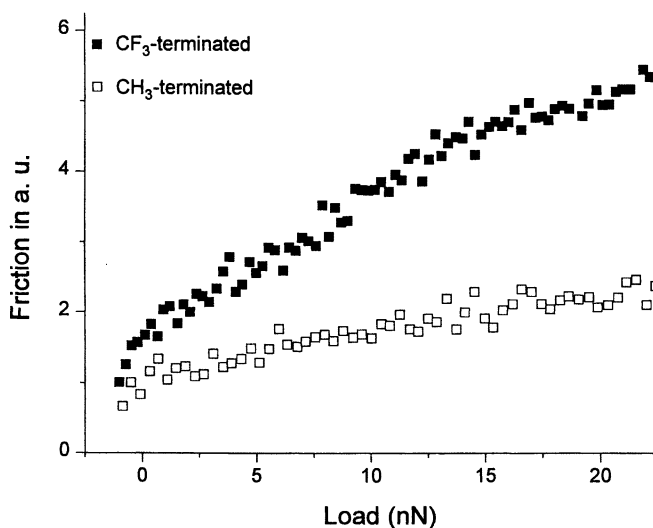
Figure 2. Frictional response of CF_3-terminated (■) and CH_3-terminated (□) tridecanethiol SAMs measured by AFM as a function of decreasing applied load.
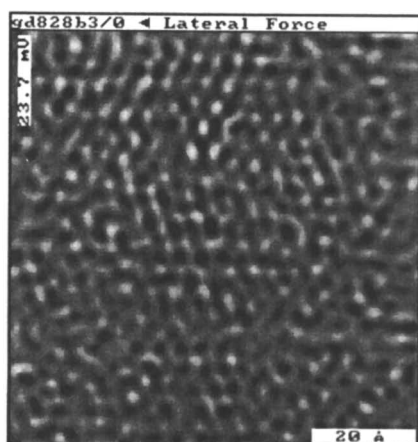
(a) CH$_3$-terminated
4.9 ± 0.2 Å spacing
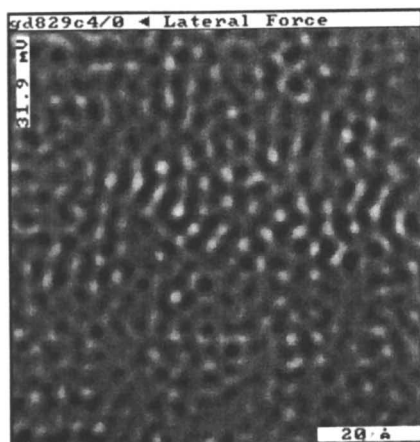
(b) CF$_3$-terminated
4.8 ± 0.2 Å spacing
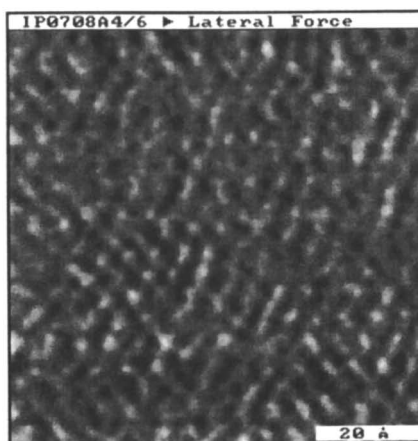
(c) i-Pr-terminated
5.0 ± 0.2 Å spacing

Figure 3. Lateral force images (80 Å × 80 Å) and lattice constants of (a) CH$_3$-terminated, (b) CF$_3$-terminated, and (c) i-Pr-terminated SAMs.
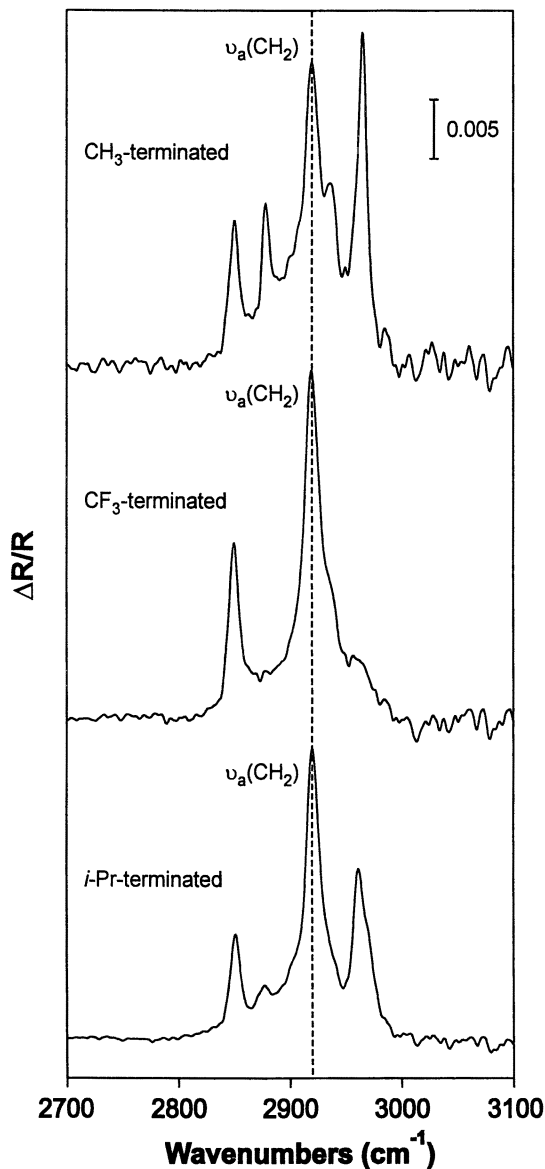
Figure 4. PM-IRRAS spectra of the hydrocarbon stretching region for CH_3-terminated, CF_3-terminated, and i-Pr-terminated SAMs derived from $\omega(CH_2)_{13}SH$, where ω = CH_3, CF_3, and $CH(CH_3)_2$. The antisymmetric band position ($v_a^{CH_2}$) is indicated by the dashed line at 2919 cm^{-1}.

conformational order of the terminal groups could lead to increased friction by permitting the dissipation of energy into additional local excitation modes (e.g., gauche defects) [15,17,28,29]. However, our AFM and IR results suggest that CF_3- and CH_3-terminated films possess similar degrees of conformational order. Hence, this factor is an unlikely contributor to the observed frictional difference. Next, a difference in the rotational barriers of the terminal C-C bonds could contribute to the frictional difference [15,17,30,31]. The barrier for rotation about a CF_3-CH_2 bond is indeed higher (by ~26%) than the barrier for rotation about a CH_3-CH_2 bond [13,32]. The magnitude of this increase, however, might not fully account for the observed threefold increase in frictional response. Further studies involving molecular dynamics simulations might lend further insight into the relationships between rotational barriers and the frictional properties of organic thin films [31,33,34].

Another possibility is that differences in adhesion between the AFM tip and the samples give rise to the differences in frictional response [9,22-27,35,36]. Indeed, the introduction of terminal CF_3 groups creates dipoles (aligned with the CF_3-CH_2 bonds) at the surface of the film [16,37]. Evidence for these dipoles is found in the wettability studies of SAMs generated from a series of terminally fluorinated alkanethiols and SAMs generated from an analogous series of normal alkanethiols using contact angle goniometry (Figures 5a and 5b) [11,12,20,37,38]. Due to the weak dispersive interactions between fluorocarbons and hydrocarbons, the nonpolar and weakly polar contacting liquids (hexadecane and methylene iodide, respectively) wet the CF_3-terminated surfaces less than they wet the CH_3-terminated surfaces. Polar protic contacting liquids, such as water and glycerol, however, wet the CF_3-terminated surfaces more than they wet the CH_3-terminated surfaces. To determine whether the observed increase in the wettability of the CF_3-terminated films arose from hydrogen bonding between the liquids and the terminal groups, we conducted further studies with polar aprotic contacting liquids (e.g., acetonitrile, dimethylformamide, and nitrobenzene). The data revealed that the observed increases in wettability arise from factors other than hydrogen bonding because the aprotic liquids, which cannot plausibly hydrogen bond to the CF_3 groups, exhibited the same wettability discrimination (i.e., CF_3-termination was more wettable than CH_3-termination) as the polar protic liquids. We propose instead that the enhanced wettabilities on the CF_3-terminated SAMs are consistent with the presence of oriented CF_3-CH_2 dipoles at the surface of the films. These dipoles strengthen the attractions with the polar contacting liquids through additional dipolar interactions that are absent with the non-polar CH_3-CH_2 moieties at the surface of the CH_3-terminated films [37,38].

Additional support for this hypothesis was provided by the observation of an inverse "odd-even" or parity effect for the wettabilities of polar contacting liquids on the CF_3-terminated films (see Figure 5). The parity effect has been observed in CH_3-terminated monolayer films and arises from the dependence of the orientation of the terminal methyl groups upon the total number of carbon atoms in the adsorbates (i.e., the chain length) [39,40]. Films comprised of adsorbates with odd chain lengths (odd-numbered SAMs) have terminal methyl groups oriented more parallel with respect to the surface of gold than films comprised of adsorbates with even chain
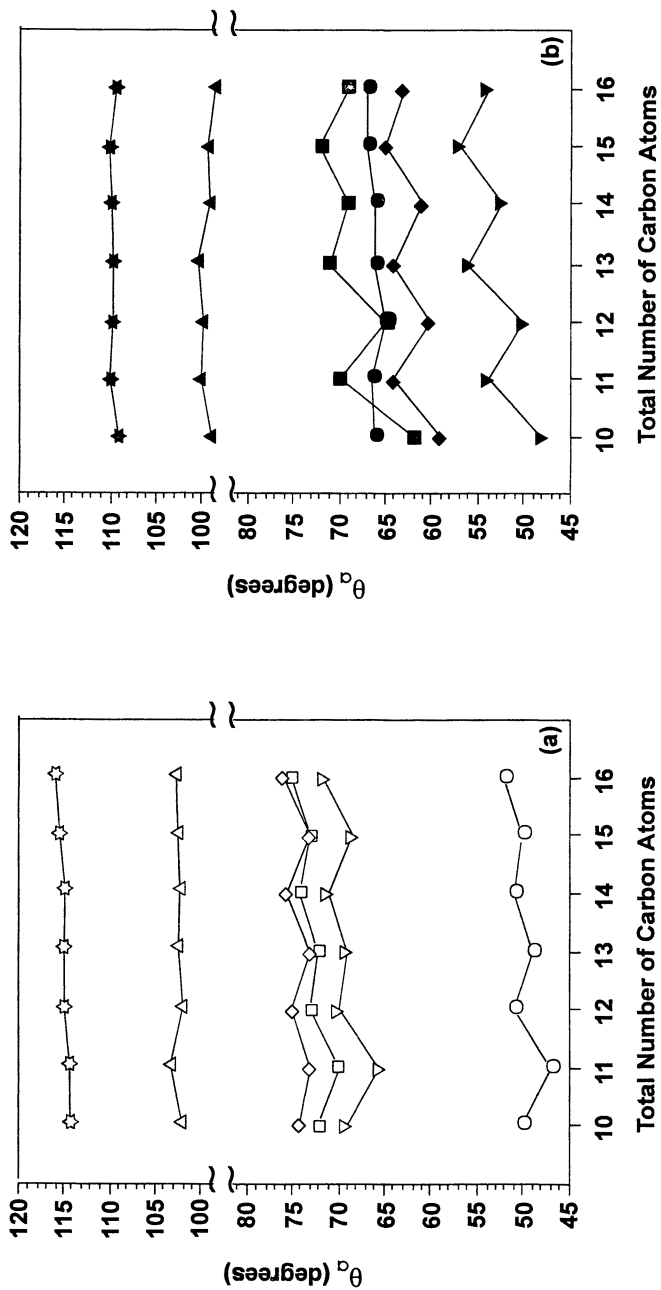
Figure 5. Advancing contact angles of hexadecane ($\bigcirc$, $\bullet$), water ($\star$, $\bigstar$), glycerol ($\triangle$, $\blacktriangle$), acetonitrile ($\triangledown$, $\blacktriangledown$), DMF ($\diamondsuit$, $\blacklozenge$), and nitrobenzene ($\square$, $\blacksquare$) on (a) CH$_3$- terminated SAMs (open symbols) and (b) CF$_3$-terminated SAMs (filled symbols).

lengths (even-numbered SAMs). An increase in tilt leads to increased exposure of the underlying methylene moieties that increases the dispersive interactions and consequently increases the wettability for odd-numbered SAMs relative to that for even-numbered SAMs [41,42]. The parity effect for the CF_3-terminated SAMs, however, differs in two respects: (1) it is only observed with polar contacting liquids, and (2) the wettabilites of odd-numbered SAMs are *lower* than the wettabilities of even-numbered SAMs. These two differences can be rationalized by the surface dipole model. First, nonpolar liquids by definition can interact exclusively by dispersive means and should therefore be insensitive to polar changes in the surfaces. Second, the more parallel orientation of the terminal groups in odd-numbered SAMs should allow the terminal dipoles to partially compensate one another by aligning themselves in a head-to-tail fashion (Figure 6). This compensation would lead to an overall decrease in the magnitude of the electrostatic field presented at the surface of odd-numbered SAMs, which would diminish the interaction with a polar contacting liquid and thus diminish the wettability of the film. The near-perpendicular orientation of the dipoles in even-numbered SAMs offers little opportunity for compensation and thus presents stronger electrostatic fields and enhanced wettabilities [37].

While our contact angle measurements demonstrated the strong influence of these surface dipoles on the wettabilities of CF_3- versus CH_3-terminated films, AFM measurements of tip-sample adhesion revealed little evidence for the contribution of surface dipoles to the frictional properties of the films [9,22-28]. The pull-off forces between the AFM tip and the samples were indistinguishable for both CF_3- and CH_3-terminated films (~12.1 ± 0.9 nN) [28,36,43], which suggests that the AFM tip used in our experiments experiences similar adhesive forces on both types of films [44]. This issue was further examined by studying mixed monolayers of ω-terminated hexadecanethiols on Au in which the surface concentration of the CF_3 groups was systematically increased (0, 15, 22, 38, 51, 75, and 100% as measured by XPS) [13,45]. If surface dipoles were responsible for the observed frictional difference, then the frictional response of these mixed films would be expected to increase progressively with an increase in the surface concentration of CF_3 groups, assuming that the CF_3 groups are randomly dispersed among the CH_3 groups. To determine whether the mixed monolayers consisted of large domains of randomly mixed CF_3- and CH_3-terminated adsorbates or of phase-segregated domains of single-component islands, we collected lateral force images of these films. If the CF_3- and CH_3-terminated adsorbates did in fact phase segregate, one would expect to see islands of contrasting lateral force in these images due to the different frictional responses of the two terminal groups [25]. Lateral force images of the mixed films, however, were homogeneous over the investigated areas (0.5 μm × 0.5 μm) and revealed no evidence of domain formation [36,45]. Figure 7 shows the lateral force image for the 51% CF_3 film and is representative of all the images obtained on the mixed films. These results suggest that, under the conditions used for film formation, random mixing of the different terminal groups occurs. Remarkably, the frictional responses of the mixed films failed to increase with the increasing surface concentration of CF_3 groups. The friction-load plots of the mixed films revealed that just a 15%
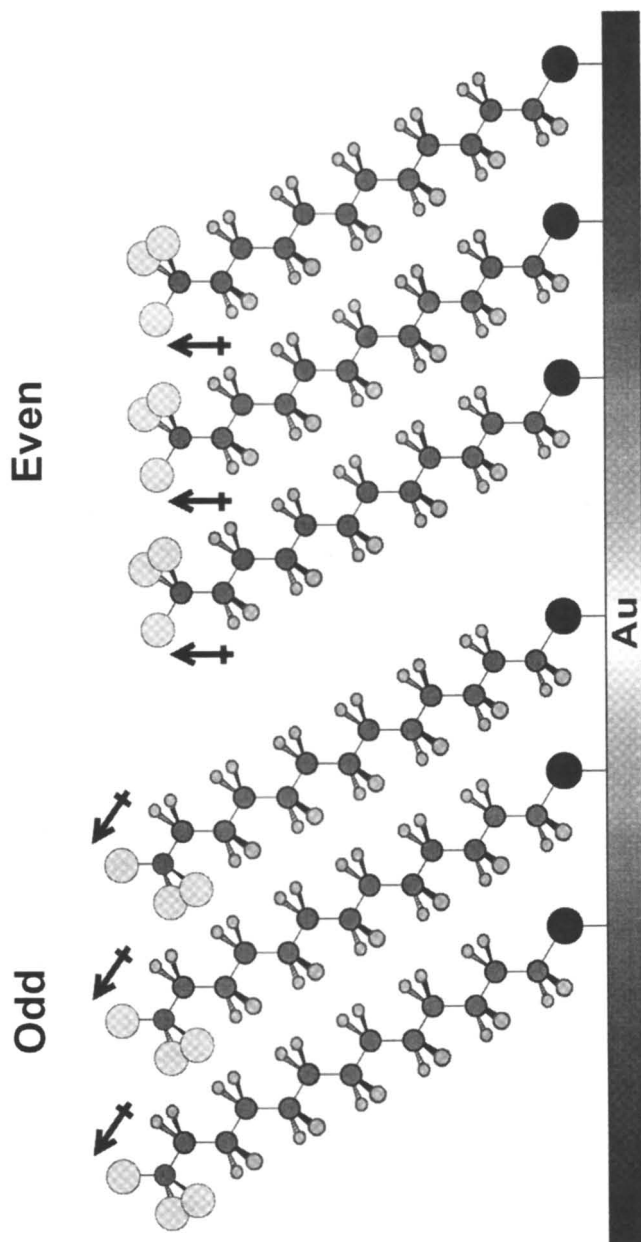
Figure 6. Schematic representation of the odd-even effect on the orientation of the CF_3-CH_2 surface dipoles in CF_3-terminated SAMs on gold. (Note: The depicted structure serves only to illustrate the relative alternation of the average terminal group orientation as a function of chain length.)

concentration of CF_3 groups induces an increase in frictional response to values that are significantly higher than that of the CH_3-terminated film (Figure 8). Furthermore, films with higher concentrations of CF_3 groups all exhibit frictional responses that are indistinguishable from the response for the 15% CF_3 film. These data argue against the influence of CF_3-CH_2 surface dipoles upon the increased frictional response of the CF_3-terminated films and suggest that a threshold of surface fluorination gives rise to the higher frictional response.

Perhaps the most significant difference between terminal CF_3 vs. CH_3 groups is the greater steric bulk of the CF_3 group [9,18]. The fact that the lateral force images for the two films exhibit indistinguishable periodicities despite the larger cross-sectional area of the CF_3 group demonstrates that the film structure within the fluorinated monolayer must accommodate the increased bulk without changing the lattice spacing [9,13]. As a consequence, the intermolecular interactions of the terminal groups with their nearest neighbors should be greater in the fluorinated films. Consequently, the local movement of the terminal CF_3 groups should be highly correlated with the motion of neighboring moieties. These correlated motions might give rise to long range intermolecular lateral and rotational interactions that provide additional pathways for the dissipation of energy, which in turn lead to the higher frictional response for the CF_3-terminated films. Since this model limits itself to interactions at the terminal portion of the films, we believe that it is consistent with the structural characterizations of film order, which argue that the underlying backbones are structurally indistinguishable. This model can also be used to rationalize the results from the mixed monolayer studies. In an idealized hexagonal surface structure for a perfectly mixed 10% CF_3-terminated film (Figure 9), the CF_3 groups could interact sterically with a majority of the film structure through nearest-neighbor interactions with the surrounding CH_3 groups. These interactions serve to increase the "effective" packing density of the terminal groups and give rise to long range correlated interactions that enhance the frictional response [13].

Given our hypothesis that the frictional responses of ω-substituted SAMs are greatly influenced by the size of the terminal groups, we evaluated the frictional response of a SAM terminated with isopropyl groups (i-Pr), which afford no strong terminal dipoles (due to their purely non-polar aliphatic composition), and like CF_3 groups, are sterically larger than CH_3 groups (Figure 10) [13,18,46]. The wettability of this film by water (advancing contact angle = 115°) reveals that the i-Pr-terminated films are as hydrophobic as the CH_3-terminated films. Moreover, neither of these films expose oriented dipoles at the surface. The higher wettability by hexadecane of the i-Pr-terminated film (advancing contact angle = 41°) compared to that of the CH_3-terminated film (advancing contact angle = 49°) suggests that the i-Pr groups possess a higher surface free energy than the CH_3 groups [47]. Analyses of the i-Pr-terminated film by AFM (Figure 3) and PM-IRRAS (Figure 4) showed that the lattice spacings and the conformational order, respectively, of the film were indistinguishable from those of the CF_3- and CH_3-terminated films. Given the relatively large size of the i-Pr group, these results highlight the fact that the monolayer structure can accommodate a significant amount of steric bulk at the surface.
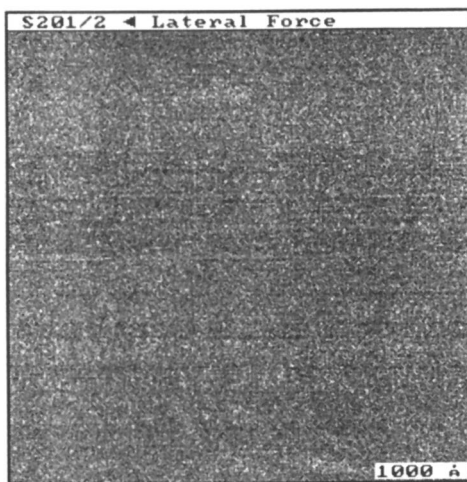
Figure 7. Lateral force image (0.5 μm × 0.5 μm) of a mixed monolayer with a surface concentration of 51% CF$_3$ groups and 49% CH$_3$ groups as determined by XPS. The observed constancy of the lateral force suggests that the film components are well mixed over this area.
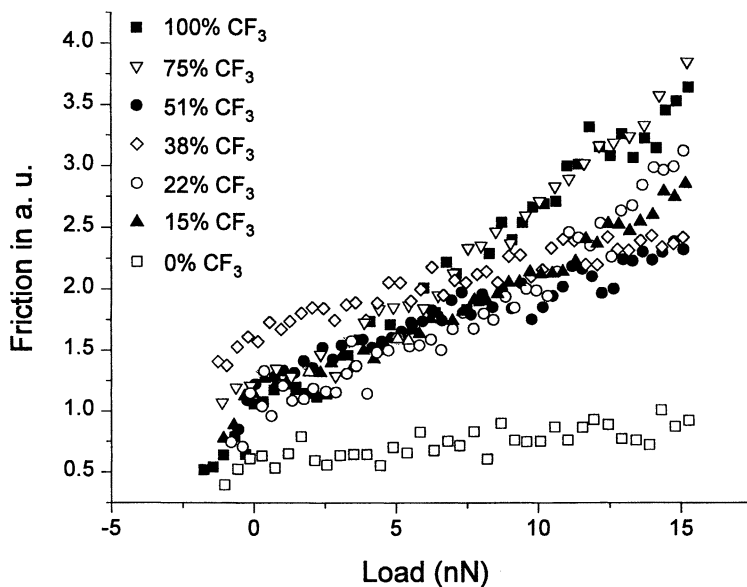
Figure 8. Frictional response of mixed monolayers derived from CF$_3$-terminated and CH$_3$-terminated hexadecanethiols (0% CF$_3$: □, 15% CF$_3$: ▲, 22% CF$_3$: ○, 38% CF$_3$: ◇, 51% CF$_3$: ●, 75% CF$_3$: ▽, and 100% CF$_3$: ■) measured by AFM as a function of decreasing applied load.
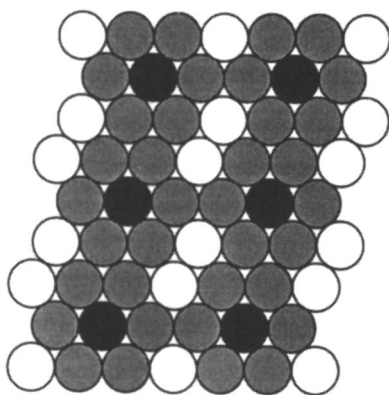
Figure 9. Schematic representation of the degree of multimolecular influence in a hexagonal lattice structure for an ideally mixed monolayer containing 10% CF_3 groups. The filled circles represent CF_3 groups, and the shaded circles represent nearest neighbor CH_3 groups influenced by the steric bulk of adjacent CF_3 groups.
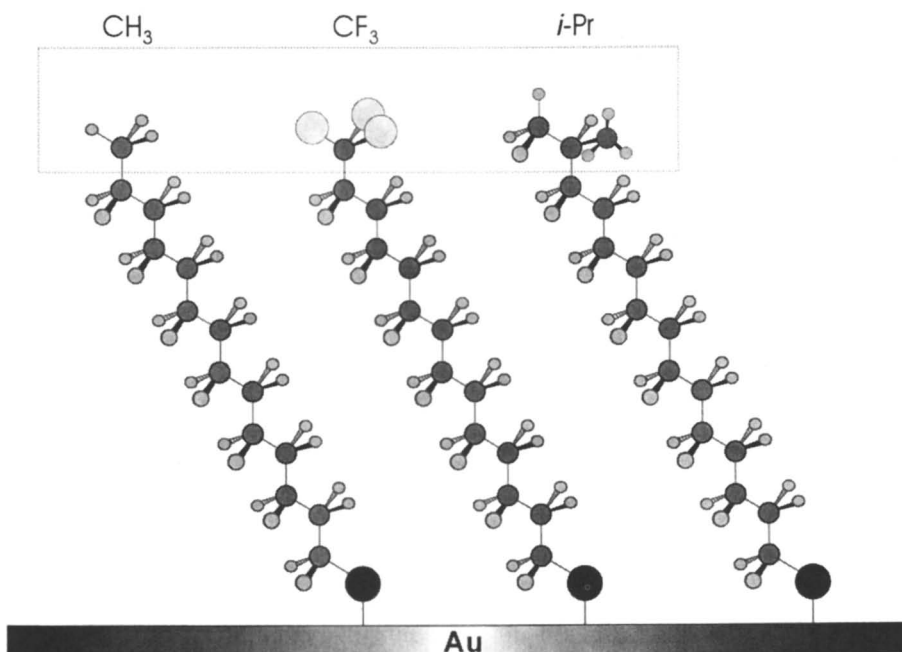
Figure 10. Schematic representation of CH_3-terminated, CF_3-terminated, and *i*-Pr-terminated SAMs derived from $\omega(CH_2)_{13}SH$, where $\omega = CH_3$, CF_3, and $CH(CH_3)_2$.

Figure 11 shows friction versus load plots of CF$_3$-, i-Pr-, and CH$_3$-terminated SAMs. Like the CF$_3$-terminated film, the i-Pr-terminated film exhibits a frictional response that is greater than that of the CH$_3$-terminated film. Since the lattice spacing, conformational order, and chemical composition of the films are the same, this higher frictional response can be rationalized in terms of the additional steric interactions that accompany the larger size of the i-Pr group. The results are consistent with a model in which the frictional responses of the i-Pr and CF$_3$-terminated films are influenced by the increased sizes of their terminal groups relative to those of a CH$_3$-terminated film. Studies to further explore these systems are currently underway in our laboratories.

Conclusions

We prepared and characterized a series of SAMs generated from ω-substituted alkanethiols to explore the relationship between film structure/composition and the interfacial properties. The lattice spacings and the conformational order of CF$_3$- and CH$_3$-terminated SAMs comprised of adsorbates having methylene backbones of equivalent length were found to be similar. Friction-load maps, however, collected by AFM showed that the CF$_3$-terminated SAMs have higher frictional responses than the CH$_3$-terminated SAMs. The contribution of the greater rotational barrier about a CF$_3$-CH$_2$ bond compared to a CH$_3$-CH$_2$ bond to the frictional response was considered; however, the 26% greater rotational barrier is perhaps insufficient to account for the threefold increase in frictional response. The potential influence of surface dipoles on interfacial properties was probed by evaluating the wettabilities of CF$_3$-terminated SAMs and CH$_3$-terminated SAMs. The results revealed strong interactions between oriented surface dipoles and polar contacting liquids. The similar frictional responses of mixed CF$_3$- and CH$_3$-terminated monolayers with progressively increasing surface concentrations of CF$_3$ groups suggest, however, that the influence of surface dipoles fails to contribute significantly to the enhanced friction of CF$_3$-terminated SAMs. Lateral force images and antisymmetric methylene band positions obtained for an i-Pr-terminated SAM, which also possesses a larger terminal group than that of the CH$_3$-terminated SAMs, were indistinguishable from those of CF$_3$- and CH$_3$-terminated SAMs and suggest that the lattice periodicity and methylene conformational order, respectively, of these ω-substituted films are unaffected by the size of the terminal functional group. Furthermore, contact angle measurements revealed that the i-Pr-terminated SAM is wet more by hexadecane and wet equivalently by water when compared to the CH$_3$-terminated SAM. The i-Pr-terminated SAM, which posseses no oriented terminal dipoles, exhibited a greater frictional response than that of the CH$_3$-terminated SAM. Overall, these results are consistent with a model in which the friction of the CF$_3$- and i-Pr-terminated SAMs are influenced by the relatively large size of their terminal functional groups. We are currently exploring chain length effects that alter the orientation of the terminal groups (odd-even effects) and the use of larger terminal groups (phenyl, *tert*-butyl) to gain further insight into the frictional responses of these ω-substituted films.
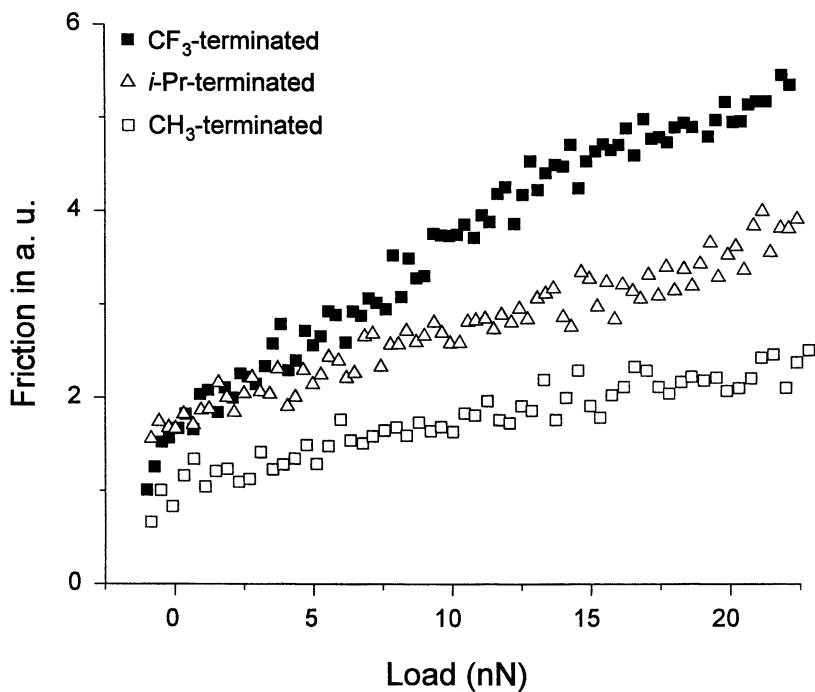
Figure 11. Frictional responses of CF$_3$-terminated (■), *i*-Pr-terminated (▲), and CH$_3$-terminated SAMs (□) measured by AFM as a function of applied load.

Acknowledgments

References

1. Garbassi, F.; Morroca, M.; Occhiello, E. *Polymer Surfaces*, Wiley: Chichester, 1994.
2. Meyer, E.; Overney, R.; Lüthi, R.; Brodbeck, D.; Howald, L.; Frommer, J.; Güntherodt, H.-J.; Wolter, O.; Fujihara, M.; Takano, H.; Gotoh, Y. *Thin Solid Films* **1992**, *220*, 132.
3. Overney, R.; Meyer, E.; Frommer, J.; Brodbeck, D.; Howald, L.; Güntherodt, H.-J.; Fujihara, M.; Takano, H.; Gotoh, Y. *Nature* **1992**, *359*, 133.
4. Overney, R.; Meyer, E.; Frommer, J.; Güntherodt, H.-J.; Fujihara, M.; Takano, H.; Gotoh, Y. *Langmuir* **1994**, *10*, 1281.
5. DePalma, V.; Tillman, N. *Langmuir* **1989**, *5*, 868.
6. Chaudhury, M. K.; Owen, M. J. *Langmuir* **1993**, *9*, 29.
7. Levine, O.; Zisman, W. A. *J. Phys. Chem.* **1957**, *61*, 1068.
8. Briscoe, B. J.; Evans, D. C. B. *Proc. R. Soc. Lond. A* **1982**, *380*, 389.
9. Kim, H. I.; Koini, T.; Lee, T. R.; Perry, S. S. *Langmuir* **1997**, *13*, 7192.
10. Kim, H. I.; Koini, T.; Lee, T. R.; Perry, S. S. *Tribol. Lett.* **1998**, *4*, 137.
11. Graupe, M.; Koini, T.; Kim, H. I.; Garg, N.; Miura, Y. F.; Takenaga, M.; Perry, S. S.; Lee, T. R. *Mat. Res. Bull.* **1999**, *34*, 447.
12. Graupe, M.; Koini, T.; Kim, H. I.; Garg, N.; Miura, Y. F.; Takenaga, M.; Perry, S. S.; Lee, T. R. *Coll. Surf. A* **1999**, *154*, 239.
13. Kim, H. I.; Graupe, M.; Oloba, O.; Koini, T.; Imaduddin, S.; Lee, T. R.; Perry, S. S. *Langmuir* **1999**, *15*, 3179.
14. Graupe, M.; Koini, T.; Wang, V. Y.; Nassif, G. M.; Colorado, R., Jr.; Villazana, R. J.; Dong, H.; Miura, Y. F.; Shmakova, O. E.; Lee, T. R. *J. Fluorine Chem.* **1993**, *93*, 107.
15. Xiao, X.; Hu, J.; Charych, D. H.; Salmeron, M. *Langmuir* **1996**, *12*, 235.
16. Shafrin, E. G.; Zisman, W. A. *J. Phys. Chem.* **1957**, *61*, 1046.
17. McDermott, M. T.; Green, J.-B. D.; Porter, M. D. *Langmuir* **1997**, *13*, 2504.
18. Using the van der Waals radii provided in Seebach, D. *Angew. Chem. Int. Ed. Engl.* **1990**, *29*, 1320, we calculate the following cross-sectional areas: $CH_3 = 13$ Å^2, $CF_3 = 23$ Å^2, and i-Pr $= 28$ Å^2.
19. The substitution of CF_3 groups for CH_3 groups in organic compounds introduces no change in the solid-state structure: Seebach, D.; Renaud, P.; Schweizer, W. B.; Züger, M. F.; Brienne M.-J. *Helv. Chem. Acta* **1984**, *67*, 1843.

20. Colorado, R., Jr.; Graupe, M.; Takenaga, M.; Koini, T.; Lee, T. R. *Proc. Mat. Res. Soc. Symp.* **1999**, *546*, 237-242.
21. Porter, M. D.; Bright, T. B.; Allara, D. L.; Chidsey, C. E. D. *J. Am. Chem. Soc.* **1987**, *109*, 3559.
22. Noy, A.; Frisbie, C. D.; Rozsnyai, L. F.; Wrighton, M. S.; Lieber, C. M. *J. Am. Chem. Soc.* **1995**, *117*, 7943.
23. van der Vegte, E. W.; Hadziioannou, G. *Langmuir* **1997**, *13*, 4357.
24. van der Vegte, E. W.; Hadziioannou, G. *J. Phys. Chem. B* **1997**, *101*, 9563.
25. Wilbur, J. L.; Biebuyck, H. A.; MacDonald, J. C.; Whitesides, G. M. *Langmuir* **1995**, *11*, 825.
26. Sinniah, S. K.; Steel, A. B.; Miller, C. J.; Reutt-Robey, J. E. *J. Am. Chem. Soc.* **1996**, *118*, 8925.
27. Green, J.-B. D.; McDermott, M. T.; Porter, M. D. *J. Phys. Chem.* **1995**, *99*, 10960.
28. Lio, A.; Charych, D. H.; Salmeron, M. *J. Phys. Chem. B.* **1997**, *101*, 3800.
29. Lio, A.; Morant, C.; Ogletree, D. F.; Salmeron, M. *J. Phys. Chem. B.* **1997**, *101*, 4767.
30. Koike, A.; Yoneya, M. *Langmuir* **1997**, *13*, 1718.
31. Harrison, J. A.; White, C. T.; Colton, R. J.; Brenner, D. W. *Thin Solid Films* **1995**, *260*, 205.
32. Rotational barriers of 14.0 kJ/mol for the CH_3-CH_2 bond and 17.6 kJ/mol for the CF_3-CH_2 bond were estimated by *ab initio* methods (uncorrected for entropy effects) using Gaussian 90 at the Hartree-Fock level using the 6-31G* basis set.
33. Tupper, K. J.; Brenner, D. W. *Thin Solid Films* **1994**, *253*, 185.
34. Tutein, A. B.; Stuart, S. J.; Harrison, J. A. *Langmuir* **2000**, *16*, 291.
35. Weisendanger, R. *Scanning Probe Microscopy and Spectroscopy, Methods and Applications*; Cambridge University: Cambridge, 1994.
36. Beake, B. D.; Leggett, G. J. *Langmuir* **2000**, *16*, 735.
37. Graupe, M.; Takenaga, M.; Koini, T.; Colorado, R., Jr.; Lee, T. R. *J. Am. Chem. Soc.* **1999**, *121*, 3222.
38. Miura, Y. F.; Takenaga, M.; Koini, T.; Graupe, M.; Garg, N.; Graham, R. L., Jr.; Lee, T. R. *Langmuir* **1998**, *14*, 5821.
39. Tao, Y.-T. *J. Am. Chem. Soc.* **1993**, *115*, 4350.
40. Nuzzo, R. G.; Dubois, L. H.; Allara, D. L. *J. Am. Chem. Soc.* **1990**, *112*, 558.
41. Shon, Y.-S.; Lee, S.; Colorado, R., Jr.; Perry, S. S.; Lee, T. R. *J. Am. Chem. Soc.*, submitted.
42. Bain, C. D.; Troughton, E. B.; Tao, Y.-T.; Evall, T.; Whitesides, G. M.; Nuzzo, R. G. *J. Am. Chem. Soc.* **1989**, *111*, 321.
43. The pull-off force, which is the negative load at which the sample loses contact with the tip, was taken as a measure of the adhesion interactions between the tip and sample. All measurements were conducted in air at ambient temperatures and humidities (24° C and 40%, respectively) using a silicon nitride AFM tip with a radius of ~500 Å and a normal spring constant of 0.58 N M^{-1}. Due to the hydrophobicity of the two films, capilliarity effects on the measured pull-off forces and frictional responses are expected to be negligible [22-27].

44. Differences in adhesive forces between CF_3- and CH_3-terminated films have been reported to be small: Burnham, N. A.; Dominguez, D. D.; Movery, R. L.; Colton, R. J. *Phys. Rev. Lett.* **1990**, *64*, 1931.

45. Phase segregation in monolayers generated from the co-adsorption of two adsorbates having different terminal groups or different chain lengths has been reported by various research groups: Stranick, S. J.; Parikh, A. N.; Tao, Y.-T.; Allara, D. L.; Weiss, P. S. *J. Phys. Chem.* **1994**, *98*, 7636; Tamada, K.; Hara, M.; Sasabe, H.; Knoll, W. *Langmuir* **1997**, *13*, 1558; and reference 4. Under particular conditions, however, the random mixing of two components has been observed: Bertilsson, L.; Liedberg, B. *Langmuir* **1993**, *9*, 141.; Bain, C. D.; Evall, J.; Whitesides, G. M. *J. Am. Chem. Soc.* **1989**, *111*, 7155; and reference 36.

46. Previously (see reference 13 and reference 3 therein), the size of the *i*-Pr group was underestimated due to an erroneous omission of the contribution of the hydrogen $HC(CH_3)_2$ in calculating the cross-sectional area.

47. As in reference 38, the surface free energies of the SAMs ($\gamma_S{}^d$) were estimated from the ·advancing contact angles of hexadecane (θ_a) using the following relationships (discussed in van Oss, C. J.; Chaudhury, M. K.; Good, R. J. *Chem. Rev.* **1988**, *88*, 927): $W_a = \gamma_L(1 + \cos\theta_a)$, $W_a = W_a{}^d + W_a{}^p$, and $W_a{}^d = 2(\gamma_L{}^d \gamma_S{}^d)^{1/2}$, where $W_a{}^d$ and $W_a{}^p$ are the dispersive and polar components, respectively, of the work of adhesion (W_a) between the contacting liquid and the SAM, $W_a{}^p = 0$ (assuming that the interactions between hexadecane and the SAMs are entirely dispersive), and the surface free energy of hexadecane is $\gamma_L = \gamma_L{}^d = 27.5$ mJ m^{-2}. The following values were obtained: $\gamma_S{}^d$ (CH_3-terminated film) $= 18.9 \pm 0.3$ mJ m^{-2}, $\gamma_S{}^d$ (CF_3-terminated film) $= 13.6 \pm 0.3$ mJ m^{-2}, and $\gamma_S{}^d$ (*i*-Pr-terminated film) $= 21.2 \pm 0.3$ mJ m^{-2}. The value of $\gamma_S{}^d$ (CF_3-terminated film) might be underestimated by hexadecane due to the non-ideal nature of the dispersive interactions between hydrocarbons and fluorocarbons, but no more than 4 mJ m^{-2}, which was determined through the use of *cis*-perfluorodecalin as the non-polar contacting liquid in the estimation of $\gamma_S{}^d$.

Chapter 5

Glass Transition Measurements of Ultrathin Polystyrene Films

Cynthia Buenviaje, Franco Dinelli, and René M. Overney

Department of Chemical Engineering, University of Washington, Seattle, WA 98195–1750

Data from various experiments suggest that the mechanical properties of thin polymer films depend, in a complex manner, on the film preparation process, in conjunction with interfacial interactions. In this paper, we discuss how and why interfacial interactions can affect the shear mechanical properties of spin-coated polymer films. For example, confinement effects due to the spin coating process have been observed to exceed the nearest neighbor interaction distances by one order of magnitude. We introduce shear modulation scanning probe microscopy (SPM) as a technique to measure local shear property changes in thin polymer films as a function of temperature. Comparisons with bulk and lateral force measurements demonstrate the reliability of the technique. Using the shear modulation SPM, we observe a molecular weight dependence on the bulk glass transition. Measurements taken on polystyrene surfaces of various film thickness provide insight into how the glass transition of films are affected by substrate confinement.

Introduction

Although bulk properties of polymers have been studied extensively, many properties of thin films, specifically the glass transition temperature, T_g, are not as well understood. The T_g of amorphous polymers is an important parameter in determining if a polymer can be used in a particular application. Below T_g, an amorphous polymer takes on the characteristics of a glass becoming hard, stiff, and brittle. Above T_g, extensive molecular motions soften the polymer, which then behaves like rubber. For bulk polymers, T_g is primarily measured either by differential thermal analysis (DTA) or differential scanning calorimetry (DSC). However, for thin films, the amount of polymer in the film is insufficient to obtain reliable results. In recent years, the T_g of thin polymer films, ranging in thickness from several to thousands of nanometers, has been successfully studied using a variety of experimental techniques. A collection of these techniques is listed in Table 1 along with the phenomena measured.

Table 1. Ultrathin Polymer Glass Transition Temperature Techniques

Volume Expansion	
Ellipsometry	(1-3)
X-Ray Reflectivity	(4, 5)
Positron Annihilation Lifetime Spectroscopy	(6, 7)
Brillouin Light Scattering	(8, 9)
Optical Reflectance	(10)
Acoustic Wave Spectroscopy	(11)
Segmental Mobility	
Probe Diffusion	(12, 13)
Excimer Recombination	(14)
Viscoelasticity	
Scanning Force Microscopy	(15-20)

Experimental results obtained with the techniques, listed in table 1, on similar systems (such as polystyrene with comparable molecular weights) have been found to be inconsistent. Although there is agreement that near the substrate interface, the value of T_g is shifted from the bulk due to confinement and size effects, there is evident contradiction in the direction of the shift. Problems such as local density variations normal to the interface, interfacial roughness, and film imperfections due to partial dewetting are listed as potential causes for these contradicting interpretations (21).

To minimize effects of film inhomogeneities, we proposed local scale measurements. The tool of choice is scanning probe microscopy (SPM) by virtue of its high spatial resolution. A variety of SPM approaches are available in order to probe the temperature dependence and a list of these modes include:

Phase Lag Method. The phase lag between a small sinusoidal perturbation (applied normally to the sample surface) and the cantilever response is recorded. T_g is determined as the onset of change in the phase lag (15-17).

Stiffness Method. The stiffness of the polymer surface is determined by force vs. displacement curves. Very stiff cantilevers are used, and T_g is defined as the temperature where a change occurs in the slope of the force-displacement curve (18, 19).

Lateral Force Rate Method. The sample is scanned at low load and the lateral force is measured as function of the scan rate at a fixed temperature. Below T_g the lateral force is expected to be independent of the scan velocity. T_g is defined as the temperature at which the onset of rate dependence is observed (16, 17, 20).

Lateral Force Method. Lateral forces are obtained at low scan velocity while the temperature is increased. T_g is determined as the increase in the lateral force or friction coefficient (19).

In several SPM studies, a T_g higher than the bulk value was observed, even for very thick bulk-like films. It has been suggested that the pressure the tip exerts on the surface could be interpreted as a hydrostatic pressure (22). At a macroscopic level, it is well known that T_g linearly increases with increasing hydrostatic pressure (0.3 K/MPa for polystyrene) (23). This is interpreted as the effect of subduing the thermal expansion of the material, therefore limiting the formation of free-volume necessary for the glass transition to take place.

In this paper, we will address the complex issue of the mechanical determination of T_g at surfaces of thick bulk-like, as well as interfacially confined ultrathin polymer films. First, we will show that the pressure exerted by the tip does not affect the glass transition. Then, we will introduce a novel contact mechanical technique to determine the T_g of thin films, shear modulation SPM. Finally we will present T_g results on films where interfacial interactions, remaining stress and conformational changes, formed during film preparation, alter the bulk T_g.

Experimental

Monodispersed polystyrene (PS) (M_w 3 k to 6.5 M M_w/M_n < 1.1) (Aldrich Chemical Company Inc. and Polymer Source, Inc) was spin cast on to silicon (100) wafers from toluene solution. The solution concentration was varied to achieve thicknesses ranging from 20 to 350 nm, as determined by ellipsometry (Rudolph, AutoEL). The wafers were hydrogen passivated via HF etching prior to spin casting, and samples were annealed under vacuum (< 400 mtorr) for 4 hours at 165 to 170 °C prior to SPM experiments.

SPM measurements were conducted with a commercial instrument (Explorer, Thermomicroscopes, Inc.) which was mounted onto a modified heating/cooling stage (Model R2700-2, MMR Technologies). The stage, manufactured by MMR Technologies, utilizes the Joule-Thompson effect to cool by gas expansion. Unlike thermoelectric heaters, this stage is very stable over a wide range of temperatures

(230 to 425 K). Investigations were carried out in a nitrogen flooded dry box to avoid strong capillary forces between the tip and sample. The humidity was maintained around 5 %. Bar-shaped cantilevers were employed, with normal spring constants ranging from 0.1 to 0.8 N/m.

Conventionally, the lateral force is obtained by taking the difference of the average lateral force acting on the tip when scanning along two opposite directions (divided by 2) (24). The tip was moved in the y direction at the end of each line in order not to scan the same region twice. The scan length was 5 μm at a speed of 5 μm/s. The results presented were obtained with positive loads only. (It was not possible with the lateral force SPM method to perform T_g measurements at negative applied load.) The sample temperature in the lateral force studies was adjusted in increments of 2 to 3 K, and a waiting time of approximately ten minutes was considered sufficient to stabilize the sample temperature.

In figure 1, a schematic of the operative principle for the shear modulation SPM is shown. A sinusoidal signal is applied to the x-piezo inducing an oscillatory local perturbation of the sample surface. The amplitude is chosen below the stick slip threshold between the cantilever tip and sample. A force feedback loop is used to keep the tip in contact with the sample surface. During the course of the entire T_g experiment, the tip response is measured using a dual phase lock-in amplifier (SR830, Stanford Research Systems). The sample temperature is increased in stepwise increments of 0.5 to 1 K per minute over a temperature range from 300 to 410 K. The rate with which the temperature is changed guarantees sample thermal equilibrium. The sample response is recorded at the end of each period before the next incremental temperature step was initiated.

Shear Response

Cantilever Tip

Sample

Shear Displacement
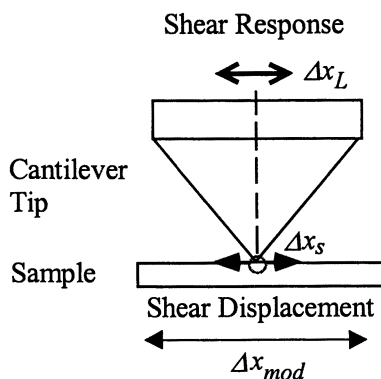
Figure 1. Schematics of the stationary shear modulation SPM. An externally applied lateral displacement, Δx_{mod}, causes a shear response, Δx_s, within the tip sample junction which is counteracted by the cantilever motion, Δx_L. Here, $\Delta x_{mod} = \Delta x_s + \Delta x_L$.

Results and Discussion

First, we will discuss the effect of pressure exerted by the tip on the measurement of T_g and the implications of an applied hydrostatic pressure. Assuming a Hertzian contact between the tip and sample, the contact radius a is given by (25):

$$a^3 = \frac{3RL(1-v^2)}{4E},\qquad(1)$$

where R is the radius of curvature for the tip, E the Young's modulus of the sample, v the Poisson's ratio, and L the applied load. Below T_g, with $L = 12$ nN and $E = 3$ GPa (26), $R = 10$ to 50 nm, the contact radius is equal to 3 to 5 nm. Assuming that the induced strain cannot be laterally released, a hydrostatic pressure in the range of 0.2 to 0.5 GPa would result. It has been found for PS that the glass transition changes with a hydrostatic pressure rate of 0.3 K/MPa (23) if we assume that the contact pressure shows a similar effect as a hydrostatic pressure, then SPM contact experiments would shift T_g significantly by 60 to150 K.

As the pressure exerted by the tip is localized and limited in time, a shift in T_g due to the applied load is not expected. The sample is typically scanned over several µm with a scan rate of 0.5 Hz. Assuming values of 3 to 5 nm and 30 to 80 nm^2 for the contact radius and area, the volume affected would be equal to a cylinder that is 5 times the length of the contact radius with a volume, approximately, 450 to 2000 nm^3 (25). In our case, the radius of gyration R_g, is about 5 nm and the volume occupied by one molecule is $V = 4/3\pi R_g^3 = 500$ nm^3 (27). This leaves only 1 to 4 molecules in the compression zone. Such a limited volume could not have such a dramatic effect over the properties of the polymer. In fact, the contact radius is so small compared to the scan length, the time of permanence over a specific area is only a few milliseconds per cycle. For the rest of the scan cycle, the molecules are unconstrained and can relax. If creep or thermal drift is taken into consideration, it is quite likely that the tip never passes over the same molecule twice. Hence, the pressure exerted by the tip cannot be considered hydrostatic. In addition, the lateral force is measured after the temperature has stabilized (20, 22, 28-30). Therefore, under these isothermal conditions, the polymer can be considered incompressible, i.e. it undergoes mechanical deformations but its density and free volume remain constant.

In figure 2, we present plots of lateral force as a function of temperature for three different loads. The results show an apparent transition temperature, T_c, which we define as the intersection of two line fits, decreases with increasing applied load. At high load (250 nN), T_c is in good agreement with bulk T_g, but it is shifted to higher values at an intermediate load, (80 nN). Strikingly, no T_c is observed at low load, (12 nN), where the lateral force remains constant over a wide range of temperatures even above T_g. These measurements follow our argument that the pressure exerted by the tip does not effect the T_g of polymer as a hydrostatic pressure. To further support this statement, we also measured the effect of scan speed on the transition temperature. Figure 3 shows a plot of lateral force as a function of temperature for three scanning speeds. The scanning length was 5 µm and the applied load 15 nN. At high speed (20 µm/s) no transition was observed. At intermediate speeds, a transition is observed at a T_c higher than T_g. Below a critical speed v_c, a T_c corresponding to T_g
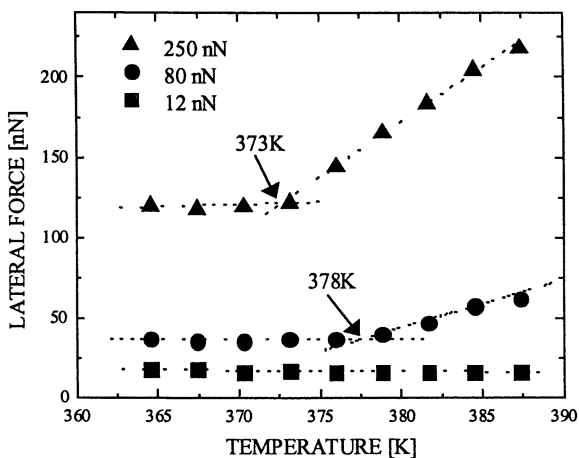
Figure 2. Lateral force vs. Temperature. At three loads, 12 nN, 80 nN, and 250 nN, the lateral force was measured as a function of temperature for PS (M_w 22.2 k, thickness = 100 nm). Scan length and scan speed were 5 μm and 5 $\mu m/s$, respectively. At 12 nN, no transition was observed. At 80 nN, an apparent transition was observed at 378 K, and at high load, 250 nN, a transition at 373 K was observed, matching the bulk T_g.
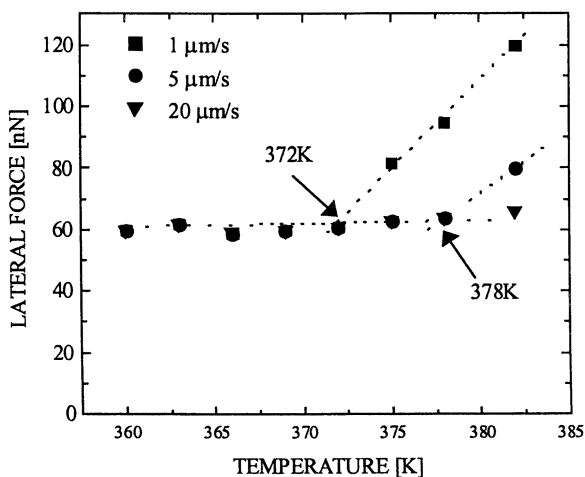
Figure 3. Lateral force vs. Temperature. The lateral force was measured as a function of temperature for three different speeds at a constant load of 15 nN for PS (M_w 22.2 k, thickness = 100 nm). At high speed, 20 $\mu m/s$, no transition is observed. At intermediate speed, an apparent transition is observed at 378 K. At low speed, a transition was observed at the bulk T_g.

was determined. These results indicate that lateral force microscopy is very sensitive to the scanning parameters.

If we consider the viscoelastic nature of the polymer films above T_g, equation 1 is no longer valid and needs to be corrected as follows (25):

$$a^3(t) = \frac{3RL_o}{8}\Phi(t) \tag{2}$$

where t is time and $\Phi(t)$ is the creep function derived from an appropriate viscoelastic model. Assuming a steady creep (Maxwell) model, $a^3(t)$ takes the following form (25):

$$a^3(t) = \frac{3RL_o}{8}\left(\frac{1}{E} + \frac{1}{\eta}t\right) \tag{3}$$

where η is the viscosity. We can assume that the contact area below and at T_g is not significantly affected by changes in the Young's Modulus, E. We expect, however, that changes in viscosity alter the lateral forces significantly.

Considering the time dependence of our model, we define the time of tip permanence over the contact area as t_S, which is given by the ratio of the contact area and scan velocity, v_S.

$$t_S = \frac{a}{v_S} \tag{4}$$

Below T_g, the time of relaxation exceeds the t_S of our experiment. Therefore, the contact area is dominated by the elastic component and becomes:

$$a^3(t_S) = \frac{3RL_o}{8}\frac{1}{E} \equiv a_o^3 \tag{5}$$

Above T_g, $a(t_S)$ is comparable to a_o if

$$t_S << \frac{\eta}{E} \tag{6}$$

With this, we document the complexity of the tip-sample penetration while scanning. Therefore, taking the onset of the penetration as a material property, i.e. the value of T_g, can be very misleading for friction measurements as experimentally confirmed. This is in contrast to shear modulation measurements where the contact location is fixed in space.

From our results, we can exclude any large hydrostatic pressure effects induced by contact mechanical SPM approaches such as lateral force or shear modulation methods. The lateral force method has strong potential for heterogeneous surfaces. On homogeneous surfaces, however, the shear modulation mode is much more reliable without the difficulties of calibrating the load and scan velocity dependence. In figure 4, tip response vs. temperature measurements on thick (476 nm) PS (M_w 90 k) films are presented for various loads. As the temperature is increased, we see a distinct increase in the amplitude response. We identify T_c as the intersection between the two line fits. The precision of the value is estimated to ±2 K. At an applied load of

32.3 nN, we see a transition at 374 K which corresponds well with the T_g measured for the bulk polymer (PS M_w 90 k) by DSC. However, for lower loads of 10.8 nN and 21.5 nN, we observe that the intersections do occur at higher temperatures. As with force measurements, we observed apparent transitions for shear modulation SPM measurements taken at lower loads due to unsteady contacts (e.g. partial slip). However, the onset of change does occur at T_g regardless of the applied load. At higher load ($\geq$ 30 nN), the transitions were not load dependent.

The reproducibility of the shear modulation SPM measurements is illustrated with continuous shear measurements at constant applied (high) load, figure 5. Measurements were taken on thick samples by continuous cycling of the temperature above and below T_g.
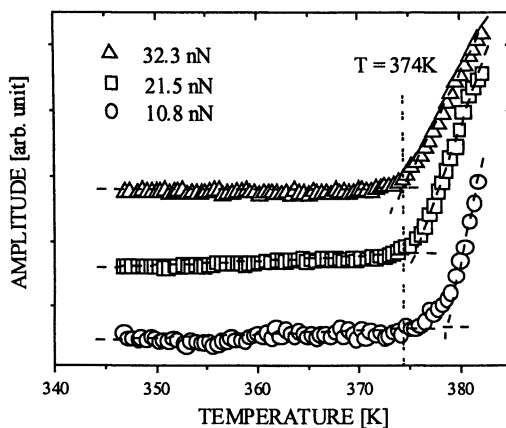
Figure 4. Shear Modulation SPM Amplitude vs. Temperature. Shear modulation SPM measurements on PS (M_w 90 k, thickness = 476 nm) films are shown at various loads, 32.3 nN, 21.5 nN, and 10.8 nN. Using straight line fits, the transition is observed to change with increase load. Although the transition is slightly shifted, the start of the transition is observed at the same point regardless of load (at 374 K).

To test the capabilities of shear modulation SPM, we measured the dependence of T_g on the molecular weight and compared the results with values for the bulk polymer (31, 32). Relatively thick films (> 150 nm) were used to avoid any interfacial effects. In figure 6, the T_g as a function of the number-averaged molecular weight is plotted. The transition temperatures are plotted along with values reported in the literature for DSC by Claudy et al (31) and electron spin resonance (ESR) by Kumler et al (32). From figure 6, the T_g measured using the shear modulation SPM agrees well with bulk
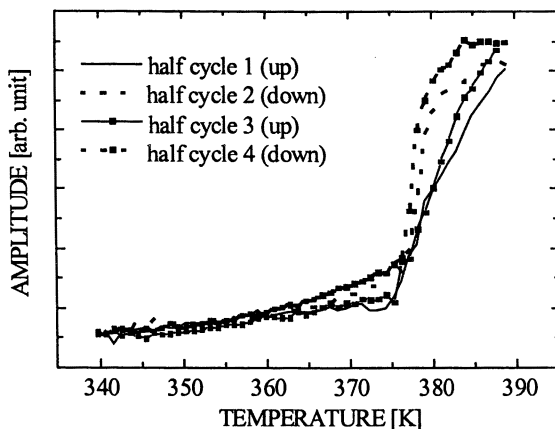
Figure 5. Ramped Shear Modulation SPM vs. Temperature. The reproducibility of the modulated measurements is proven by ramping the temperature above and below T_g. Half cycles shear modulation measurement were made on PS (M_w 90 k, thickness =200 nm).

values over a wide range of molecular weights (3.6 k to 6.5 M). The dependence of T_g on the molecular number follows the equation developed by Fox-Flory (33, 34),

$$T_g = T_g^\infty - \frac{K}{(\alpha_r - \alpha_g)M_n} \qquad (7)$$

where T_g^∞ is the glass temperature at infinite molecular weight, M_n is the molecular weight, K is a fitting constant, α_r and α_g are the cubic (volume) expansion coefficients in the rubbery and glassy states (35). For our results, the values of T_g^∞, K, and $(\alpha_r - \alpha_g)$ are 374 K (using the T_g of 1.8 M and 6.5 M as T_g^∞), 26.5 and 3.0 x 10^{-4} K^{-1} (36). As can be seen from figure 6, our data correlates well with literature values and the general relationship developed by Fox and Flory.

The dependence of the bulk T_g on the molecular weight is explained as a free volume effect of the polymer chain ends. For a low molecular weight polymer, there are more chain ends per unit mass than for a high molecular weight polymer. Therefore, less energy is required to achieve the same free volume as in a lower molecular weight polymer (37). This implies that the value of T_g should decrease with decreasing molecular weight.

After extensive investigations, we consistently observed that once the temperature has reached T_g, the sample begins to soften and the tip sinks into the surface (creep). At a constant temperature of 384 K (10 degrees above T_g), after thermal equilibrium was obtained (30 minutes), a load was applied to a film of PS (M_w 6.5 M). A hole is formed, which is 0.65 μm in diameter, figure 7a. The time the cantilever was in contact with the sample at constant load and temperature will be referred to as the
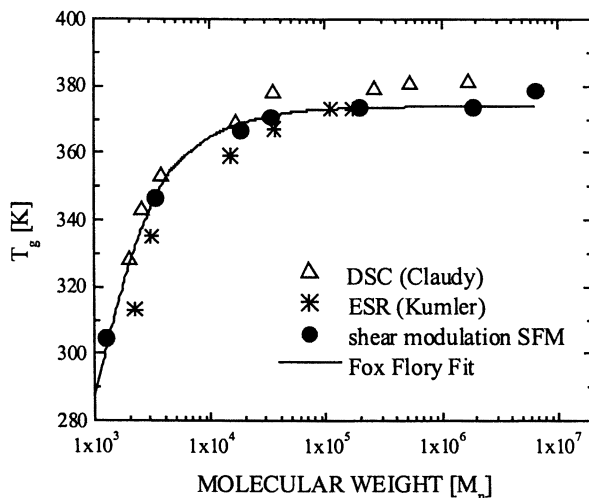
Figure 6. Glass Transition vs. Molecular Weight. The T_g of PS films (thickness > 150 nm) is presented as a function of the number averaged molecular weight. Results can be modeled using a Fox-Flory fit and corresponds well with DSC (31) and ESR (32) measurements reported in literature.

'dwell time'. In figure 7a, the depression formed is approximately 42 nm at its deepest point, figure 7b. The applied load was 149 nN and the dwell time was 2 minutes. Similar results were obtained at lower applied loads above T_g. No plastic deformation occurred at temperatures below T_g. In figure 8, we show that data has a trend well represented by an exponential function of the type:

$$\delta = \delta_0 + ke^{-t/\alpha}. \tag{8}$$

where δ_0, k, and α are 70, 55, and 3 respectively.

The local damage of a temperature half cycle was measured by cooling the sample to room temperature and imaging the affected area. The shear modulation measurement and the observed depression are presented in figures 9a, b. Line measurements of the hole revealed that the depth of penetration is 150 nm at the deepest point. Ellipsometry measurements of the sample estimate the thickness of the sample as approximately 230 nm ± 5 nm. Comparing the two values, we are assured that we do not reach the silicon substrate during our measurement, even after dwelling on the surface for a long time at a temperature well above T_g. Imaging after a successive heating/cooling cycle, we observed that the polymer heals itself and therefore have ruled out the possibility of hole formation by dewetting at the tip sample interface.
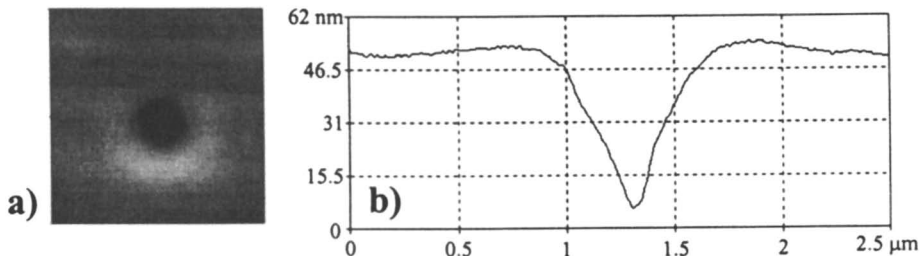
Figure 7. Tip indentation. a) 2.41 x 2.41μm² image of a whole formed in the film by tip indentation. A load of 149 nN was applied for 2 minutes. b) Line measure taken at the center of the hole indicating a depth of 42 nm. Tip indentation measurements were made on PS films (Mw 6.5 M, thickness = 350 nm).

$$\delta = \delta_o + k \exp(-t/\alpha)$$
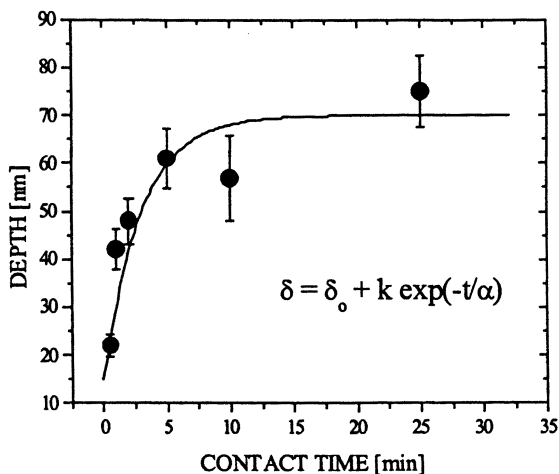
Figure 8. Hole Depth vs. Contact Time. Using an applied load of 149 nN, the sinking process is measured as a function of time. The depth of the hole increased with time in contact on PS (Mw 6.5 M, thickness = 350 nm).

With this information, we can interpret the load dependence of shear modulation SPM measurements (figure 4). At low loads, the pressure under the tip is low, and the tip sinks into the polymer very slowly. At high loads, the pressure under the tip is significant and allows the tip to break through the polymer's surface at T_g. At high loads, the tip sinks more quickly into polymer.

From contact mechanics, the response amplitude is generally a measure of the contact stiffness: the higher the contact stiffness the higher the response amplitude. For a simple elastic contact with sphere-plane geometry, the lateral stiffness of contact, k_c, is given by:

$$k_c = 8aG \qquad (9)$$

with the shear modulus, G and the contact area, a.. Below T_g no plastic deformation is observed, while above T_g, plastic deformation occurs. Therefore in amplitude response curves, we should expect to see a decrease in amplitude response. According to equation 7, above T_g, the contact area must increase significantly to overcome the decrease in G. One possibility to explain an increasing contact stiffness is due to pinning of the tip during the sinking process. As the tip sinks into the polymer, (figure 10) it is pinned by the surrounding material. The added energy required for movement increases the amplitude response, therefore, we propose an additional time-dependent term in the equation for the contact stiffness:

$$k_c = 8aG + \Phi(\eta, t). \qquad (10)$$

Setting $\Phi = 0$ for $T < T_g$, we have a simple elastic contact below T_g and an added time dependence viscous term, $\Phi(\eta, t)$, above T_g.

Finally, we studied the effect of the interfacial confinement on the glass transition. In figure 11a, T_g is plotted as a function of film thickness. Films were made of PS (M_w 90 k). It is noticeable that the glass transition temperature is steadily increasing with decreasing thickness below a critical thickness, t_c. The critical thickness is defined here as the thickness which divides the bulk and boundary regimes (as shown by the changing values for T_g) and is equal to ~125 nm. In figure 11b, the lateral force at a constant load is plotted against film thickness. An increase in lateral force is observed as the film thickness increases until t_c is reached. The bulk value of lateral force for this load was 107 nN for film thicknesses greater than t_c.

An increase in T_g indicates that the material is mechanically confined and more thermal energy is necessary to induce a transition from a glass-like behavior to a melt. This is in excellent agreement with lateral force measurements taken on PS, figure 11b. This heterogeneous layer can be separated, normally to the substrate, into two regimes: a gel-like sublayer at the interface (density loss of about 10% compared to the bulk polymer), and an intermediate and gradually changing boundary layer (with a thickness of 7 to 10 R_g) (29) weight PS films.

The influence of interfacial interaction is usually neglected. This is because in classical mean-field theories or molecular dynamic simulations it is assumed that interfacial interactions are completely screened within a distance corresponding to the persistence length of the polymer (38). Thus, confinement effects induced during film preparation are not taken into account. However, it has been shown that interfacial interactions can effect the polymer films up to a distance of 200 nm from the interface even after annealing of the polymer films (29, 39, 40).
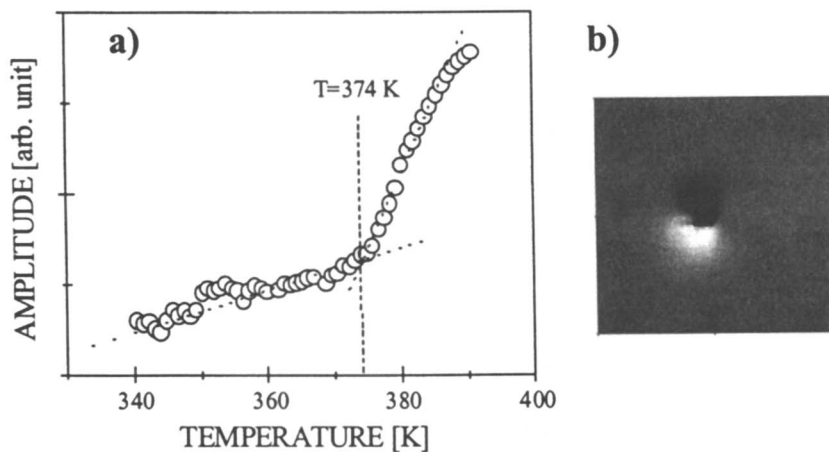
Figure 9. Shear Modulation SPM Amplitude vs. Temperature. a) A typical shear modulated measurement is shown on PS (M_w 6.5 M, thickness = 230 nm). b) The corresponding depression left by the tip after the measurement is presented. The hole is 150 nm at its deepest point. The image shown is a 6.78 x 6.78 μm^2 image of the indentation.

Figure 10. Tip Movement and Sinking. As the tip sinks into the polymer above Tg, the movement at the tip is restricted due to the surrounding polymer. Increased material must be moved by the tip to achieve the same amplitude response

It is fairly easy to understand the change in mechanical properties and mobility for film thicknesses on the order of two times the radius of gyration (R_g), where almost every chain has at least one point of contact with the surface. On the other hand, the persistence of the effect at distances much larger than R_g, where most of the chains are not in direct contact with the surface, is far more difficult to explain. Existing classical mean field or molecular dynamic theories assume that the surface interaction is completely screened within a distance corresponding to the persistence length of the polymer (about 0.6 nm) (41, 42). It was, however, found that this assumption is not valid in the case of spin-coated films where a layer immediately adjacent to the silicon substrate is pinned to the surface (40, 43). Consequently, the large spin-coating-induced deformation of the chains cannot relax. The strained interfacial sublayer can be pictured as highly disentangled and laterally anisotropic, with a thickness on the order of R_g (43). The polymers adjacent to the surface immobilized sublayer can diffuse through the sublayer's pores forming a two-fluid-system, as observed in diffusion measurements in a PS system (40). At a distance of about 7 to 10 R_g apart from the substrate, the polymer behaves like the bulk elastomer and loses any memory of the presence of the silicon surface and the spin-coated induced interfacial alignment (40, 43). We observe this transition from an induced interfacial alignment to the bulk elastomer as t_c.

Conclusions

The glass transition of amorphous polymeric films was investigated by SPM under various conditions. We established, using lateral force measurements, that the pressure exerted by the tip does not have an effect similar to a hydrostatic pressure on the properties of the polymer. Instead, an apparent transition is observed due to the viscoelastic nature of the sample. We confirm the existence of a critical load and scan speed, which need to be determined to obtain accurate glass transition temperature measurements.

The shear modulation SPM was introduced as a new technique to measure the glass transition temperature. We have shown that this mode is sensitive to the viscous properties of the films. At T_g, the tip sinks into the sample and a hole begins to form. This sinking process causes the response amplitude to increase. For thick films of PS, i.e. thicknesses about 200 nm, we have verified that the glass transition at the air-polymer interface is bulk-like within an uncertainty of ± 2 K.

The dependence of the glass transition temperature on the molecular weight for thick films was studied. Relatively thick films were used to avoid possible interfacial effects. On PS films with molecular weight between 3 k and 6.5 M, we observed decreasing values of glass transition temperature, which compared well with values reported in the literature using DSC and ESR. Data also followed the well-known Fox-Flory model.

In the end, we have shown that the glass transition depends on film thickness. On films of PS between 20 nm and 500 nm in thickness, we found an increase of glass
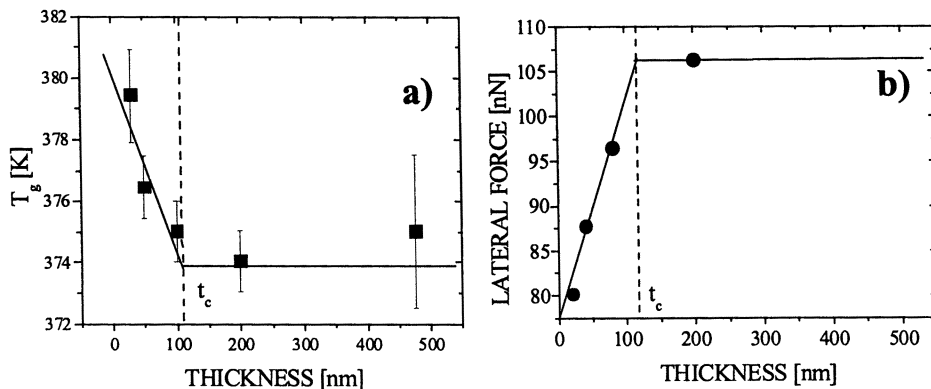
Figure 11. T_g and Lateral force vs. Thickness. a) The effect of confinement is observed for PS films (M_w 90 k) of various thickness. Below a critical thickness t_c, the T_g of the polymer film increases from the bulk T_g observed on thick films greater than 150 nm. b) This t_c is also observed in lateral force measurements on the same samples and is thought to be induced by the spin coating process.

transition temperature below a critical thickness of 150 nm. This increase is due to confinement of the molecules within a boundary layer towards the silicon substrate. In this boundary layer, surface effects reduce the local mobility of the polymer and thus increase the value of the glass transition temperature by a few degrees.

These findings prove that modulated SPM is a unique and very powerful technique to measure local properties of thin polymer films; it is a local, load independent, contact mechanical approach to measuring surface properties of polymers.

Acknowledgements

References

(1) Beaucage, G.; Composto, R.; Stein, R. S. *J. Polm. Sci. B; Poly. Phys.* 1993, *31* , 319.

(2) Keddie, J. L.; Jones, R. A. L.; Cory, R. A. *Faraday Discuss* 1994, *98* , 219.

(3) Keddie, J. L.; Jones, A. L.; Cory, R. A. *Europhys. Lett.* 1994, *27* , 59.

(4) Wallace, W. E.; van Zanten, J. H.; Wu, W. L. *Phys. Rev. B* 1995, *52* , R3329-R3332.

(5) Van Zanten, J. H.; Wallace, W. E.; Wu, W. L. *Phys. Rev. B* 1996, *53* , R2053.

(6) Xie, L.; DeMaggio, G. B.; Frieze, W. E.; DeVries, J.; Gidley, D. W.; Hristov, H. A.; Yee, A. F. *Phys. Rev. Lett.* 1995, *74* , 4947.

(7) DeMaggio, G. B.; Frieze, W. E.; Gidley, D. W.; Zhu, M.; Hristov, H. A.; Yee, A. F. *Phys. Rev. Lett.* 1997, *78* , 1524-1527.

(8) Forrest, J. A.; Dalnoki-Veress, K.; Stevens, J. R.; Dutcher, J. R. *Physical Review Letters* 1996, *77* , 2002-2005.

(9) Forrest, J. A.; Dalnoki-Veress, K.; Dutcher, J. R. *Physical Review E* 1997, *56* , 5705-5716.

(10) Prucker, O.; Christian, S.; Bock, H.; Ruehe, J.; Frank, C.; Knoll, W. *Macromolecular Chemistry and Physics* 1998, *199* , 1435-1444.

(11) Bretz, R. C.; Lee, Y.-C.; Wise, F. W.; Sachse, W. *Bull. Amer. Phys. Soc.* 1998, *March* , S13.07.

(12) Hall, D. B.; Miller, R. D.; Torkelson, J. M. *Journal of Polymer Science: B Polymer Physics* 1997, *35* , 2795-2802.

(13) Hall, D. B.; Torkelson, J. M. *Macromolecules* 1998, *31* , 8817-8825.

(14) White, C. C.; Wu, W.-L.; Wise, F. W.; Sachse, W. *Bull. Amer. Phys. Soc.* 1999, *44* , 1674.

(15) Tanaka, K.; Taura, A.; Ge, S.; Takahara, A.; Kajiyama, T. *Macromolecules* 1996, *29* , 3040.

(16) Kajiyama, T.; Tanaka, K.; Takahara, A. *Macromolecules* 1997, *2* , 280-285.

(17) Kajiyama, T.; Tanaka, K.; Takahara, A. *Polymer* 1998, *39* , 4665-4673.

(18) Gracias, D. H.; Zhang, D.; Lianos, L.; Ibach, W.; Sen, Y. R.; Somorjai, G. A. *Chem. Phys.* 1999, *245* , 277.

(19) Gracias, D. H.; Zhang, D.; Shen, Y. R.; Somorjai, G. A. *Mat. Res. Soc. Symp. Proc.* 1998, *522* , 175-180.

(20) Hammerschmidt, J. A.; Gladfelder, W. L.; Haugstad, G. *Macromolecules* 1999, *32* .

(21) Kuebler, S. C.; Heuer, A.; Spiess, H. W. *Phys. Rev., E* 1997, *56* , 741-9.

(22) Schmidt, R. H.; Haugstad, G.; Gladfelter, W. L. *Langmuir* 1999, *15* , 317.

(23) Goldblett, P. H.; Porter, R. S. *Journal of Applied Polymer Science* 1970, *9* , 463.

(24) Meyer, E.; Overney, R.; Dransfeld, K.; Gyalog, T. *Nanoscience: Friction and Rheology on the Nanometer Scale* ; World Scientific Publ.: Singapore, 1998.

(25) Johnson, K. L. *Contact Mechanics* ; Cambridge University Press, Cambridge, 1985.

(26) Brandrup, J.; Immergut, E. H. ; Wiley and Sons, 1989.

(27) Rodriguez, F. *Principles of polymer systems* ; Taylor & Francis, 1996.

(28) Hammerschmidt, J. A.; Moasser, B.; Gladfelter, W. L.; Haugstad, G.; Jones, R. R. *Macromolecules* 1996, *29* , 8996.

(29) Buenviaje, C.; Ge, S.; Rafailovich, M.; Sokolov, J.; Drake, J. M.; Overney, R. M. *Langmuir* 1999, *15* , 6446-6450.

(30) Overney, R. M.; Buenviaje, C.; Luginbuhl, R.; Dinelli, F. *Journal of Thermal Analysis and Calorimetry* 2000, *59* , 205-225.

(31) Claudy, P.; Letoffe, J. M.; Camberlain, Y.; Pascault, J. P. *Polymer Bulletin* 1983, *9* , 208-215.

(32) Kumler, P. L.; Keinath, S. E.; Boyer, R. F. *J. Macromol Sci -Phys* 1977, *B13* , 631-646.

(33) Fox, T. G.; Flory, P. J. *J. Appl. Phys.* 1950, *21* , 581.

(34) Fox, T. G.; Flory, P. J. *J. Polym. Sci.* 1954, *14* , 315.

(35) Sperling, L. H. *Introduction to Physical Polymer Science* , 2nd ed.; John Wiley & Sons, Inc.: New York, 1992.

(36) Wood, L. A. *J. Polym. Sci* 1958, *28* , 319.

(37) Eisele, U. *Introduction to Polymer Physics* ; Springer-Verlag: Berlin, 1990.

(38) Brogley, M.; Bistac, S.; Schultz, J. *Macromol. Theor. Simul.* 1998, *7* , 65-68.

(39) Overney, R. M.; D.P. Leta, D. P.; Pictroski, C. F.; Rafailovich, M.; Liu, Y.; Quinn, J.; Sokolov, J.; Eisenberg, A.; Overney, G. *Phys. Rev. Lett.* 1996, *76* , 1272-1275.

(40) Overney, R. M.; Guo, L.; Totsuka, H.; Rafailovich, M.; Sokolov, J.; Schwarz, S. A. *Mat. Res. Soc. Symp. Proc.* 1997, *464* , 133-144.

(41) Hu, H. W.; Granick, S. *Science* 1992, *258* , 1339.

(42) Reich, S.; Choen, Y. *J. Polym. Sci. Polym. Phys.* 1981, *599* , 19.

(43) Zheng, X.; Rafailovich, M. H.; Sokolov, J.; Strzhemechny, Y.; Schwarz, S. A.; Sauer, B. B.; Rubinstein, M. *Phys. Rev. Lett.* 1997, *79* , 241-244.

Chapter 6

Atomic Scale Friction: From Basic Characteristics to Control

Markus Porto, Michael Urbakh, and Joseph Klafter

School of Chemistry, Tel Aviv University, 69978 Tel Aviv, Israel

We review the basic characteristics of frictional response within the framework of a model of a monolayer embedded between two plates one of which is externally driven. The model accounts for the coupled lateral and normal motions of the driven plate. We concentrate on two main aspects: (a) the response of the embedded system to the external drive, and (b) how to modify and control the frictional force. For describing the response of the embedded system, we apply the concept of shearons, which are collective modes of well defined spatial/temporal patterns in the particles density. Shearons, which are shown to dominate the frictional response of the driven system, are found to be useful in tuning the frictional behavior and predicting new methods to control friction, in addition to the established mechanical ones.

The field of nanotribology evolves around the attempts to understand the relationship between macroscopic frictional forces and the microscopic properties of the embedded system. Recent revival of interest in friction [*1, 2, 3, 4, 5, 6, 7, 8*] has unraveled a broad range of phenomena and new behaviors which help shed light on some fundamental concepts which are already considered textbook material. These include the static and kinetic friction forces, transition to sliding, thinning, and memory effects, which have been widely discussed but whose microscopic origins are still lacking.

New experimental tools have been developed that allow for detailed investigations of confined molecules and macromolecules down to nanometer length scales. As an example, the surface forces apparatus (SFA) has been modified to explore shear forces between two atomically flat solid surfaces separated by molecularly thin liquid layers [*9, 10, 11, 12*]. Based on the experimental observations, one distinguishes between a low driving velocity region, where the system behavior is characterized as 'solid'-like, and higher driving velocities, which correspond to a more 'liquid'-like behavior. Characteristic of the low velocity regime is stick-slip motion which is determined by the static and kinetic friction forces and whose details depend on the mechanical properties of the probing system. For high velocities the system exhibits smooth sliding which

94

resembles thinning of the effective viscosity [*13*]. Typical of the intermediate range between low and high driving velocities is a chaotic behavior [*13, 14*]. While most studies of frictional forces, using SFA, have focused on the lateral response to a lateral driving force, there have been a few theoretical and experimental observations of response in the normal direction [*15, 16, 17, 18, 19, 20, 21*]. A feature characteristic of the response in the normal direction is the dilatancy during slippage and sliding, observed in experiments and molecular dynamics calculations. The interest in coupling between lateral and normal motions has recently gained additional attention due to the possibility to modify the lateral response by imposing a controlling normal drive [*20, 21, 22, 23, 24*].

What one wishes to deduce from the experimental observations are new insights that will help establish the basics of nanotribology, differentiate among different embedded systems, and enable to control friction and maintain the desired type of motion. A lot of activity has been devoted to theoretical studies of interfacial friction of sheared systems, but in spite of the many efforts [*25, 26, 27, 28, 29, 30, 31, 32, 33, 34, 35, 36, 37, 38, 39, 40*], both numerical and analytical, many questions have remained unresolved. In particular, the relationship between macroscopic observables and the microscopic properties of the embedded molecular system under shear is not well understood. Some of the questions have been addressed already in previous works based mainly on large scale molecular dynamics calculations [*23, 41, 42, 43, 44*]. Atomistic molecular dynamics simulations have a wide range of applicability and have reached a high level of accuracy. They have, however, their inherent limitations. Right now time scales of tens of nanoseconds and length scales of tens of nanometers are attainable in computer simulations. These time and length scales may not be sufficient for the slow relaxation processes which play an important role in friction and lubrication phenomena of liquid films. As an example, critical velocities for nanoscale confined liquids have been experimentally found to be in the range $50 - 500 \, \text{nm/s}$ [*9, 10, 11, 12*], while molecular dynamics simulations give values of the order of $1 \, \text{m/s}$ [*23, 41, 42, 43*]. This means that there is a difference of *seven* orders of magnitude between the experimental and theoretical results. Nevertheless, the time scale limitation is not a principal problem of atomistic molecular dynamics simulations, as it will be hopefully resolved in the future. The basic open questions concerning molecular dynamics simulations relate to derivations of general laws which are not sensitive to the specific details of the simulations and the discovery of the few parameters controlling the processes under consideration.

In this paper we use another approach and address the questions raised above within a simple yet general and rich enough model, that includes most of the parameters relevant to the problem of friction. Although the model cannot be expected to provide quantitative results, it serves as an example of how to establish basic relationships between the microscopic characteristics and the macroscopically observed quantities. We believe that our conclusions are mostly model independent.

The Model

We start from a *microscopic* model [*13, 32, 33, 34, 45, 46*], which captures many of the experimental findings obtained in measurements on nanoscale confined liquids [*9,*
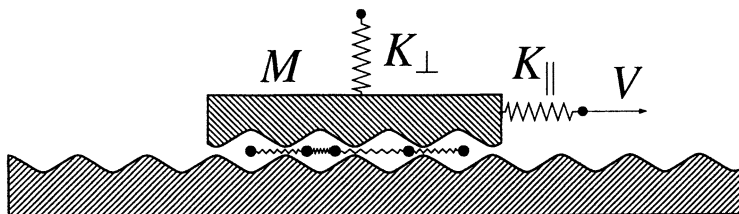
Figure 1: Schematic sketch of the model geometry.

11, 47], and granular layers [48]. The model includes both lateral and normal motions of the top plate [49], see Figure 1 for a sketch of the geometry. The model consists of two rigid plates and of a monolayer of N particles, each with a mass m and lateral coordinate x_i, embedded between them. The top plate of mass M and center of mass coordinates X (lateral) and X' (normal) feels a normal load applied by a linear spring of spring constant $K_\perp$ and is laterally pulled with a linear spring of spring constant $K_\parallel$ by a stage which moves with constant velocity V. This system is described by $N+2$ equations of motion

$$M\ddot{X} + \sum_{i=1}^{N} \eta_\parallel(X') \left[\dot{X} - \dot{x}_i\right] + K_\parallel \left[X - Vt\right] + \sum_{i=1}^{N} \frac{\partial \Phi(x_i - X, X')}{\partial X} = 0 \quad , \tag{1}$$

$$M\ddot{X}' + \eta_\perp(X')\, \dot{X}' + K_\perp \left[X' - X_0'\right] + \sum_{i=1}^{N} \frac{\partial \Phi(x_i - X, X')}{\partial X'} = 0 \quad , \tag{2}$$

$$m\ddot{x}_i + \eta_\parallel(X') \left[2\dot{x}_i - \dot{X}\right] + \sum_{\substack{j=1 \\ j\neq i}}^{N} \frac{\partial \Psi(x_i - x_j)}{\partial x_j}$$

$$+ \frac{\partial \Phi(x_i, X')}{\partial x_i} + \frac{\partial \Phi(x_i - X, X')}{\partial x_i} = 0 \quad i = 1, \ldots, N. \tag{3}$$

The second term in eqs. 1-3 describes the dissipative forces between the particles and the plates and is proportional to their relative velocities and to the X'-dependent damping $\eta_{\parallel,\perp}(X') = \eta_{\parallel,\perp}^0 \exp(-X'/\Lambda)$, accounting for dissipation that arises from interaction with phonons and other excitations. The interactions between the particles and the plates are represented by the periodic potential with respect to x, $\Phi(x, X') = -\Phi_0 \exp(-X'/\Lambda) \cos(2\pi x/b)$. Concerning the inter-particle interaction, we assume here nearest neighbor harmonic interaction $\Psi(x_i - x_{i\pm 1}) = (k/2)[x_i - x_{i\pm 1} \pm a]^2$ and free boundary conditions, although the Lennard-Jones interaction and periodic boundary conditions have been investigated as well [45]. The two plates do not interact directly. These equations are integrated numerically [50].

The basic frequency in the problem is chosen as the frequency of the top plate oscillation in the periodic potential $\Omega \equiv (2\pi/b)\sqrt{N\Phi_0/M}$. The other frequencies in the model are the frequency of the particle oscillation in the potential $\omega \equiv (2\pi/b)\sqrt{\Phi_0/m}$, the characteristic frequency of the inter-particle interaction $\hat{\omega} \equiv \sqrt{k/m}$, and the frequencies of the free lateral and normal oscillations of the top plate $\hat{\Omega}_{\parallel,\perp} \equiv \sqrt{K_{\parallel,\perp}/M}$. Under experimental conditions where $Nm/M \ll 1$, our model predicts critical velocities which are in the range observed experimentally. Under these experimental conditions, our calculations demonstrate that the motion of the top plate is not sensitive to the microscopic frequencies ω and $\hat{\omega}$, except for the limit $a/b \to 1$, which corresponds to monolayer-potential commensurability, and/or when $k \to 0$. In these limits the system exhibits the independent particle behavior discussed in [13].

To simplify the discussion, we introduce the unitless coordinates $Y \equiv X/b$, $Y' \equiv X'/b$ ($Y_0' \equiv X_0'/b$), and $y_i \equiv x/b$ of the top plate and the particles, respectively, as well as the unitless time $\tau \equiv \Omega t$ [51]. We define the following quantities: The misfit between periods of the substrate and the inter-particle potentials $\Delta \equiv 1 - a/b$, the ratio of masses of the particles and the top plate $\varepsilon \equiv Nm/M$, the unitless dissipation coefficients $\gamma_{\parallel,\perp} \equiv N\eta_{\parallel,\perp}^0/(M\Omega)$, the unitless damping length $\lambda \equiv \Lambda/b$, the ratios of frequencies of lateral and normal free oscillations of the top plate and the oscillation of the top plate in the potential $\alpha_{\parallel,\perp} \equiv \hat{\Omega}_{\parallel,\perp}/\Omega$, the ratio of the frequencies related to the inter-particle and particle/plate interactions $\beta \equiv \hat{\omega}/\omega$, and the dimensionless velocity $v \equiv V/(b\Omega)$. In addition, the friction force f_k and the normal force f_n, both per particle, are defined as $f_k \equiv F_k/(NF_0)$ and $f_n \equiv F_n/(NF_0)$, respectively, where F_k and F_n are the total forces measured with the external lateral ($K_{\parallel}$) and normal ($K_{\perp}$) springs, and $F_0 \equiv 2\pi\Phi_0/b$ is the 'natural' force unit given by the plate potential.

Basic Characteristics

In Figure 2 shown are the mean friction force per particle $\langle f_k \rangle$ and the force fluctuations $\langle f_k^2 \rangle - \langle f_k \rangle^2$ vs stage velocity v, respectively ($\langle \cdot \rangle$ denotes time average). All points have been obtained for the same initial condition. For very low driving velocities $v \ll 0.01$ [not shown in Figure 2], stick-slip behavior is found. In this regime the force fluctuations are of the order of the mean force. A transition to sliding is observed at higher velocities. In the transition regime the force fluctuations are approximately constant, and the top plate is never at rest. The force fluctuations sharply decrease at the critical velocity $v_c \cong 0.32$, so that for velocities $v > v_c$ the top plate moves practically with a constant velocity. For the chosen parameter values, the embedded layer in any time partially follows both the bottom and the top plate [13, 32, 33, 45, 46]. Namely, the layer does not stick to any of the plates and moves on average with a velocity that is half of the stage verlocity.

With the exception of very small driving velocities the dynamics of the system is chaotic for velocities which are smaller than v_c. Namely, the largest Liapunov exponent, which provides a quantitative measure of the degree of stochasticity, is positive [13, 14]. The velocity dependence of the Liapunov exponent gives a clear manifestation of the
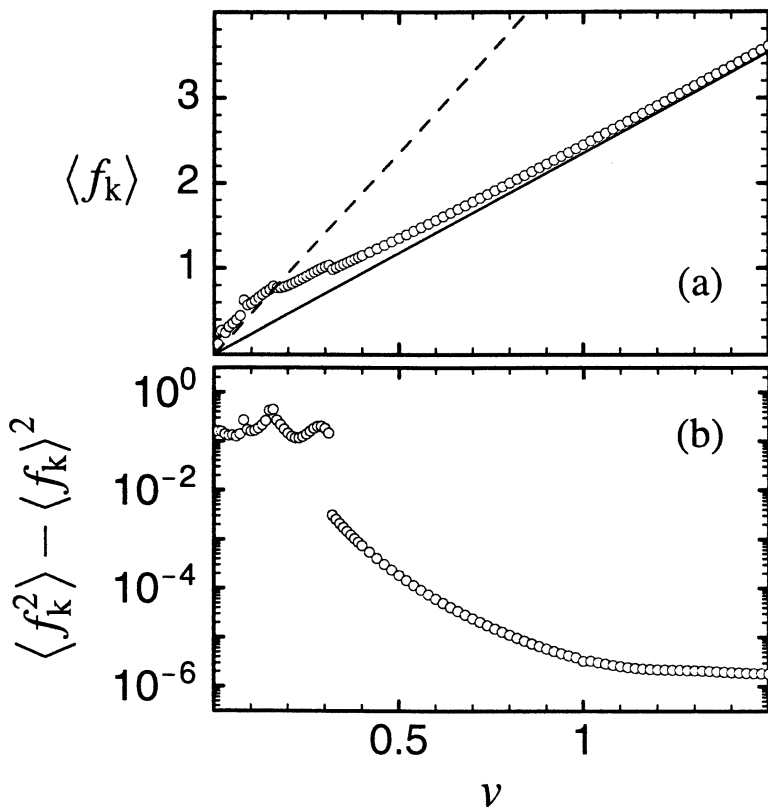
Figure 2: Plot of the mean friction force per particle $\langle f_k \rangle$ *and the force fluctuations* $\langle f_k^2 \rangle - \langle f_k \rangle^2$ *vs stage velocity v, respectively. In (a) the solid and dashed lines have the slope* $\pi\gamma$ *and* $2\pi\gamma$, *respectively, which correspond to sliding of the particles with a constant velocity* $v/2$ *(solid), and to a motion with a mean velocity* $v/2$ *and velocity fluctuations* $v/\sqrt{2}$ *(dashed), c.f. eq. 5 and [33, 35]. The model parameters are* $\alpha_\parallel = 1$, $\alpha_\perp = 0.5$, $\beta = 1$, $\gamma_\parallel = 0.75$, $\gamma_\perp = 0.75$, $\Delta = 0.1$, $\varepsilon = 0.01$, $\lambda = 1$, $Y_0' = 0$, *and* $N = 15$. *(Reproduced with permission from* Europhys. Lett. **2000**, *50,* 326–332. Copyright 2000).*

transition to sliding [*14*]. As the stage velocity increases and approaches a critical velocity v_c, the largest Liapunov exponent decreases steeply and becomes negative at $v = v_c$, suggesting the disappearance of chaos in the transition and the onset of the sliding regime. This concurs with the decrease in the amplitude of the spring force fluctuations.

In order to analyze the motion of the embedded system more closely, we seperate the motion of the particles into the center of mass part $y_{cms} \equiv 1/N \sum_{i=1}^{N} y_i$ and the fluctuations $\delta y_i \equiv y_i - y_{cms}$. It has been observed in similar models [*52, 53, 54*] that different modes of motion can coexist for a given set of parameters and lead to different frictional forces. Here, we concentrate on those solutions of the coupled dynamical equations 1-3

which correspond to smooth or to stick-slip motion of the top plate. To understand the nature of the motion of the embedded system in these regimes and the relationship to the frictional response, we choose the particles density ρ as a observable. Instead of defining the density as $\sum_{i=1}^{N} \delta(y - y_{cms} - \delta y_i)$, we represent each particle by a Gaussian of width $\sigma = 1$, namely

$$\rho(y - y_{cms}, \tau) \equiv \sum_{i=1}^{N} \exp\left\{-\left[\frac{y - y_{cms} - \delta y_i}{\sigma}\right]^2\right\} \quad . \tag{4}$$

This allows to visualize correlated motions of the particles on length scales which exceed nearest neighbor distance and are of the order of 2σ to 3σ. Using eq. 4 we find that the response of the embedded system to shear can be described in terms of collective modes which display well defined spatial and temporal patterns in the density, which we call "shearons" [45, 46]. These shearons are the spatial/temporal manifestation of parametric resonance between the external drive and the embedded system [35, 54], and are characterized by their wave vector q [see Figure 3]. The results presented here have been obtained for a certain set of parameters describing the embedded system. However, the collective effects discussed below are general and have been found in a wide range of parameters, except for the limits $N \to 1$ and $\beta \to 0$ (corresponding to the limit of independent particle motion), $\Delta \to 0$ (corresponding to embedded system/plate commensurability), and $\gamma_{\parallel} \to 0$ (corresponding to the limit of low dissipation).

In the upper part of Figure 3 we present the resulting shearons for three values of the velocity $v = 0.02$ [(a),(b)], $v = 0.04$ [(c)], and $v = 0.4$ [(d)]. In Figure 3, despite identical initial conditions [as in Figure 2], the different velocities and preparation conditions yield density patterns of different wave vectors, namely shearons of small [q_1 in (a)], medium [$q_2 \approx q_3$ in (b) and (c)], and large [q_4 in (d)] wave vectors with $q_1 < q_2 \approx q_3 < q_4$. In Figure 3(b) a shearon for the same stage velocity $v = 0.02$ as in Figure 3(a) but with larger wave vector $q_2 > q_1$ is shown, which has been prepared by first driving the system with $v = 0.04$ and hence creating a shearon with wave vector q_3 and then maintain it by decelerating the stage velocity to $v = 0.02$. We find that the observed mean friction force per particle $\langle f_k \rangle$, which is directly related to the spatial/temporal fluctuations by [35]

$$\langle f_k \rangle = \pi \gamma v + \frac{2\pi \gamma}{v} \left\langle \sum_{i=1}^{N} \delta \dot{y}_i^2 \right\rangle \quad , \tag{5}$$

always decreases with increasing shearon wave vector q for fixed stage velocity v, i.e. $(\partial \langle f_k \rangle / \partial q)_v < 0$. This means that the mean friction force can be reduced by increasing the shearon wave vector. In our particular case, applying the procedure described above reduces the mean friction force from $\langle f_k \rangle \cong 0.276$ [Figure 3(a)] to $\langle f_k \rangle \cong 0.189$ [Figure 3(b)] and gives rise to a hysteretic behavior observed in many experimental systems [9, 10, 11, 12]. We find that the regions of high density fluctuations exhibit low velocity fluctuations and, according to eq. 5, low dissipation. The lowest possible mean
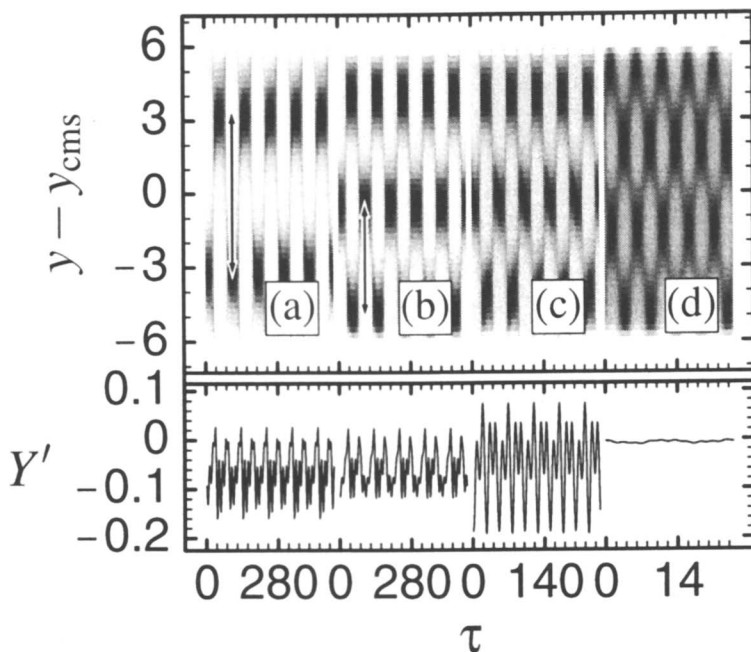
Figure 3: In the upper part the particles density ρ vs position $y - y_{cms}$ and time τ is shown for three different velocities (a),(b) $v = 0.02$, (c) $v = 0.04$, and (d) $v = 0.4$, respectively. The white and black colors indicate low and high density, respectively [the gray scales are chosen independently for each subfigure to maximise contrast]. The definition of the shearon wave vector q is examplified in (a) and (b), where the arrows indicate $1/(2q_1)$ and $1/(2q_2)$, respectively. In the lower part the resulting normal motion of the top plate Y' is represented. The model parameters are $\alpha_\| = 1$, $\alpha_\perp = 0.5$, $\beta = 1$, $\gamma_\| = 0.75$, $\gamma_\perp = 0.75$, $\Delta = 0.1$, $\varepsilon = 0.01$, $\lambda = 1$, $Y'_0 = 0$, and $N = 15$.

friction force $\langle f_k \rangle = \pi \gamma v$ can be achieved for vanishing velocity fluctuations corresponding to the limit $q \to \infty$. In the lower part of Figure 3 the respective normal motion of the top plate Y' is shown. The wave vectors of the different shearons in the embedded system result in different types of normal motion [in particular compare Figures 3(a) and (b) obtained for the same velocity], so that different shearons can be distinguished by analyzing the corresponding normal motion.

We now explore the concept of shearons in relationship to varios frictional behaviors. We start from the well known stick-slip phenomenon observed in many nanoscale systems at low driving velocity. The start of a slip event has been commonly attributed to the 'melting' of the embedded system, namely a transition from an ordered 'solid'-like to a disordered 'liquid'-like structure, that 'refreezes' at the end of the slip event. In Figure 4 we show that during slippage the motion of the embedded system is *highly ordered* and *highly correlated*. At the start of the slip event, the moment of the highest spring force, a shearon is created, persisting with a constant wave vector until it gets an-
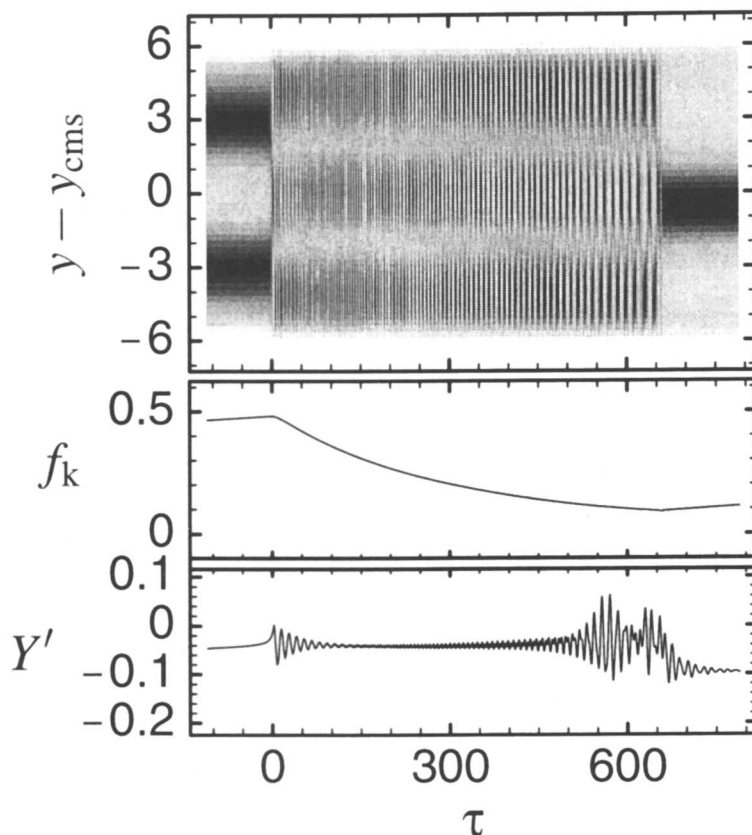
Figure 4: In the upper part shown is the particles density ρ vs position $y - y_{cms}$ and time τ for parameters that correspond to a periodic stick-slip motion. In the lower part the resulting lateral spring force f_k and normal motion of the top plate Y' are represented. We focus on the time interval of a single slip event. The slip starts at $\tau \cong 0$ [largest lateral spring force] and persits until $\tau \cong 657$ [smallest lateral spring force]. The model parameters are $\alpha_\| = 0.02$, $\beta = 1$, $\alpha_\perp = 0.5$, $\gamma_\| = 0.1$, $\gamma_\perp = 0.75$, $\Delta = 0.1$, $\varepsilon = 0.01$, $\lambda = 1$, $Y_0' = 0$, $N = 15$, and $v = 0.06$.

nihilated at the moment of the lowest spring force. The shearon gets annihilated since it cannot persist below a certain shear force needed to compensate the energy dissipation. As a result we find that the static force f_s needed to be overcome in order to initiate the motion is the shear force needed to create the shearon. For the given choice of parameter the decay of the friction force f_k is found to be approximately exponential exhibiting a single characteristic time scale. In the case where the decay displays more than one characteristic time scale [32], a transition from a fast decay corresponding to a sticking of the embedded system at the top plate to a slow decay corresponding to a shearon state is observed. It should be noted that in the example shown in Figure 4 the process
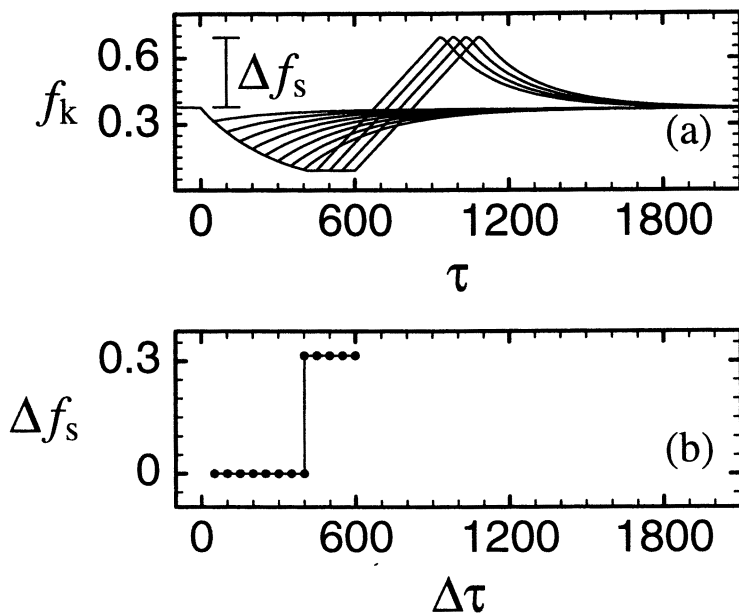
Figure 5: (a) Plot of the friction force f_k vs time τ. In all cases, the drive of the upper plate is stopped at $\tau = 0$ and restarted with the same velocity v after a certain waiting time $\Delta\tau$, ranging from 50 to 600. (b) Plot of the resulting additional static force (peak hight) Δf_s vs waiting time $\Delta\tau$. The lifetime of the shearon is $\delta\tau \cong 400$. The model parameters are $\alpha_{\parallel} = 0.02$, $\alpha_{\perp} = 0.5$, $\beta = 1$, $\gamma_{\parallel} = 0.1$, $\gamma_{\perp} = 0.75$, $\Delta = 0.1$, $\varepsilon = 0.01$, $\lambda = 1$, $Y_0' = 0$, $N = 15$, and $v = 0.5$.

displays two oscillating rest states resulting in two different normal rest position Y' of the top plate.

Using stop/start experiments with a smoothly sliding upper plate, it has been demonstrated [55] that if the external drive is stopped for a certain time, smaller than some upper limit, and then reinitiated with the same velocity, the additional static force $\Delta F_s \equiv F_s - F_k$ (F_s and F_k denote the static and kinetic friction force, respectively) to be overcome might vanish, giving rise to an interesting memory effect in the embedded system. In Figure 5 we present results for the case that the external drive applied on the top plate, which slides smoothly with a given velocity v, is stopped for a certain waiting time $\Delta\tau$ and is then reinitiated with same velocity v. For relatively long waiting times, $\Delta\tau > \delta\tau$, a finite additional static friction has to be overcome, $\Delta f_s \equiv \Delta F_s/(NF_0) > 0$. For shorter waiting times, $\Delta\tau < \delta\tau$, the motion continues smoothly without any additional static friction after reinitiating the drive, i.e. $\Delta f_s = 0$. This behavior can be interpreted in terms of a shearon that exists during the smooth sliding. Shearons have a lifetime $\delta\tau$ for decay after the drive ceases. For waiting times shorter than this lifetime, $\Delta\tau < \delta\tau$, the initial shearon still exists in the embedded system when the drive is restarted. However, since the shearon is annihilated at $\delta\tau$, it has to be recreated for long waiting times

$\Delta\tau > \delta\tau$. The maximum waiting time allowed for a vanishing static friction is therefore determined by the lifetime $\delta\tau$ of the shearon, which is in our example $\delta\tau \cong 400$. We note that the lifetime of a shearon is determined not only by the parameters of the embedded system such as β or $\gamma_{\parallel,\perp}$, but also to a large extent by the external parameters such as the lateral spring constant $\alpha_{\parallel}$. A weaker lateral spring lengthens the lifetime of the shearon, whereas a stiffer spring shortens it.

Control

From a practical point of view one wishes to be able to control frictional forces so that the overall friction is reduced or enhanced, the chaotic regime is eliminated, and instead, smooth sliding is achieved. Such control can be of high technological importance for micromechanical devices, for instance in computer disk drives, where the early stages of motion and the stopping processes, which exhibit chaotic stick-slip, pose a real problem [56].

Mechanical Methods

Controlling frictional forces has been traditionally approached by chemical means, namely by using lubricating liquids. A different approach, discussed here, is by controlling the system mechanically [20, 21]. Our goal is twofold: (a) to achieve smooth sliding at low driving velocities, which otherwise correspond to the stick-slip regime; (b) to decrease the frictional forces. Although we discuss here a specific simple model, the possibility to control friction mechanically, and the methods applied for the control, are model independent and amenable to experimental verification. Two different methods of control are discussed here: The first one uses a feedback control, and the second one relies on a "brute-force" modification of the system dynamics without a feedback.

Feedback Method
We start from the feedback mechanism of control. The analysis of the mechanism has been done with a one-dimensional model, which includes two rigid plates and non-interacting particles embedded between them [20]. The effect of normal motion was not included explicitly [57]. In order to mimic the effect of normal load, we introduce the dependence of the amplitude of the periodic potential on the load p,

$$\Phi_0(p) = \Phi_0 \left[1 + \chi \left(p - p_0 \right) \right] \quad . \tag{6}$$

Here, Φ_0 is the value of the potential for some nominal value of the normal load p_0, and χ is a dimensional constant. We use the normal load as the control parameter to modify friction. Eq. 6 assumes small load variations around p_0, which, as shown below, are sufficient to achieve control. The control method is characterized by two independent steps: (a) reaching the vicinity of an unstable periodic orbit (UPO), and (b) stabilizing it. The control has been realized by small variations of the normal load, which has been externally adjusted employing a proportional feedback mechanism [20].
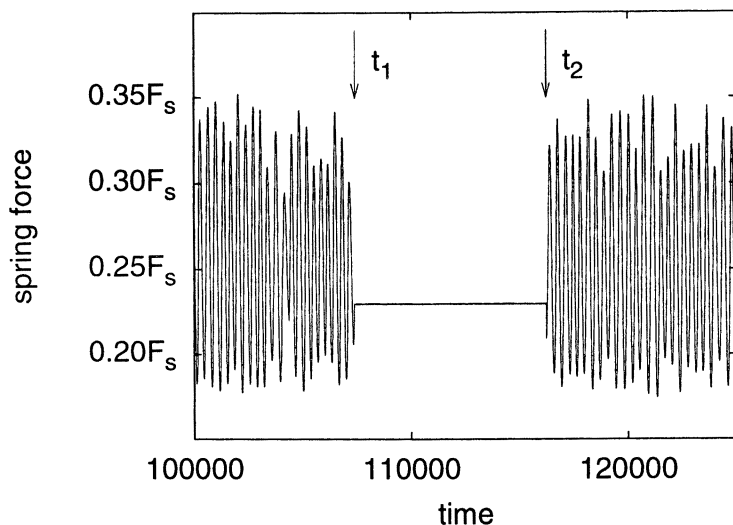
Figure 6: Eliminating the chaotic stick-slip motion under mechanical control; plot of the lateral spring force (presented in units of $F_s = 2\pi\Phi_0/b$) vs time (in units of ω^{-1}). The model parameters are $\alpha_\| = 0.057$, $\gamma_\| = 0.035$, $\varepsilon = 0.125$, $N = 1$, and $v = 0.962$ [13, 57]. (Reproduced with permission *Phys. Rev. E.* **1998**, *57*, 7340. Copyright 1998.)

The aim is to stabilize a sliding state for driving velocities $v < v_c$, where one would expect chaotic stick-slip motion. Sliding states correspond to stable periodic orbits of the system with two periods: (a) period $T = 1/v$, which corresponds to a motion of the particles being trapped by one of the plate; and (b) period $T = 2/v$, which corresponds to the particles moving with the drift velocity $v/2$. In the chaotic region both orbits still exist, but are unstable. Our approach is therefore to drive the system into a sliding state by controlling these UPO. This makes it possible to extend the smooth sliding to lower velocities. The control of such orbits in dynamical systems have been proposed [58] and experimentally applied to a wide variety of physical systems including mechanical systems, lasers, semiconductor circuits, chemical reactions, biological systems etc. (see [59] for references).

We are interested in controlling the chaotic friction at small velocities and also in maintaining smooth sliding when starting at $v > v_c$ and decelerating the system. Here we present the results for the control of the trapped-sliding state, in which the particles cling to one of the plates and move either with velocity 0 (sticking at the bottom plate) or velocity v (sticking at the top plate). Figure 6 demonstrates the effect of the mechanical control on the time dependence of the spring force. The control is switched on at time t_1 and is shut down at time t_2. We clearly see that as a result of the control the chaotic motion of the top plate is replaced by smooth sliding which corresponds to a trapped state with the frictional force $F(\dot{x}) \cong \eta\dot{x}$.

We have demonstrated the possibility to control friction in a model system described by differential equations [20]. Usually in realistic systems time series of dy-

namical variables, rather than governing equations, are experimentally available. In this case the time-delay embedding method [60] can be applied in order to transform a scalar time series into a trajectory in phase space. This procedure allows to find the desired UPO and to calculate variations of parameters required to control friction.

"Brute-Force" Method

In order to demonstrate another, "brute-force", approach to control friction, we have introduced a coarse grained description of the motion of the driven top plate, which is the basic observable in SFA measurements. The motion of the top plate has been described in terms of two coupled equations corresponding to lateral and normal directions [21]. The coupled equations account for the interaction of the plate with the embedded system and with the mechanical springs, and present a generalization of the one-dimensional Tomlinson model [25] to include the normal direction

$$M\ddot{X}(t) = -\eta_{\parallel}(Z)\,\dot{X}(t) - \frac{\partial\Phi(X,Z)}{\partial X} + K_d\,[X_d(t) - X(t)] - K_r\,X(t) \quad , \tag{7}$$

$$M\ddot{Z}(t) = -\eta_{\perp}(Z)\,\dot{Z}(t) - \frac{\partial\Phi(X,Z)}{\partial Z} + K_n\,[Z_P(t) - Z(t)] \quad . \tag{8}$$

Here, $\eta_{\parallel,\perp}(Z) = \eta^0_{\parallel,\perp}\exp(-Z/\Lambda)$ is the effective dissipation coefficient, $\Phi(X,Z) = \Phi_0\exp(-Z/\Lambda)\,[1 - \sigma^2\cos(2\pi X/b)]$ is the effective potential experienced by the plate due to the presence of the embedded system, b is its periodicity, and σ characterizes the corrugation of the potential in the lateral direction. The parameters $\eta_{\parallel}$ and $\eta_{\perp}$ are responsible for the dissipation of the plate kinetic energy due to the motion in the lateral and normal directions. In contrast to the traditional Tomlinson model [25], here we take into account the dependence of $\Phi(X,Z)$ and $\eta_{\parallel,\perp}(Z)$ on the distance Z between plates. The detailed distance dependence is determined by a nature of the interaction between the plate and embedded system. As an example, we assume an exponential decrease of $\Phi(X,Z)$ and $\eta_{\parallel,\perp}(Z)$ with a rate Λ^{-1} as Z increases. The coordinate of the laterally driven stage is denoted as $X_d(t)$. The possibility of an external modulation of the normal load $P_n(t) \equiv K_n\,[Z_P(t) - Z(t)]$, is taken into account by introducing a time dependence into the position of the normal stage, $Z_P(t)$. This approach can be justified under the conditions that the response of the embedded system is faster than that of the top plate, which means that there is a seperation of time scales.

A relevant property of the coupled equations is the existence of two stable surface separations Z_0 and Z_S, which correspond to the plate being either at rest or in fast motion. At rest the plate feels the lateral corrugation of the potential, $\Phi(X,Z)$, and sits at the minima of the potential, while during fast motion there is a decoupling from this potential corrugation. From eqs. 7 and 8, together with $\Phi(X,Z)$, one obtains the following equation for the maximal dilatancy

$$\Delta Z_D = Z_S - Z_0 = \frac{P_n^0}{K_n}\left[\frac{1}{1-\sigma^2}\exp\left(-\frac{\Delta Z_D}{\Lambda}\right) - 1\right] \quad , \tag{9}$$
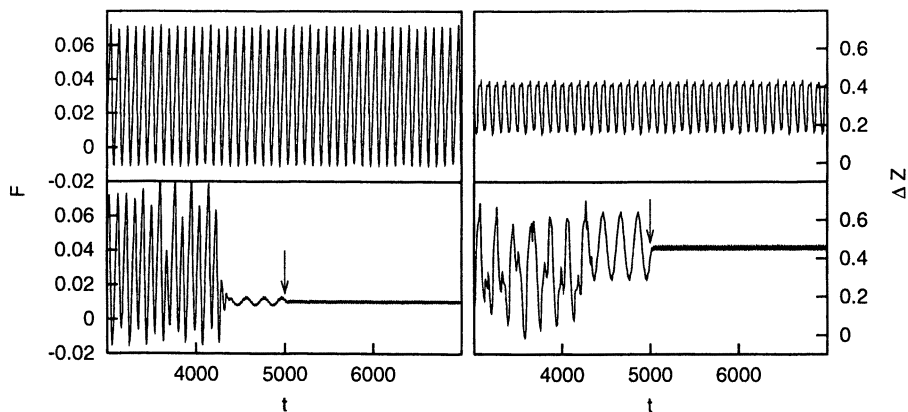
Figure 7: The time series of the lateral force F (in units of Φ_0/b) and the dilatancy ΔZ (in units of b), without (top panels) and with (bottom panels) external oscillations $Z_P(t) = Z_P^0 + \Delta Z_P \sin(\omega_n t)$ [21]. The arrows indicate the time when the normal oscillations $Z_P(t)$ are turned off. The driving velocity is $V = 0.15b\omega_0$ with $\omega_0 = (2\pi/b)\sqrt{\Phi_0/M}$, the other parameters are $\Lambda = b$, $\eta_{\parallel} = 0.1M\omega_0$, $\eta_{\perp} = 5\eta_{\parallel}$, $\sqrt{(K_r + K_d)/M} = 0.1\omega_0$, $K_n = K_r + K_d$, $\sigma = 0.7$, $P_n^0 = 1.3 \times 10^{-2} 4\pi^2\Phi_0/b$, $\Delta Z_P = 0.5b$, and $\omega_n = 3.1 \times 10^{-2} \omega_0$.

(Reproduced with permission from *Phys. Rev. Lett.* **1999,** *82,* 4823. Copyright 1999.)

where $P_n^0 = [1 - \sigma^2][\Phi_0/\Lambda] \exp(-Z_0/\Lambda)$ is the normal load at rest. Equation 9 demonstrates that the dilatancy ΔZ_D explicitly depends on the potential corrugation and on the normal spring constant. It is quite evident that measuring the dilatancy helps in determining the amplitude of the potential corrugation. This stems from the additional information due to the two limiting behaviors in the normal direction.

Figure 7 shows that the effect of oscillations of $P_n(t)$ in smoothing the stick-slip behavior is correlated with an increase of the dilatancy. The smoothing in this case originates from using the oscillations to force the plate into a sliding state which corresponds to a larger dilatancy state. The sliding state is only locally stable below the critical velocity in the absence of the oscillations. Normal oscillations push the system into the region of attraction of this locally stable state and it remains there even when the oscillations are turned off. Namely, the dilatancy introduces a long range memory effect which is a manifestation of the stability of the sliding state even below the critical velocity. This memory effect is amenable to verification in stop/start experiments [55]. In real systems one expects metastability rather than stability of the sliding states.

"Chemical" Methods

As it was shown in the section dealing with the basic characterization, the mean friction force $\langle f_k \rangle$ always decreases with increasing shearon wave vector q for fixed stage velocity v, i.e. $(\partial \langle f_k \rangle/\partial q)_v < 0$. This suggests other possible methods to con-
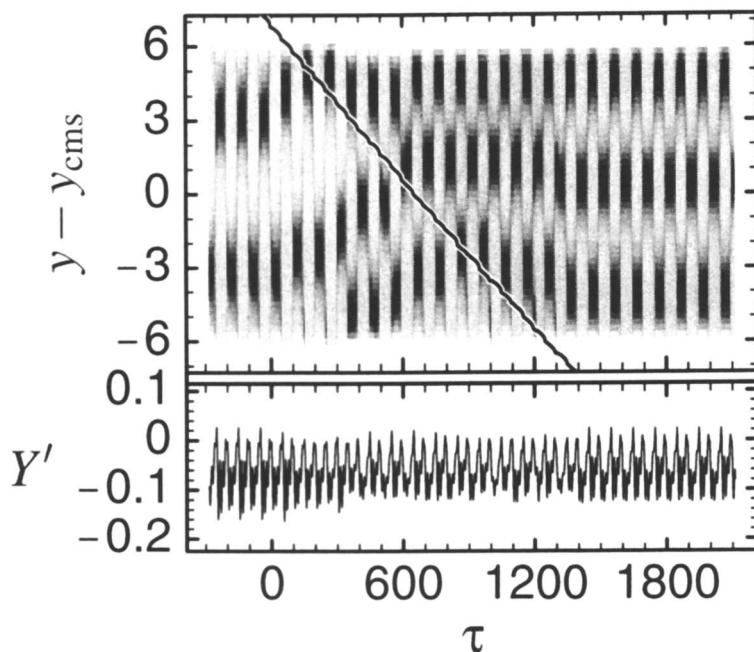
Figure 8: Modifying a shearon by a defect; in the upper part plotted is the particles density ρ vs position $y - y_{cms}$ and time τ. The shallow defect is reached by the first particle at $\tau \cong 0$ and left by the last particle at $\tau \cong 1346$. The relative position of the defect is shown as a black line. In the lower part the resulting normal motion of the top plate Y' is represented. The model parameters are $\alpha_{\parallel} = 1$, $\alpha_{\perp} = 0.5$, $\beta = 1$, $\gamma_{\parallel} = 0.75$, $\gamma_{\perp} = 0.75$, $\Delta = 0.1$, $\varepsilon = 0.01$, $\lambda = 1$, $Y'_0 = 0$, $N = 15$, $v = 0.02$, and $h = 0.5$.

trol friction by modifying the modes of motion in the embedded system. Returning to the model described by eqs. 1-3, in what follows we discuss a microscopic "chemical" method, where the modes of motion are manipulated by introducing a defect at one of the plates. This results in a change in the mode of motion by scattering the shearon. We examplify this by placing a defect at the bottom plate at an integer position y_0. This leads to a modified bottom plate potential $\Phi'_{y_0}(y, Y') = \Phi_0 \exp(-Y'/\lambda) (1 - h\{1 + \cos(2\pi[y - y_0])\})$ for $|y - y_0| \leq 1/2$ and $\Phi'_{y_0}(y, Y') = \Phi(y, Y')$ otherwise. The defect parameter h defines the relative depth of the minimum at position y_0, with $h = 1$ corresponding to the case without defect. As an example, the resulting density pattern for $h = 0.5$ is shown in Figure 8, where it can be seen that scattering by the defect changes the shearon wave vector q_1 into a new wave vector $q_2 > q_1$. The new shearon with wave vector q_2 is *stable*, leading to a decrease of the mean friction force from $\langle f_k \rangle \cong 0.263$ before passing the defect to $\langle f_k \rangle' \cong 0.178$ afterwards. It has already been observed in similar models that disorder can significantly change the frictional behavior [37, 38, 53].

Depending on the amplitude of h, both a decrease and an increase of the friction force are possible, as shown in Figure 9 for a given constant stage velocity. This
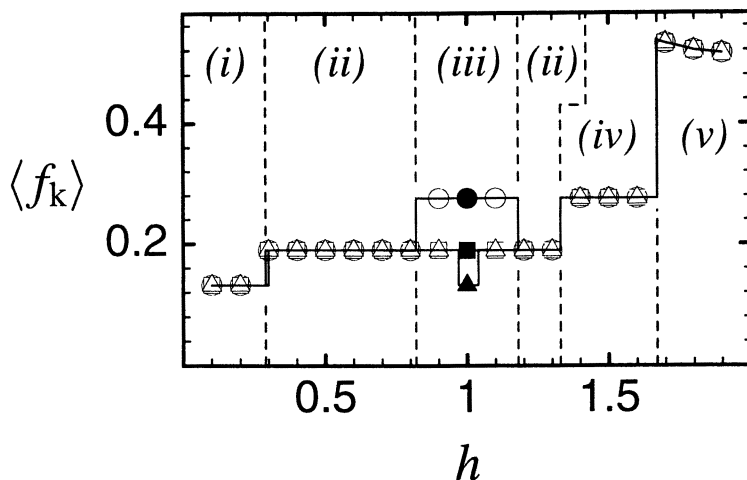
Figure 9: Plot of the mean friction force $\langle f_k \rangle$ after passing the defect vs the defect parameter h for three different shearons with different wave vector q_1 (O/●), q_2 (□/■), and q_3 (△/▲) before passing the defect, with $q_1 < q_2 < q_3$. For clarity, symbols are shown only at defect parameters that are integer multiples of 0.1, whereas the lines show all available data. The full symbols mark the mean friction force of the unperturbed case [i.e. $h = 1$] and hence of the initial shearons, whereas open symbols are used for all other values of h. The model parameters are $\alpha_\parallel = 1$, $\alpha_\perp = 0.5$, $\beta = 1$, $\gamma_\parallel = 0.75$, $\gamma_\perp = 0.75$, $\Delta = 0.1$, $\varepsilon = 0.01$, $\lambda = 1$, $Y_0' = 0$, $N = 15$, and $v = 0.02$.

provides a method to tune $\langle f_k \rangle$. In Figure 9 shown is the mean friction force $\langle f_k \rangle$ after passing the defect vs the defect parameter h for three different initial shearons with wave vectors q_1, q_2, and q_3 [see Figure 10(a)-(c)]. One observes five distinct regimes (i)-(v): For defect parameters $h \lesssim 1.67$ [regimes (i)-(iv)], scatterings among the three wave vectors occur (i.e. six different scatterings $q_1 \rightarrow q_2$, $q_1 \rightarrow q_3$, $q_2 \rightarrow q_1$, $q_2 \rightarrow q_3$, $q_3 \rightarrow q_1$, and $q_3 \rightarrow q_2$) which result in three distinct mean friction forces in Figure 9. For $h \lesssim 0.29$ [regime (i)] all shearons are scattered to the shearon with wave vector q_3. When $0.29 \lesssim h \lesssim 1.33$ [regime (ii)] all shearons are scattered to the shearon with wave vector q_2, except the region with $h \approx 1$ [regime (iii)], where the scattering depends on the initial shearon. For $1.33 \lesssim h \lesssim 1.67$ [regime (iv)] all shearons are scattered to the shearon with wave vector q_1. For defect parameters $h \gtrsim 1.67$ [regime (v)] one of the particles is stuck at the defect and the shearon is annihilated [61].

In Figure 10 the particles density ρ of the embedded system after passing the defect is shown for different values of h. The density patterns for $h = 1$ and for three different shearons q_1, q_2, and q_3 are shown in Figures 10(a)-(c). Since the parameter $h = 1$ corresponds to the case without a defect, no scattering occurs and the obtained final density patterns are equivalent to the respective initial ones before passing the defect. In Figures 10(d)-(f) shown is the particles density ρ for $h = 0.2$, $h = 0.8$, and $h = 1.5$, respectively, where for all three initial shearons the respective final shearons are identi-
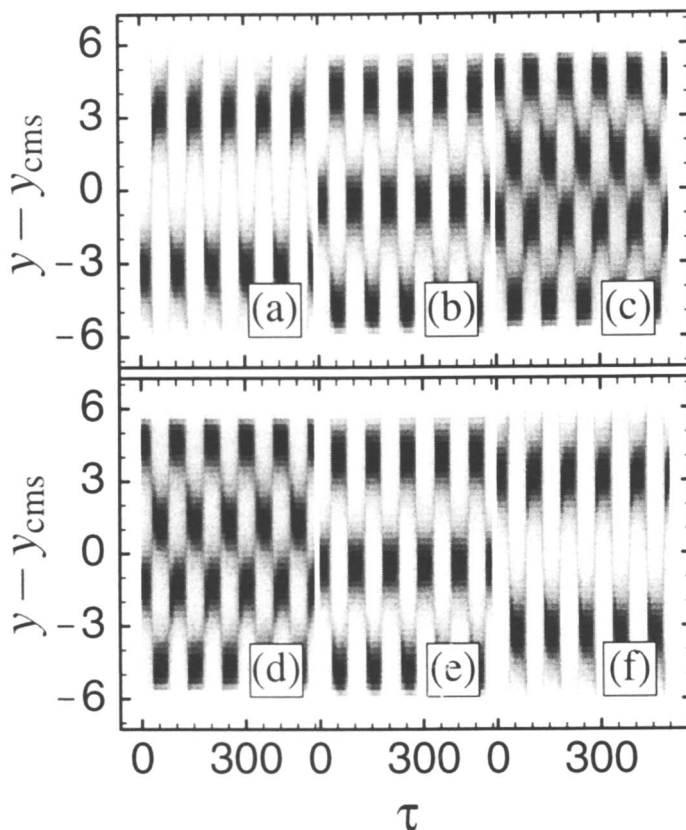
Figure 10: Plot of the particles density ρ after passing the defect vs position $y - y_{cms}$ and time τ for the three different shearons and different defect parameters h. In (a)-(c) the three different shearons with wave vector q_1, q_2, and q_3 are shown for the unperturbed case [i.e. h = 1]. For h = 0.2, h = 0.8, and h = 1.5 the respective final shearons are identical for all three initial shearons and are shown in (d)-(f), respectively. The model parameters are $\alpha_\parallel = 1$, $\alpha_\perp = 0.5$, $\beta = 1$, $\gamma_\parallel = 0.75$, $\gamma_\perp = 0.75$, $\Delta = 0.1$, $\varepsilon = 0.01$, $\lambda = 1$, $Y_0' = 0$, N = 15, and v = 0.02.

cal. One should notice, that the shearons shown in Figures 10(d) and (c), Figures 10(e) and (b), and Figures 10(f) and (a), respectively, are the same.

Conclusion

We have discussed frictional properties within the framework of a model of a sheared monolayer embedded between two plates. The model accounts for the coupled lateral and normal motions in the system, and includes the relevant parameters

which characterize actual experiments. It has been demonstrated that the model leads to the same dynamical behaviors that are observed experimentally, i.e. stick-slip and chaotic motion, transition to sliding, memory effects, and also static and kinetic friction forces. The model allows to establish relationships between the microscopic characteristics and the macroscopically observed quantities. Emphasis has been put on the response of the embedded system and its connection to the macroscopic observables. We have introduced the concept of shearons, which are shear-induced collective modes in the embedded system, and have demonstrated that their properties dominate the frictional behavior of the driven system. Based on this concept, we have established that the mean friction force $\langle f_k \rangle$ always decreases with increasing shearon wave vector q for a given stage velocity v, so that $(\partial \langle f_k \rangle / \partial q)_v < 0$. This property has led to novel methods to control friction forces which are based on modifying the shearon wave vector. Such a modification is possible, for example, by introducing defects at the plates. We have also introduced other methods of control, which rely on the possibility to manipulate the system mechanically, either by feedback methods or by "brute-force" modifications of the system dynamics.

Acknowledgements

References

1. Browden, F.P.; Tabor, D.; *The Friction and Lubrication of Solids*; Claredon Press, Oxford, 1985.
2. *Fundamentals of Friction*, Series E: Applied Sciences, NATO Advanced Sciences Institutes; Singer, I.L.; Pollock, H.M., Eds; Kluwer Academic Publishers, Dortrecht, 1992.
3. Bhushan, B.; Israelachvili, J.N.; Landman, U.; *Nature (London)* **1995**, *374*, 607.
4. *Physics of Sliding Friction* Persson, B.N.J.; Tosatti, E.; Kluwer Academic Publishers, Dortrecht, 1996.
5. *Langmuir* **1996**, *12*.
6. *Micro/Nanotribology and Its Applications*, Series E: Applied Sciences, NATO Advanced Sciences Institutes; Bhushan, B., Ed.; Kluwer Academic Publishers, Dortrecht, 1997.
7. Persson, B.N.J.; *Sliding Friction, Physical Properties and Applications*; Springer Verlag, Berlin, 1998.
8. Granick, S.; *Physics Today* **1999**, *52*, 26.
9. Yoshizawa, H.; McGuiggan, P.; Israelachvili, J.N.; *Science (Washington, D.C.)* **1993**, *259*, 1305.

10. Hu, H.-W.; Carson, G.A.; Granick, S.; *Phys. Rev. Lett.* **1991**, *66*, 2758.

11. Klein, J.; Kumacheva, E.; *Science (Washington, D.C.)* **1995**, *269*, 816.

12. Berman, A.D.; Drucker, W.A.; Israelachvili, J.N.; *Langmuir* **1996**, *12*, 4559.

13. Rozman, M.G.; Urbakh, M.; Klafter, J.; *Phys. Rev. Lett.* **1996**, *77*, 683.

14. Rozman, M.G.; Urbakh, M.; Klafter, J.; *Phys. Rev. E* **1996**, *54*, 6485.

15. Thomson, P.A.; Grest, G.S.; *Phys. Rev. Lett* **1991**, *67*, 1751.

16. Luengo, G.; Schmitt, F.-J.; Hill, R.; Israelachvili, J.N.; *Macromolecules* **1997**, *30*, 2482.

17. Demirel, A.L.; Granick, S.; *J. Chem. Phys.* **1998**, *109*, 6889.

18. Nasuno, S.; Kudrolli, A.B.A.; Golub, J.P.; *Phys. Rev. E* **1998**, *58*, 2161.

19. Geminard, J.C.; Losert, W.; Gollub, J.P.; *Phys. Rev. E* **1999**, *59*, 5881.

20. Rozman, M.G.; Urbakh, M.; Klafter, J.; *Phys. Rev. E* **1998**, *57*, 7340.

21. Zaloj, V.; Urbakh, M.; Klafter, J.; *Phys. Rev. Lett.* **1999**, *82*, 4823.

22. Elmer, F.-J.; *Phys. Rev. E* **1998**, *57*, R4903.

23. Gao, J.P.; Luedtke, W.D.; Landman, U.; *J. Phys. Chem. B* **1998**, *102*, 5033.

24. Heuberger, M.; Drummond, C.; Israelachvili, J.N.; *J. Phys. Chem. B* **1998**, *102*, 5038.

25. Tomlinson, G.A.; *Phil. Mag.* **1929**, *7*, 905.

26. Tompson, P.A.; Robbins, M.O.; Grest, G.S.; *Isr. J. Chem.* **1995**, *35*, 93.

27. Carlson, J.M.; Batista, A.A.; *Phys. Rev. E* **1996**, *53*, 4253.

28. Batista, A.A.; Carlson, J.M.; *Phys. Rev. E* **1998**, *57*, 4986.

29. Braiman, Y.; Family, F.; Hentschel, H.G.E.; *Phys. Rev. E* **1996**, *53*, R3005.

30. Braiman, Y.; Family, F.; Hentschel, H.G.E.; *Phys. Rev. B* **1997**, *55*, 5491.

31. Gao, J.P.; Luedtke, W.D.; Landman, U.; *Phys. Rev. Lett.* **1997**, *79*, 705.

32. Rozman, M.G.; Urbakh, M.; Klafter, J.; *Europhys. Lett.* **1997**, *39*, 183.

33. Rozman, M.G.; Urbakh, M.; Klafter, J.; Elmer, F.-J.; *J. Phys. Chem. B* **1998**, *102*, 7924.

34. Zaloj, V.; Urbakh, M.; Klafter, J.; *Phys. Rev. Lett.* **1998**, *81*, 1227.

35. Weiss, M.; Elmer, F.-J.; *Z. Phys. B* **1997**, *104*, 55.

36. Baumberger, T.; Caroli, C.; *Eur. Phys. J. B* **1998**, *4*, 13.

37. Sokoloff, J.B.; *Phys. Rev. B* **1995**, *51*, 15573.

38. Sokoloff, J.B.; Tomassone, M.S.; *Phys. Rev. B* **1998**, *57*, 4888.

39. Röder, J.; Hammerberg, J.E.; Holian, B.L.; Bishop, A.R.; *Phys. Rev. B* **1998**, *57*, 2759.

40. He, G.; Müser, M.H.; Robbins, M.O.; *Science (Washington, D.C.)* **1999**, *284*, 1650.

41. Thompson, P.A.; Robbins, M.O.; *Science (Washington, D.C.)* **1990**, *250*, 792.

42. Thompson, P.A.; Robbins, M.O.; Grest, G.S.; *Isr. J. Chem.* **1995**, *35*, 93.

43. Robbins, M.O.; Smith, E.D.; *Langmuir* **1996**, *12*, 4543.

44. Bordarier, P.; Shoen, M.; Fuchs, A.H.; *Phys. Rev. E* **1998**, *57*, 1621.

45. Porto, M.; Urbakh, M.; Klafter, J.; unpublished, see cond-mat/9908042.

46. Porto, M.; Urbakh, M.; Klafter, J.; unpublished.

47. Demirel, A.L.; Granick, S.; *Phys. Rev. Lett.* **1996**, *77*, 4330.

48. Nasuno, S.; Kudrolli, A.B.A.; Golub, J.P.; *Phys. Rev. Lett.* **1997**, *79*, 949.

49. For small normal motion of the top plate, and assuming a corresponding damping factor $\exp(-x_i'/\Lambda)$ (x_i' denoting the normal position of particle i), the normal motion of the particles can be neglected, since the normal forces due to the plates will be in average proportional to $\exp(-x_i'/\Lambda) + \exp(-[X'-x_i']/\Lambda) = [1 + \exp(-X'/\Lambda)] + [x_i'/\Lambda][-1 + \exp(-X'/\Lambda)] + [x_i'/\Lambda]^2[1 + \exp(-X'/\Lambda)]/2 + O([x_i'/\Lambda]^3)$. Taking $\exp(-X'/\Lambda) \approx 1$ ($|X'/\Lambda| \ll 1$), this yields $\exp(-x_i'/\Lambda) + \exp(-[X'-x_i']/\Lambda) \cong 2 + [x_i'/\Lambda]^2 + O([x_i'/\Lambda]^3)$, which is a constant up to quadratic terms in x_i'/Λ.

50. The standard package CVODE (authored by S.D. Cohen and A.C. Hindmarsh) for solving ordinary differential equations is used.

51. These as well as the later unitless quantities are based on the 'natural' frequencies, lengths, forces, etc. of the model, which contain the 'physical' quantities such as mass, potential amplitudes, etc.

52. Smith, E.D.; Robbins, M.O.; Cieplak, M.; *Phys. Rev. B* **1996**, *54*, 8252.

53. Braiman, Y.; Hentschel, H.G.E.; Family, F.; Mak, C.; Krim, J.; *Phys. Rev. E* **1999**, *59*, R4737.

54. Hentschel, H.G.E.; Family, F.; Braiman, Y.; *Phys. Rev. Lett.* **1999**, *83*, 104.

55. Yoshizawa, H.; Israelachvili, J.N.; *J. Phys. Chem.* **1993**, *97*, 11300.

56. Mate, C.M.; Homola, A.M.; in *Micro/Nanotribology and Its Applications*, Series E: Applied Sciences, NATO Advanced Sciences Institutes; Bhushan, B., Ed.; Kluwer Academic Publishers, Dortrecht, 1997.

57. In [*13*] the normal motion of the top plate was not included into the calculations, which corresponds to a very stiff normal spring $\alpha_\perp \rightarrow \infty$.

58. Ott, E.; Grebogi, C.; Yorke, J.A.; *Phys. Rev. Lett.* **1990**, *64*, 1196.

59. Barreto, E.; Kostelich, E.J.; Grebogi, C.; Ott, E.; Yorke, J.A.; *Phys. Rev. E* **1995**, *51*, 4169.

60. Abarbanel, H.D.I.; Brown, R.; Sidorowich, J.L.; Tsimring, L.S.; *Rev. Mod. Phys.* **1993**, *65*, 1331.

61. In this regime, the slight dependence of the mean friction on the defect parameter h is due to the fact that the mean friction force depends on which particle i is stuck at the defect: The mean friction force is highest if the last particle [$i = 1$] arriving at the defect is stuck, and it decreases the deeper the defect is and hence the earlier the embedded system is stuck. If the defect is deep enough [$h \gtrsim 2$] so that already the first particle [$i = N$] arriving at the defect is stuck, the mean friction force saturates.

Chapter 7

Individual Supramolecular Host–Guest Interactions Probed by Dynamic Single Molecule Force Spectroscopy

Holger Schönherr[1], Marcel W. J. Beulen[2], Jürgen Bügler[2], Jurriaan Huskens[2], Frank C. J. M. van Veggel[2], David N. Reinhoudt[2,3], and G. Julius Vancso[1,3]

[1]Materials Science and Technology of Polymers and [2]Laboratory of Supramolecular Chemistry and Technology, MESA† Research Institute and Faculty of Chemical Technology, University of Twente, P.O. Box 217, 7500 AE Enschede, The Netherlands

Until now single molecule force spectroscopy experiments have been performed almost exclusively on biologically relevant systems consisting of receptors with high molar masses and very slow unbinding kinetics. In this paper we report on force spectroscopy results of the complexation behavior of ferrocene moieties, self-assembled on an AFM tip, in β-cyclodextrin (β-CD) receptors, immobilized in highly ordered self-assembled monolayers on Au(111). For this system the unbinding kinetics are on a shorter time scale than the AFM time scale. Multiple pull-off events could be observed, while the addition of an external guest was shown to reversibly block the β-CD cavities. The adhesion between β-CD and ferrocene was found to be quantized. The force of 56 ± 10 pN could be identified as *single* host-guest complex rupture force. This rupture force was found to be independent of the (un-)loading rate which is indicative for a thermodynamically controlled experiment. Our report is the first example where single supramolecular host-guest interactions could be monitored for complexation reactions with fast unbinding kinetics.

The lock and key principle [1,2] can be regarded as the central principle for molecular recognition in Nature [3]. Supramolecular chemistry mimics Nature *e.g.* by using artificial receptors for selective recognition [4]. It is fair to say that molecular recognition by synthetic receptors in solution has reached a high level

---

[3]Corresponding authors.

113

of sophistication [5]. With the invention of scanning probe techniques, such as atomic force microscopy (AFM), real space nanometer scale structural characterization and measurements of forces with piconewton resolution have become possible with the same instrument [6,7]. Consequently, much effort has been devoted to the measurement of single molecule interactions [8,9]. Studies on the lock and key principle on the level of individual molecules focussed primarily on natural receptors with relatively high molar masses and thus sizes, and *very* slow unbinding kinetics [10].

In this paper, a study of supramolecular host-guest interactions between small molecules is reported. Interactions between β-cyclodextrin (β-CD) receptors in highly ordered self-assembled monolayers (SAMs) on Au(111) and ferrocene moieties immobilized on AFM tips were measured in dynamic force spectroscopy measurements [11].

Experimental

Materials. The synthesis of the β-CD adsorbate is described in references 12, 13, and 14. 6-ferrocenyl-hexanethiol (Fc) was synthesized according to the literature [15] 8-anilino-1-naphthalenesulfonic acid (1,8-ANS), 2-hydroxy-ethanethiol, and octadecanethiol were purchased from Aldrich and used as received.

Electrochemical Impedance Spectroscopy. Electrochemical impedance spectroscopy measurements were performed in an aqueous solution of 0.1 M K_2SO_4 and 1 mM $K_3Fe(CN)_6/K_4Fe(CN)_6$ as described reference 12. The experimental titration curve of the β-CD monolayer was fitted with the program Table Curve V 1.0 by Jandel Scientific.

Cyclic Voltammetry [12]. The composition of the mixed monolayer of 6-ferrocenyl-hexanethiol and 2-hydroxy-ethanethiol used in the AFM-measurements was determined by separate cyclic voltammetric experiments. The redox signal of the ferrocene unit was integrated in cyclic voltammograms measured in 0.1 M $NaClO_4$ for monolayers of different ratios of the two adsorbates in the adsorption solution (1-100% Fc).

AFM and Tip Modification. The AFM measurements were performed on a NanoScope III multimode AFM (Digital Instruments, Santa Barbara, CA). The piezo positioner was calibrated in z-direction by measuring step heights of Au(111) [16]. The cantilever spring constants were calibrated as described in the literature [17]. Triangular shaped silicon nitride cantilevers and silicon nitride tips (Digital Instruments (DI), Santa Barbara, CA, USA) were coated with ca. 2 nm Ti and ca. 75 nm Au in high vacuum (Balzers). The tips were immersed in 1 mM solutions of the corresponding thiols in ethanol:chloroform (1:2). A 99:1 mixture of 2-hydroxy-ethanethiol and 6-ferrocenyl-hexanethiol, pure 2-hydroxy-ethanethiol, and pure octadecanethiol were used. After 10-15 hours the cantilever substrates were rinsed with pure solvent and dried briefly in air. Without delay the cantilevers were mounted in the liquid cell (DI) of the AFM. After an equilibration period of ca. 1 hour in pure water (Millipore Milli-Q) the tip was engaged on a SAM of β-CD **1** on Au(111) and 300 to 400 force-distance curves were recorded at different positions on the sample surface. The maximum external load was limited to < 1.0 nN. The (un-)loading rate was varied between 2.4× 10^5

pN/s and 2.0×10^2 pN/s. After withdrawal of the tip, the cell was flushed with more than 20 times the cell volume of aqueous 1,8-ANS (100 µM). After a brief equilibration period the tip was engaged again and a second set of force curves was recorded. After withdrawal of the tip from the surface, the cell was flushed with pure water. The repeated force measurements in absence and in presence of 1,8-ANS were carried out up to 4 times. The corresponding force-distance curves changed reproducibly (see Results and Discussion). The reference measurements with 2-hydroxy-ethanethiol and octadecanethiol functionalized tips were all carried out in pure water.

Data Evaluation. For quantitative analysis 100 force curves of a given set were analyzed. The observed individual pull-off events were analyzed individually and plotted in histograms. An autocorrelation function of the histograms of the pull-off forces was calculated according to equation (1):

$$G(x) = \frac{1}{N_x} \sum_{k=1}^{N_x} \Delta f(k) \Delta f(k+x) \quad (1)$$

$$\text{with } \Delta f(k) = f(k) - \frac{1}{N} \sum_{j=1}^{N} f(j).$$

Results and Discussion

For the current studies the receptor β-CD was immobilized in self-assembled monolayers (SAMs) on Au(111). β-CD is a cyclic heptamer of glucose (see Figure 1) and is well known to bind apolar guests, including ferrocene, in aqueous environment [18]. Prior to the force spectroscopy experiments SAMs of β-CD heptasulfide derivative **1** on Au(111) were investigated by a variety of techniques to ensure that the monolayers fulfill the requirements for a successful determination of single molecular interactions on the level of *small* molecules [14].

Study of Monolayers of the Receptor Adsorbates

These requirements include high structural order of the assembly (preferably 2-dimensional translational order), as well as an optimized functional design in order to expose the receptor cavities in an accessible manner. In the experiments mentioned, SAMs of **1** were found to be highly ordered (*vide infra*).

In addition, the interactions of β-CD with the anionic guest 8-anilino-1-naphthalenesulfonic acid (1,8-ANS) in aqueous solution were monitored by electrochemical impedance spectroscopy (EIS) [19]. The response curve of a SAM of β-CD **1** for 1,8-ANS is shown in Figure 2. Even at very low concentrations of the guest high responses are obtained. The complete complexation curve shows that the charge-transfer resistance reaches a plateau-value at concentrations around 100 µM [20]. These results prove that 1,8-ANS
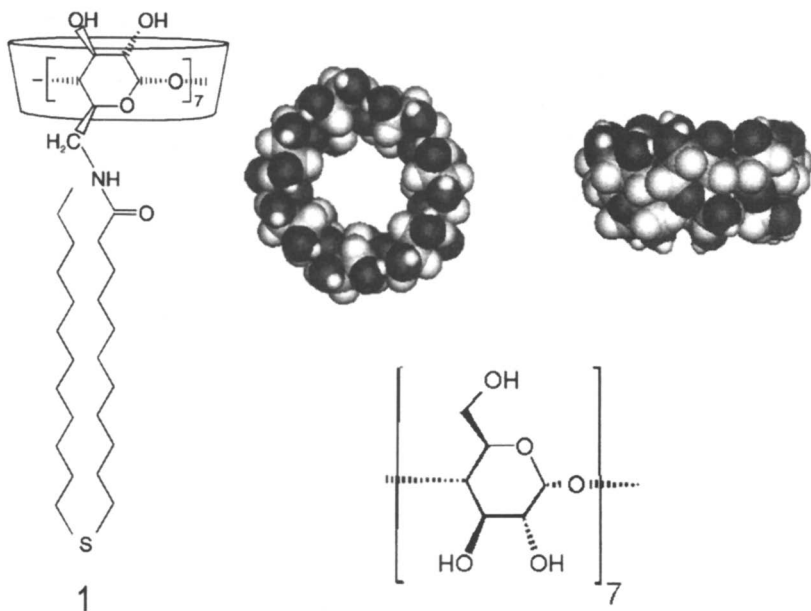
Figure 1. Structure of β-CD adsorbate **1** (left), space-filling models of β-CD cavity in top- and side-view (top middle and right, respectively), and molecular structure (bottom). (Adapted with permission from reference 11. Copyright 2000 American Chemical Society.)
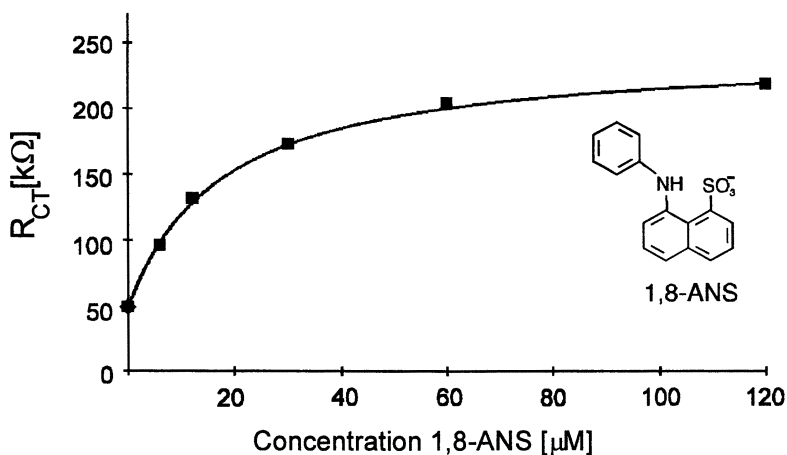
Figure 2. Dependence of the charge transfer resistance R_{CT} of the β-CD monolayer on the concentration of anionic guest (1,8-ANS) obtained by electrochemical impedance spectroscopy measurements. The solid line is a fitted Langmuir isotherm [20]. (Adapted with permission from reference 11. Copyright 2000 American Chemical Society.)

binds effectively to the cyclodextrin cavities. Thus, 1,8-ANS can be used to reversibly block the receptor sites in force spectroscopy measurements (*vide infra*).

The degree of lateral order of the SAMs of *permethylated* β-CD sulfide derivatives on Au(111) was investigated by AFM using unmodified tips [21]. SAMs of permethylated β-CD derivatives of **1** on Au(111) were imaged with minimized forces in water. A clear periodic lattice could be observed (Figure 3). The quasi-hexagonal array of β-CD adsorbates as imaged by AFM (lattice constant: 20.6 ± 1.3 Å, angle: 60 ± 4°) is in good agreement with the geometrical size of the heptasulfide derivatized adsorbates [22].

Dynamic Single Molecule Force Spectroscopy

The complexation behavior of SAMs of β-CD **1** was measured by single molecule force spectroscopy (Figure 4). Gold-coated AFM tips were modified with a mixed SAM of 2-hydroxy-ethanethiol and 6-ferrocenyl-hexanethiol. As shown by cyclic voltammetry experiments the mixed SAMs contained 1 % - 2 % 6-ferrocenyl-hexanethiol. The dilution was carried out in order to reduce the number of possible interactions and to maximize the conformational freedom of the immobilized ferrocene moieties.

Force distance curves measured in pure water with these functionalized tips on SAMs of β-CD **1** on atomically smooth Au(111) showed multiple pull-off events as shown in Figure 5 (top). After replacing the water by an aqueous solution of the external guest (1,8-ANS, 100 µM), the number of resolved pull-off events was drastically reduced. In ca. 50 % of the force distance curves single pull-offs were observed (Figure 5, bottom). The other force-distance curves showed up to three pull-offs, indicating some residual free β-CD cavities.

After replacing the solution by pure water, the multiple pull-offs were observed again (Figure 6). The observations can be interpreted as reversible blocking of the β-CD cavity by the external guest. The electrochemical impedance spectroscopy results fully support this interpretation (*vide supra*).

Separation distances larger than the length of the adsorbate molecules can be rationalized by taking the granular morphology of the gold coating of the film into account (grain diameter ca. 25 – 50 nm). In case of several gold grains in the contact area a slight torsion of the cantilever is also possible. The tip, which stays in contact with the surface at all times during the multiple individual pull-off events, may lose contact at different grains at a time. This results in separation distances as observed. It should be noted that the piezo travel is always smaller than the maximum grain size observed by high resolution SEM.

Control experiments were carried out with 2-hydroxy-ethanethiol and octadecanethiol modified tips (no guest) on β-CD SAMs and with mixed 2-hydroxy-ethanethiol and 6-ferrocenyl-hexanethiol modified tips on octadecanethiol and 2-hydroxy-ethanethiol SAMs (no host). The corresponding force distance curves showed "normal" (single) pull-offs which indicated the absence of specific interactions (Figure 7). The magnitude of the pull-off forces in the control experiments is characteristic for interactions measured in water [23].
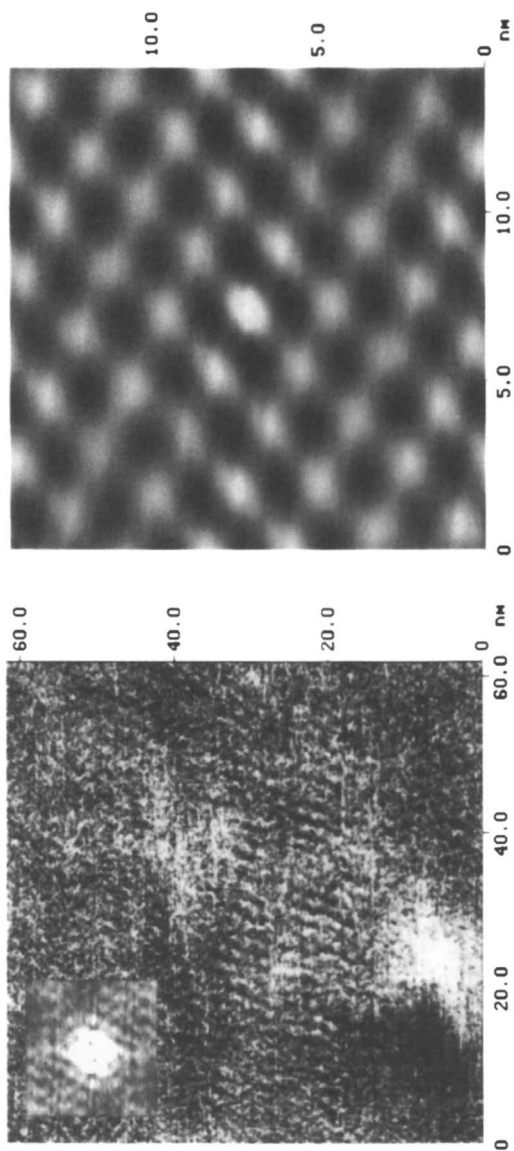
Figure 3. AFM images of SAMs of methoxy-substituted β-CD sulfide derivatives on Au(111) obtained in water. Unprocessed friction image (inset: autocovariance filtered section, left) and autocovariance filtered height image of a different SAM (right). (Adapted with permission from reference 11. Copyright 2000 American Chemical Society.)
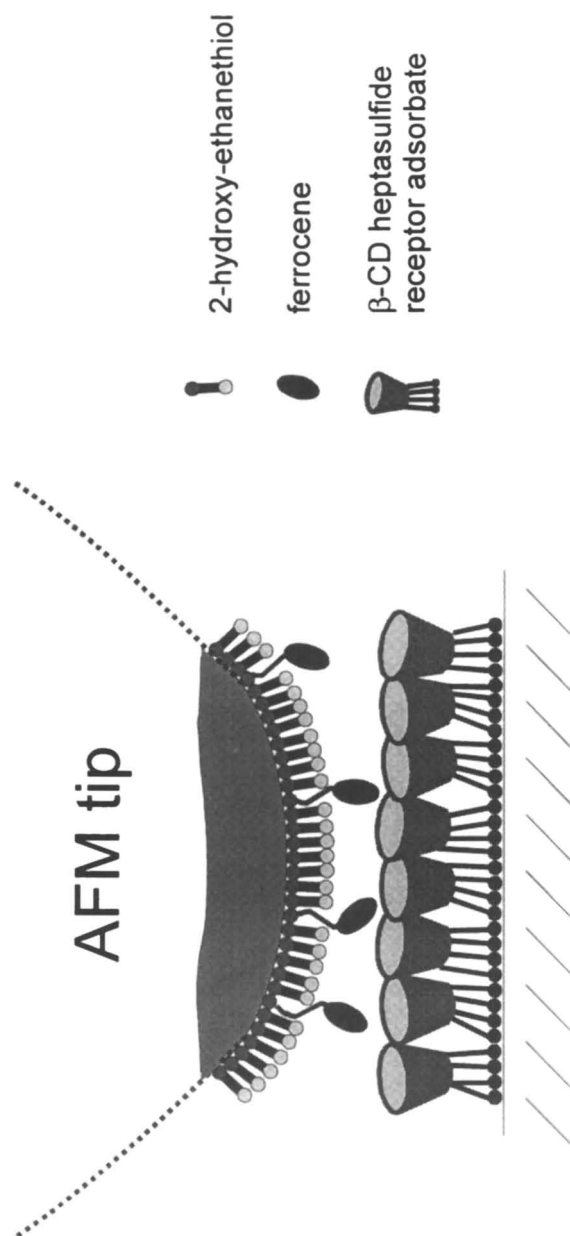
Figure 4. Schematic drawing of single molecule force spectroscopy between an AFM tip, modified with a mixed SAM of 2-hydroxy-ethanethiol and 6-ferrocenyl-hexanethiol, and a SAM of β-CD on Au(111). (Adapted with permission from reference 11. Copyright 2000 American Chemical Society.)
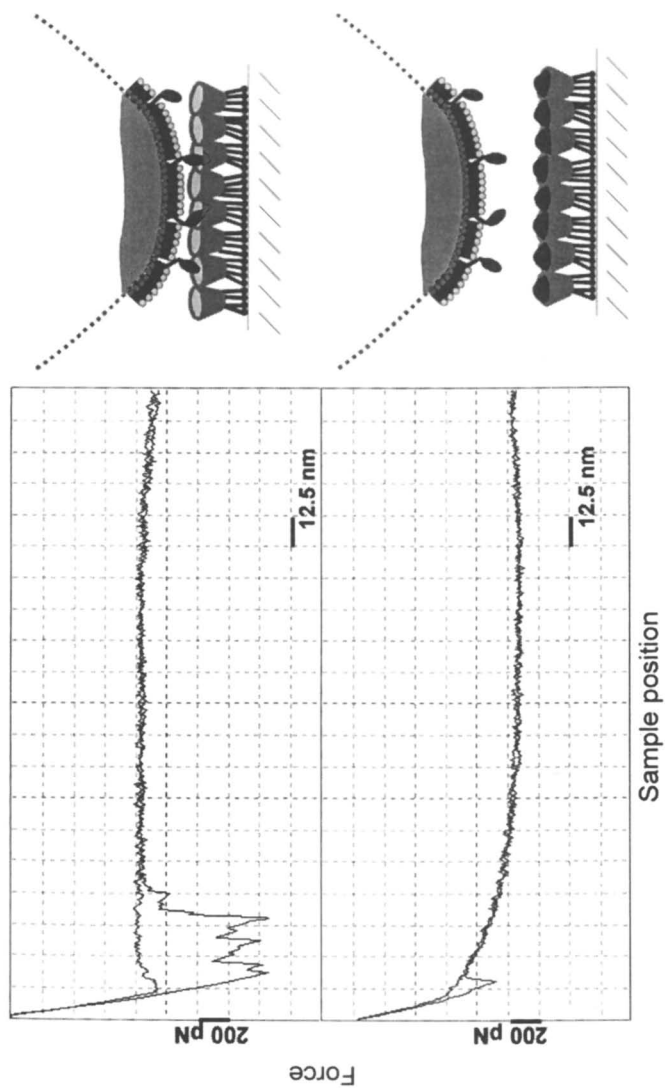
Figure 5. Force-distance curves recorded for interaction between tips covered with mixed hydroxyl-ferrocene SAMs and β-CD 1 substrate in water prior to addition of 1,8-ANS (top), after the addition of 1,8-ANS (bottom). The (un-) loading rate was 5.00×10^4 pN/s. (Adapted with permission from reference 11. Copyright 2000 American Chemical Society.).
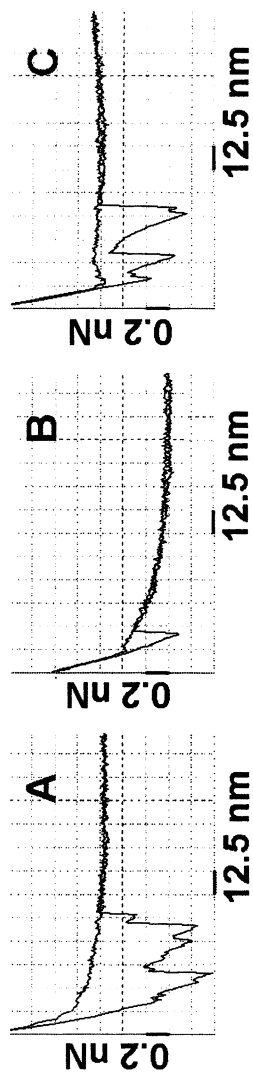
Figure 6. Force-distance curves recorded for interaction between mixed hydroxyl-ferrocene tip and β-CD 1 in water prior to addition of 1,8-ANS (A), after the addition of 1,8-ANS (B), and after a subsequent flush with water (C). (Reproduced with permission from reference 11. Copyright 2000 American Chemical Society.)
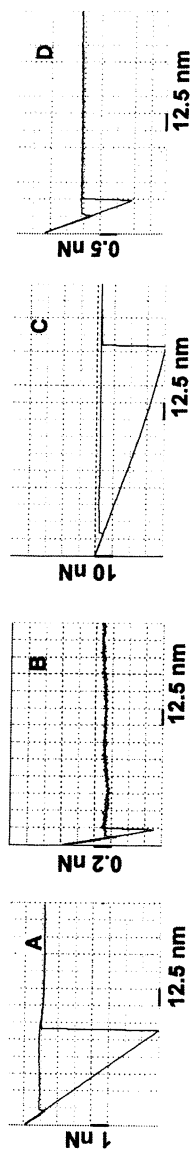
Figure 7. Force-distance curves obtained in control experiments on pure β-CD 1 SAMs on Au(111) using octadecanethiol (A) and 2-hydroxy-ethanethiol functionalized tips (B) [no guest], and on octadecanethiol (C) and 2-hydroxy-ethanethiol (D) SAMs on Au(111) using the mixed hydroxyl-ferrocene-modified tips [no host]. (Adapted with permission from reference 11. Copyright 2000 American Chemical Society.)

Forces between *single* molecules were previously studied with various techniques, including AFM and optical trapping techniques [8,9], predominantly on molecules with relatively high molecular masses and thus with large sizes. Examples include *e.g.* binding of cell adhesion proteoglycans [8d] or complementary strands of DNA [8c]. Gaub and co-workers showed that single molecule adhesion forces for biotin and different (strept)avidins seem to correlate with the enthalpy of the binding reactions for different avidin - biotin pairs [8a,8b,24,25]. These conclusions have been questioned recently based on (un-)loading rate-dependent measurements [10].

Similar to the studies mentioned before, the occurrence of multiple individual pull-off events during one retraction of the β-CD sample from the Fc tip can be attributed to the rupture of host-guest complexes at the edge of the contact area between probe and surface [8]. As seen in the corresponding test experiments (*vide supra*), the multiple pull-off events were only observed with mixed hydroxyl-ferrocene functionalized tips on β-CD SAMs. The analysis of the individual pull-offs revealed a "quantized" adhesion force. In the histograms shown in Figure 8, distinct force maxima could be observed.

The normalized data is summarized in Table I. The maxima observed were also confirmed in the autocorrelation analysis which is included in Figure 8. The positions of these maxima were not altered after blocking of the cavity with 1,8-ANS and subsequent removal by flushing with water [26,27].

Table I. Normalized maxima observed in histograms shown in Figure 8

Maxima in force (pN)	Normalized force
56	1.00
113	2.02
170	3.04
226	4.04
283	5.05

Recently, the (un-)loading rate dependence of forces measured between biotin and streptavidin (or avidin) was reported [10]. Thus, in order to check whether the rupture force of the ferrocene - β-CD complexes is rate-dependent, the adhesion between ferrocene and β-CD was measured over a frequency range of three decades. No significant dependence of the host-guest complex rupture force on (un-)loading rate could be detected for loading rates between 2.00×10^2 and 2.34×10^5 pN/s (Figure 9) [28]. The local maxima in the pull-off force histograms are multiples of 56 ± 10 pN regardless of the (un-)loading rate as confirmed by the autocorrelation analysis [29].

This observation supports the interpretation that the experiment is carried out under thermodynamic control. The decomplexation itself is fast compared to the force spectroscopy experiment [28]. As long as the exerted force is smaller than the rupture force, spontaneous decomplexation *and* recomplexation occur at the edge of the contact area between tip and sample. The exertion of force is translated into strain energy in the spacer of the ferrocene guest on the tip and the alkyl chains of the β-CD adsorbate. On the time scale of the host-guest binding
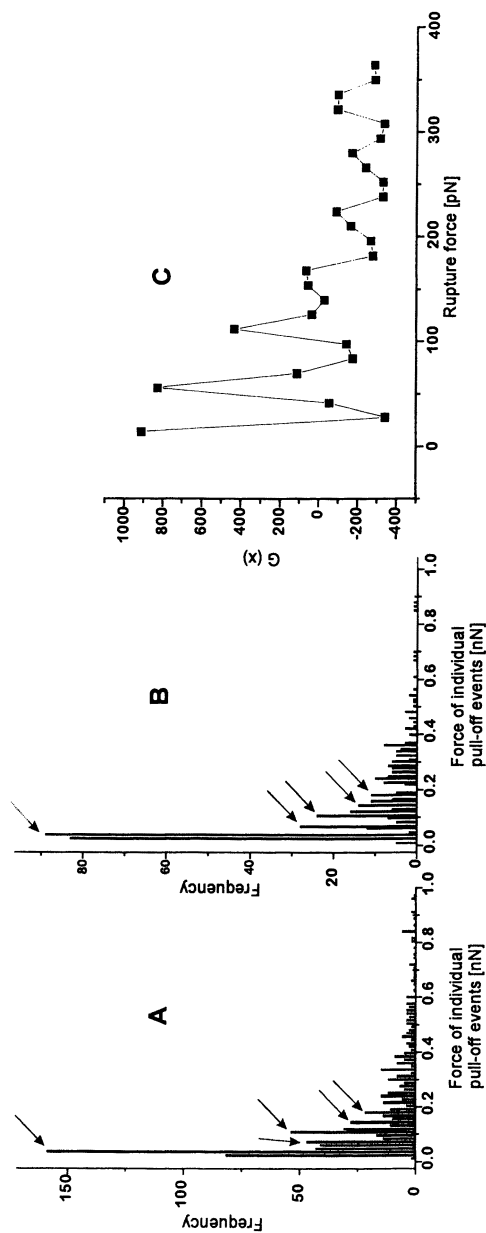
Figure 8. Histogram of individual pull-off forces measured in AFM force distance curves between a SAM of β-CD 1 and a mixed hydroxyl-ferrocene tip in water (A), after presence of 1,8-ANS and thorough flush with water (B) (arrows indicate force maxima). The autocorrelation analysis of the data obtained in three independent experiments is shown in C [32].(Reproduced with permission from reference 11. Copyright 2000 American Chemical Society.)
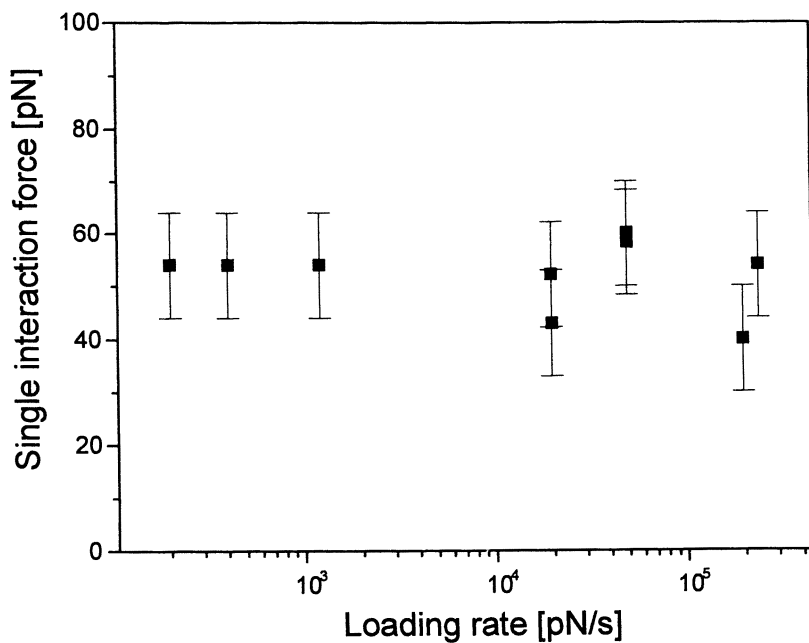
Figure 9. Rate dependence of single host-guest complex rupture forces. (Reproduced with permission from reference 11. Copyright 2000 American Chemical Society.)

kinetics, the tip remains stationary and rapid spontaneous decomplexation still occurs. As long as the strain energy in the bound state is overcome by the energy release upon complexation recomplexation remains possible. Retraction of the tip occurs when the strain energy becomes larger than binding energy.

In the theoretical analysis of the physics of bond rupture, four different regimes were predicted by Evans, Ritchie et al. [10,25] For very small loading rates, the spontaneous dissociation of the complex is the most frequent process and the most frequent rupture force f* is zero [30]. Subsequently, there are three further regimes showing rate dependence. In the slow loading regime f* grows as a weak power of the loading rate, in the fast loading regime there is a logarithmic dependence of f* on rate, and in the ultrafast loading regime only viscous frictional drag retards the separation. Based on the comparison of equilibrium kinetics, and in particular the insignificant (un-)loading rate dependence in our experiments, we can assume that we measure the ferrocene - β-CD interactions in the slow-loading regime. Unlike for the complicated interactions between streptavidin and biotin which involve multiple barriers, we can expect in our case only a single barrier on the decomplexation pathway. However, due to the fact that the AFM experiment is slow relative to the unbinding kinetics, the corresponding distances x_β [10] cannot be determined from the slope of the force versus loading rate plot. Future work on the β-CD SAMs must certainly address the measurement of single complex rupture forces for guests with different complexation constants and the influence of temperature on the values measured [31].

Conclusions

In conclusion, the complexation behavior of ferrocene moieties in highly ordered SAMs of β-CD on Au(111) was investigated by dynamic single molecule force spectroscopy. Multiple pull-off events were observed for the interaction between ferrocene (immobilized in a mixed hydroxyl-ferrocene SAM on an AFM tip) and β-CD SAM on Au(111) in water. Addition of a guest (1,8-ANS) causes reversible blocking of the cavities. The adhesion between β-cyclodextrin and ferrocene moieties was found to be a multiple of 56 ± 10 pN. The observed "quantum" of adhesion force can be identified as the value for a *single* rupture force of the ferrocene - β-CD complex. This force was found to be independent of the (un-)loading rate between 2.00×10^2 and 2.34×10^5 pN/s.

Acknowledgment

References

1. *The Lock and Key Principle: the State of the Art;* Behr, J.-P. (Ed.); Wiley, Chichester, 1994.
2. Buckingham, A. D.; Legon, A. C.; Roberts, S. M. *Principles of Molecular Recognition;* Blackie, London, 1993.
3. Stryer, L. *Biochemistry;* 4th ed., Freeman, New York, 1995.
4. (a) Lehn, J.-M. *Angew. Chem. Int. Ed. Engl.* **1988**, *27*, 89; (b) Cram, D. J. *Angew. Chem. Int. Ed. Engl.* **1988**, *27*, 1009; (c) Pedersen, C. J. *Angew. Chem. Int. Ed. Engl.* **1988**, *27*, 1021.
5. (a) Lehn, J.-M. *Supramolecular Chemistry;* VCH, Weinheim, 1995; b) Rudkevich, D. M.; Brzøzka, Z.; Palys, M.; Visser, H. C.; Verboom, W.; Reinhoudt, D. N. *Angew. Chem. Int. Ed. Engl.* **1994**, *33*, 467; (c) Reichert, A.; Ringsdorf, H. Schuhmacher, P. in *Comprehensive Supramolecular Chemistry;* Vol. 9; Sauvage, J.-P.; Hosseini, M. W. (Eds.); Pergamon, Oxford, 1996, 313; (d) Philp, D.; Stoddart, J. F. *Angew. Chem. Int. Ed. Engl.* **1996**, *35*, 1154.
6. Binnig, G.; Quate, C. F.; Gerber, Ch. *Phys. Rev. Lett.* **1986**, *56*, 930.
7. (a) Frommer, J. *Angew. Chem. Int. Ed. Engl.* **1992**, *31*, 1298; (b) Magonov, S. N.; Whangbo, M.-H. *Surface Analysis with STM and AFM;* VCH, Weinheim, 1996.
8. Single molecule force spectroscopy by AFM has been carried out until now only on biologically relevant molecules with high molar masses and very slow unbinding kinetics. Examples include: (a) Florin, E.-L.; Moy, V. T.; Gaub, H. E. *Science* **1994**, *264*, 415; (b) Moy, V. T.; Florin, E.-L.; Gaub, H. E. *Science* **1994**, *266*, 257; (c) Lee, G. U.; Chrisey, L. A.; Colton, R. J. *Science* **1994**, *266*, 771; (d) Dammer, U.; Popescu, O.; Wagner, P.; Anselmetti, D.; Güntherodt, H.-J.; Misevic, G. N. *Science* **1995**, *267*, 1173; (e) Allen, S.; Chen, X. Y.; Davies, J.; Davies, M. C.; Dawkes, A. C.; Edwards, J. C.; Roberts, C. J.; Sefton, J.; Tendler, S. J. B.; Williams, P. M. *Biochemistry* **1997**, *36*, 7457; (f) Ros, R.; Schwesinger, F.; Anselmetti, D.; Kubon, M.; Schäfer, R.; Plückthun, A.; Tiefenauer, L. *Proc. Natl. Acad. Sci. USA* **1998**, *95*, 7402 and references therein.
9. (a) Svoboda, K.; Schmidt, C. F.; Schnapp, B. J.; Block, S. M. *Nature* **1993**, *365*, 721; (b) Finer, J. T.; Simmons, R. M.; Spudich, J. A. *Nature* **1994**, *368*, 113; (c) Smith, S. B.; Cui, Y.; Bustamante, C. *Science* **1996**, *271*, 795; (d) Cluzel, P.; Lebrun, A.; Heller, C.; Lavery, R.; Viovy, J.-L.; Chatenay, D.; Caron, F. *Science* **1996**, *271*, 792.
10. As shown recently, the *very* slow unbinding kinetics lead to a pronounced rate dependence of the measured unbinding forces. Merkel, R.; Nassoy, P.; Leung, A.; Ritchie, K.; Evans, E. *Nature* **1999**, *397*, 50.
11 Schönherr, H.; Beulen, M. W. J.; Bügler, J.; Huskens, J.; van Veggel, F. C. J. M.; Reinhoudt D. N.; Vancso, G. J. *J. Am. Chem. Soc.* **2000**, *122*, 4963.
12. Beulen, M. W. J. Ph.D. Thesis, University of Twente, The Netherlands, 1999.
13. Characterization methods including wettability studies, electrochemistry,

XPS, and SIMS, show that ordered monolayers are formed and that the substitution pattern of the CD molecules has only a very minor influence on the structural properties. Preliminary data can be found in: Beulen, M. W. J.; Bügler, J.; Lammerink, B.; Geurts, F. A. J.; Biemond, E. M. E. F.; van Leerdam, K. G. C.; van Veggel, F. C. J. M.; Engbersen, J. F. J.; Reinhoudt, D. N. *Langmuir* **1998**, *14*, 6424.

14. The details of the characterization are summarized in: Beulen, M. W. J.; Bügler, J.; de Jong, M. R.; Lammerink, B.; Huskens, J.; Schönherr, H.; Vancso, G. J.; Boukamp, B. A.; Wieder, H.; Offenhäuser, A.; Knoll, W.; van Veggel, F. C. J. M.; Reinhoudt D. N. *Chem. Eur. J.* **2000**, *6*, 1176.

15. Creager, S. E.; Rowe, G. K. *J. Electroanal. Chem.* **1994**, *370*, 203.

16. (a) Schönherr, H.; Vancso, G. J.; Huisman, B.-H.; van Veggel, F. C. J. M.; Reinhoudt, D. N. *Langmuir* **1999**, *15*, 5541; (b) Schönherr, H. Ph.D. Thesis, University of Twente, The Netherlands, 1999.

17. Cantilevers were calibrated using micromachined calibration cantilevers (Park Scientific Instruments, Sunnyvale, CA, USA) with exactly known spring constant. The procedure as well as the specifications are given in: Tortonese, M.; Kirk, M. *Proc. SPIE* **1997**, *3009*, 53.

18. (a) Szejtli, J.; Osa, T. *Comprehensive Supramolecular Chemistry*; Vol. 3, *Cyclodextrins*, Elsevier Science Publishers, Oxford, 1996; (b) Inoue, Y.; Wada, T. in *Advances in Supramolecular Chemistry*; Vol. 4, Jai Press, 1997, p. 55.

19. Electrochemical impedance spectroscopy is a very sensitive technique for the detection of interactions at interfaces. A charged redox couple is used as the reporter ion. For details of the technique see: Flink, S.; Boukamp, B. A.; van den Berg, A.; van Veggel, F. C. J. M.; Reinhoudt, D. N. *J. Am. Chem. Soc.* **1998**, *120*, 4652.

20. Fitting of the experimental charge-transfer data on a Langmuir isotherm results in an association constant of about 289.000 M^{-1} for this system.

21. Tapping mode (in air) and contact mode (in water and ethanol) AFM images of SAMs of heptathiol derivatives of CD on Au(111) (described *e.g.* in Rojas, M. T.; Köninger, R.; Stoddart, J. F.; Kaifer, A. E. *J. Am. Chem. Soc.* **1995**, *117*, 336) revealed a disordered surface. Irregular clusters were observed on the atomically smooth Au(111). These clusters may be attributed to CD molecules which are bound with only few thiol groups and hence do not expose the cavities in a well-defined manner. In order to avoid problems related to disorder, the corresponding sulfide derivatives, which yield homogeneous SAMs, were investigated.

22 A diameter of ca. 19.8 Å can be calculated based on the area requirement of the alkyl substituents. The cavity itself has a diameter of 15.4 Å.

23. (a) Frisbie, C. D.; Rozsnyai, L. F.; Noy, A.; Wrighton, M. S.; Lieber, C. M. *Science* **1994**, *265*, 2071; (b) Noy, A.; Vezenov, D. N.; Lieber, C. M. *Annu. Rev. Mater. Sci.* **1997**, *27*, 381; (c) Sinniah, S. K.; Steel, A. B.; Miller, C. J.; Reutt-Robey, J. E. *J. Am. Chem. Soc.* **1996**, *118*, 8925.

24. Recent advances in modeling enabled several groups to model the unbinding processes for biotin - streptavidin complexes. (a) Grubmüller, H.; Heymann, B.; Tavan, P. *Science* **1996**, *271*, 997; (b) Moore, A.; Williams, P. M.; Davies, M. C.; Jackson, D. E.; Roberts, C. J.; Tendler, S. J. B. *J. Chem. Soc.,*

Perkin Trans. 2 **1998**, 253; (c) Izrailev, S.; Stepaniants, S.; Balsera, M.; Oono, Y.; Schulten, K. *Biophys. J.* **1997**, *72*, 1568.

25. Further theoretical treatments have been reported: (a) Evans, E.; Ritchie, K. *Biophys. J.* **1997**, *72*, 1541; (b) Vijayendra, R.; Hammer, D.; Leckband, D. *J. Chem. Phys.* **1998**, *108*, 7783.

26. The number of pull-off events was reduced by 20 % - 25 % for each cycle. This observation indicates a gradual change in the number of available ferrocene units on the tip as a result of the experiment or the flushing of the liquid cell. It should be noted however, that the positions of the maxima in the force histograms do not change.

27. The maximum contact area between the tip and the monolayer was estimated based on the Johnson-Kendall-Roberts theory of contact mechanics (Johnson, K. L.; Kendall, K.; Roberts, A. D. *Proc. R. Soc. London A* **1971**, *324*, 301) The number of ferrocene-terminated molecules in the estimated maximum contact area of the mixed SAM can be estimated to be ~ 14 - 28 molecules (assuming a homogeneous dispersion of the 1% - 2% of ferrocene-terminated thiol in the SAM). This agrees reasonably well with the experimental observation of ca. 10 - 20 interactions per pull-off event. The load ($L = 1.0$ nN), surface energy per unit area ($W = 10^{-3}$ N/m), and tip radius ($R = 100$ nm) were experimentally determined. The following parameters for the SAMs were assumed: Young's modulus $E = 0.5$ GPa, Poisson's ratio $\nu = 0.3$.

28. The rate constant for decomplexation k_d can be estimated based on the known $K = 2400$ M^{-1} for the complexation of ferrocene carboxylic acid in β-CD (Godínez, L. A.; Schwartz, L.; Criss, C. M.; Kaifer, A. E. *J. Phys. Chem. B* **1997**, *101*, 3376) and the assumption of diffusion limited complexation with a k_c of 10^8 to 10^9 (M^2 s)$^{-1}$. The estimated value for k_d is of the order of 10^5 to 10^6 (M s)$^{-1}$. Thus, processes occur on a time scale of 10^{-6} s, while the AFM is limited to measurements on the order of 10^{-4} s - 10^{-3} s and slower.

29. The error was calculated based on Gauss error analysis: $\Delta F = [((dF/dk) \Delta k)^2 + ((dF/dz) \Delta z)^2]^{1/2}$.

30. In the experiments of Evans, Ritchie et al. [10] the number of binding events in one cycle of the experiment was reduced to one (with a probability of binding < 1). From the histograms of the single complex rupture forces most frequent rupture force f* was determined. In the experiments discussed in here, most unbinding events will not be detected as the unbinding occurs on a time scale of microseconds while the AFM experiment is limited to the millisecond range. As only the resolved individual pull-off events were evaluated, the histograms in Figure 8 cannot be used to determine the most frequent rupture force f* precisely.

31. Within a series of similar host-guest complexes a linear relationship between rupture forces and thermodynamical binding enthalpies may exist [8a,b]. A conversion of the rupture force to binding enthalpy is, however, not generally possible since the experimentally determined force is the derivative at a single inflection point of the potential energy curve while the binding enthalpy results from the integration of the path of binding.

32. Since the only evenly spaced maxima observed are multiples of 56 pN, the single interaction force must correspond to this value.

Chapter 8

Interfacial Properties of Soft Matter Thin Films Studied by X-ray Reflectivity

O. H. Seeck[1], I. D. Kaendler[1], D. Shu[1], Hyunjung Kim[1], K. Shin[2], M. Rafailovich[2], J. Sokolov[2], M. Tolan[3], and S. K. Sinha[1]

[1]XFD/APS Argonne National Laboratory, 9700 South Cass Avenue, Argonne, IL 60439
[2]Department of Materials Science and Engineering, State University of New York, Stony Brook, NY 11794
[3]Institut für Experimentelle und Angewandte Physik, Leibnizstraße 17, 24098 Kiel, Germany

Thin film polymer bilayers and confined liquids have been investigated by x-ray specular reflectivity. First, it is shown that x-ray scattering on polymer bilayers can be superior to neutron scattering if special methods to analyze the data is applied, although neutrons are usually preferred. Second, confined liquids are addressed. The experimental setup for x-ray scattering is presented. Preliminary results are shown, which suggest quantized film thicknesses of the confined liquid.

Introduction

Scattering methods at small angles using x-rays or neutrons are powerful tools to investigate the properties of soft matter thin films. Several different scattering techniques can be applied. Grazing Incidence Diffraction (GID) is sensitive to in-plane ordering of molecules [1], Crystal Truncation Rod (CTR) measurements yield information about the crystalline structure of the films perpendicular to the surfaces [2]. Diffuse scattering can be used to determine details about random surface height fluctuations [3]. In this article we concentrate on reflectivity experiments which have been used to investigate polymer bilayer systems and confined liquids.

In the following, the basics of reflectivity theory and the setup for scattering experiments are presented. The advantages and disadvantages compared to other

129

methods are discussed. The differences between neutron and x-ray reflectivity measurements are worked out in detail. After the theory sections two examples of x-ray reflectivity measurements are given. First, it is shown that x-ray scattering on polymer-polymer interfaces can be superior to neutron scattering if small length scales of a few angstroms are of interest. To analyze the reflectivity data a new Fourier method was developed which is quite sensitive to the interfacial parameters. Confined liquids are addressed in the last section, in which the experimental and theoretical challenges are discussed. Preliminary experimental results on such a system are shown. Finally, we conclude with a summary.

Principles of X-ray and Neutron Reflectivity

When investigating thin film systems, x-ray and neutron scattering methods have several advantages. First, they penetrate the whole sample and can be used to look at buried interfaces or layers. Second, they are extremely sensitive to any kind of ordering and to statistical properties of the sample such as the height-height correlation functions of the interfaces. Third, they cover length scales from molecular sizes (several angstroms) up to mesoscopic distances (several micrometers). Fourth, they average over the illuminated sample area of some mm^2 and yield a complete global picture of the film. Last, they are mostly non-destructive.

However, there are also disadvantages: The scattered intensity usually does not yield the sample properties directly because it is only the mean square value of the amplitude of the scattered wave. The loss of the phase information prevents an unambiguous inversion of the data and a time consuming refinement process (often involving least-squares fitting) has to be applied

Nevertheless, by excluding unreasonable results and taking into account pre-existing knowledge of the system (such as estimated film thicknesses and densities) very reliable results can be achieved from the scattering experiments which cannot be deduced by other methods.

The specular reflectivity experiment

X-ray and neutron specular reflectivity data are taken at small incident angles α_i and exit angles α_f with respect to the surface (typically $\alpha_{i,f} < 5°$) with the condition $\alpha_i = \alpha_f$. A sketch of a typical x-ray reflectivity scattering experiment is depicted in Fig. 1. Usually, the photon source is an x-ray tube or a synchrotron radiation device. The x-ray beam has to be prepared for the experiment: First, an optional mirror focuses the primary beam to increase the flux at the sample position. It also removes high energy photons. Second, a monochromator defines the wavelength λ of the photons by selecting a special photon energy.

The divergence of the monochromatic beam is defined by some slits. The beam intensity is monitored by an ion chamber and can be attenuated if required. Usually,

θ denotes the incident angle α_i with respect to the sample. The scattered intensity is detected at an angle ϕ. The exit angle α_f is determined by $\alpha_f = \phi - \theta$. For the experiments in this article an NaI-scintillation counter was used as a detector.
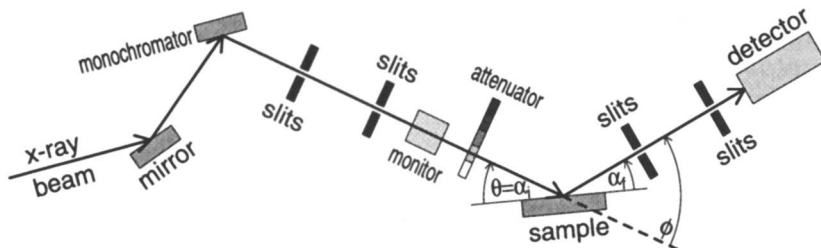
Figure 1: Sketch of a typical setup for an x-ray reflectivity experiment.

Basics of the Reflectivity Theory

For a scattering experiment the wave vectors k_i and k_f define the directions and the mean values of the incoming and the outgoing beam, respectively. As previously mentioned, the orientation of the vectors are defined with respect to the surface, in particular by α_i and α_f (see Fig. 2). In the case of elastic scattering the mean value of the scattered wave vector is conserved and given by $|k_f| = |k_i| = 2\pi/\lambda$. The intensity of the outgoing beam as a function of the wave vector transfer $q = k_f - k_i$ is determined by the sample properties. For specular reflectivity $\alpha_f = \alpha_i$ holds (see above). Therefore, the wave vector transfer is always parallel to the surface normal (the z-direction) and a reflectivity scan only yields information about the sample density profile along z, averaged over the (x, y)-plane (see Fig. 2).

In a scattering experiment, the results differ depending on what the probe being used couples to. X-rays are electromagnetic waves and sensitive to the electron distribution in the sample. In contrast, neutrons are dominantly scattered by the atomic nuclei. However, by introducing a generalized scattering density ρ and a wave vector transfer $q_z = |q| = (4\pi/\lambda)\sin(\phi/2)$ a simple equation for the specularly reflected intensity $I_{spec}(q_z)$ can be formulated. With the density profile $\rho(z)$ perpendicular to the sample surface $I_{spec}(q_z)$ is given in first order Born approximation [4] by

$$I_{spec}(q_z) \propto \frac{1}{q_z^4} \left| \int \frac{d\rho(z)}{dz} \exp(-iq_z z)\, dz \right|^2 \tag{1}$$

which means, that the scattered intensity is proportional to the modulus squared of the Fourier transform of the gradient of $\rho(z)$. For x-rays the electron density has to be taken, while for neutrons, it is the scattering length density of the nuclei.
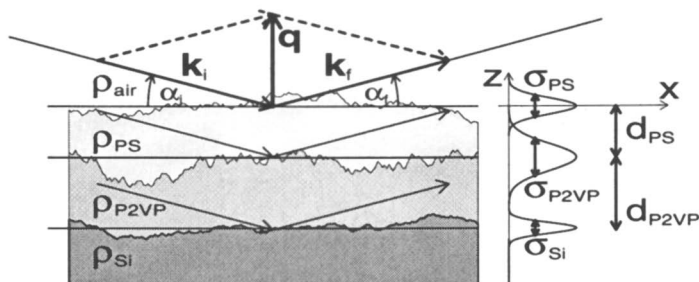
Figure 2: Sketch of a polymer bilayer on silicon. The bottom layer is polyvinyl-pyrridine (P2VP) the top layer polystyrene (PS). The respective sample properties and the corresponding wave vectors for a reflectivity experiment are also depicted.

Therefore, the suitability of the probe (x-rays or neutrons) depends on the sample being studied, e.g., polymer layer systems are usually investigated by neutron scattering: By deuterating one polymer and hydrogenating the other one a high scattering length density difference (contrast) can be achieved because the scattering lengths of deuterium and hydrogen are extremely different and in fact of opposite sign [5]. In contrast, for x-rays the electron density is almost the same for every polymer (less than 10% difference). Fig. 3 displays the x-ray density and the neutron density of a typical polymer bilayer on a silicon substrate.
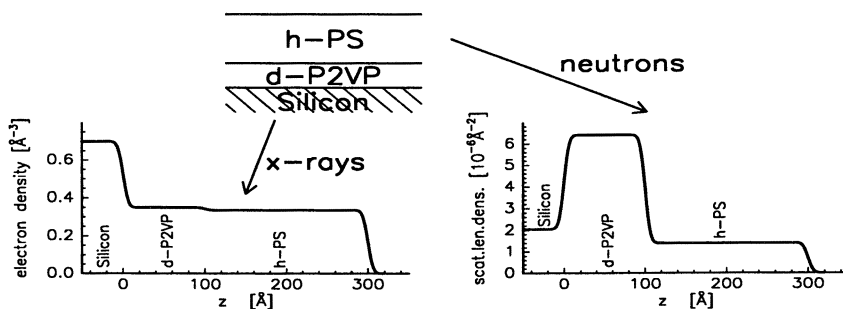
Figure 3: Density profiles of a polymer bilayer (hydrogenated polystyrene [h-PS] on deuterated polyvinylpyrridine [d-P2VP]) on silicon. The x-ray density is shown on the left hand, the respective neutron density on the right side.

The importance of the scattering length density contrast for reflectivity experiments on layered systems is shown in Fig. 4. It depicts model calculations of x-ray reflectivity data using different density profiles. The profiles (left column of

Fig. 4) can be parametrized by the density ρ_j of each layer, the layer thickness d_j and the root-mean-square (rms) roughness σ_j of each interface with number j (starting from $j=0$ at $z_0=0$) given by the density probability function. This is not necessarily an error-function but could be, for example a tanh-profile for a polymer-polymer interface [6]. However, for the considerations in this chapter the exact form of the profile is not of importance and error-function profiles are assumed. Later on, tanh-profiles are taken for the refinements.
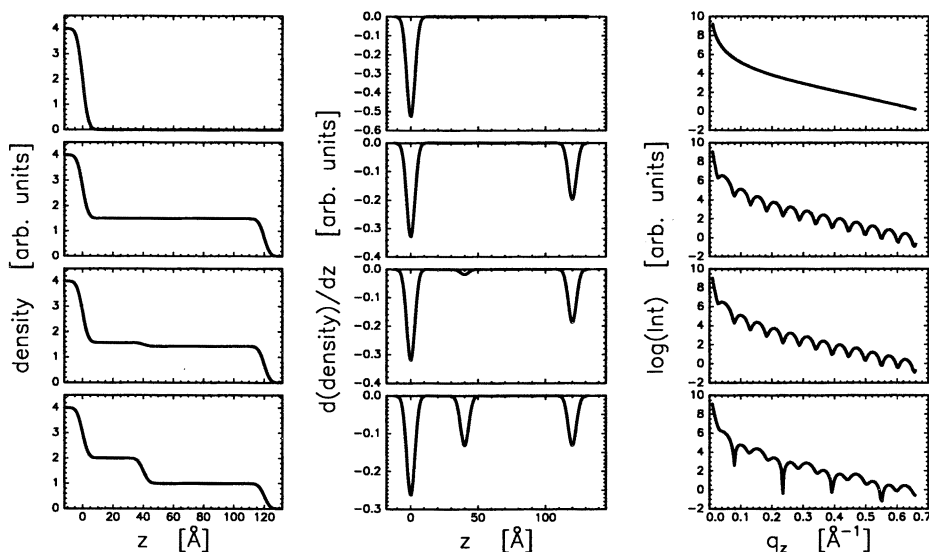
Figure 4: Examples for calculated x-ray reflectivities. The left column displays the density profile $\rho(z)$ the center column $d\rho(z)/dz$ and the right column the specular reflected intensity of the respective profile. Top row: single Si-surface. Second row: Si-substrate with one polymer layer. Third row: Si-substrate with a polymer bilayer, the contrast is 10%. Fourth row: Si-substrate with a „high-contrast" bilayer.

If the rms-roughnesses are considerably smaller than the film thicknesses the gradient $d\rho(z)/dz$ can be expressed by a sum of well separated gaussians at the positions of the interfaces z_j and with the widths σ_j (center column of Fig. 4). The right column of Fig.4 shows the calculated specularly reflected intensity using Eq. 1.

The simplest model is a bare substrate with density ρ_0 and a surfaces roughness σ_0. The derivative of $\rho(z)$ yields a gaussian at $z=0$ with the width σ_0. Using Eq. 1, the reflected intensity is given by $q_z^4 I_{spec}(q_z) \propto \rho_0 \exp(-q_z^2 \sigma_0^2)$ which is shown in the top row of Fig. 4. In the case of a monolayer system the distances of the interface from $z=0$ yields oscillations of the reflected intensity given by $q_z^4 I_{spec}(q_z) \propto \kappa_0^2 \exp(-q_z^2 \sigma_0^2)$ $+\kappa_1^2 \exp(-q_z^2 \sigma_1^2) + 2\kappa_0 \kappa_1 \exp(-q_z^2 [\sigma_0^2 + \sigma_1^2]/2) \cos(q_z d_1)$ with the contrasts $\kappa_j = \rho_j - \rho_{j+1}$.

Thus, small contrasts lead to less pronounced oscillations. Similarly, a bilayer system should show two significant oscillation periods in the reflectivity depending on the thicknesses d_1 and d_2 of each layer. The visibility of the resulting beating of the intensity depends on the contrast κ_1 between layer 1 and 2 (see Fig. 4, lower rows). If κ_1 is very small, the reflectivity of a bilayer system may be almost identical to a monolayer system. Therefore, usually neutron scattering methods are used to investigate polymer layer systems because κ_1 can be increased dramatically by deuterating one compound as mentioned above [5].

However, the low intensity of the neutron beam and the coarse resolution compared to x-rays often result in quite large error bars. The flux of a neutron beam is typically more than 5 orders of magnitude smaller than the photon flux of a synchrotron radiation source with up to 10^{11} photons/sec on an area of $(0.2{\times}2)mm^2$. From Eq. 1 it is known that the specularly reflected intensity at least falls with $1/q_z^4$. Thus, the low intensity of a neutron beam restricts the accessible q_z-range (a neutron reflectivity almost never exceeds a q_z-value of $q_{z,max}= 0.2Å^{-1}$). This means a relatively coarse resolution Δz in real space via $\Delta z \propto 2\pi/q_{z,max}$. In contrast, an x-ray reflectivity easily covers about 9 orders of magnitude which corresponds to a q_z-range of $0.7Å^{-1}$ to $1.0Å^{-1}$. This yields a 4 times better resolution in real space if x-rays are used.

Fig. 5 demonstrates the effect of the restriction in q_z. A bilayer system with high contrast has been chosen to calculate a reflectivity. The density profile was successively approximated by histograms of step-width 1.6Å and then with 4.8Å step-width. Comparing the respective reflectivities shows that both these approximations match the exact calculation up to $0.25Å^{-1}$ almost perfectly.
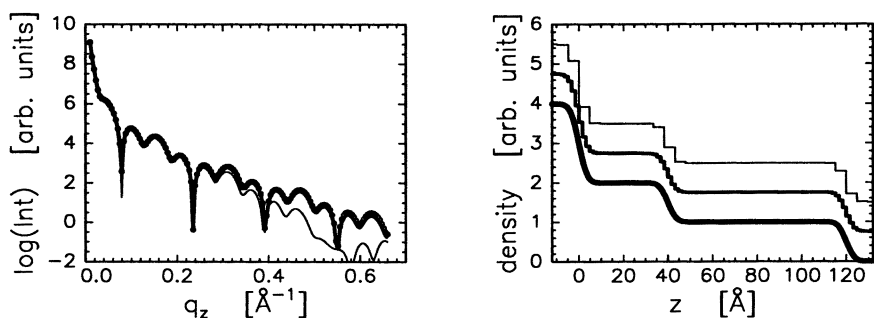
Figure 5: Model calculations of reflectivities (left) with different bilayer density profiles (right). The exact profile (thick line) yields the reflectivity displayed by symbols. The coarse profile (thin line) yields the thin-lined reflectivity. The reflectivity of the fine profile (medium line) matches the exact reflectivity well.

Thus, neutron data are quite insensitive to the rms-roughness and can provide only an estimate of the general shape of interfaces. The errors in determining the

rms-roughnesses are at least ±5Å. If a maximum q_z-range of 0.7Å^{-1} is considered, the histogram slicing width has to be smaller than 1.6Å to reproduce the reflectivity over the whole range. This approximation is much better and also yields the shape of the density profile close to the interfaces quite accurately.

Examples

In the following, two examples of x-ray reflectivity measurements on soft matter thin films are presented. First, some results on polymer-polymer interfaces are shown. Second, some results on confined liquids are presented.

X-Ray Scattering on Polymer Bilayers

The properties of polymer-polymer interfaces are the focus of many current research projects. Interdiffusion can be investigated depending on the composition or the temperature. Also the microscopic properties of the interfaces are of great interest, especially when thin films are considered and the interaction with the substrate affects the system [7,8,9].

It is well known for bulk polyvinylpyrridine-polystyrene (P2VP-PS) systems, that the surface tension at the PS-P2VP interface is reduced compared to a PS- or P2VP-vacuum interface. This leads to strong capillary wave fluctuations and thus to an increase of the interfacial rms-roughness. It is still unknown whether this also holds for thin film systems, where capillary waves are modified due to the van der Waals interaction with the substrate, and whether there are significant changes which depend on the film thicknesses. The interfacial properties may also depend on the order of the films due to different wetting behavior of the two polymers. Finally, the system can be doped with the respective block co-polymer. These molecules may accumulate at the interface also changing its properties (see Fig. 6).
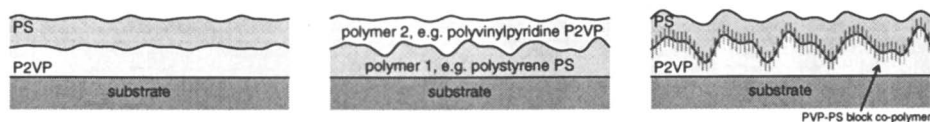
Figure 6: Examples for PS-P2VP thin film systems. Left: PS on P2VP on silicon. Center: Reversed order of the polymer films. Right: Same system but doped with the respective block co-polymer.

It was stated in the previous section that usually neutron scattering is used to investigate polymer-polymer interfaces with however the disadvantage of the limited q_z-range. If a large q_z-range is required x-rays have to be used. But it turns out that

the reflectivity of a monolayer and a bilayer are almost identical because of the low x-ray contrast (see Fig. 4). Simply performing a least squares fit can hardly yield the information if one or two polymer layers are present. Advanced methods such as maximum entropy refinements can be applied to analyze the data. In the following, a more straightforward approach will be discussed.

Our starting point is the Fourier backtransformation $F_{spec}(d)$ of the specularly reflected intensity $I_{spec}(q_z)$ which has to be multiplied with q_z^4 before performing the transformation

$$F_{spec}(d) = \left| \int_{q_{z,low}}^{q_{z,up}} q_z^4 I_{spec}(q_z) \exp(iq_z d)\,dq_z \right|^2 . \tag{2}$$

The limits of integration are denoted by $q_{z,up}$ and $q_{z,low}$. Essentially, $F_{spec}(d)$ is the modulus squared of the one-dimensional Patterson function obtained from the reflectivity and has occasionally been used in the past to refine density profiles of organic monolayers especially in the regime of the interface to the substrate [10,11]. In this article it is used to get information about the polymer-polymer interface.

$F_{spec}(d)$ is extremely sensitive to any oscillations in the reflectivity such as the small beating due to a low-contrast interface. This is demonstrated in Fig. 7 where model calculations of a polymer monolayer and a polymer bilayer are displayed. Each characteristic length scale causes a distinct peak in the Fourier back-transformation $F_{spec}(d)$.
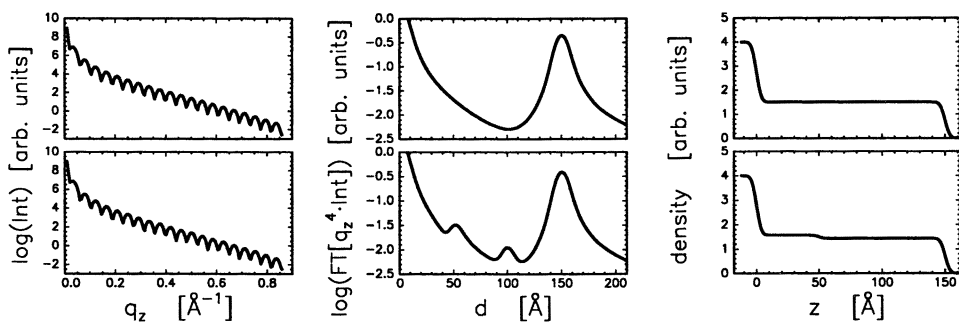
Figure 7: Model calculations of reflectivities (left column), the Fourier backtrans-formation using Eq. 2 (center column) and the density profiles (right column). Top row: monolayer system. Bottom row: low density contrast (10%) bilayer.

The top row demonstrates, that $F_{spec}(d)$ of the monolayer reflectivity shows only one characteristic length scale at $d=150\text{Å}$ which is the film thickness. In contrast, the Fourier backtransformation of the bilayer looks very different even though both

reflectivities are almost identical. $F_{spec}(d)$ exhibits two small peaks which are due to the length scales of the single polymer films and a large peak which again represents the total film thickness. From this information **and** the reflectivity the density profile can easily be deduced which is hardly possible if only the reflectivity is considered.

Several polymer monolayer and bilayer systems have been prepared to test the Fourier method and to get the rms-roughnesses from P2VP-PS interfaces. The P2VP-films were spin coated on silicon wafers. The PS-films were spin coated on glass pieces, floated on water and afterwards picked up by the P2VP-coated silicon pieces. All samples were annealed for 24 hours at 165°C under high vacuum conditions. The x-ray measurements were performed at the NSLS (Brookhaven National Laboratory) at beamline X10B using a photon energy of 11keV. Fig. 8 depicts the measurements and refinements.
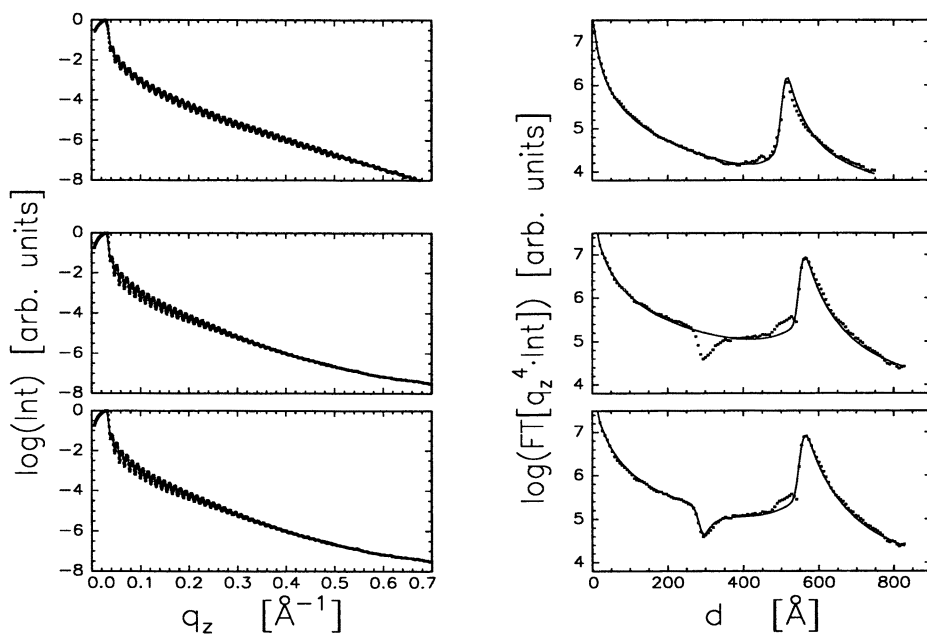
Figure 8: Examples of x-ray reflectivity measurements and refinements of polymer thin films. Top row: single 510Å thick P2VP film, center and bottom row: 280Å PS on 280Å P2VP (center row: a monolayer fit, bottom row: a bilayer fit). The data are displayed with symbols the refinements with solid lines.

The signature of the monolayer and the bilayer system, respectively, can easily be seen at $F_{spec}(d)$ (right column). This is almost impossible by just analyzing the reflectivities (left column). The top row of Fig. 8 depicts the measurement of a single layer P2VP and the fit of the reflectivity which matches perfectly. The Fourier

backtransformation of the data only shows one characteristic length scale. In this case, the backtransformation of the reflectivity refinement also fits perfectly.

Using a P2VP-PS bilayer, the center and the bottom row demonstrate how sensitive the Fourier method is. First, the reflectivity was refined assuming a monolayer and without taking into account $F_{spec}(d)$. The fit is shown in the left picture of the center line. It is almost identical to the data. A very close look would yield very tiny systematic deviations but just from the reflectivity it cannot easily be decided if the refinement is perfect. In contrast, if the Fourier backtransformations are compared significant deviations are visible at a characteristic length scale of 280Å which corresponds to the film thickness of each single layer. Therefore, the fit was redone now assuming a bilayer. To be more sensitive to the polymer-polymer interface $F_{spec}(d)$ was refined simultaneously with the reflectivity data. The result is depicted in the bottom row of Fig. 8.

The reflectivity fit is again perfect but now also the Fourier backtransformation agrees well. A small shoulder in the backtransformed data at $d{\approx}500$Å cannot be explained by the fit. However, an additional length scale in the density profile can be excluded because it would automatically cause other length scales such as 300Å+500Å. This is not observed in the Fourier backtransformation. A possible explanation for the shoulder would be an interfacial density profile different from an error- or a tanh-function which has not been considered for the refinement. The density contrast and the rms-roughness can be determined with an accuracy of about 20%. Table I lists the results on PS-P2VP thin film systems.

Table I. Results on PS-P2VP Thin Film Systems

d_{P2VP} [Å]	$\sigma_{P2VP-PS}$ [Å]	d_{PS} [Å]	$\sigma_{Poly-Air}$ [Å]
226	-	-	5.2
510	-	-	7.3
225	15.6	220	7.2
277	14.6	279	9.3
277	16.4	382	9.4
925	14.5	355	11.1
927	19.8	1095	13.9

NOTE: The error bars of the rms-roughnesses are about 20%, the error bars of the thicknesses about 1Å. The first to rows are the results of P2VP-monolayers.

They show that the rms-roughnesses $\sigma_{P2VP-PS}$ of the polymer-polymer interface is larger than the polymer air interface of a monolayer system. Also, the PS-air interface seems to become rougher with increasing film thickness whereas the P2PV-PS interface is unaffected. However, these results are preliminary and need to be confirmed by further investigations.

X-ray Scattering on Confined Liquids

A very recent research topic is the investigation of confined liquids [12]. In this article they are defined as liquid films which are infinite in the (x,y)-plane and only a few molecular diameters thick in z-direction. Additionally, **both** interfaces of the thin film are in contact with a substrate (in contrast to a thin film, where only one side contacts the substrate). Due to the confinement the film properties are expected to be very different from the bulk properties, e.g., density modulations perpendicular to the interfaces are expected [13]. Even in-plane ordering may occur which would mean that the „liquid" is in fact no longer liquid but solid (see Fig. 9).
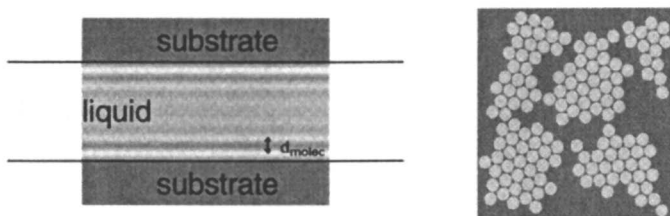
Figure 9: Properties which may be investigated at confined liquids. Left: Layering (density modulations) perpendicular to the interfaces (side view of the film). Right: In-plane ordering of the liquid molecules (top view on the substrate).

It is a challenge to design an experimental setup that works for the investigation of confined liquids especially if x-ray scattering is used. The major problem is, how to get two surfaces very close to each other and to control the gap distance. The following list addresses the most important points which have to be taken into account for x-ray experiments on confined liquids.

1. The gap size between the two surfaces has to be controllable in a range from 10Å to 1000Å. The accuracy of the gap distance should be better than 5Å.
2. The area of confinement has to be at least $(2{\times}2)mm^2$ (required by the x-ray reflectivity experiment).
3. The rms-roughnesses of the substrates need to be smaller than 3Å.
4. The curvature of the substrates should result in a gap variation smaller than 5Å in the area of confinement.
5. The substrates have to be transparent for x-rays.
6. The scattering background from the substrates has to be as low as possible.
7. Dust free conditions are required.
8. The area of confinement has to be stabilized in temperature and sealed to prevent evaporation of the liquid.

This list only addresses the most critical points. For the actual realization of the setup one has to compromise, e.g., point 5 requires substrates such as beryllium, boron nitride or organic compounds made from elements with very low atomic numbers. But these materials have either an enormous scattering background or cannot be polished to the required value of 3Å (point 3 and 6). Thus, silicon was taken as the substrate material. The x-ray photon energy has to be larger than 20keV for sample sizes of $(2\times2)mm^2$ to penetrate the silicon without being absorbed. Figure 10 depicts the experimental setup and the silicon substrates which have been used.
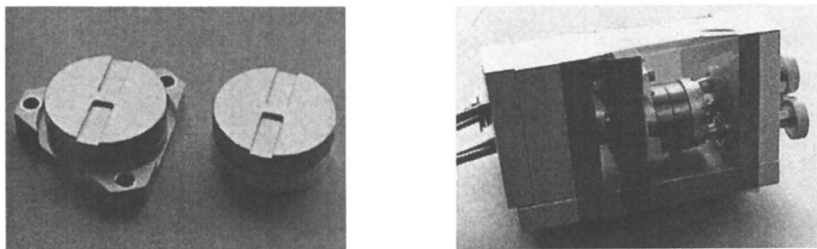
Figure 10: Realization of the experimental setup for x-ray scattering on confined liquids. Left: Special designed silicon substrates (25.4mm diameter). The area of confinement is the bridge in the center. Right: The sample cell.

The silicon substrates are specially designed. They have a diameter of 1 inch (25.4mm), an rms-roughness of 3Å (determined by x-ray scattering) and a convex curvature with a height variation of less than 100Å over the whole sample area (determined by interferometry). Two grooves are etched in each surface which leave a bridge of the size $(2\times4)mm^2$ in the center part. The bridge is the area of confinement with a resulting height variation of less than 10Å. For the experiment, the liquid is spread over the surface of one substrate in a class 1 clean room. Both substrates are put together so that the grooves form tunnels which are the paths for the x-rays to the area of confinement. The gap distance between both silicon pieces can be controlled by piezo drivers.

The x-ray reflectivity experiments have been performed at the APS (Argonne National Laboratory). The characteristics of the setup were checked at station 2BMB where the liquid hexadecane $(C_{16}H_{34})$ was used. Some reflectivity measurements taken at 30keV photon energy are depicted in Fig. 11. They show that the gap size shrinks linearly with increasing pressure of the piezo devices.

Further reflectivity measurements using octamethylcyclotetrasiloxane (OMCTS) were performed at station 1IDC, again with a photon energy of 30keV (see Figure 12). We could achieve 10 times higher pressure compared to the run at 2BMB and thus could get much smaller gap distances. Also the flux was much higher so that more details of the reflectivities can be seen.
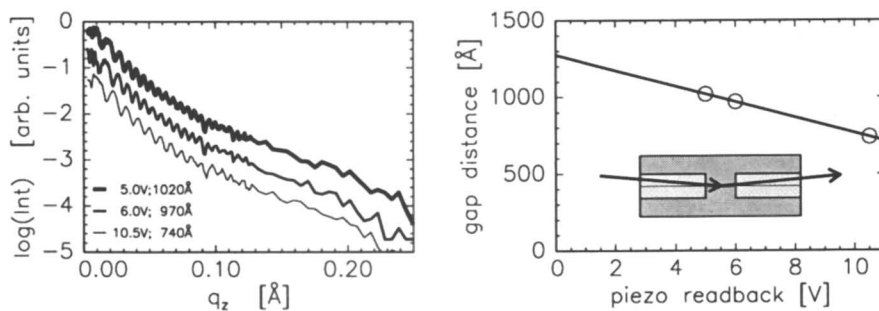
Figure 11: Gap measurements of the confined liquid setup. Left: Some reflectivity measurements at different readbacks of the piezos. They show oscillations due to the gap size. Right: Characteristics of the piezos and a sketch of the sample with the area of confinement in the center.
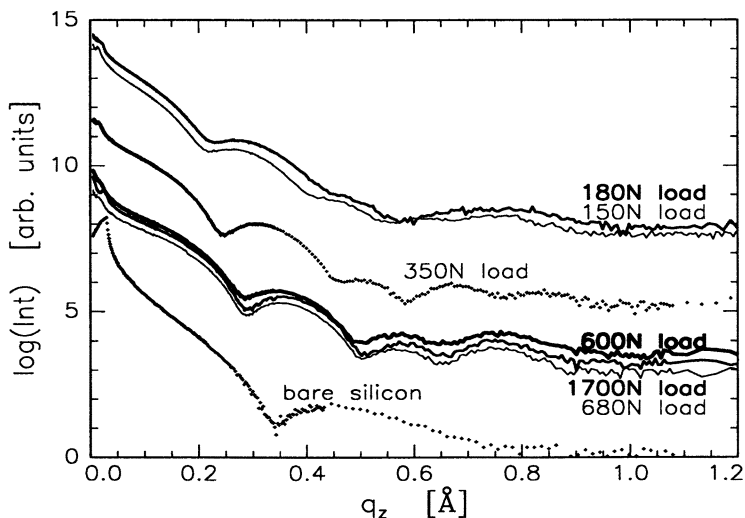
Figure 12: Reflectivities on confined OMCTS. Different pressures have been applied on the silicon substrates. Essentially, only three different reflectivities can be seen.

They show that the gap size was in the range of 30...60Å. The molecular size of OMCTS, which was determined by measuring the liquid structure factor, is 7.5Å. Thus, we reached the state of extremely confined liquids. This can also be seen by the fact that the gap size seems to be quantized: Even though many different pressures have been applied to the system only three different kinds of reflectivity

curves could be measured in which the highest loads yield the smallest gap. The reason may be that only gap sizes which accommodate integral numbers of layers of OMCTS are allowed.

Summary

In this article we have shown that x-ray reflectivity measurements can be applied successfully even for systems where the structure cannot be solved by normal x-ray scattering. The technique was used to determine the interfacial roughnesses of low contrast P2VP-PS bilayers where a special Fourier method was performed to analyze the data. The results suggest that the interface is strongly affected by the interaction with the silicon substrate. Furthermore, OMCTS in an extremely confined state has been investigated with high energy x-ray reflectivity. The analysis of the data yields, that only integer numbers of molecular layers seem to be allowed for the thickness of the confined film.

References

1. Dosch, H. *Critical Phenomena at Surfaces and Interfaces*; Springer Tracts in Modern Physics; Springer: Berlin, Heidelberg, 1992; Vol. 126.
2. Robinson, I.K. *Phys. Rev. B* **1986**, *33*, 3830.
3. Sinha, S.K.; Sirota E.B.; Garoff S.; Stanley H.B. *Phys. Rev. B* **1988**, *38*, 2297.
4. Als-Nielsen, J. *Structure and Dynamics of Surfaces;* Topics in Current Physics; Springer: Berlin, Heidelberg, 1986; Vol 2.
5. *Proceedings of the workshop on „Methods of Analysis and Interpretation of Neutron Reflectivity Data“*; Felcher, G.P.; Russell ,T.P., Eds., Physica B *173*, 1991.
6. Helfand, E.; Tagami, Y. *J. Chem. Phys.* **1972**, *56*, 3592
7. Sferrazza, S.; Xiao, C.; Jones, R.A.L.; Bucknall, D.G.; Webster, J.; Penfold, J. *Phys. Rev. Lett.* **1997**, *78*, 3693.
8. Wang, J.; Tolan, M.; Seeck, O.H.; Sinha, S.K.; Bahr. O.; Rafailovich, M.H.; Sokolov, J. *Phys. Rev. Lett.* **1999**, *83*, 564.
9. Tolan, M.; Seeck, O.H.; Schlomka, J.-P.; Press, W.; Wang, J.; Sinha, S.K.; Li, Z.; Rafailovich, M.H.; Sokolov, J. *Phys. Rev. Lett.* **1998**, *81*, 2731.
10. Tidswell, I.M.; Ocko, B.M.; Pershan, P.S.; Wasserman, S.R.; Whitesides, G.M.; Axe, J.D. *Phys. Rev. B* **1990**, *41*, 1111.
11. Toney, M.F.; Thompson, C. *J. Chem. Phys.* **1990**, *92*, 3781.
12. Granick, S. *Physics Today* July, 1999, p 26.
13. Yu, C.-J.; Richter, A.G.; Datta, A.; Durbin, M.K.; Dutta, P. *Phys. Rev. Lett.* **1999**, *82*, 2326.

Chapter 9

Constant Velocity versus Harmonic Drive Friction Measurements

V. Pasquier[1], J. M. Drake[1], and J. Klafter[2]

[1]Exxon Research and Engineering Company, Route 22 East, Annandale, NJ 08801
[2]School of Chemistry, Tel Aviv University, Tel Aviv 69978, Israel

In this article we investigate atomic force microscope friction (AFM) measurements at the SiO_2/SiO_2 interface. We use two approaches which differ in the way in which the surfaces are driven relative to each other in contact. The silicon tip of the AFM is driven at constant velocity or harmonically. The resulting response corresponds to either the tribological or the rheological properties at the contact. Here we bridge the gap between the two approaches which do not always lead to the same conclusions.

Nanoindentation and nanotribology have been active research topics since the introduction of experimental tools such as the surface forces apparatus (SFA) and the atomic force microscope (AFM). These tools allow for detailed investigations of frictional properties of confined molecular systems at nanometer length scales(*1,2,3,4,5*).

Two approaches have been used to investigate frictional forces in confined systems: the tribological, where a constant drive velocity is applied(*6*), and the rheological, which applies an oscillatory external drive: $X(t)=\Delta x \sin \omega t$ (*7,8*). When the oscillatory drive is applied, the response of the system is analyzed in terms of complex moduli (*9*). The rheological analysis of the moduli enables to distinguish between the elastic and viscous components of the response. The viscous part is directly related to the energy dissipation in the system. A few interesting questions arise:

- What is the relationship between these two types of drives?
- Are the frictional properties obtained using a constant velocity drive and an oscillatory drive the same?
- To what extent is the velocity defined in rheology $v=\Delta x \omega$ meaningful?

Here we try to address these issues by comparing the tribological and rhelogical methods in the case of *dry* friction at a SiO_2/SiO_2 interface. We show, by using an

144

AFM, that the friction coefficients obtained by the two approaches are similar, provided that the rheological velocities Δx ω are higher that some transition value of velocity. The relationship between tribology and rheology of confined molecular systems has been investigated theoretically for models that mimic SFA(*10,11*).

Description of the experiment.

The principle of the atomic force microscope (AFM) consists in rastering the sample surface with a sharp tip -about 10-100nm of radius- that is placed at the end of a -200µm long- cantilever driven by a 3-dimensional transducer. A laser beam is reflected off the backside of the cantilever onto a 4-quadrant Position Sensitive Photodetector (PSD). The output photocurrent signals enable the torsional and normal bendings of the cantilever to be measured, which are proportional to the lateral and normal forces experienced by the tip in contact with the surface (*12,13,14,15,16*). The same cantilever is used in both tribological and rheological methods. We used a pure silicon bar-shaped cantilever. Knowing the metrics, measured using optical and scanning electron microscopes and the Silicon Young modulus, the spring constants were calculated. The normal spring constant is 0.31±0.01N/m and the torsional spring constant is 24±8N/m

The constant velocity drive is created by applying a sawtooth voltage ramp to the lateral piezoceramic transducer. The second method is achieved by applying a harmonic drive to the piezo making it extend and retract cyclically. The lateral torsion of the cantilever, while the tip is sliding at constant velocity under a constant load, is averaged over the sliding distance and analyzed in term of friction force. If the input modulation drive is a harmonic sine wave, we use the phenomenological theory of linear viscoelasticity to describe our output in term of storage and loss moduli giving an insight into the dissipative and elastic modes of the system (*17,18*).

Constant velocity sliding measurements.

One commonly measures of the friction force at a constant velocity using the friction loop. The tip is forced to slide in the lateral direction by the cantilever. The friction force makes the cantilever twist by an angle that is proportional to the friction force. When the movement is reversed and the tip slides in the opposite direction, the cantilever bends by the same but opposite angle. This friction loop corresponds to the difference of the lateral force signal between the back and forth scans. Therefore, the friction force equals half the amplitude of the friction loop.

We used the friction loop method to probe the friction at the SiO_2/SiO_2 nanocontact. We measured the averaged friction force by scanning at a constant velocity of 10µm/s over a 10µm x 3µm area at constant load. Then, the measurement is repeated for another constant load and averaged over the same surface area. The normal force between the tip and the surface is maintained constant when scanning with an electronic feedback loop. A compromise has to be found in order to set the feedback parameters high enough to keep the normal force constant without introducing parasitic vibrations that might impact the friction force measurement (*19,20*).

Figure 1 shows the sliding friction dependence on the total normal load. The result is analyzed using the Amontons' law that states that the friction force and the load are related by a porportionality constant, the friction coefficient,

$$\mu = \frac{F_f}{L} \quad , \tag{1}$$

where F_f is the frictional force and L, the total load is

$$L = F_n + F_{adh}. \tag{2}$$

Here F_n is the applied normal force and F_{adh} is the adhesion force.

The slope in fig.1 provides a friction coefficient which here is $\mu=0.108\pm0.001$. We have chosen to consider the total load instead of the commonly used applied load, F_n. The measured adhesive force obtained from the intercept of the friction versus applied load plot is $F_{adh.}=3.9\pm0.8nN$. Assuming an ideal Hertzian contact area, we estimate that the surface energy equals $18mJ/m^2$, which is consistent with the value of $13mJ/m^2$ observed for the *dry* sliding of silica on silica (*21*).
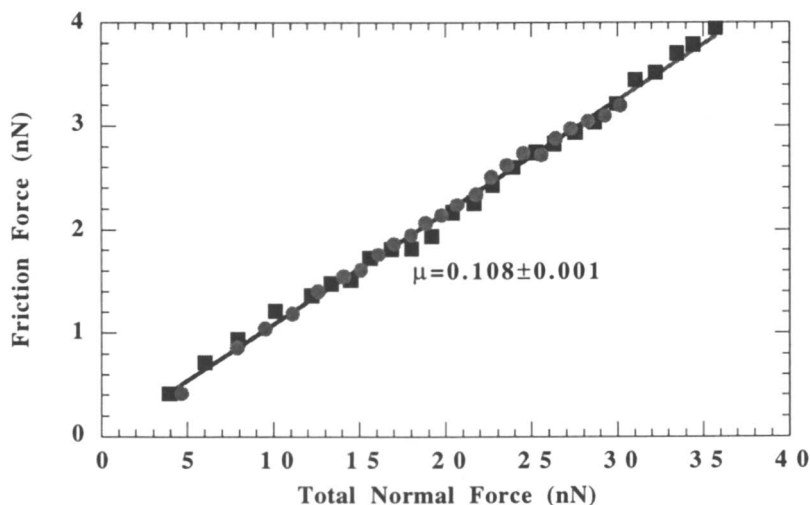
Figure 1:Load dependence of the friction force at a constant sliding velocity of 10µm/s (● loading, ■ unloading)

This observation of the friction coefficient provides the averaged frictional property at the nanocontact. Indeed, the observed Amontons' law suggests that the contact between the silicon tip and the surface is actually a multiasperity contact, or that the contact is somehow wearing out during the process.

Harmonic Drive Measurements.

We now study the sliding contact properties using the rheological approach. The lateral stress is applied using an oscillatory external drive. Assuming that the system adopts a viscoelastic behavior, the strain can be investigated in terms of complex moduli (*9,22,23,24*). Measuring the in-phase and out of phase responses allows a direct measure of the storage and loss components of the sliding contact and therefore provides additional information about the dissipation.

The harmonic drive approach which is basic in rheological experiments was first implemented by Colchero et al. (*25*) for an AFM. The basic idea couples a lock-in technique with the lateral force microscope and has been essentially used for measuring the lateral contact stiffness (*26,27*). If the tip is modulated periodically in successive back and forth scans the lateral force signal is periodic too. The lock-in technique is particularly appropriate to analyze a signal in reference to another signal of the same frequency.

The first step consists in establishing the experimental procedure which essentially means the choice of the appropriate modulation frequency.
The modulation frequency must be chosen so that it reduces unexpected correlations and avoids damped response or over-enhanced noise. We have focused our investigation in the frequency window from 0 to 1kHz since the ultimate frequency needs to be well below the resonance frequency of the transducer to insure the linear response of the lateral drive.
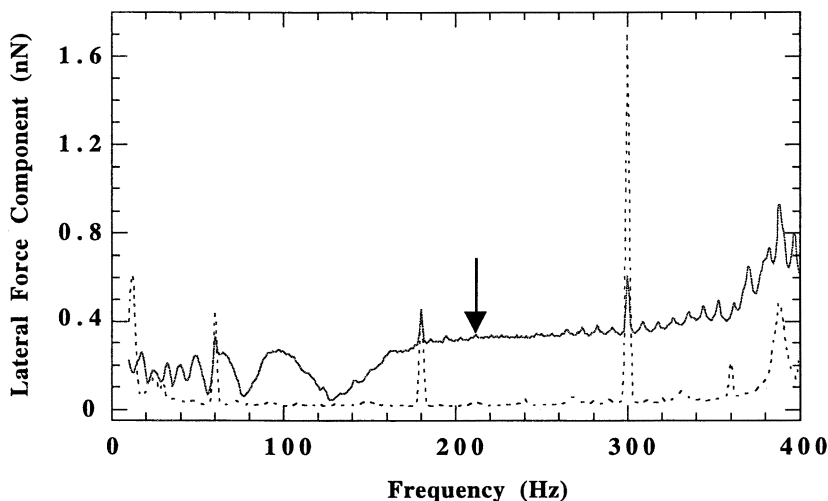
Figure 2: The average cantilever frequency response(———) to a lateral modulation sweep, and the free resonance spectrum in contact (-------). The arrow indicates the frequency chosen to drive the cantilever laterally.

We have measured the frequency response of the lateral mode of the cantilever while sweeping the drive frequency of the voltage applied to the piezoceramic transducer (figure 2). Below 180Hz the spectrum shows frequencies for which lateral vibrations seem to be totally damped. It is important to notice that these frequencies do not correspond to any of the free vibrational modes present in the system.

We have searched for a frequency that does not exhibit any overdamping or resonant properties. We noticed in the spectrum (figure 2) a plateau between 180Hz and 270Hz, where the cantilever response is constant and independent of the modulation frequency. Therefore, we have chosen the modulation frequency of 213Hz.

As it has already been pointed out (28) the frequency response of the cantilever is quite complex and reveals coupling between normal and lateral modes. Therefore, we checked the magnitude of the coupling by looking at the orthogonal modes of the cantilever. We found that when the modulation is applied at 213Hz, the normal - lateral coupling occurs at harmonic modes of 213Hz and also at higher frequencies. The energy transfer between normal and lateral vibrational modes of the system creates a non-random noise in the normal force and consequently in the friction force. These force fluctuations represent as much as 10% of the forces observed in the friction measurement.

First, in order to validate the modulation technique we compared the results with the constant velocity measuremem. To do so, we chose a sawtooth drive voltage, so that the lateral displacement takes place at constant velocity.

While the tip is oscillating in the transverse or lateral direction, the cantilever is brought into contact by extending the Z-piezoceramic transducer at constant speed by a known distance and is then retracted to its initial position. The friction force is proportional to the amplitude of the tip's lateral displacement analyzed by the lock-in technique. Measuring the lateral component while varying the load achieves in one step the measurement of the friction versus load.

Figure 3 shows the *total load* dependence of the friction force measured for modulation amplitudes of 50nm and 100nm. The contact location was arbitrarily chosen on the same surface. Both curves are described by the same Amontons' law. The friction coefficient defined by the slope of the linear fit is $\mu=0.087\pm0.001$. When plotted as the friction force versus the total load, the intercept is zero. It is important at this point to specify that the error associated to the friction coefficient arises from the fitting analysis of our data, which therefore, determines the precision of the experiment and not the overall acuracy of the experiment. Indeed, the main source of uncertainty in our measurements originates in the precision in the cantilever metrics measured by optical microscopy and SEM which is of the order of 3% to 5%. Some other sources (19,28), like the position of the laser spot on the backside of the cantilever affects the absolute accuracy of the friction measurements to an extend that is difficult to evaluate. We expect the overall accuracy on the friction measurement to be less than 60%(28). Nevertheless, since the crucial experimental conditions were optimized and kept constant from an experiment to the other, the comparison remains valid.
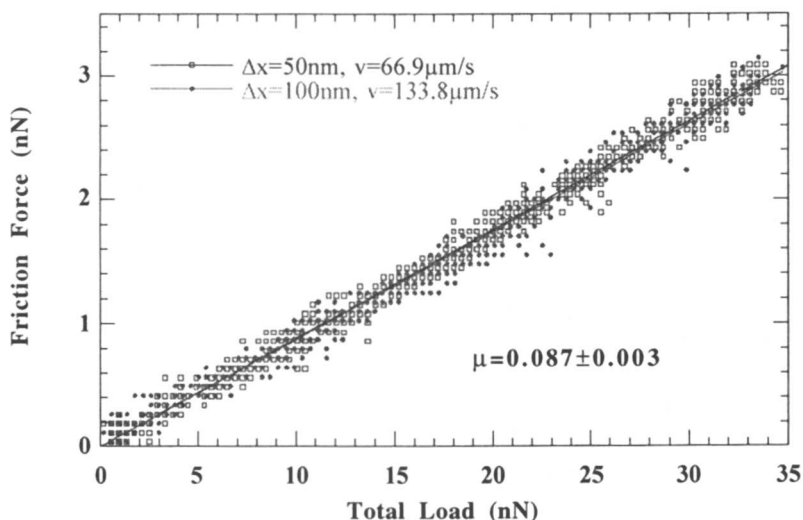
Figure 3: Load dependence of the friction force measured for an oscillatory motion at constant speeds (lateral displacement amplitude 50nm and 100nm at frequency 213Hz)

Figure 4 shows the difference between the drive (periodical sawtooth) and the lateral force experienced by the cantilever.
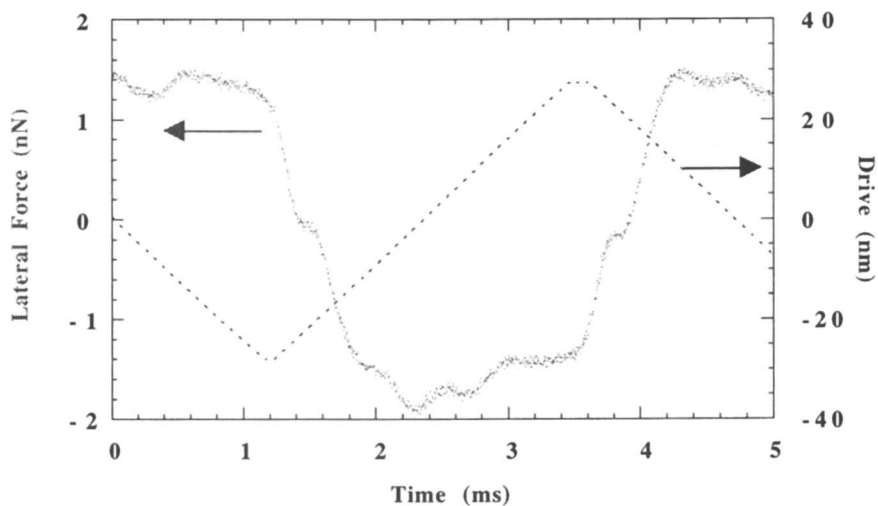
Figure 4: The shape of the friction loop obtained for an oscillatory drive at constant velocity.

After a sticking time the tip starts to slide, and the cantilever therefore bends under the effect of the friction force. Assuming that the steady state sliding regime is reached instantaneously (i.e. after a time short enough relative to the complete cycle), and that the friction force is constant over the covered distance the ideal shape of the response is a square wave. We recognize in the experimental response (figure 4) vertical jumps which correspond to the turning points and fluctuating friction force during sliding. The slight difference between the real and ideal shape introduces an additional source of error in the measurement since the lock-in provides the amplitude of the first component of signal decomposed into a Fourier series. We apply a correction coefficient defined by the ratio between the real friction loop area and the square wave area over the same half period. This coefficient tends to reach $4/\pi$ (*25*) for a lateral displacement of more than 100nm. For small lateral displacement, the correction factor is smaller and varies with the amplitude.

We chose a suitable frequency range inside which the measurements are not affected by the mechanical coupling of the system. We checked the validity of our modulation approach by comparing two friction coefficients obtained by two different sliding drives at constant velocity.

A harmonic drive voltage has been applied to the transverse piezo transducer. We increased the amplitude of the sine wave drive at a constant frequency, which led to a progressive increase in the the sliding velocity defined in rheological conditions by $v=\Delta x \, \omega$. Figure 5 presents the lateral force, the friction coefficient and the loss tangent, as a function of the sliding velocity of the cantilever, $v=\Delta x \, \omega$.

The main feature in Figure 5 is the existence of two regimes. At low velocities or small displacements, the friction force builds up towards a constant value. The same trend is observed for the friction coefficient that grows with v and then becomes independent of velocity. In the local regime –small displacements, low velocities- the loss tangent increases significantly, indicating that sliding occurs at the contact. Indeed, if the contact were not sliding, it would undergo elastic lateral deformation. The drive and the response would be in phase. Therefore the loss tangent would be constant and equal to zero. In addition, the slope dF/dx should provide a measurement of the contact stiffness (*26,27*). We have estimated the contact stiffness, knowing the tip radius, the elastic modulus of the tip and the substrate. The lateral siffness of the cantilever leads to a slope that would be much steeper than the one observed in the local regime, indicating that it would be observable for much smaller displacement or velocity that the ones probed by our measurement.

We observe a transition regime between pure rocking and pure sliding. This intermediate transition regime suggests that the contact has not been steadily established yet. The loss tangent, which is a measure of the dissipation, is the only information that allows us to distinguish between the two regimes and identify when the steady state is reached. When defining the friction coefficient by the ratio of the friction force and the normal force, the curves that belong to different loads collapse into a single curve. This behavior has been recently observed in a theoritical spring model which mimics an SFA geometry (*10,11*). Although a friction coefficient can be defined for the whole range of displacements and velocities, we only refer to the range for which the friction coefficient fulfills Amontons' law, i.e. it is constant and independent of the velocity.
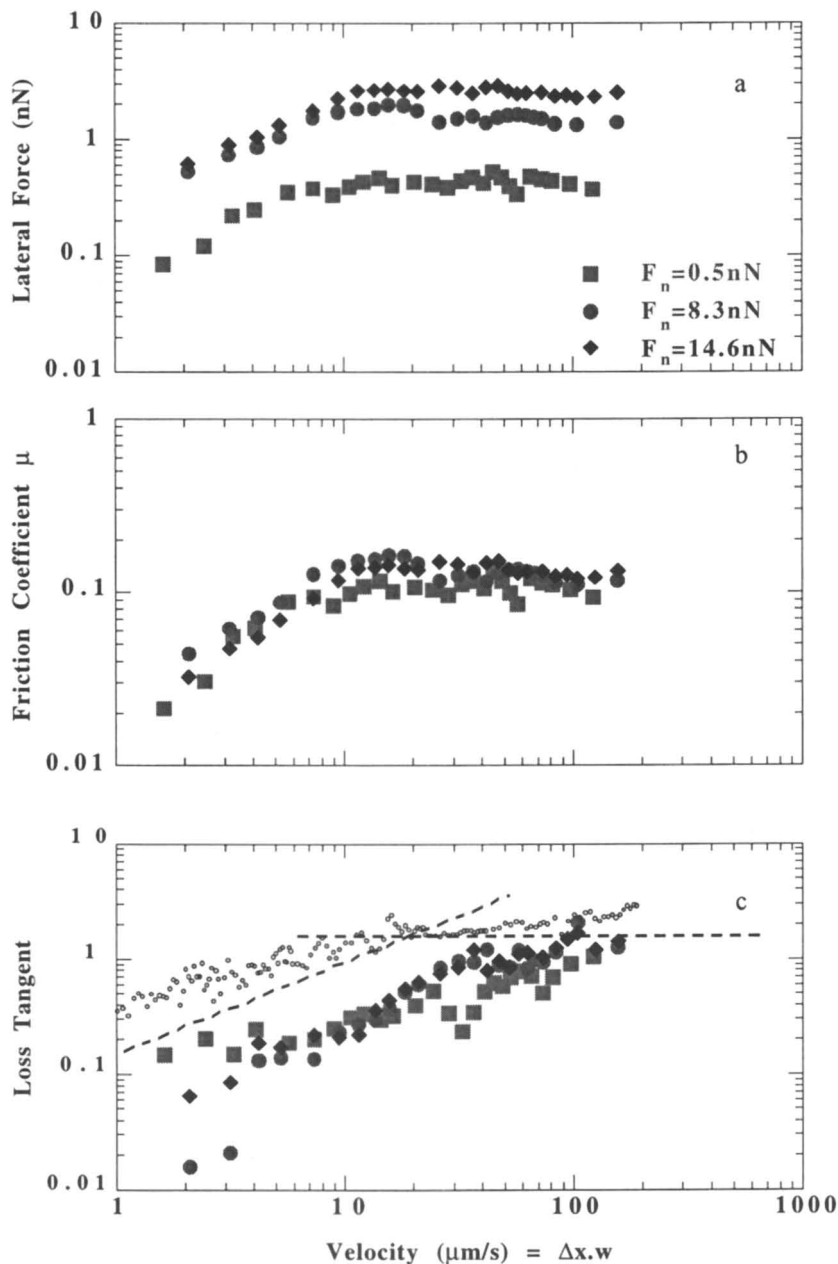
Figure 5: Velocity dependence of the friction force(a), of the friction coefficient (b), and of the loss tangent (c) for an increasing normal load at the SiO₂/ SiO₂ sliding contact. In (c) shown are also loss tangent results under a different load condition (small circles). The lines are a guide to the eye.

Figure 6 illustrates the load dependance of the friction force in the steady state sliding regime when the tip describes an oscillatory motion at constant velocity . The friction coefficient defined by the slope is in agreement the friction coefficient obtained from figure 5.
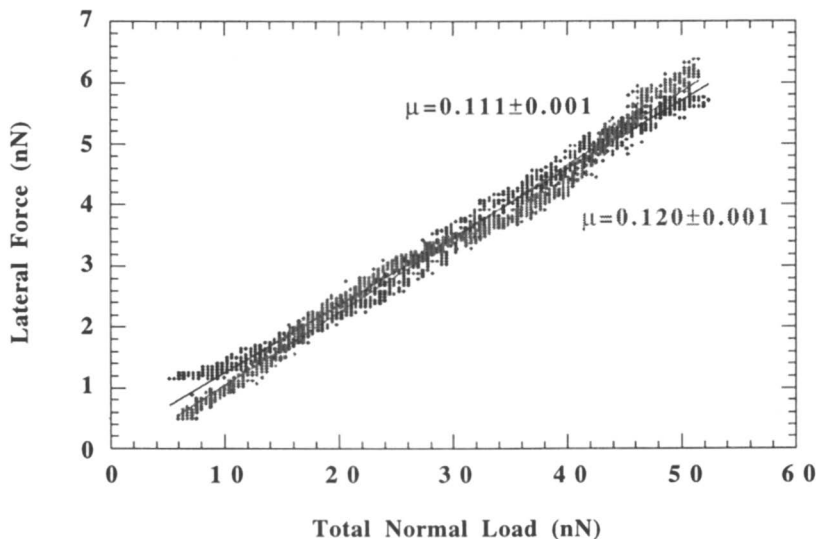
Figure 6: Load dependence of the friction force force at constant sliding velocity (● 33.4µm/s, ■ 133.8µm/s)

We have investigated the relationship between tribological and rheological measurements of friction coefficients. We have demonstrated that the friction coefficients, obtained using the AFM, are the same for different drives; namely constant velocity vs. harmonic drive. The meaning of the rheological velocity $\Delta x\ \omega$ has been shown to exist for velocities higher than a transition velocity. An interesting collapse of the friction coefficient results, as a function of velocity, has been observed as predicted theoretically.

The two tribological and rheological methods resolve the friction over a large spatial scale length (10µm-0.01µm). They both provide the same information in terms of friction force or friction coefficient. They can be used in conjunction to establish the homogeneity or the inhomogeneity of the friction over these length scales. However, we have shown that the friction force measurement is not sufficient to determine whether or not the system is sliding. The loss tangent, measured using the rheological or modulation method, enables us to distinguish between an elastic and a dissipative response of the contact to a strain.

Literature Cited

1. Yoshizawa H. and Israelachvili J., *J. Chem. Phys.* **1993**, 97, 11300.
2. Hu H.W. , Carson G.A and Granick S., *Phys. Rev. Lett.* **1991**, 66, 2758.

3. Meyer E., Overney R., Brodbeck D., Howald L., Gutmannsbauer W. and Guntherodt H.J., *Phys. Rev. Lett.* **1992**, 69, 1777.
4 Overney R.M., Meyer E., Frommer J., Brodbeck D, Luthi R., Howald L., Guntherodt H.J., Fujihara M., Takano H. and Gotoh Y., *Nature* **1992**, 359, 133.
5 Frisbie C.D., Rozsnyai L.F., Noy A., Wrighton M.S. and Lieber C.M., *Science* **1994**, 265, 2071.
6. Yoshisawa H., Chen L.Y. and Israelachvili J., *J. Chem. Phys.* **1993**, 97, 4128.
7. Peachey J, Van Alsten J. and Granick S., *Rev. Sci. Instrum.* **1991**, 62, 463.
8 Van Alsten J. and Granick S., *Langmuir* **1990**, 6, 876.
9 . Ferry J.D., *Viscoelastic properties of polymers*, 3rd Ed., John Wiley & Sons, **1980**.
10. Rozman M.G., Urbakh M., Klafter J. and Elmer F.J., *J. Phys. Chem.* **1998**, 102, 7924.
11. Zalov V., Urbakh M. and Klafter J., *Phys. Rev. Lett.* **1998**, 81, 1227.
12. Mate C.M., McClelland G.M., Erlandsson R. and Chiang S., *Phys. Rev. Lett.* **1987**, 59, 1942.
13 Meyer G., Amer N.M. , *Appl. Phys. Lett.* **1990**, 57, 2089.
14 Marti O., Colchero J., Mlynek J., *Nanotechnololy* **1990**, 1, 141.
15 Erlandsson R., McClelland G.M., Mate C.M. and Chiang S., *J. Vac. Technol.A* **1988**, 6, 266.
16 Bouhacina T., Aimé J.P., Gauthier S., Michel D. and V. Heroguez, *Phys. Rev. B* **1997**, 56, 7694.
17. Salmeron M., Neubauer G, Folch A., Tomitori M., Ogletree D.F. and Sautet P., *Langmuir* **1993**, 9, 3600.
18 Overney R.M., Takano H. and Fujihira M., *Europhys.Lett.* **1994**, 26, 443.
19. Schwarz U.D., Köster P., Weisendanger R., *Rev. Sci. Instrum.* **1996**, 67, 2560.
20. Pasquier V., Drake J.M , to be published.
21. Vigil G., Xu Z., Steinberg S., and Israelachvili J., *J. Coll. & Interf. Sci.* **1994**, 165, 367.
22. Maivald P.; Butt H.J.; Gould S.A., Prater C.B, Drake B., Gurley J.A., Ellings V.B. and Hansma P.K., *Nanotechnology* **1991**, 2, 103.
23 Radmacher M, Tillmann R.W., Fritz M. and Gaub H.E. , *Science* **1992**, 257, 1900.
24 Overney R.M., Takano H. and M. Fujihira M., *Europhys.Lett.* **1994**, 26, 443.
25. Colchero J., Luna M. and Baro A.M., *Appl. Phys. Lett.* **1996**, 68, 2896.
26. Lantz M.A., O'Shea S.J., Welland M.E., and Johnson K.L., *Phys. Rev. B* **1997**, 55, 10776.
27 . Carpick R.W., Ogletree D.F., and Salmeron M., *Appl. Phys. Lett.* **1997**, 70, 1548.
28 . Pasquier V. and Drake J.M., *Mat. Res. Soc. Symp. Proc.* **1999**, 543, 51.

Chapter 10

Friction and Flow with Slip at Fluid–Solid Interfaces

L. Léger, H. Hervet, and R. Pit

Laboratoire de Physique des Fluides Organisés, URA CNRS 792, 11 Place Marcelin Berthelot, 75231 Paris Cedex 05, France

The flow velocity of a fluid at submicrometric distances from a solid wall is investigated using a novel optical technique based on fluorescence recovery after photobleaching and evanescent wave induced fluorescence. For a polymer melt, three different friction regimes, all characterized by slip at the wall, are identified and modeled at the molecular level. For a simple fluid (alkane), slip at the wall is put into evidence and factors influencing the extend of slip are identified.

Introduction

To know the exact boundary condition for the flow velocity at a solid – fluid interface is of special importance in a number of practical applications such as lubrication, surface coating, or polymer extrusion for example. In such practical situations the fluid is often complex (oil base plus additives or emulsion for lubrication, high molecular weight entangled polymers for the two other examples). It is then not obvious that the usual assumption of a zero fluid velocity at the wall (no slip at the wall) is indeed valid. The situation is schematically presented in figure 1: the extrapolation length of the velocity profile to zero, b, is usually admitted to be comparable to a few molecular sizes, either below the surface (positive b) or above (negative b) depending on the fact that the fluid – solid interactions are weaker or stronger than the interactions within the liquid, in any case very small compared to the dimensions of the sample (figure 1a). Indeed, no specific surface effects are visible in most macroscopic hydrodynamics experiments with simple fluids. The no slip at the wall hypothesis however does not rely on strong theoretical basis and it is natural to wonder about its validity, especially in the case of flow of simple fluids at submicrometer scales (thin slits or capillaries), or of complex fluids, two situations in which surface effects may lead to large slip length (figure 1b).

154
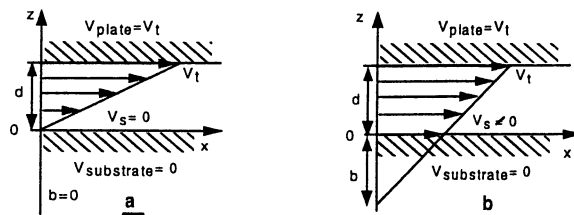
Figure 1: Schematic representation of a no slip (1a) or a slip (1b) boundary condition for the fluid velocity at the solid wall.

In fact, b is directly related to the friction coefficient between the fluid and the surface. This can be easily seen by evaluating the friction force transmitted to the solid by the sheared fluid, either as the product of the velocity at the interface, V_s, by friction coefficient between the solid and the fluid, k, or as the product of the fluid viscosity by the velocity gradient at the surface, i.e. $F_f = kV_s = \eta \partial V/\partial z\big|_{z=0} = \eta\, V_s /b$ One sees that the friction coefficient k is inversely proportional to the slip length b. Any direct experimental information on the local velocity profile close to the solid wall can thus be translated in terms of surface friction if the viscosity close to the surface is known. On the other hand, if the local viscosity differs from the bulk one, the surface friction can only be determined by measuring both the velocity at the interface and the friction force.

The above remarks point out the interest of direct measurements of the boundary condition (BC) for the fluid velocity at a fluid solid interface. To obtain reliable information on the flow velocity BC of a fluid, with a spatial resolution from the wall down to molecular sizes, is a particularly difficult challenge. Conventional velocimetry techniques (even laser velocimetry) are far from such a resolution. We have developed a near field laser velocimetry technique which allows to increase significantly the spatial resolution compared to more conventional velocimetry techniques. This technique has been used to characterize the friction between a polymer melt and a solid wall and to understand how surface modifications weakening the interactions between a solid and a given simple fluid affected the fluid – wall friction.

We review these results in the present paper. In a first part we briefly introduce the principle of the technique, and discuss its main limitations. In a second part we present the results for a polymer melt sheared along a solid wall on which polymer chains are end grafted. These end grafted chains deeply affect the fluid – wall friction, leading to three distinct friction regimes as the shear rate is progressively increased. We show that this complex friction behavior is due to a progressive disentanglement between the surface attached chains and the bulk fluid. In the third part the results obtained for a simple fluid (hexadecane) sheared along either oleophilic or oleophobic surfaces are presented

Principle of the Near Field Laser Velocimetry technique

Up to recently, direct determinations of flow velocity close to a solid wall were scarce and generally obtained using small spheres as flow tracers, i.e. with a spatial resolution of the order of the diameter of the spheres, not better than 150 nm (*1-3*). To investigate the fluid velocity BC at the solid interface without perturbing the flow, tracers of molecular dimensions are needed. It is also essential to reduce the dimension of the observation volume in the direction normal to the interface, ideally down to a molecular size. We have developed an experiment aiming to fulfill these two requirements, first for polymer fluids (*4,5*), and second for simple fluids (*6*). In both cases, the condition on the size of the tracers is matched by the use of fluorescent molecules chosen so that they easily photobleach under intense illumination. The photobleached probes produced by a local intense illumination of the sample (writing period of the experiment) act as flow tracers. The way they are transported by the flow is followed by monitoring the fluorescence intensity excited with an attenuated illumination so that no further photobleaching is produced during the reading period of the experiment. The confinement of the investigated volume close to the solid – fluid interface is achieved by the use of optical evanescent waves for reading the fluorescence and eventually also to produce the photobleached probes. This technique, based on fluorescence recovery after photobleaching and evanescent wave induced fluorescence, has been named Near Field Laser Velocimetry (NFVL).

Case of Polymer Fluids:

A first experimental set up, devised to investigate polymer melts flowing on modified silica surfaces, is schematically presented in figure 2.
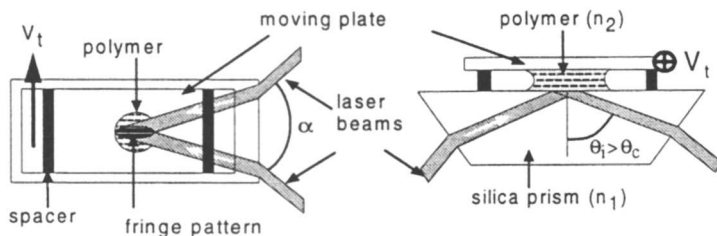
Figure 2: Schematics of the NFLV experimental set up for polymer melts

A few polymer chains chemically end labeled with a fluorescent probe (NBD) are mixed to the polymer melt (*4*). The sample is a drop of this mixture (optical index, n_2), squeezed between a moving plate and the upper surface of a silica prism (optical index, $n_1 > n_2$) which form the walls of a plane Couette cell. Two laser beams (wavelength in vacuum λ_0) impinge on the prism surface at an incidence angle θ_i greater than the critical angle for total internal reflection, $\theta_c = \sin^{-1} (n_2/n_1)$. They both

form an evanescent wave in the polymer fluid, with a penetration depth $\Lambda = \lambda_0 \Big/ 4\pi \sqrt{n_1^2 \sin^2 \theta_i - n_2^2}$. With $\lambda_0 = 476$ nm, $n_1 = 1.46$ $n_2 = 1.41$ and $\theta_i = 90°$, one gets $\Lambda = 100$ nm. This is comparable to the radius of a high molecular weight polymer molecule (but much larger than the size of the molecule of a simple liquid). The two beams cross at the prism surface, and interfere within the evanescent wave, with a fringe spacing $i = \lambda_0/2 \sin(\alpha/2)$ (α is the angle between the two beams).

The experimental sequence is the following:

i)   a laser pulse with a high intensity is shone for about 100 ms and bleaches some of the fluorescent probes located in the bright fringes. A sinusoidal modulation of the concentration of fluorescent molecules is thus created (wavelength i) and acts as a pattern printed in the fluid.

ii)   then, simultaneously, the shear is turned on (by translating the upper plate at a velocity V_t), the laser beams are attenuated by 10^4 and the fluorescence intensity is recorded as a function of time.

Due to chain entanglements the self diffusion coefficient of the labeled macromolecules is very small ($<10^{-13}$ m²/s), and the transport of the photobleached tracers takes place predominantly through convection. If there is no slip at the polymer - prism interface, the fluorescence intensity decreases steadily with time as the concentration pattern is progressively tilted by the shear. If slip occurs, the concentration pattern is translated (and tilted) in front of the interference fringes creating a damped periodic oscillation of the fluorescence intensity with a period $T = i/V_s$, if V_s is the average slip velocity within the distance Λ from the prism surface. Measuring T and i yields directly V_s.

Case of Simple Fluids:

In simple fluids the diffusion is much faster and prevents using the same experimental the set up. In order to identify the experimental limits, let us estimate the diffusion times associated with the different characteristic length scales in the above described experiment. The shortest length is the penetration depth of the evanescent wave, Λ. Assuming a diffusion time over Λ, $\tau_\Lambda = \Lambda^2/2D$, with D the diffusion coefficient in the fluid, we get $\tau_\Lambda = 50$ µs for $\Lambda = 100$ nm and $D = 10^{-10}$ m²/s. If evanescent writing beams are used, the bleached zone will be blurred out within 50 µs due to diffusion. This precludes the use of evanescent writing beams. The second length scale is the fringe spacing, i. The corresponding diffusion time is $\tau_i = i^2/4\pi^2 D$. For $i = 4$ µm and $D = 10^{-10}$ m²/s, $\tau_i = 4$ ms. This is far too short to allow for measuring T. A modified experimental set up, overcoming these limitations, is schematically presented in figure 3.
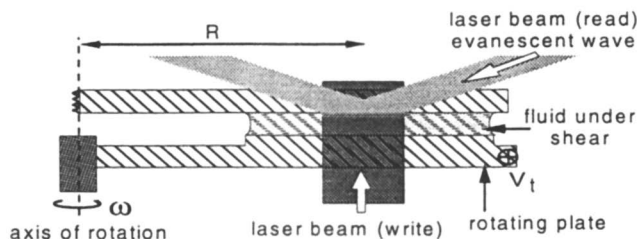
Figure 3: Schematics of the NFLV experimental set up for simple fluids

Single beams are used (instead of two interfering beams) for both the writing and reading steps. The bleaching beam goes through the sample, normal to the solid surfaces to minimize the effect of diffusion normal to the surface. During the writing step a bleached line is printed through the sample. A new length scale, the diameter σ of this bleached line, comparable to the diameter of the bleaching beam comes into play. The diffusion time over σ is $\tau_\sigma \approx \sigma^2/D$; with $\sigma = 30$ μm and $D = 10^{-10}$ m^2/s, one gets τ_σ of the order of a few seconds, long enough to follow how the bleached line is convected by the flow. To confine the information to the vicinity of the surface, an evanescent reading beam is used which hits the surface exactly at the location of the bleaching beam. High enough shear rates are necessary so that convection is not a weak correction in front of diffusion. Working at high shear rates implies a high speed for the moving plate, achieved with a motor driven disk rotating at the angular frequency ω. The shear cannot be started after the bleaching pulse, because of the transient regime of the motor ($\approx$.5s). During this time lag in which the shear rate is not stationary, diffusion would wipe out the initial bleached area significantly decreasing the signal to noise ratio. Thus the moving plate permanently rotates. The velocity at the distance R from the rotation axis is $V_t = \omega R$. Shear rates up to 10^4 s^{-1} can be reached.

The sequence of the experiment is as follows:

i)   The rotation of the moving plate is turned on;

ii)   The evanescent low intensity reading beam is switched on and remains on permanently. The initial fluorescence intensity is recorded,

iii)   The intense writing beam is shone during typically 100 ms;

iv)   The fluorescence intensity is again recorded versus time.

The kinetics at which the fluorescence intensity recovers after the bleaching pulse contains the information on the flow velocity close to the solid wall. If slip occurs the relaxation time of the fluorescence intensity is shorter than if there is no slip at the wall. The determination of an average velocity close to the wall is not however as straightforward as for polymers: both diffusion and convection contribute to the kinetics of the fluorescence recovery curves (FRAP curves) and unraveling the two contributions is delicate. We detail below the procedure used to analyze the data.

Analysis of FRAP Curves for Simple Liquids:

Since the information on the velocity close to the solid wall is contained in the recovery dynamics and not in the absolute values of the fluorescence intensities, the intensity axis is scaled such that the recovery curves range from I(%) = 0 to I(%) = 100. The flow pattern of photobleached probes is strongly affected by the fast diffusion: during the fluorescence recovery time ($\tau_c \sim 50$ ms) a probe travels by diffusion over a distance Δz of the order of 3 µm (assuming $\Delta z = (2Dt)^{1/2}$ and $D = 10^{-10} m^2/s$). Thus the fluorescence recovery is characteristic of an average of all velocities within Δz from the wall, $\overline{v}$. For a shear rate $\dot{\gamma}$ and a slip length b,

$$\overline{v} = \frac{1}{\Delta z} \int_0^{\Delta z} (\dot{\gamma} + b)z.dz = \frac{\dot{\gamma}}{2}(\Delta z + 2b).$$ As shown in figure 4a, the same $\overline{v}$ can be

obtained with a no slip BC (b = 0) replacing the imposed shear rate $\dot{\gamma}$ by the effective shear rate $\dot{\gamma}_b = 2\overline{v}/\Delta z$. Curves obtained at different shear rates with or without slip should thus all appear alike. This is indeed observed experimentally (see Figure 6) and by a two dimensional simulation of the experiment (with or without slip – Figure 4b).
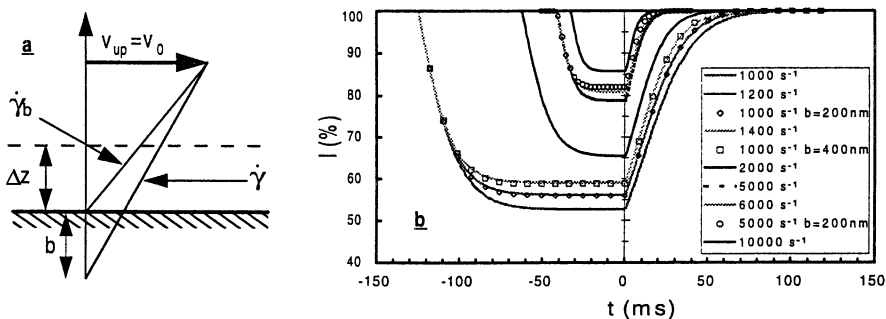
Figure 4: a) Schematic representation of the correspondence between the applied and the effective shear rate; b) Equivalence between wall slip and shear rate for simulated FRAP curves of simple fluids.

The fluorescence recovery time, τ_c, can be estimated as the time necessary for a probe to cross the reading beam at the average velocity $\overline{v}$, i.e. $\tau_c = 2\sigma/\overline{v} = 4\sigma/\dot{\gamma}_b\Delta z$ and also as the diffusion time over Δz, $\tau_c = \Delta z^2/2D$. These two relations yield $\tau_c = 2(\sigma^2/D)^{1/3}\dot{\gamma}_b^{-2/3}$. All curves can therefore be scaled in time to a single universal curve by the transformation $t \rightarrow t^* = t \times \dot{\gamma}_b^{2/3}$. This scaling of the time axis is indeed well observed experimentally and gives Δz values and an exponent in the power law

dependence on the effective shear rate in good quantitative agreement with the values expected from the above diffusion argument.

Experimental curves are therefore analyzed as follows:

i) a reference surface for which the no-slip BC is assumed to hold is defined. On such a reference surface the effective and the imposed shear rates are the same.

ii) curves from different surfaces are compared to the reference curves and the time axis is scaled adjusting $\dot{\gamma}_b$ so that all curves fall on the universal curve.

If $\dot{\gamma}_b$ is higher than the imposed shear rate, the BC can be described using a slip BC with a slip length $b = \Delta z(\dot{\gamma}_b - \dot{\gamma})/2\dot{\gamma}$

We must point out that, contrary to the case of polymer fluids for which the slip velocity and the slip length were directly deduced from the experiment, the values of the slip length for simple fluids rely on a correct estimate of Δz. All b values given below have been obtained assuming that Δz is the diffusion length during the recovery time of the fluorescence intensity. They represent a reasonable order of magnitude of b but cannot be taken as absolute values (numerical prefactors may appear in the estimation of the averaged velocity $\bar{v}$).

It is worthwhile to notice that, due to the fast diffusion, even if the reading beam is evanescent, the measured velocities are not averaged over Λ, but over the much larger distance from the wall, Δz, (a few micrometers for hexadecane). The fluorescence recovery curves remain anyhow sensitive to the BC of the fluid velocity.

Friction and slip at polymer melt – solid interfaces

General Frame:

The flow of highly entangled polymer melts on solid surfaces is both of practical and fundamental importance. For example, in extrusion processes at constant speed, the onset of flow instabilities (melt fracture, "sharkskin" and periodic deformation of the extrudate) has been suspected to be linked with changes of the friction at the wall and possibly to wall-slip (for extensive references see the review paper (7), and (2), (8)). In 1979 de Gennes (9) suggested that a high molecular weight polymer sheared along an ideal surface (i.e. a smooth flat surface with no preferential interactions with the polymer) should always exhibit strong slip at the wall. The resulting extrapolation length of the velocity profile to zero should be $b = a \eta_b/\eta_0$, where η_b is the bulk viscosity of the polymer melt, η_0 the viscosity of the fluid of monomers, and a the monomer size. Values of b of the order of mm should thus show up for long enough polymer chains. Such large slip should have been easily observed experimentally. In fact the experimental situation long remained controversial, some experiments exhibiting wall slip and some none. This reflects the fact that practical surfaces are not ideal ones and usually attract polymer molecules. It has been suggested that a few chains adsorbed onto the surface should enormously decrease wall slip (10). We summarize here the main results of a NFLV investigation of the velocity BC for polymer melts flowing on smooth surfaces.

NVLF Investigation of Polymer Melt – Solid Friction:

The polymer under investigation was polydimethylsiloxane (PDMS, 960 kg/mol > M_w >300 kg/mol; polydispersity index, M_w/M_n, ≤1.3) at room temperature flowing along silica surfaces bearing either adsorbed PDMS chains (*11-13*) or end grafted PDMS chains (*7, 14*). Controlled chemistry at the silica – PDMS interface allowed to vary independently the molecular weights and surface densities of the surface anchored PDMS chains.

The important general result is that when the polymer melt is sheared against a surface on which polymer chains are strongly attached three different friction regimes are observed when increasing the shear rate, provided the surface chains are able to entangle with the bulk polymer. This non trivial friction behavior is illustrated in figure 5 a,b,c and d:
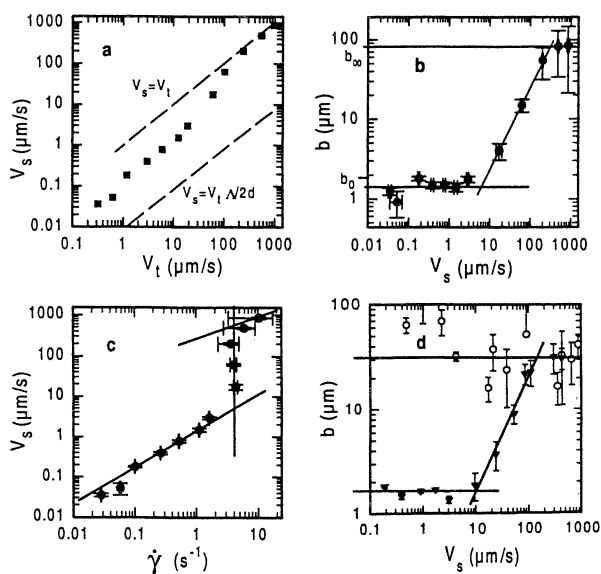
Figure 5: *Typical results for the slip velocity and the slip length, for a PDMS melt (molecular weight M_w = 970 kg/mol (M_w/M_n = 1 14)), flowing against a silica surface covered with end grafted PDMS chains. a), b) c) grafted surface chains with M_w = 96 kg/mol (M_w/M_n = 1.1) and surface density, Σ = 0.00025. (the a-dimensional surface density Σ is related to the average number of grafted chains per unit surface, v, through $v = \Sigma/a^2$, with a the size of a monomer, a = 0.5 nm for PDMS).*
d) Slip length as a function of the slip velocity for end grafted chains with M_w = 5 kg/mol and surface density Σ = 0.12(open symbols) or end grafted chains with M_w = 96 kg/mol and surface density Σ = 0.0055 (filled symbols). The average molecular weight between entanglements is M_e=8 kg/mol for PDMS.

Slip is always observed: the measured velocity, which is an average of the velocities within Λ from the surface, is larger than what would be obtained with a no slip BC, shown as the lower dashed line in figure 5a. At low top plate velocities the corresponding slip length is small (b ~ 1 μm) and constant (figure 5b), meaning that V_s is proportional to V_t. At intermediate V_t values, V_s increases more rapidly than linearly with V_t to finally reach a value close to V_t (quasi plug flow; $V_s = V_t$ is the upper dashed line in figure 5a), at high shear rates. In the intermediate regime, b appears proportional to V_s (see the log – log plot of figure 5b). As b is inversely proportional to the friction coefficient, this is a non linear friction regime, with a friction coefficient inversely proportional to the interfacial velocity. In the high shear rate regime V_s becomes again proportional to V_t and b is constant (linear friction regime), of the order of 100 μm, implying a friction coefficient two orders of magnitude smaller than in the initial low shear rate regime. The striking feature is that the shear rate experienced by the polymer, $\dot{\gamma} = (V_t - V_s)/d$ (d is the cell thickness) remains constant all through the intermediate regime, a fact which has been confirmed by direct measurements of the shear stress transmitted by the polymer fluid to the prism.

Molecular Mechanism of Polymer – Wall Friction:

de Gennes and coworkers (*15-17*) have developed a molecular model describing how a weak density of polymer molecules end grafted on the solid surface (surface chains independent of each other) and entangled with the bulk polymer affect the BC for the velocity at the polymer – solid interface. Due to entanglements, the surface chains act as obstacles to the flow of the bulk chains and produce a large friction between the melt and the surface at low shear rates, suppressing the huge slip at the wall expected for ideal surfaces. The surface chains are deformed by that large friction force, and develop an elastic restoring force. In stationary state, both elastic and friction forces balance each other. Increasing the shear rate increases the friction force and the elongation of the surface chains. One thus departs from the initial high friction regime when the elongation of the surface chains is large enough so that they start to disentangle from the melt. A distinct friction regime, called the marginal regime, is then encountered. The surface chains keep the limiting elongation corresponding to the limit of disentanglement for a large range of slip velocities (i.e. a range of imposed V_t), because if the surface chains were elongated more, they would disentangle from the melt, the friction force would strongly decrease and would no longer balance the elastic restoring force. The surface chains would then re-entangle. In the marginal regime the shear force is thus fixed and independent of the slip velocity, implying a friction coefficient inversely proportional to V_s. The marginal regime ends when the frequency at which the surface chains are excited by the flow (entangling and disentangling from the melt) becomes larger than their relaxation frequency (*16*). The surface chains then get fully disentangled, the melt dynamically de-couples from the surface, and the friction becomes constant and low, with a slip length b_{∞} independent of V_s and comparable to what would be obtained on an ideal surface.

This model quantitatively agrees with all the NFLV results obtained with PDMS at weak densities of surface chains. In all three friction regimes the shear force per surface chain (which is directly measured in the experiment) is always much smaller

than the force necessary to break a hydrogen or a covalent bond (*18*). The observed transition from low to high slip at the wall is thus not due to tearing out of the surface chains. For PDMS melts with lower molecular weights mixed with glass beads (*19*) a slip transition has been observed and attributed to de-sorption of the PDMS chains from the glass surface. This may not be contradictory. The low to high slip transition is in fact the signature of a dynamic de-coupling between the surface and the bulk polymer. Depending on the physico-chemical conditions, this de-coupling may take place through different modes: tearing off of the surface chains under the shear stress, if the bonding force is weak, or elongation and disentanglement of surface and bulk chains when the bonding force is large. Only the disentanglement mechanism is associated with the existence of a marginal regime extending over several decades in slip velocities. In figure 5d comparative measurements of the slip length for the same PDMS melt in contact with a surface layer able to entangle with the melt (filled symbols) or not able to entangle (open symbols) are shown. Clearly, the marginal regime only exists when the surface chains can entangle with the bulk polymer.

Experiments to characterize how this disentanglement mechanism affects the interfacial friction in the case of crosslinked elastomers are presently underway and should provide a link between fluid and solid friction in the case of soft polymers.

Case of simple fluids

General Frame:

In the case of Newtonian fluids, macroscopic experiments have not proven the breakdown of the no-slip boundary condition. On microscopic scales different techniques, such as surface force apparatus (SFA) (*20*), quartz crystal microbalance (QCM) (*21,22*) or flow through very thin capillaries (*23*) and also molecular dynamics simulations (MD) (*24-27*) have suggested the possibility of slip at the wall for simple liquids. Very different slip length from molecular to macroscopic sizes have been reported. It has also been suggested that roughness or chemical heterogeneity could drastically hinder slip (*28,29*). This would explain why large slip lengths have never been observed in macroscopic flow experiments. A discussion of these results can be found in (*6*). The question of a possible slip BC for simple fluids in contact with a smooth non attracting wall appears still open. We have therefore undertaken experiments using the NFVL technique to investigate the BC for the flow velocity of hexadecane in contact with surfaces having different wetting properties. We summarize below how these surfaces are produced, and the main results of these investigations.

Material:

Hexadecane was studied as a model non-polar lubricant with a relatively high surface energy (γ_L = 27.4 mJ/m^2 at 20°C). The fluorescent probe was NBD dihexadecylamine at 5 ppm. The surface under study was a disk of sapphire (α-Al$_2$O$_3$ {001}) with a rms roughness of 0.4 nm as measured by x-ray reflectivity. Sapphire has a high refractive index and the surface can be chemically modified. Three surface

treatments have been used : (a) the surface was cleaned by UV/Ozone procedure (*30*), yielding a wetting surface for hexadecane ($\gamma_s > 72$ mJ/m^2); (b) the surface was modified by grafting a monolayer of octadecyltrichlorosilane (OTS) following a procedure similar to that used for silica (*31-33*), yielding an oleophobic surface ($\gamma_s = 21$ mJ/m^2); (c) the cleaned surface was put in contact with a 1% solution of stearic acid (SA; n-octadecanoic acid) in hexadecane and an adsorbed SA monolayer was formed *in situ* in the flow cell.

Results:

We first assume that the no–slip BC holds at the hexadecane – bare sapphire interface, (high energy surface) so that the fluorescence recovery curves obtained with surface (a) are taken as reference curves.

Hexadecane on OTS:

Figure 6a compares the FRAP curves (scaled intensities) for hexadecane flowing over a wetting sapphire surface (black symbols) and over a grafted OTS monolayer (open symbols) at different shear rates.
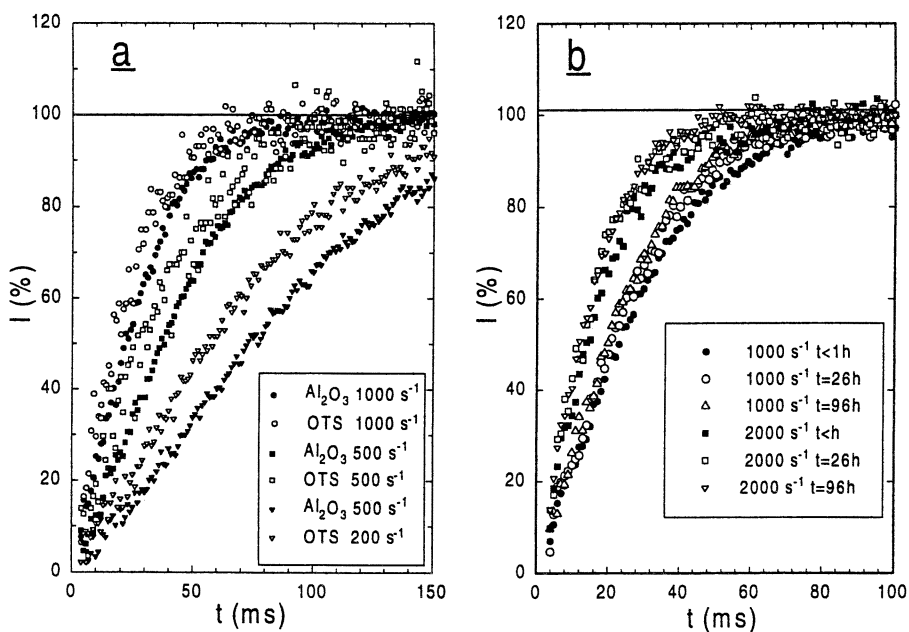
Figure 6: a) *Fluorescence recovery after photobleaching for hexadecane flowing aver a sapphire surface (filled symbols) and over a dense OTS monolayer (open symbols).* b) *Evolution of the FRAP curves with incubation time t for a 1% solution of stearic acid in hexadecane. t = 0 means less than one hour.*

Unquestionably, the recovery is faster on the OTS surface, indicating a slip BC, as compared to the wetting sapphire surface. Scaling the time, an effective shear rate 30% ($\pm$ 10%) higher than the imposed shear rate at 1000 s^{-1} is obtained on this OTS surface. The corresponding slip length is b = 300 nm ($\pm$ 100 nm). Slip however appears to be very sensitive to the quality of the grafted OTS layer. A subsequent experiment performed on a second OTS layer gave a different result. Wetting experiments showed that the surface energy of this second layer was close to 21 mJ/m^2 (similar to that of the first layer) but high contact angle hysteresis with reference liquids indicated that the monolayer was not as complete as the first one. Analysis of FRAP curves showed that the fluorescence recovery on this second OTS surface appeared slower than on the bare sapphire surface, with an effective shear rate 5% ($\pm$ 5%) below the imposed one, suggesting a slightly larger friction. This indicates that wall slip in simple liquids is very sensitive to the exact structure of the surface and that even a wetting surface may not be the correct reference for no-slip.

Flow of hexadecane + 1% stearic acid on a bare sapphire surface:

Passive adsorption of stearic acid, a classic lubricant additive, from an alkane solution on metal oxides has been studied by several authors (*34,35*). Over a period of 1 minute to several days (probably depending on the reactivity of the surface) stearic acid self-assembles on the surface to form a dense monolayer. This is an alternative method to form a methylated surface. Figure 6b shows FRAP curves obtained at different incubation times between the SA – hexadecane solution and the sapphire surface. Unlike the previous experiment the system was not dismantled and readjusted between different measurements, eliminating errors due to alignment. The fluorescence recovery appears faster after a few days of contact compared to short times of incubation, revealing that hexadecane slips on the adsorbed stearic acid layer formed *in situ*.

First, curves obtained at short incubation time ("t = 0") can be compared to the reference one (pure hexadecane on a bare sapphire surface). Experiments at 1000 and 2000 s^{-1} show an effective shear rate about 10% *lower* than the applied one. Since the uncertainty on the imposed shear rate is at most 6%, this suggests that the friction is higher on this surface than on the bare sapphire surface, similarly to what has been observed on the incomplete OTS layer. Again this indicates that hexadecane may actually slip on the wetting sapphire surface and the choice of the bare sapphire as a reference surface is questionable. We analyzed the curves at long incubation times using as references either data on a wetting sapphire surface or at short incubation times. Regardless the no-slip reference surface, at 1000 and 2000 s^{-1}, the effective shear rate increased by 15 to 20% during the first 26 hours of incubation and by another 5 to 10% between 26 and 96 hours of contact. At 1000 s^{-1}, the effective shear rate no longer increased between 96 and 116 hours. Overall, the slip length increased by 250 nm ($\pm$ 50 nm) over the time of the experiment. This is consistent with the slip length found on the dense OTS surface (b = 300 nm). The BC seemed to reach a stable situation after two or three days.

Discussion:

The main result of these experiments is that a simple liquid can slip at the wall at high but not extreme shear rates. Directly probing the velocity field near the surface, it was found that the flow of hexadecane corresponds to a slip BC, with a slip length of of 300 nm on a dense methylated surface. Results on incomplete OTS or stearic acid layers showed that the surface energy is not the only parameter governing liquid solid friction: the surface roughness (either physical or chemical) at molecular scale is also an important parameter. Roughness allows an effective momentum transfer between the molecules in contact with the surface and the bulk fluid, tending to impose a no-slip BC. It was also observed that the correct BC on a wetting sapphire surface was a slip BC with a slip length of at least 100 nm (if there is no-slip on the incomplete stearic acid layer). Finally, although the amount of adsorbed stearic acid has not been directly correlated with the slip BCs, the observed kinetics is not inconsistent with reported adsorption kinetics.

Additional experiments on other simple fluids are presently underway to test the generality of the above results.

Conclusion:

We have summarized the main results of direct investigations of the boundary condition for the fluid velocity at a solid wall based on a novel velocimetry technique (NFVL). NFVL gives access to an average of the fluid velocities over distances from the solid surface governed either by the penetration depth of the evanescent reading beam, in high viscosity fluids, or by the diffusion length during the experimental time in the case of low viscosity fluids. These two different averages are indeed sensitive to the boundary condition of the fluid velocity at the solid wall. For a polymer melt in contact with a solid covered by surface attached polymer chains, it has been shown that slip at the wall was always the rule. The different friction regimes observed depending on the shear rate have been attributed to a progressive de-coupling between the surface and the fluid through disentanglement between the bulk and surface chains. A simple fluid, hexadecane, flowing along different surfaces, has been investigated with a modified set up. Experiments have clearly put into evidence that a simple fluid can exhibit slip at the wall. Both the strength of the fluid - solid interactions and the surface roughness (either topological or chemical) govern the extend of wall slip. Additional experiments are needed to fully characterize the mechanisms of this dynamic de-coupling. The present results may have important implications in lubrication for example.

References:

1   Maxwell, B.; Galt, J. C. *J. of Polym. Sc.* **1962**, 62, S50-S53.
2   Mhetar, V.; Archer, L. A. *Macromol.* **1998**, 31, 6639-6649.
3   Atwood, B. T.; Scholwater, W. R. *Rheol. Acta* **1989**, 28, 134.
4   Migler, K. B.; Hervet, H.; Léger, L. *Phys. Rev. Lett.* **1993**, 70, 287.

5   Léger, L.; Hervet, H.; Marciano, Y.; Deruelle, M.; Massey, G. *Isr. J. Chem.* **1995,** 35, 65-74.

6   Pit, R.; Hervet, H.; Léger, L. *Tribo. Lett.* **1999,** to be published.

7   Léger, L.; Raphaël, E.; Hervet, H. *Adv. Polym. Sci.* **1999,** 138, 185-225.

8   Drda, P. P.; Wang, S.-Q. *Phys. Rev. Lett.* **1995,** 75, 2698-2701.

9   De Gennes, P. G. *C. R. Acad. Sci. Paris* **1979,** t. 288, 219-220.

10 Brochard-Wyart, F.; De Gennes, P. G.; Pincus, P. *C. R. Acad. Sci. Paris* **1992,** t. 314, 873-878.

11 Massey, G.; Léger, L.; Hervet, H. *Europhys. Lett.* **1998,** 43, 83-88.

12 Léger, L.; Hervet, H.; Massey, G. *Trends Polym. Sci.* **1997,** 5, .

13 Léger, L.; Hervet, H.; Massey, G.; Durliat, E. *J. Phys. : Cond. Matter* **1997,** 9, 7719-7740.

14 Durliat, E.; Hervet, H.; Léger, L. *Europhys. Lett.* **1997,** 38, 383-388.

15 Brochard-Wyart, F.; De Gennes, P. G. *Langmuir* **1992,** 8, 3033-3037.

16 Brochard-Wyart, F.; Gay, C.; De Gennes, P. G. *Macromol.* **1996,** 29, 377-382.

17 Ajdari, A.; Brochard-Wyart, F.; Gay, C.; De Gennes, P. G.; Viovy, J. L. *J. Phys. II* **1995,** 5, 491-495.

18 Durliat, E. Ph.D. Thesis, Université Paris VI, Paris, 1997.

19 Inn, Y.; Wang, S.-Q. *Phys. Rev. Lett.* **1996,** 76, 467.

20 Dhinojwala, A.; Cai, L.; Granick, S. *Langmuir* **1996,** 12, 4537-4542.

21 Krim, J.; Watts, E. T.; Digel, J. *J. Vac. Sci. Technol. A* **1990,** 8, 3417.

22 Persson, B.N.J. *Sliding Friction;* K. von Klitzing and R. Wiesendanger, Ed.; Springer-Verlag: Berlin, 1998; 462

23 Churaev, N. V.; Sobolev, V. D.; Somov, A. N. *J. Coll. Int. Sci.* **1984,** 97, 574-581.

24 Hu, Y.-Z.; Granick, S. *Tribo. Lett.* **1998,** 5, 81-88.

25 Thompson, P. A.; Troian, S. M. *Nature* **1997,** 389, 360-362.

26 Gupta, S. A.; Cochran, H. D.; Cummings, P. T. *J. Chem. Phys.* **1997,** 107, 10316-10326.

27 Barrat, J.-L.; Bocquet, L. *Phys. Rev. Lett.* **1999,** 82, 4671-4674.

28 Einzel, D.; Panzer, P.; Liu, M. *Phys. Rev. Lett.* **1990,** 64, 2269-2272.

29 Alexeyev, A. A.; Vinogradova, O. I. *Colloids and Surfaces A* **1996,** 108, 173-179.

30 Vig, J. R. in *Treatise on Clean Surfaces Technology*; K.L. Mittal, Ed.; Plenum Press: New York, 1987; p. 1.

31 Silberzan, P.; Léger, L.; Ausserré, D.; Benattar, J. J. *Langmuir* **1991,** 7, 1647-1651.

32 Brzoska, J. B.; Ben Azouz, I.; Rondelez, F. *Langmuir* **1994,** 10, 4367-4373.

33 McGovern, M. E.; Kallury, K. M. R.; Thompson, M. *Langmuir* **1994,** 10, 3607-3614.

34 Allara, D. L.; Nuzzo, R. G. *Langmuir* **1985,** 1, 45-52.

35 Thompson, W. R.; Pemberton, J. E. *Langmuir* **1995,** 11, 1720-1725.

Chapter 11

Nanoscale Frictional Properties of Pure and Mixed Alkanethiols on Au(111) by Scanning Force Microscopy

Lingyan Li, Shengfu Chen, and Shaoyi Jiang*

Department of Chemical Engineering, University of Washington, Seattle, WA 98195–1750

We present a quantitative study of frictional properties of pure self-assembled monolayers (SAMs) of alkanethiols as a function of chain length and mixed SAMs of dodecanethiol and 11-mercapto-1-undecanol as a function of surface composition on Au (111) using atomic force/friction force microscopy (AFM/FFM). The lateral and normal forces were calibrated *in situ* using a combined two-slope and added-mass method. Molecular dynamics simulations were also carried out to interpret the chain length dependence of frictional properties of alkanethiols. We then extended the *in situ* force calibration method to the mixed SAMs and investigated the effects of chemical nature and relative humidity on the frictional properties. Friction coefficients were plotted as a function of surface composition with different relative humidity. Such a plot could serve as a reference in determining surface composition in a nano-scale domain by measuring its friction coefficient.

Introduction

Understanding molecular-scale adhesion, friction, lubrication, and wear is crucial to modern technologies, such as microelectromechanical systems (MEMS) and hard disk drives.[1,2] With atomic force/friction force microscopy (AFM/FFM),[3,4] several studies have shown the correlation of frictional properties of self-assembled monolayers (SAMs) of alkanethiols with their chain lengths[5-7] and terminal groups.[8] The long chain monolayers (more than 12 carbon units) have lower friction coefficients compared with their short chain counterparts. Recently, Kim *et al.*[8] investigated the effect of the size of chain termination on frictional properties and found that the difference in friction arises predominantly from the difference in the size of the terminal groups. The AFM/FFM has also been applied to study frictional

properties of alkylsilane SAMs,[5,9] Langmuir-Blodgett films[10,11] and alkanethiol/Au(111) with chemically modified tips.[12,13]

While many striking qualitative frictional properties are revealed, a fundamental understanding of these phenomena requires a quantitative analysis. Most of previous studies use formulae or calculations based on numerical methods to estimate the normal and lateral spring constants.[14-18] These calculations require the dimensions and relevant elastic moduli of the cantilever, which are not easy to measure. Measurements of nano-scale friction and adhesion based on calculated spring constants are unlikely to yield reproducible results. Thus, comparative studies are often carried out using the same tip. Recently, Ogletree *et al.*[14] presented the two-slope method, the only *in situ* method of lateral force calibration, assuming that the normal force is known. For normal force calibration, the added-mass method proposed by Cleveland *et al.*[19] has been widely used. We have combined the two-slope and the added-mass methods for quantitative frictional and normal force measurements and have demonstrated the reliability of nano-scale frictional and normal forces measured with two calibrated cantilevers.[7] In parallel, the interpretation of AFM/FFM measurements is still difficult due to a lack of understanding of the fundamental processes involved in these techniques. The molecular dynamics (MD) method is an ideal tool to interpret AFM/FFM experiments. In this work, tip-based MD simulations are carried out to interpret AFM/FFM experiments.

The combined added-mass and two-slope approach is further used in this work to obtain quantitative frictional forces in mixed SAMs in nano-scale domains. There are a number of important questions to be answered. First, how does the chemical nature (hydrophobic or hydrophilic) of terminal groups of alkanethiol monolayers affect friction? Second, is there any relationship between surface composition and frictional properties? Third, how does the relative humidity (RH) affect frictional properties? In order to address these issues, a comparative study of frictional properties of dodecanethiol, 11-mercapto-1-undecanol, and their mixtures (3:1, 1:1, 1:3) on Au (111) is carried out. It is expected that relative humidity will affect frictional properties, particularly for hydrophilic surfaces. Thus, all our experiments were carried out in a homebuilt environment-controlled chamber.

Experimental Section

Materials

Dodecanethiol and 11-mercapto-1-undecanol were purchased from Aldrich Chemical Company, Inc. (Milwaukee, WI) and used as received. Glassware for the preparation of SAMs was cleaned with chromic acid cleaning solution (Fisher Scientific). Gold shots (99.99%) were purchased from D.F. Goldsmith. Glass beads (10-30 μm) from Polyscience were used for the normal force calibration. The faceted

$SrTiO_3(305)$ surface was annealed for 20h at 1100°C in flowing oxygen as discussed in the literature[20] and used for the lateral force calibration.

Sample Preparation

Gold substrates were prepared by the vapor deposition of gold onto freshly cleaved mica (Asheville-Schoonmaher Mica Co.) with the BOC Edwards AUTO306 thermal evaporator. Gold was deposited in a high vacuum system with diffusion pump at 325°C using evaporation rates of 1nm/s for the first 20nm and 0.1nm/s for the rest of the layer. The gold-coated substrates were then annealed in the chamber at 325°C for half an hour. Before immersion into dilute (1mM) alkanethiol-containing ethanol solutions for 24 h, the gold-coated substrates were further annealed in a H_2 flame. Prior to imaging, all of the samples were rinsed extensively with ethanol and dried under a stream of N_2.

Friction Measurements

The experiments were performed with a MultiMode NanoScope III AFM with a commercial Si_3N_4 cantilever of a nominal spring constant of 0.58 N/m (Digital Instruments, Santa Barbara, CA). The instrument was allowed to equilibrate thermally in the homebuilt chamber for ~1 h after mounting a sample. For the measurements of friction vs. load, the microscope was operated in a constant force mode, where the tip was scanned back and forth along the same horizontal line (slow scan direction disabled) while a feedback loop holds the externally applied load constant. The normal force between the tip and the sample, F_N, was estimated from force vs. z-displacement curves, with $F_N=0$ designated as the point at which the tip breaks contact with the surface. Thus, F_N is the sum of adhesion and external load. Frictional forces, f, were measured from plots of frictional signal vs. lateral displacement (e.g., friction loop) during 10nm trace/retrace cycles along a single scan line at 407nm/s. Friction vs. load was obtained by varying F_N.

The combined added-mass and two-slope method was described previously.[7] In short, the normal spring constant of a micro-fabricated cantilever was determined by measuring their resonant frequencies after adding small end masses (e.g., glass spheres).[19] The tip was used as a micro-manipulator to pick up a sphere. Several different sized spheres were used instead of based on a single point calculation. The results showed very good linear relationship between the added mass and $(2\pi v)^{-2}$ as expected. The lateral force was calibrated using the $SrTiO_3(305)$ sample proposed by Ogletree et al.[14] The calibration was made by sliding the tip across the surface of the known slopes and measuring the lateral force signal as a function of normal force signal. With this in situ method for lateral force, the voltage signal from the photodiode can be converted to lateral force directly without assuming equal normal and lateral optical deflection sensitivities. The piezo scanner sensitivity for X-Y directions was calibrated from lattice resolution images of mica and Au(111) while the

Z piezo calibration was determined using the faceted $SrTiO_3(305)$ surfaces[14] and from a monatomic step height on Au(111) substrate.

The AFM on the vibration base was enclosed in the homebuilt chamber. Relative humidity in the chamber was reduced by flow dry N_2 gas and the gas inlet was sealed during the measurements.

Results and Discussion

We have obtained *quantitative* measurements of the frictional properties of self-assembled alkanethiol monolayers on Au(111) using AFM/FFM as shown in Figure 1. The frictional forces were investigated for the total loads up to 60 nN in an effort to probe the frictional properties of only the outermost portions of the SAMs. The higher loads will cause damage on the monolayers. Hysteresis in the measured friction is small. Thus, the data points obtained upon decreasing loads are not shown. As seen in Figure 1, an approximately linear response is observed for the range of loads investigated. The friction curves for C18, C12, and C8 layers lie well below that for a bare Au(111) surface. Furthermore, friction increases as the chain length decreases. To demonstrate the reproducibility of experimental data, the friction versus load curves were also measured by using another calibrated cantilever. The results are also shown in Figure 1. As we can see, the friction curves obtained from both cantilevers agree quite well. The friction coefficients differ by less than 15% for the same system with different cantilevers and the difference is within experimental uncertainties, indicating the reliability of nano-scale frictional and normal force measurements using AFM/FFM. Measurements using cantilevers either without calibration or with estimated spring constants are unlikely to yield reproducible results. Our results show that with *in situ* force calibration, different cantilevers yield comparable frictional forces.

To interpret the AFM/FFM experiments on the chain length dependence of friction[5-7], we have carried out tip-based MD simulations where an AFM/FFM tip scans at a constant velocity over thin films of C8 and C15 thiols at constant load mode (Figure 2). For the shorter chain (C8), AFM/FFM tip penetrates into the thin film. In other words, the pressure-induced terminal defects are sufficiently large to cause the disorder of the shorter chain alkanethiol, leading to higher friction. Under the same load, however, for the longer chain (C15), AFM/FFM tip floats over the film which leads to lower friction.[21] For the MD simulations, the AFM/FFM tip is connected to a rigid holder via three orthogonal springs. Two of them deflect in proportion to the normal (Z) and lateral (X) forces in the scan direction with both spring constants (k_x and k_z) determined in our experiments[7] while the other spring (Y) is kept very stiff. Damping is introduced to reduce the lever response to rapid SAM motions and to mechanical instabilities. Due to high sliding velocity used in MD simulations compared with that in AFM/FFM experiments, we recently develop a novel simulation technique which combines MD simulations for the SAMs with continuum mechanics modeling for the cantilever.[21] The coupling between MD and continuum mechanics can dramatically extend simulation time scales to overlap with those of AFM/FFM

experiments. The results show that the phenomena found from the combined method are similar to those from MD simulations, except that the values of friction coefficient could be different, depending on whether stick-slip occurs or not. The details of the combined simulation method and its application for the interpretation of AFM/FFM experiments will be published elsewhere.[21]
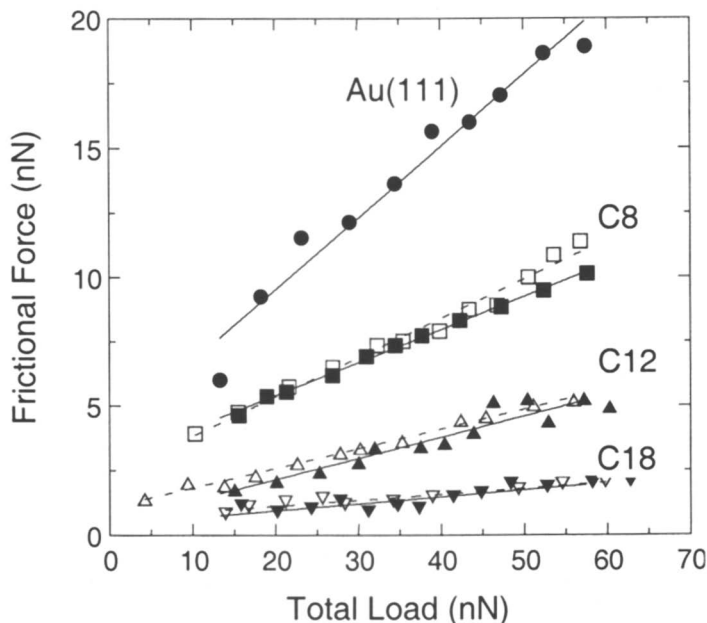
Figure 1. Friction vs. load curves obtained for C18, C12, and C8 alkanethiol monolayers on Au(111) using AFM/FFM. The cantilevers were calibrated using the combination of the two-slope[14] and the added-mass[19] methods. Solid lines represent the results obtained from cantilever 1 while dashed lines from cantilever 2.

(a)   (b)
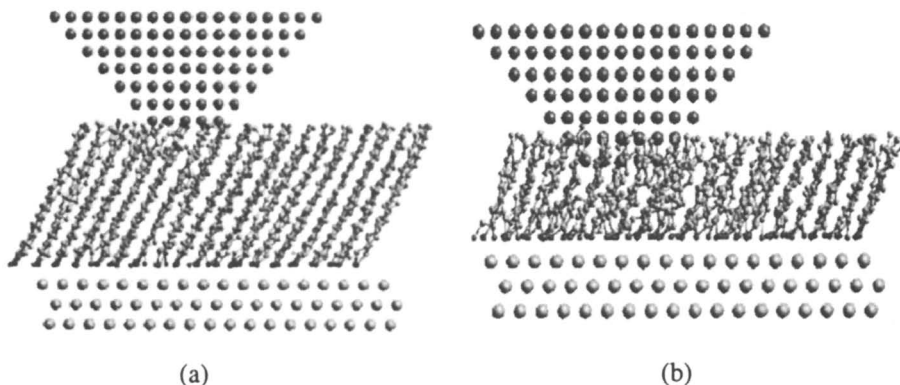
*Figure 2. MD simulations of AFM/FFM experiments on (a) C15 and (b) C8 SAMs.
under the same load (0.65 GPa). The AFM/FFM tip penetrates more into the thin
film formed by the shorter chain than the longer chain leading to a higher friction
as observed in experiments.[5-7]*

Frictional properties of SAMs depend on chain length,[5-7] and the size[8] and the
chemical nature of terminal group. Here we further examine the effect of the chemical
nature of terminal group on frictional properties of SAMs. Two types of pure SAMs
(dodecanethiol and 11-mercapto-1-undecanol) and their 1:3, 1:1, and 3:1 mixtures
were prepared on Au (111) surfaces for this study. Dodecanethiol is denoted as C12
and 11-mercapto-1-undecanol as C11OH. Both C12 and C11OH are similar in chain
length, but with very different terminal groups — one is hydrophobic and the other is
hydrophilic. The nano-scale frictional images of pure C11OH and mixed C12 +
C11OH SAMs were observed and the Fast Fourier Transform (FFT) spectra of these
two images clearly shows a periodicity of 0.5 nm, which is the same as that of
alkanethiols. This indicates that all systems studied here have the similar packing
structure. The topography images and the simultaneously captured frictional images
scanning from 20×20 nm^2 to 5×5 μm^2 scales were investigated carefully. All of
these results clearly show that the two-component monolayers do not separate into
single-component domains large enough to be detectable by AFM/FFM. In another
work, we carried out the systematic studies of the effect of chain length on phase
separation. Our results show that phase separation occurs in 3 days for mixed C18 +
C11OH SAMs while 17 minutes for mixed C18 + C4 SAMs.[22] Based on the fact that
C12 and C11OH are homogeneously mixed on Au(111), we studied the effect of
surface component on frictional properties at nano-scale domains.

Figure 3 shows frictional force vs. load curves for C12, C11OH and their 1:1
mixture on Au(111) scanning under RH of 50%. It is observed that friction
coefficients for C11OH (hydrophilic surface), C12 (hydrophobic surface) and their
mixtures are similar. Under high humidity (e.g., RH=50%), both hydrophilic (due to

adsorbed water layer) and hydrophobic surface have lower surface energy. Thus, contribution from the chemical nature of terminal group to frictional properties is small compared to that from chain length. Thus, the similar chain length of C12 and C11OH leads to the similar friction coefficients. Figure 4 gives frictional force vs. load curves of C12, C11OH and their 1:3, 1:1, and 3:1 mixtures under RH of 31%. Friction coefficient increases as C11OH composition increases. For hydrophilic surfaces, interactions between OH groups on hydrophilic SAM and Si_3N_4 tip surfaces cause higher friction under lower humidity. As humidity increases, adsorption of water on both SAM and tip surfaces decrease friction. For hydrophobic SAM surfaces, frictional properties are not affected much by the change of humidity as expected. We should point out that due to the effect of humidity, one must be very careful when studying frictional properties by AFM/FFM in air.
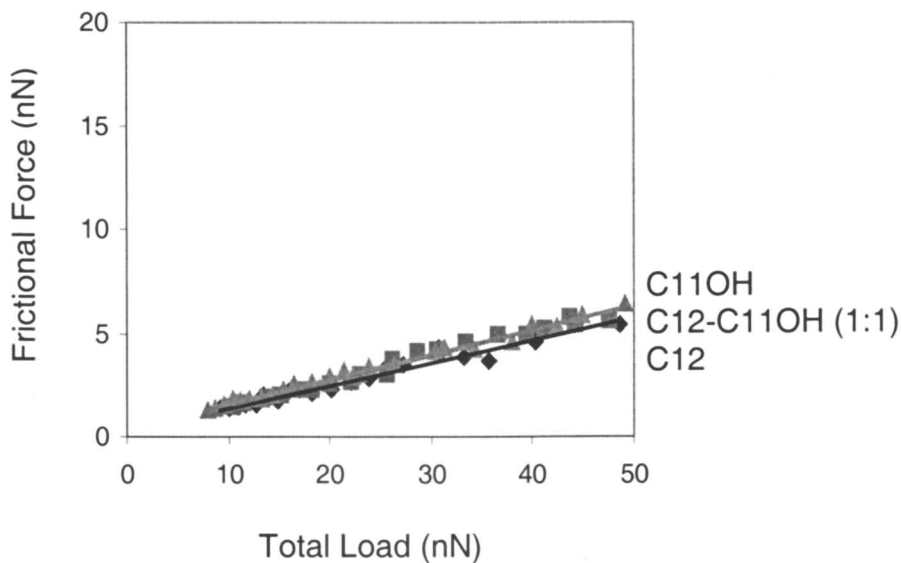
Figure 3. Frictional force vs. load curves for dodecanethiol, 11-mercapto-1-undecanol, and their 1:1 mixture on Au (111) scanning under RH of 50%.
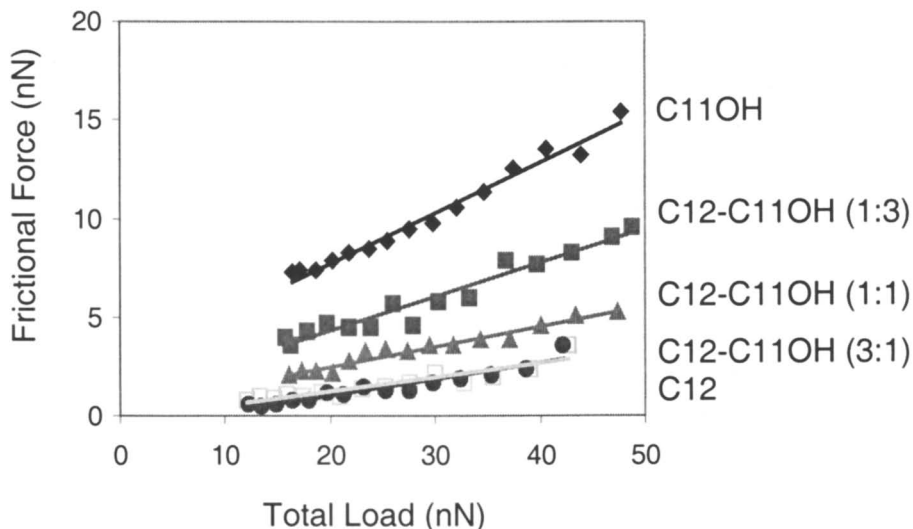
Figure 4. Frictional force vs. load curves for dodecanethiol, 11-mercapto-1-undecanol, and their 1:3, 1:1 and 3:1 mixtures on Au (111) scanning under RH of 31%.

Friction coefficients are plotted as a function of surface composition with different RHs in Figure 5. Due to the preferential adsorption of one component than another for co-adsorption from mixtures, it is expected that surface composition is different from solution composition. The average surface composition could be determined from X-ray photoelectron spectroscopy (XPS) experiments. Since our system is very similar to that studied previously,[23] we obtained surface compositions from data given in the reference. It should be pointed out that friction coefficients reported here are based on quantitative measurements, making it possible to compare these results directly even though they may be obtained with different AFM/FFM cantilevers. The plot of friction coefficient vs. surface composition such as the one shown in Figure 5 could serve as a reference in determining surface composition of mixed SAMs in a nano-scale domain by measuring its friction coefficient. A number of techniques can establish the average composition of mixed SAMs. XPS can ascertain the composition over an area of the size of the X-ray spot (approximately $1mm^2$)[23], and scanning electron microscopy can detect heterogeneity of SAMs on the dimension of the order of $1\mu m$. While FFM can be used for the direct visualization of phase-separated regions of nano-scale sizes in an organic monolayer, none of analytical techniques are available to determine surface composition in a nano-scale domain. Since frictional properties depend on surface composition as shown in this work, friction coefficients as a function of surface composition can be predetermined over the entire composition range such as the one shown in Figure 5. One could then estimate the surface composition of a nano-scale domain from its friction coefficient.

To prepare such a reference plot, homogeneous phases of mixed SAMs should be prepared and the surface composition of such a homogeneous phase can be determined by XPS measurements. For mixed SAMs containing two components of different chain lengths, direct co-adsorption from solutions of mixed alkanethiols will lead to phase separation. One of solutions is to prepare uniform phases of mixed SAMs co-adsorbed from solutions of mixed symmetrical and asymmetrical disulfides as found recently from our experiments.[22] The success of this technique for determining surface composition in a nano-scale domain depends on the ability to obtain quantitative measurements of forces and to prepare homogeneous phases.
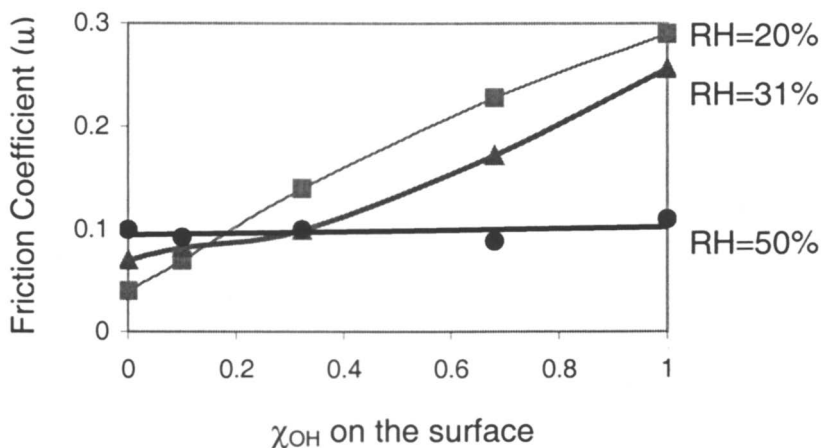
Figure 5. Friction coefficient vs. surface composition of C11OH for dodecanethiol, 11-mercapto-1-undecanol, and their mixtures on Au(111) with different RHs.

Conclusions

Quantitative measurements of nano-scale frictional properties of pure and mixed SAMs on Au (111) were achieved by *in situ* normal and lateral force calibration of AFM/FFM. For pure SAMs, the friction coefficients for the same alkanethiol system but with different tips, differ by less than 15%, indicating the reliability of nano-scale frictional and normal force measurements using a scanning force microscope. The friction coefficient increases as the chain length decreases as also found previously by other workers. Tip-based molecular dynamics simulations were carried out to interpret the chain length dependence on frictional properties of alkanethiols. Simulation results show that AFM/FFM tip penetrates deeper into films formed by shorter chain SAMs, causing higher friction.

For mixed SAMs, friction coefficient is similar under a RH of 50%, while friction coefficient increases as C11OH composition increases under the relatively lower RH

(e.g., 20% and 31%). Due to the effect of humidity on frictional properties, one must be very careful when measuring and analyzing frictional properties by AFM/FFM in air. Friction coefficients are plotted as a function of surface composition under different RHs. Such a plot could serve as a reference in determining surface composition in a nano-scale domain by measuring its friction coefficient.

References

(1) Carpick, R. W.; Salmeron, M. *Chemical Reviews,* **1997**, 97, 1163.
(2) Bhushan, B.; Israelachvili, J. N.; Landman, U. *Nature,* **1995**, 374, 607.
(3) Binnig, G.; Quate, C. F.; Gerber, C. *Phys. Rev. Lett.* **1986**, 56, 930.
(4) Mate, C.M.; McClelland, G.M.; Erlandsson, R.; Chiang, S. *Phys. Rev. Lett.* **1987**, 59, 1942.
(5) Lio, A.; Charych, D. H.; Salmeron, M. *J. Phys. Chem. B,* **1997**, 101, 3800.
(6) McDermott, M. T.; Green, J.-B. D.; Porter, M. D. *Langmuir,* **1997**, 13, 2504.
(7) Li, L.; Yu, Q.; Jiang, S. *J. Phys. Chem B,* **1999** 103, 8290.
(8) Kim, H. I.; Koini, T.; Lee, T. R.; Perry, S. S. *Langmuir,* **1997**, 13, 7192.
(9) Xiao, X.; Hu, J.; Charych, D. H.; Salmeron, M. *Langmuir,* **1996**, 12, 235.
(10) Bhushan, B.; Kulkarni, A. V.; Koinkar, V. N.; Boehm, M.; Odoni, L.; Martelet C.; Belin, M. *Langmuir,* **1995**, 11, 3189.
(11) Meyer, E.; Overney, R.; Brodbeck, D.; Howald, L.; Luthi, R.; Frommer, J.; Guntherodt, H.-J. *Phys. Rev. Lett.* **1992**, 69, 1777.
(12) Frisbie, C. D.; Tozsnyai, L. F.; Noy, A.; Wrighton, M. S.; Lieber, C. M. *Science,* **1994**, 265, 2071
(13) Green, J.B.D.; McDermott, M.T.; Porter, M.D.; Siperko, L.M., *J. Phys. Chem.* **1995**, 99, 10960.
(14) Ogletree, D. F.; Carpick, R. W.; Salmeron, M. *Rev. Sci. Instrum.* **1996**, 67, 3298.
(15) Albrecht, T. R.; Akamine, S.; Carver, T. E.; Quate, C. F. *J. Vac. Sci. Technol. A,* **1990**, 8, 3386.
(16) Butt, H.-J.; Siedle, P.; Seifert, K.; Fendler, K.; Deeger, T.; Bamberg, E.; Weisenhorn, A. L.; Goldie, K.; Engel, A. *J. Microsc.* **1993**, 169, 75.
(17) Neumeister, J. M.; Ducker, W. A. *Rev. Sci. Instrum.* **1994**, 65, 2527.
(18) Sader, J. E. *Rev. Sci. Instrum.* **1995**, 66, 4583.
(19) Cleveland, J. P.; Manne, S. Bocek, D. Hansma, P. K. *Rev. Sci. Instrum.* **1993**, 64, 403.
(20) Sheiko, S. S.; Möller, M.; Reuvekamp, E. M. C. M.; Zandbergen, H. W. *Phys. Rev. B,* **1993**, 48, 5675.
(21) Leng, Y.; Jiang, S. Annual AIChE Meeting, Dallas, TX, Nov. 1999; Leng, Y.; Jiang, S. submitted to *Phys. Rev. Lett.* **2000**.
(22) Chen, S.; Li, L.; Jiang, S. Annual AIChE Meeting, Dallas, TX, Nov. 1999.
(23) Bain, C.D.; Evall, J.; Whitesides, G.M. *J. Am. Chem. Soc.* **1989**, 111, 7155.

Nanobiotribology at the Confined Biomaterial Interface

Reto Luginbühl[1], René M. Overney[2], and Buddy D. Ratner[1-3]

[1]Engineered Biomaterials and [2]Chemical Engineering, University of Washington, Seattle, WA 98195

Modern biomaterial research proposes that precision engineered recognition surfaces will trigger biological responses. Ideally, engineered biomaterial surfaces will have mechanical and chemical properties directed to a specific in vivo function. The science of tribology has made a substantial contribution to a better understanding of interfacial problems. We apply in this contribution the term *nanobiotribology* to embrace all mechanical investigations of biological and biomaterial interfaces at the cellular and molecular level. The potential impact of *nanobiotribology* to the biomaterial and biomedical science is discussed. Progress in this science field strongly depends on the development of appropriate techniques used to analyze surfaces at the micro- and nanometer level. In the first part, this paper is focused on the possibility of measuring contact mechanical properties on ultrathin biomaterial films with the help of lateral or shear modulation experiments with the scanning force microscope. Shear techniques prove to be in particular successful in determining crosslinking densities and structural phase transitions of ultrathin films. Finally, we will briefly review and critically disscuss recent SFM applications, which were applied to determine molecular interaction forces.

[3]Corresponding author.

Introduction

Interactions at biological interfaces play a central role in any biological process. In particular in biomedical science, interfacial interactions define the performance of biomaterial devices. Unfortunately these interactions are still poorly understood. Nature has developed its own way of organizing biological enties at interfaces and it even provides tools for "quality control". Deviations from the normal, expected information codes or unknown interfaces are recognized and removed. All interfacial interactions are defined through variations in chemical and spatial organization. This elegance and synergism of design is a challenge for research. Many strategies have been developed and are applied for mimicking and building functional structures in the manner of nature. However, many strategies fail due to the complexity and the lack of understanding of the interfacial events, especially at the molecular level. Novel techniques and tools emerging from modern science will help in a better understanding of interactions at the biological interfaces.

Tribology, the study of friction, wear, lubrication, and adhesion, embraces not only inorganic and organic applications, but also applications at biological interfaces on the macroscopic and molecular scale. We encounter tribological phenomena with every physical step and action we take in our daily life. The study of tribological phenomena is belongs to one of the oldest scientific research fields. In ancient Egypt, tribological problems were solved by primitive yet sophisticated means. The basis for "modern" tribology was established some five hundred years ago and first documented in the classical studies of Leonardo da Vinci (1470), Guillaume Amontons (1699) and Charles A. Coulomb (1785) (1-3). However, tribology did not emerge as an engineering science until the late 19th century. At that time, problems and limitations of the developing industry boosted research. From this era, important contributions were made, such as the elastic contact theory by Hertz (4), the introduction of fluid lubrication by Petrov, Tower and Reynolds (5-7), and the fundamental hydrodynamic lubrication theory by Reynolds (1886) (8). The 20th century brought some of the most spectacular developments. The reliability and lifetime of machinery, hydraulics, and motors were dramatically improved by applying tribological principles to bearings and lubricants. Increasingly, synthetic fluids and polymers replaced natural materials. Economic aspects became the driving force in tribology. In modern times, the general subject of tribology has moved towards fundamental research leading to a greatly enhanced understanding of basic phenomena. Recent advances in instrumentation, in particular the development of the Scanning Force Microscope (SFM) (9) , have opened up a totally new tribological research field at the molecular and atomic level. Wearless atomistic models that were predicted as early as 1928/29 by Prandtl (10) and Tomlinson (11), could finally be experimentaly verified by SFM (12). Since the invention of the SFM, thousands of tribological investigations at the nanometer scale have been published, and today it is a research field of its own. A comprehensive review on the historical aspects of tribology is found elsewhere (13, 14).

Bio-Tribology

In the late 1960's advances in medicine, e.g. orthopedic technology, allowed using artificial prosthesis as replacements for worn, broken, or diseased joints and bones. With the introduction of medical and biological applications, new aspects and challenges arose to tribology. In 1973 the term *bio-tribology* was introduced by Duncan Dowson and co-workers in order to embrace *all aspects of tribology related to biological systems* (15). One of the first papers dealing with biotribological aspects had already been published in 1936 by Jones (16). He reported measurements and calculations of the friction coefficient in animal joints. Since then many studies on friction, wear and lubrication have been published. Today the term of "biotribology" commonly refers to all aspects of biomechanical investigations including (I) friction, wear, and lubrication of skin and hair, (II) embracing dental tissue and restorative materials, (III) dealing with the fluid mechanics and lubrication of plasma fluids in blood vessels, and (IV) involving the large field of biomedical and biomaterial applications. The aspects named above are illustrative rather than comperhensive (Figure 1).

The impact of biotribology to medicine is illustrated by investigations to understand complex processes in natural synovial joints and artificial replacements . The most extensive investigations on lubrication, friction, and wear have been completed in the field of artificial replacement joints (17). Today, more than 500'000 operations are carried out worldwide each year to implant artificial hip prosthetics. The choice of materials is today one of the major focuses for hip implants. The femoral stem and head part is typically made of stainless steel or titanium with or without special coatings, while the acetabular socket is made of polymeric materials. Initially, polytetrafluoroethylene (PTFE) was used for the acetabular system, since it exhibited the lowest friction under dry conditions. Later, it was replaced by ultra-high molecular weight and highly crosslinked polyethylene, which is still regarded as the standard.

Artificial implants, however, may cause many problems. Polyethylene, for example, will wear over time. Microscopic particles may break off and settle around the implant and surrounding tissue. The immune system of the body rejects the polyethylene debris and may react with a chronic local inflammation reaction, often causing osteolysis or "eating away" of the bone. As the patient loses bone in his or her hip, the implant may become loose and no longer function properly. The patient then must undergo major surgery once more to replace the implant (17, 18).

As mentioned earlier, in in-vivo settings, the biological response to foreign material is strongly dependent on interfacial interactions. The surface recognition of proteins and cells defines the cellular response, and consequently it determines success or failure for an implant. Commonly the body reacts to implanted devices with the so-called "foreign body response", which is characterized by the encapsulation of the implant, leading to a ubiquitous inflammation reaction. It is assumed that this response is triggered through unfavorable protein adsorption, inducing macrophage activation. Parameters like surface chemistry, surface energy,

molecular orientation, and morphology all influence the initial protein adsorption (19-21).

In modern biomaterial science, there are two distinct fundamental approaches to solve the problem of biocompatibility. The first one is based on an active biological recognition of the surfaces, while the second employs non-fouling, also called "stealth" surfaces, in order to inhibit protein adsorption, and therefore escape macrophage detection. A combined approach of a non-fouling surface with biological recognition elements is commonly used in biosensor and biomedical assay settings.

Testing of engineered biomaterial/sensor surfaces requires appropriate and highly sensitive analytical methods. In the case of biosensor surfaces, the system can be
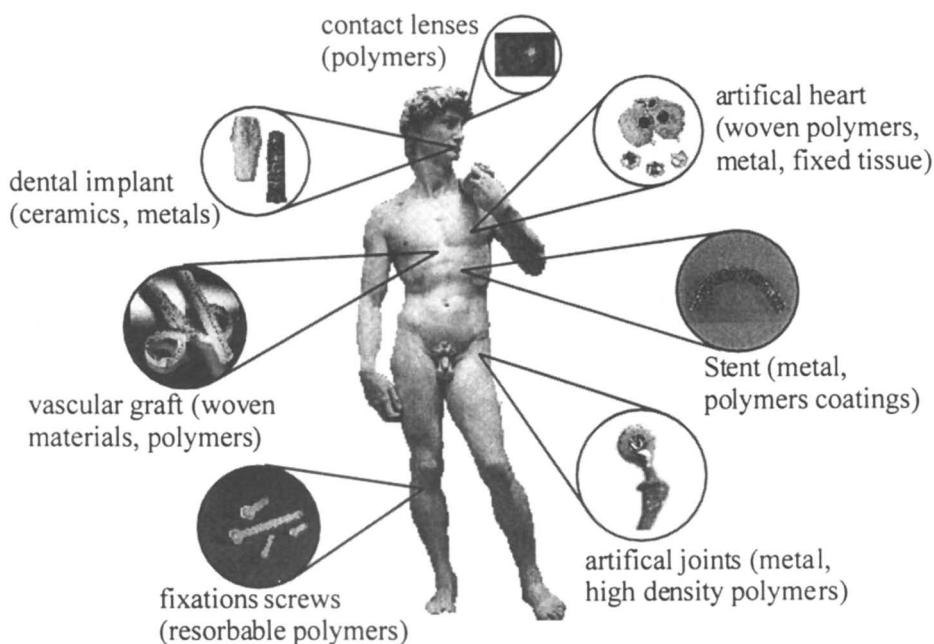
Figure 1
Many different material are used as biomedical implants ranging from metals for artificial bones and joints to ceramics for restorative dental materials, from high density polymers for joints to biodegradable polyacids for non permanent fixations. The variety of materials reflects as well the wide range of material properties. Tribology plays a key role in the investigation of these materials and their interactions with an in-vivo setting. More recently evolving new instrumentation allows for investigations at the cellular and molecular level, for nanobiotribological experiments.

tested based on its response signal to background noise ratio. However, other techniques have to be employed for implant setting or when fundamental information on recognition and mechanical information at the molecular level is required.

Nanobiotribology on confined biointerfaces with the SFM

Surface analysis and tribological investigations have profited tremendously in the last 10 to 20 years from the development of the surface force apparatus (SFA) and the scanning force microscope (SFM). These two instruments have enabled measurements of rheological properties of nm thick films, and dry friction contact on a single asperity to molecular scale. They closed the gap for experiments between the macroscopic and the molecular scale. Today, the SFM and the SFA are well established in research and development. Numoerous SFM operational modes exist providing information about various tribological, rheological, and contact mechanical properties. Investigations can be carried out spectroscopically at a fixed location vs space, or dynamically during mapping surfaces. Virtually any surface of interest can be probed, provided that the sample surfaces are resonably smooth on a micrometer scale. Moreover, the SFM allows for experiments at ambient conditions as well as in liquid environment. This has proven to be one of the major advantages making the SFM a huge success for biological applications.

These achievements have resulted in a considerable impact on different fields of biomaterial research. It is well known that the chemical and physical nature of the surface of a biomedical device plays an essential role in determining the host response and thus biocompatibility. For many years, improvements in biomaterial surfaces were based on phenomenological observations at the macroscopic level. However, the scientific principles were often not understood as in-situ investigations and analysis were not possible. With the evolving SFM technique, new biotribological aspects can be addressed at the cellular and molecular level in the rapidly growing field of bioengineering and biomaterial research. A subfield to biotribology opens up: the *nanobiotribology* covering any tribological or rheological investigations of biological and biomaterial interfaces at the cellular and molecular level. It embraces traditional tribology conducted on the nanometer scale, interaction force studies of biological systems at surfaces, and the study of interfacial interactions between biological systems. Nanobiotribological investigations require instrumental access under physiological conditions, which is provided by the SFM setup. In the following paragraphs some recent studies on ultrathin biomaterial films are discussed that were obtained in our laboratory.

Accessing Contact Mechanical Properties of Ultrathin Biomaterial Polymers

Ultrathin polymers films are widely used in biomaterial and medical settings as protective coatings and to control material properties. Surface properties of these polymer films are of particular interest. Both crosslinking density and the phase behavior influence the structural integrity, the interfacial compatibility, and the kinematic behavior. Contact mechanical investigations with the SFM on ultrathin biomaterial coatings provide insight into the origin of problems such as delamination and degradation, and help to improve the biocompatibility of materials. Such investigations are of importance in biomedical settings as polymers are exposed to a variety of mechanical and chemical attacks and biological degradation. For property characterization it is critical that the substrate and the coating technique chosen for model systems are identical with the implant and the coating procedure, respectively, due to interfacially induced structural molecular recombination and pinning (22). Furthermore, variations (for instance in the film thickness) have to be considered in mesoscopic systems such as thin films.

The structural integrity of thin protective coatings is improved by crosslinking. Therefore, it is imperative that the crosslinking density is determined at the material surface. The crosslink behavior of polymers may be measured with the SFM as it influences the contact mechanical behavior. Recent attempts employing adhesion sensitive modes showed some sensitivity to crosslinking (23, 24). However, the relation is often coincidental with near-surface structural changes and does not necessarily agree with changes in the crosslinking density. Measurements of pull-off forces are strongly dominated by the contact area, which is a function of the internal pressure of the polymer film, the applied load, and the surface energies. Changes in these properties are responsible for changes in adhesion. Although, the film pressure and surface energies are influenced by the crosslink density, the contact area cannot be directly related to it. Lateral force or shear modulation can be used to monitor the degree of crosslinking (25). While state-of-the-art friction force microscopy is sensitive to the chemical nature of the sample surface (26), lateral modulation is more sensitive to the mechanical surface properties. Briefly, the SFM cantilever is brought into contact with the sample and laterally modulated with amplitudes that are significantly smaller than the stiction amplitude (Figure 2). The stiction amplitude, i.e., the amplitude necessary to overcome static friction, depends on the material and the applied load. The shear modulation response is measured by a laser beam deflection scheme (27) and reflects the lateral contact stiffness (14). Isothermal lateral stiffness images are recorded by scanning the surface while modulating the tip. A high frequency modulation is chosen in order to work within the inertia regime of the system.

The sensitivity of the SFM to changes in crosslink density has been exemplified with a plasma deposited hexafluoropropylene (HFP) films (25, 28). This fluorinated polymer plays an important role in biomedical applications, especially the coating of vascular grafts. Plasma deposited fluoropolymer films promote tight protein adsorption, and are relatively non-reactive to blood platelets (29). As mentioned
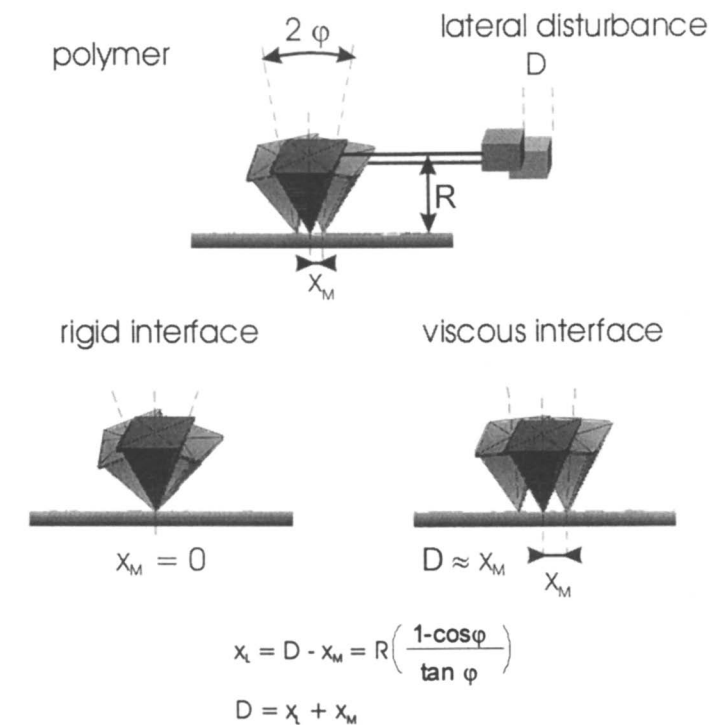
x_M	x_L	crosslinking	k_C	phase state of material
small	large	large	small	glass-like
large	small	small	large	liquid-like

Figure 2
The response to a small sinusoidal high frequency stimulation, applied in lateral direction, is recorded with a look-in amplifier providing amplitude, A_{resp}, and phase, φ, components. The magnitude of applied amplitude is very small (typically < 5 nm) and far below the slip regime. On a rigid surface the tip is pinned and does not move at all ($x_M=0$). In contrast, on a viscous interface the tip movement is close to the lateral disturbance ($x_M \approx D$). The measurements were carried out with a modified stand alone SFM (Explorer, ThermoMicroscopes) and conventional bare-shaped cantilevers (NT-MDT, Russia). As the lateral stimulation frequency exceeds the inertia of the sample measurement can be carried out while scanning.

previously it is essential to control and optimize the polymerization process out of the gas phase, since coatings have to withstand considerable mechanical stresses. The plasma deposited HFP polymer is a sample of choice, because its crosslinking reaction can be easily distinguished in thick films by electron spectroscopy for chemical analysis (ESCA) due to the large chemical shifts between different species.
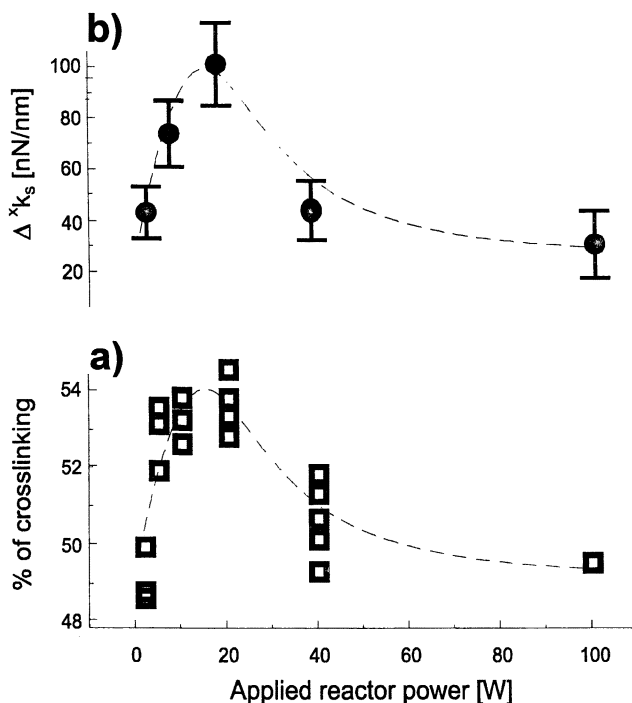
Figure 3
Thin hexafluoropropylene (HFP) films were deposited applying different reactor conditions by a radio frequency plasma enhanced chemical vapor deposition process onto photolithographic masked silicon surfaces. (a) depicts the crosslink density calculated from ESCA experiments (28). (b) shows the normalized amplitude response. The difference between silicon and HFP response was measured from recorded images allowing for an accurate statistical averaging, and converted into the difference in contact stiffness k_S. The SFM measurements were carried in a nitrogen atmosphere (humidity < 4 %) at room temperature. Scan speed was 50 μm/s, applied lateral modulation amplitude 3.5 nm, and modulation frequency 13 kHz. No external load was applied to the cantilever.

ESCA analysis of functional species was used to derive the degree of crosslinking as function of the applied deposition power, (Figure 3a) (25, 28). Comparing these data to shear modulation measurements (Figure 3b) shows an excellent agreement, suggesting that the lateral contact stiffness is a direct measure of the crosslinking density. The advantages of the SFM method over ESCA are (a) not restricted to the specific chemistry of the crosslinked species, and (b) nanometer lateral resolution. Due to the imaging capabilities of the SFM determination of the properties of vascular HFP coatings are not restricted to obtaining the crosslinking density, but also include the measurements of the uniformity and homogeneity of the coated film (28).

At this point it should be mentioned that these experiments were facilitated by patterning the polymer surface (25). Patterned surfaces provide an internal standard for assays and a background region to distiguish specific from non-specific interactions. This approach is especially important and helpful for nanobiotribolgical applications where the analyte surface area is size limited and signal levels are low. Patterning of surfaces is also extremely important for cutting edge technologies. In biosensor applications, patterning enables the construction of multiple analyte regions, miniaturization, and spatial registration (30, 31). Patterned surfaces may play also an essential role in biomaterial science. The influence of patterns and geometric factors has been recognized as an important variable in the behavior of cells at interfaces (32, 33). More aspects of patterning methods and effects regarding biomaterial and biological applications is found elsewhere (34, 35).

As mentioned earlier the phase behavior of polymers is another contact mechanical property that is of utmost importance for the structural integrity of thin films. Polymeric materials that change their structural properties upon external stimulation are of particular interest for biomaterial research (36, 37). Recently, considerable research effort has been put in the investigation of co-polymers, grafted polymers and lipid layer system containing N-isopropylacrylamide (NIPAM or p-NIPAAm) (36, 38). Linear poly-NIPAM undergoes around 304 K a thermally induced fully reversible structural phase transition. The reported critical transition temperature (T_c) depends strongly on the system conditions and is influenced by factors such as changing the molar composition, adding a co-polymer component, change in solvent composition or the ionic strength (39-41). All reported investigations on the transition behavior of NIPAM have been carried with bulk material.

Again, the SFM can be used to study the phase behavior of confined ultrathin films by applying shear modulation. The time delay, also called phase shift, between the input disturbance and the response signal can be simultaneously recorded in addition to the amplitude response. While the amplitude response is primarily sensitive to changes in the shear modulus, the origin of the time delay is fundamentally different and is only dependent on the viscosity of the material. In order to control on the sample temperature, the SFM has to be combined with a heating/cooling device that allows one to maintain the temperature around RT.
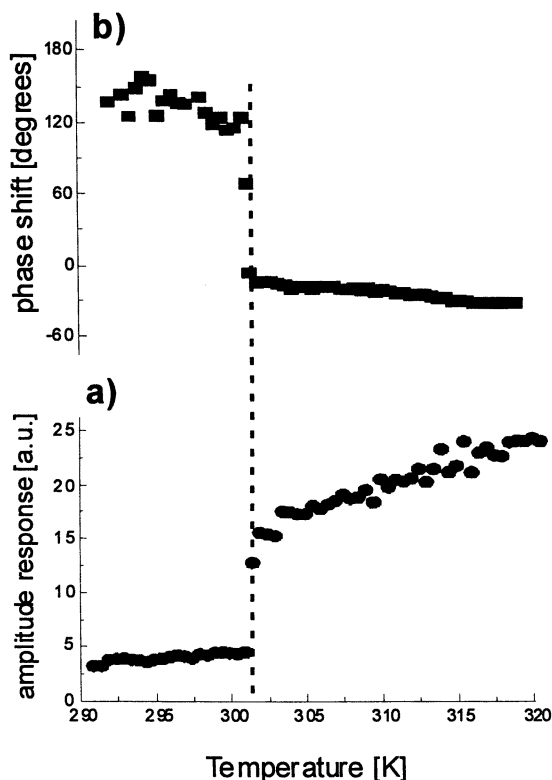
Figure 4
Structural phase transition of poly-NIPAM was studied on ultrathin films deposited by plasma enhanced chemical vapor. The tip was modulated in lateral direction and kept stationary at a constant force by an active feedback. The temperature was varied and control via a small temperature device (MMR technology), which is based on resitive heating and a the Joule-Thompson element. The change in response amplitude (a) and the phase lag (b) were simultaneously recorded as a function of temperature. Measurements were carried out in small custom-made liquid cell in ultrapure water. Applied lateral modulation amplitude was 4.5 nm, modulation frequency 5 kHz, the temperature was changed in steps of 0.5 °C at a rate of 0.2°C per minute.

Figure 4 depicts the observed shear amplitude and time delay responses as function of the temperature. Two distinct plateaus are easily recognized separated by an instantaneous transition at 301 K ± 0.5 K. Supporting evidence of this transition temperature was obtained from contact angle measurements (42). The response signals can be easily explained and is in full agreement to the behavior of NIPAM.

The pNIPAM film is in a porous, hydrogel like state below T_C. The modulation response at temperatures below T_C is only slightly higher than that of the free lever in water, due to the soft, hydrogel-like state of pNIPAM. When passing through T_C the pNIPAM water is expelled from the gel causing its collapse. After the structural collapse, the ultrathin NIPAM film becomes rigid, and its surface exhibits a hydrophobic interaction. Consequently, the SFM tip is more "pinned" on the polymer due to the structural change and an increased interaction force between sample and probe tip. The observed increase in the SFM response amplitude for temperatures above T_C (Figure 4a) reflects the changes in the contact resistance, i.e., improved pinning between SFM tip and NIPAM sample. As the measurements are carried out above the inertia response of the film, changes in the surface free energy dominate variations in shear moduli. Hence, the reported increase in modulation response amplitude is mainly due to structural changes induced at temperatures above T_C. The time delay or relaxation time signal changes significantly at T_C as well (Figure 4b). It is highly sensitive to the magnitude of the structural changes that affect the viscous properties. pNIPAM undergoes a significant change in viscosity when it transforms from a hydrated gel to a collapsed polymer system. These findings are in agreement with measurements of polymer surfaces where structural changes are found to be more isotropic when passing the glass transition of amorphous homopolymers (43).

Interaction forces at biomaterial interfaces

Another essential element of biomaterial research is the determination of interfacial interactions. Biological interaction forces always originate in hydrogen bonding, van der Waals forces or electrostatic interactions. Measuring these interactions at the bio-interface is accomplished with the SFM using modified tips. With proper design of the experiments, the SFM provides information on surface interactions with lateral resolution in the nanometer regime and a force sensitivity of a few pN. This high force sensitivity allows the discrimination of intermolecular interactions. This unique possibility was recognized early on in SFM literature (44-49). Friction or lateral force microscopy is one of the possible modes with the SFM. The method is easy to use and it reveals nanobiotribological information (50). Other operational SFM modes allowing the use of interaction forces as the contrast agent include the pulsed-force mode (51), and non-contact or tapping mode phase imaging (52, 53). Alternatively, adhesion forces can be measured by so-called force spectroscopy, also known as force versus displacement curves, where the pull-off force is related to the interaction force. The cantilever probe is brought into and out of contact with the surface while the deflection signal is monitored as a function of the z-piezo motion. A draw back of this method is that a large number of force versus displacement curves have to be acquired in order to obtain reasonable statistical data for force quantification.

System	Interaction force	Reference
COOH-COOH		
	2.8 ±0.2 nN	(54)
	7 ± 0.2 nN	(55)
	2.3 ± 1.1 nN	(56)
	0.5 nN pH > 8 8-9 nN pH < 5.5	(57)
	0.5 nN pH > 8 7 nN pH < 6	(58)
CH₂OH-CH₂OH		
	1 ± 0.2	(55)
	0.3 ± 0.2	(56)
NH₂-NH₂		
	0-2 nN pH < 6 10-14 nN pH > 8	(55)
	0-1 nN pH < 6 1.5 nN pH > 7	(58)
CH₃-CH₃		
	20 nN	(59)
	60 ± 5 nN	(55)
	12.5 ± 5 nN	(56)
	45 nN ± 5 nN	(60)
CF₃-CF₃		
	35 nN ± 4 nN	(60)

Table I
Interaction forces between different chemical functionalities
measured in an aqueous media with the SFM

The contrast in friction and adhesion images can be increased by chemically modifying the SFM probe with the functional group or biomacromolecule of choice and by changing the environment in which the measurement is carried out. At this point, it is important to differentiate between various probe modification methods such as pure chemical modification, thin film deposition, and modification of the probes with biological elements like biomacromolecules or cells. In addition, the distiction is made between functionalization of the cantilevers by gluing spheres to the lever or by direct derivatization of silicon tips.

Numerous approaches for chemical derivatization have been described in literature. Silanization and self-assembly of alkanethiols on gold coated cantilevers are probably the best known methods (49, 61, 62). More recently, chemical modification of carbon nanotube probes has become popular, as the small tip radius of a single wall carbon nanotube promises to allow for interaction force measurements between a single pair of functional groups (63). Chemically modified SFM probes have a wide range of application. Initially, tips were modified or coated in order to decrease destructive wear or to increase friction contrast. Later it was proposed to use chemically modified tips to sense specific chemical functionalities, which later became known as chemical force microscopy (61, 62, 64). The interaction forces between tip and surface are stronlgy dependent on a) the contact area, b) the chemical functionalities and c) the environmental conditions. Table I shows a list of some force values described in literature for specific interaction forces measured between different functionalities in water. Today, many research groups work with chemically modified cantilevers tips to probe surface energies, surface pK's, or to distinguish chirality of molecules (55, 59, 65). In addition, it has been suggested to use modified tips for studying surface chemical reactions (66).

The chemistry of SFM tips can also be altered by thin film deposition methods. These techniques are of utmost interest with respect to biomaterial and biomedical science. Biomedical coatings are quite often produced by a physical or chemical vapor deposition process (PVD/CVD). The probes can be coated using the exact same process conditions as for the real biomaterial. By probing tissue, single cells, or protein surfaces, an in-vitro experiment can be carried out mimicking in-vivo conditions. Many cantilevers are already modified with hard material coatings like silicon nitride or diamond-like carbon, which have potential biomaterial applications, and many more materials are possible. Another approach is to use ultrathin polymeric films. However, there have been only a few reports in literature using a polymeric coating for tip functionalization (58, 60, 67, 68).

Derivatization of SFM probes with linker molecules of appropriate functionality allows for subsequent immobilization of biomacromolecules. These probes are of particular interest for directly measuring binding forces between complementary biomacromolecules which might enable to create specific recognition images of surfaces. The first interaction force experiments were reported in 1994 for systems based on biotin-streptavidin interactions and biotin-avidin, respectively (69, 70). In these studies, functionalization of the levers was based on the spontaneous adsorption of labeled proteins on the tips and the gluing of labeled beads to the lever, respectively. Other studies used the same approach later as well (71). It appears that under certain conditions, proteins are adsorbed strongly enough, so that that they are not loosened or removed during the force vs. displacement experiments. In general, biomacromolecules have been coupled through silane or alkanethiol based linkers. So far, many different complementary biological systems have been successfully investigated, including DNA base pairs and sequences (72, 73), antibody-antigen complexes (74-82), and polysaccharides (83, 84). Interestingly, a comparison of the different methods employed to confine biomacromolecules revealed similar force

interaction findings (Table II). In many cases, biomacromolecule confinement and orientation at the interfaces did not seem to have an influence on the binding. Even more surprising is the fact that the force interactions between all biological systems are within the same order of magnitude, largely independent of the binding affinity of the biomacromolecules.

System	Interaction Force	Environment	Reference
adenine/thymine SAMs	54 pN	H2O	(73)
DNA oligonucleotides (different lengths)	69,69,76 pN for	0.1N NaCl	(72)
Avidin-biotin Avidin-desthiobiotin Avidin-iminobiotin	160±20 pN 125±25 pN 85±15 pN	PBS	(70)
SA-biotin non-specific	340±120 specific 60±40 pN	PBS	(69)
SA-biotin SA-iminobiotin	257 ± 25 pN 135 ± 15 pN		(85)
WT SA-biotin W120F-biotin	253 ± 20, 393±10 92±19	PBS	(71)
HAS - αHSA	244 ± 22 pN	HEPES	(76)
OPN - αOPN	49 ± 10 pN quantized	PBS	(74)
Ferritn -αferritin	49 ± 10 pN quantized	PBS	(77)
bBSA -αBSA	111.5 ± 98.6 pN	PBS	(81)
GroEL - citrate synthase GroEL - β lactamase	420 ± 100 pN 240 ± 70 pN	PBS	(80)
Adhesive proteoglycans	40±15 pN	H2O	(86)
Dextrans	800-3000pN/Å*	H2O	(83)
Titin protein unfolding	150-300 pN	PBS	(87)

Table II
Interaction forces between biomacromolecules measured with the SFM

Protein interactions with biomaterial surfaces have been studied in-situ with the SFM on other occasions (88-90) A repulsive interaction was measured on PEO surfaces when probed with protein coated tips. This is in agreement with many other studies which have found that PEO surfaces are resistant to proteins adsorption. In another study, interactions were probed between protein coated SFM tips and protein-resistant, non-fouling poly-glyme surfaces, and highly attractive plasma fluoropolymer surfaces. A large adhesion force was measured between the fluoropolymer and proteins, while the tetraglyme surfaces exhibited a strong repulsive behavior (89). These approaches will play an important role in evaluating biomaterial and biosensor surfaces regarding protein interactions.

Most of the work reviewed above has been based on measurements carried out with force spectroscopic experiments. An important development and step forward to the integration of the nanobiotribological measurements in biomedical research has been accomplished by creating specific adhesion force and friction interactions images by probing recognition forces between biological complexes (91-94).

Moving a step beyond biomacromolecule modification of the SFM tip, it is also possible to modify tips with living cells or bacteria. Bacterial infection of biomaterials is among the most important reasons for the failure of transdermal or implanted medical devices. In recently published studies (95, 96), E. coli bacteria were immobilized on SFM tips and used to probe biomaterial surfaces in physiological solutions. It was possible to evaluate the effect of lipopolysaccharide and capsular polysaccharide on the adhesion process. However, it has not yet been investigated whether confinement affects the behavior of the immobilized living cell or bacteria on the probe tip. In this respect, the high aspect ratio of the tip apex is not very favorable for the large cell. Measurements would have to be carried out either with tips modified by small spheres or with specially designed tips with a larger tip radius. However, an increased tip apex radius will reduce the ability to probe surface at high lateral resolution and multiple focal points may induce artifacts. The possibility of coating SFM probes with cells is definitely of interest, but many problems remain to be solved. In this regard, tip coating with biomaterials as discussed above is much easier, better understood, and a more versatile approach.

Summary

The science of tribology has made a substantial contribution to a better understanding of and in some cases the solution of, biological problems. Novel innovations and instrumental techniques allow for nanomechanical characterization of confinement effects at the biological interfaces. In our paper we show the impact of tribology to the biomaterial and biomedical science. We defined the term *nanobiotribology* in the context of nanometer investigations at the biological and biomaterial interface. We showed that it is possible to measure contact mechanical properties on ultrathin biomaterial films. Lateral or shear modulation experiments with the SFM proved to be in particular successful to measure crosslinking of films and the structural phase transition. The SFM is equally suited to access interfacial interactions between material surfaces and/or biological enties and single molecules. The fields of biotribology and nanobiotribology are extensive and increasing. The list of topics reviewed and discussed above is illustrative rather than comprehensive and it is noteworthy that many of the examples are concerned with the common ground between tribology and rheology.

References

(1) Coulomb, C. A. *Mém. Math. Phys* **1785,** *X,* 161-342.

(2) Amontons, G. *Mémoires de l'Académie Royale, A* **1699,** 257-282.

(3) Reti, L. *Sci. Am.* **1971,** *224,* 101-110.

(4) Hertz, H. *J. reine und angew. Math.* **1881,** *92,* 156-171.

(5) Reynolds, O. , Montreal 1884; John Murray, London; 895.

(6) Tower, B. *Proc. Instn. Mech. Engrs.* **1883,** *Nov.,* 632-59.

(7) Petrov, N. P. *Inzh. Zh., St-Peterb.* **1883,** *1-4,* 71-140, 227-279, 377-436, 535-564.

(8) Reynolds, O. *Phil. Trans. Roy. Soc.* **1886,** *177,* 157-234.

(9) Binnig, G.; Quate, C. F.; Gerber, C. *Physical Review Letters* **1986,** *56 (9),* 930-933.

(10) Prandtl, L. *Z. angew. Math. Mech.* **1928,** *8,* 85.

(11) Tomlinson, G. A. *Phil. Mag.* **1929,** *7,* 905-539.

(12) Overney, R. M.; Takano, H.; Fujihira, M.; Paulus, W.; Ringsdorf, H. *Physical Review Letters* **1994,** *72,* 3546-9.

(13) Dowson, D. *History of Tribology,* second edition ed.; Longman Group Limited: London, 1998.

(14) Meyer, E.; Overney, R.; Dransfeld, K.; Gyalog, T. *Nanoscience: Friction and Rheology on the Nanometer Scale;* World Scientific Publishing Co. Ltd.: Singapore, 1998.

(15) Dowson, D.; Wright, V. In *The Rheology of Lubrications;* Davenport, T. C., Ed.; Applied Science Publishers: Barking, 1973, pp 81-88.

(16) Jones, E. S. *Lancet* **1936,** *239,* 1043-1046.

(17) Mow, V. C.; Ateshian, G. A.; Spilker, R. L. *Journal of biomechanical engineering* **1993,** *115,* 460-7.

(18) Long, M.; Rack, H. J. *Biomaterials* **1998,** *19,* 1621-39.

(19) Hidalgo-Alvarez, R.; Galisteo-Gonzalez, F. *Heterogeneous Chemistry ReviewsHeterogeneous Chem Rev* **1995,** *2,* 249-268.

(20) Ramsden, J. J. *Journal of Statistical Physics* **1993,** *73,* 853-877.

(21) Andrade, J. D.; Hlady, V.; Van Wagenen, R. A. *Pure and Appl. Chem.* **1984,** *56,* 1345-1350.

(22) Overney, R. M.; Guo, L.; Totsuka, H.; Rafailovich, M.; Sokolov, J.; Schwarz, S. A. *Interfacially confined polymeric systems studied by atomic force microscopy;* Mat. Res. Soc. Symp. Proc., 1997.

(23) Luginbühl, R.; Garrison, M. D.; Overney, R. M.; Weiss, L.; Hild, S.; Ratner, B. D. *Polymer Preprints* **1998,** *39,* 932-933.

(24) Galuska, A. A.; Poulter, R. R.; McElrath, K. O. *Surface and Interface Analysis* **1997,** *25,* 418-29.

(25) Luginbühl, R.; Garrison, M. D.; Overney, R. M.; Ratner, B. D. *submitted to Langmuir* **2000.**

(26) Overney, R. M.; Meyer, E.; Frommer, J.; Brodbeck, D.; Luethi, R.; Howald, L.; Guentherodt, H. J.; Fujihira, M.; Takano, H.; Gotoh, Y. *Nature (London)* **1992,** *359,* 133-5.

(27) Meyer, G.; Amer, N. M. *Appl. Phys. Lett.* **1990**, *56*, 2100-1.

(28) Garrison, M. D.; Luginbühl, R.; Overney, R. M.; Ratner, B. D. *Thin Solid Films* **1999**, *352*, 13-21.

(29) Kiaei, D.; Hoffman, A. S.; Horbett, T. A.; Lew, K. R. *J Biomed Mater Res* **1995**, *29*, 729-39.

(30) Rozsnyai, L. F.; Benson, D. R.; Fodor, S. P. A.; Schultz, P. G. *Angew. Chem.* **1992**, *104*, 801-802.

(31) Jacobs, J. W.; Fodor, S. P. A. *Trends in Biotechnology* **1994**, *12*, 19-26.

(32) Singhvi, R., Amit Kumar, Gabriel P. Lopez, Gregory N. Stephanopolous, Daniel I.C. Wang, George M. Whitesides, and Donald E. Ingber *Science* **1994**, *264*, 696-698.

(33) Chen, C. S., Mrksich, M., Huang, S., Whitesides, G.M., and D.E. Ingber *Science* **1997**, *276*, 1425-1428.

(34) Blawas, A. S., and W.M. Reichert *Biomaterials* **1998**, *19*, 595-609.

(35) Luginbühl, R.; Garrison, M. D.; Golledge, S.; Goessl, A.; Ratner, B. D. *submitted to J. Biomater. Sci.-Polym. Ed.* **2000**.

(36) Saunders, B. R.; Vincent, B. *Advances In Colloid and Interface Science* **1999**, *80*, 1-25.

(37) Stayton, P. S.; Shimoboji, T.; Long, C.; Chilkoti, A.; Chen, G.; Harris, J. M.; Hoffman, A. S. *Nature* **1995**, *378*, 472-4.

(38) Tsujii, K. *Nippon Kagaku Kaishi* **1999**, 701-713.

(39) Chen, G.; Hoffman, A. S. *Nature* **1995**, *373*, 49-52.

(40) Badiger, M. V.; Lele, A. K.; Bhalerao, V. S.; Varghese, S.; Mashelkar, R. A. *Journal Of Chemical Physics* **1998**, *109*, 1175-1184.

(41) Suzuki, Y.; Tomonaga, K.; Kumazaki, M.; Nishio, I. *Polymer Gels and Networks* **1996**, *4*, 129-142.

(42) Luginbühl, R.; Pan, V. Y.; Buenviaje, C.; Overney, R. M.; Ratner, B. D. *to be submitted to Analytical Chemistry* **2000**.

(43) Overney, R. M.; Buenviaje, C.; Luginbühl, R.; Dinelli, F. *J. Therm. Anal. Cal.* **1999**, *in press*.

(44) Hoh, J. H.; Revel, J. P.; Hansma, P. K. *Nanotechnology* **1991**, *2*, 119-22.

(45) Hoh, J. H.; Cleveland, J. P.; Prater, C. B.; Revel, J. P.; Hansma, P. K. *Journal of the American Chemical Society* **1992**, *114*, 4917-18.

(46) Weisenhorn, A. L.; Maivald, P.; Butt, H. J.; Hansma, P. K. *Physical Review B (Condensed Matter)* **1992**, *45*, 11226-32.

(47) Weisenhorn, A. L.; Hansma, P. K.; Albrecht, T. R.; Quate, C. F. *Applied Physics Letters* **1989**, *54*, 2651-3.

(48) Butt, H. J. *Biophysical Journal* **1991**, *60*, 777-85.

(49) Barrat, A.; Silberzan, P.; Bourdieu, L.; Chatenay, D. *Europhysics Letters* **1992**, *20*, 633-8.

(50) Berger, C. E. H.; van der Werf, K. O.; Kooyman, R. P. H.; Degrooth, B. G.; Greve, J. *Langmuir* **1995**, *11*, 4188-4192.

(51) Rosa-Zeiser, A.; Weilandt, E.; Hild, S.; Marti, O. *Measurement Science & Technology* **1997**, *8*, 1333-8.

(52) Garcia, R.; Tamayo, J.; Calleja, M.; Garcia, F. *Applied Physics A Materials Science & Processing* **1998**, *66*, S309-S312.

(53) Chen, X.; Davies, M. C.; Roberts, C. J.; Tendler, S. J. B.; Williams, P. M.; Davies, J.; Dawkes, A. C.; Edwards, J. C. *Ultramicroscopy* **1998**, *75*, 171-181.

(54) Han, T.; Williams, J. M.; Beebe, T. P. *Anal.Chim.Acta* **1995**, *307*, 365-376.

(55) Vezenov, D. V.; Noy, A.; Rozsnyai, L. F.; Lieber, C. M. *Journal Of the American Chemical Society* **1997**, *119*, 2006-2015.

(56) Sinniah, S. K.; Steel, A. B.; Miller, C. J.; Reuttrobey, J. E. *J Am Chem Soc* **1996**, *118*, 8925-8931.

(57) van der Vegte, E. W.; Hadziioannou, G. *Journal Of Physical Chemistry B* **1997**, *101*, 9563-9569.

(58) Luginbühl, R.; Garrison, M. D.; Overney, R. M.; Ratner, B. D. *submitted* **2000**.

(59) van der Vegte, E. W.; Hadziioannou, G. *Langmuir* **1997**, *13*, 4357-4368.

(60) Luginbühl, R.; Szuchmacher, A.; Garrison, M. D.; Lhoest, J. B.; Overney, R. M.; Ratner, B. D. *Ultramicroscopy* **2000**, *82*, 171-179.

(61) Nakagawa, T.; Ogawa, K.; Kurumizawa, T.; Ozaki, S. *Japanese Journal of Applied Physics, Part 2 (Letters)* **1993**, *32*, L294-6.

(62) Noy, A.; Frisbie, C. D.; Rozsnyai, L. F.; Wrighton, M. S.; Lieber, C. M. *J.Am.Chem.Soc.* **1995**, *117*, 7943-7951.

(63) Wong, S. S.; Woolley, A. T.; Odom, T. W.; Huang, J. L.; Kim, P.; Vezenov, D. V.; Lieber, C. M. *Applied Physics Letters* **1998**, *73*, 3465-3467.

(64) Nakagawa, T.; Ogawa, K.; Kurumizawa, T. *J.Vac.Sci.Technol.B.* **1994**, *12*, 2215-2218.

(65) McKendry, R.; Theoclitou, M. E.; Rayment, T.; Abell, C. *Nature* **1998**, *391*, 566-568.

(66) Werts, M. P. L.; vanderVegte, E. W.; Hadziioannou, G. *Langmuir* **1997**, *13*, 4939-4942.

(67) Knapp, H. F.; Wiegrabe, W.; Heim, M.; Eschrich, R.; Guckenberger, R. *Biophysical Journal* **1995**, *69*, 708-15.

(68) Luginbühl, R.; Garrison, M. D.; Overney, R. M.; Ratner, B. D. *Scanning* **1998**.

(69) Lee, G. U.; Kidwell, D. A.; Colton, R. J. *Langmuir* **1994**, *10*, 354-357.

(70) Florin, E. L.; Moy, V. T.; Gaub, H. E. *Science* **1994**, *264*, 415-417.

(71) Chilkoti, A.; Boland, T.; Ratner, B. D.; Stayton, P. S. *Biophysical Journal* **1995**, *69*, 2125-30.

(72) Lee, G. U.; Chrisey, L. A.; Colton, R. J. *Science* **1994**, *266*, 771-773.

(73) Boland, T.; Ratner, B. D. *Langmuir* **1994**, *10*, 3845-3852.

(74) Garrison, M. D.; McDevitt, T. C.; Luginbuhl, R.; Giachelli, C. M.; Stayton, P.; Ratner, B. D. *Ultramicroscopy* **2000**, *82*, 193-202.

(75) Stuart, J. K.; Hlady, V. *Langmuir* **1995**, *11*, 1368-1374.

(76) Hinterdorfer, P.; Baumgartner, W.; Gruber, H. J.; Schilcher, K.; Schindler, H. *Proceedings Of the National Academy Of Sciences Of the United States Of America* **1996**, *93*, 3477-3481.

(77) Allen, S.; Chen, X.; Davies, J.; Davies, M. C.; Dawkes, A. C.; Edwards, J. C.; Roberts, C. J.; Sefton, J.; Tendler, S. J. B.; Williams, P. M. *Biochemistry* **1997**, *36*, 7457-7463.

(78) Roberts, C. J.; Allen, S.; Chen, X.; Davies, M. C.; Tendler, S. J. B.; Williams, P. M. *Nanobiology* **1998**, *4*, 163-175.

(79) Hinterdorfer, P.; Schilcher, K.; Baumgartner, W.; Gruber, H. J.; Schindler, H. *Nanobiology* **1999**, *4*, 177-88.

(80) Vinckier, A.; Gervasoni, P.; Zaugg, F.; Ziegler, U.; Lindner, P.; Groscurth, P.; Pluckthun, A.; Semenza, G. *Biophysical Journal* **1998**, *74*, 3256-3263.

(81) Dammer, U.; Hegner, M.; Anselmetti, D.; Wagner, P.; Dreier, M.; Huber, W.; Güntherodt, H. J. *Biophys.J.* **1996**, *70*, 2437-2441.

(82) Ros, R.; Schwesinger, F.; Anselmetti, D.; Kubon, M.; Schafer, R.; Pluckthun, A.; Tiefenauer, L. *Proceedings of the National Academy of Sciences of the United States of America* **1998**, *95*, 7402-7405.

(83) Rief, M.; Oesterhelt, F.; Heymann, B.; Gaub, H. E. *Science . Feb* **1997**, *275*, 1295-1297.

(84) Li, H. B.; Rief, M.; Oesterhelt, F.; Gaub, H. E.; Zhang, X.; Shen, J. C. *Chemical Physics Letters. May* **1999**, *305*, 197-201.

(85) Moy, V. T.; Florin, E. L.; Gaub, H. E. *Science* **1994**, *266*, 257-259.

(86) Dammer, U.; Popescu, O.; Wagner, P.; Anselmetti, D.; Guntherodt, H.-J.; Misevic, G. N. *Science* **1995**, *267*, 1173-1175.

(87) Rief, M.; Gautel, M.; Oesterhelt, F.; Fernandez, J. M.; Gaub, H. E. *Science* **1997**, *276*, 1109-1112.

(88) Chen, X.; Davies, M. C.; Roberts, C. J.; Tendler, S. J. B.; Williams, P. M.; Davies, J.; Dawkes, A. C.; Edwards, J. C. *Langmuir* **1997**, *13*, 4106-4111.

(89) Luginbühl, R.; Pan, Y. V.; Overney, R. M.; Ratner, B. D. *in preparation* **2000**.

(90) Feldman, K.; Hahner, G.; Spencer, N. D.; Harder, P.; Grunze, M. *Journal of the American Chemical Society* **1999**, *121*, 10134-10141.

(91) Ludwig, M.; Dettmann, W.; Gaub, H. E. *Biophysical Journal* **1997**, *72*, 445-448.

(92) Willemsen, O. H.; Snel, M. M. E.; van der Werf, K. O.; de Grooth, B. G.; Greve, J.; Hinterdorfer, P.; Gruber, H. J.; Schindler, H.; van Kooyk, Y.; Figdor, C. G. *Biophysical Journal* **1998**, *75*, 2220-8.

(93) Raab, A.; Han, W. H.; Badt, D.; Smith Gill, S. J.; Lindsay, S. M.; Schindler, H.; Hinterdorfer, P. *Nature Biotechnology* **1999**, *17*, 902-905.

(94) Allen, S.; Davies, J.; Davies, M. C.; Dawkes, A. C.; Roberts, C. J.; Tendler, S. J. B.; Williams, P. M. *Biochemical Journal* **1999**, *341*, 173-178.

(95) Razatos, A.; Ong, Y. L.; Sharma, M. M.; Georgiou, G. *Proceedings of the National Academy of Sciences of the United States of America* **1998**, *95*, 11059-64.

(96) Razatos, A.; Ong, Y. L.; Sharma, M. M.; Georgiou, G. *Journal of Biomaterials Science, Polymer Edition* **1998**, *9*, 1361-73.

Chapter 13

Nanoscale Surface Mechanical Property Measurements: Force Modulation Techniques Applied to Nanoindentation

S. A. Syed Asif[1], R. J. Colton[2], and K. J. Wahl[2]

[1]Department of Materials Science, University of Florida, Gainesville, FL 32611
[2]Code 6170, Naval Research Laboratory, Washington, DC 20375–5342

Mechanical properties of surfaces and interfaces are important for understanding the behavior of adhesive and sliding contacts, where changes in interfacial properties can result from surface treatments, sliding processes, or contaminants. Recent advances combining nanoindentation, atomic force microscopy and force modulation techniques enable examination of surface mechanical properties with substantially improved force and spatial resolution, and enable *quantitative, dynamic* measurements of surface mechanical properties of nanoscale contacts. We present examples demonstrating quantitative, surface sensitive nanomechanics of thin films and compliant polymers, damping losses and the effects of water vapor. Additionally, we present a new, quantitative stiffness imaging technique for mechanical properties mapping at the nanoscale.

Materials properties measurements at submicron scales are important not only for characterization of ever smaller electronic and mechanical devices, but also for analyses of thin interfacial films controlling friction and adhesion. Two types of instruments have been developed to facilitate studies of thin films with high spatial resolution: the depth-sensing nanoindenter *(1)* and the atomic force microscope (AFM) *(2)*. Capabilities of both instruments have been extended through the use of AC modulation techniques, enabling continuous measurement of contact stiffness *(3-6)*, enhanced imaging capabilities *(7)*, and examination of polymer creep and viscoelastic properties *(8,9)*, for example. While both instruments can be used to determine materials properties at the nanoscale, there are distinct advantages and disadvantages to both techniques. New approaches coupling AFM and depth-sensing nanoindentation *(10-12)*, which we will refer to as hybrid nanoindentation, can

198

provide the best of both techniques. In this paper, we will discuss these approaches, as well as present recent progress and examples from work carried out at NRL to develop surface sensitive, quantitative nanoscale mechanical property analyses for thin films and polymer surfaces.

Background: Mechanical Properties Measurements via Nanoindentation

Indentation has been used for over 100 years to determine hardness of materials *(13)*. For a given indenter geometry (e.g. spherical or pyramidal), hardness is determined by the ratio of the applied load to the projected area of contact, determined optically after indentation. Interest in properties of materials with smaller dimensionality (e.g. thin films and microstructures) required lower load indentation and a new way of determining the indent size, due to optical limitations. Depth-sensing nanoindentation *(1)* was developed to eliminate the need to visualize the indents, and resulted in the added capability of measuring properties like elastic modulus, E, and creep.

DC Techniques

Depth-Sensing Nanoindentation

For depth-sensing nanoindentation, a controlled, variable force is applied to a sample by the indenter and the resulting displacement of the indenter is measured. The resulting "load vs. displacement" data, together with the indenter geometry, can be analyzed to obtain hardness and elastic modulus using well established mechanical models *(14)*. The simultaneous measurement of load and displacement also allows study of creep (time dependent strain response due to a step change in stress) *(15,16)*.

In general, the instrument configuration for depth-sensing nanoindentation is a parallel plate geometry sandwiching a plate held by leaf springs between two rigid, parallel plates (Fig. 1a). A diamond indenter tip, attached to a shaft, is mounted to the middle plate, and is accommodated by a small hole in the center of the lowest plate. A force, F, is generated by applying a voltage between the middle plate by the bottom
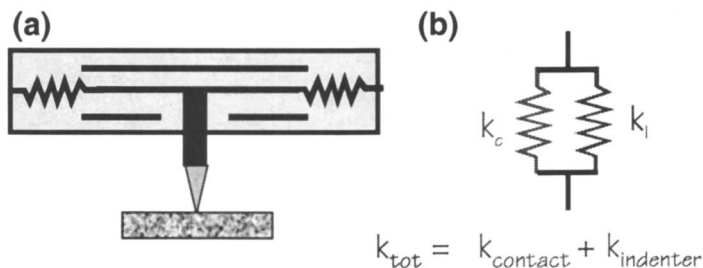
Figure 1. (a) indenter model and (b) simple mechanical model for force controlled indentation assuming purely elastic mechanics.

plate through electrostatic actuation, and the resulting displacement measured by change in capacitance between the middle plate and the outer plates. An advantage of force-controlled operation is that indentation is not limited to contacts with lower stiffness than the indenter spring stiffness, since the force is applied to the indenter against the spring by electrostatics; the simple mechanical model (two springs in parallel) is shown in Fig. 1b.
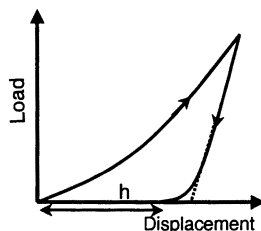
Figure 2. Typical load-displacement graph for elasto-plastic indentation.

A typical load-displacement curve is shown in Fig. 2. The loading portion of the curve results from both plastic and elastic deformation response of the contact, while the unloading portion of the curve is related to the elastic recovery of the contact. If the indenter geometry and materials properties are known, the modulus can be obtained by fitting the unloading curve to determine the contact stiffness at maximum load *(14, 17)*. In this case,

$$E^* = \frac{\sqrt{\pi} \cdot slope}{2\sqrt{A}} \tag{1}$$

where E^* is the reduced modulus ($E^* = [(1-\nu_1^2)/E_1 + (1-\nu_2^2)/E_2]^{-1}$) and A is the projected contact area determined from indenter geometry and penetration depth. Generally, the hardness can be determined by measuring the residual contact depth, h, to determine A *(14)*.

AFM-Based Nanoindentation

Mechanical properties of materials can also be obtained through analyses of force-distance curves generated with an AFM. In the AFM, measurements are displacement controlled – the sample is displaced against a cantilever indenter via a piezoelectric actuator - and forces are inferred from the measured deflection of the cantilever and its (nominally) known spring constant. Several different cantilever configurations and displacement detection schemes have been used for these measurements (Fig. 3a) *(18)*. Early work by Burnham and Colton *(19)* employed double beam and crossed beam spring configurations, with spring deflection measured via STM tunneling current. More recently, simple diving-board cantilevers and optical detection are being used *(20-22)*. Because the AFM uses displacement control configuration, the simple mechanical model is that of two springs in series (Fig. 3b). This simple difference has several ramifications for indentation via AFM. First, the indenter spring stiffness must be matched to the contact stiffness in order to get a

measurable deformation in the sample itself, rather than simple deflection of the cantilever spring. Secondly, depth of penetration (and projected contact area), for all but the most compliant materials, is difficult to determine due to piezo creep and hysteresis effects *(23)*.
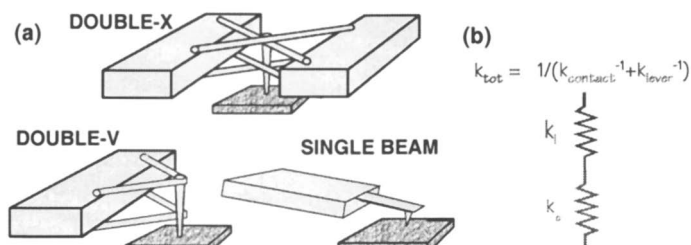
Figure 3 (a) Various AFM cantilever configurations for indentation experiments and (b) simple mechanical model for AFM indentation (by sample displacement).

Trends in the unloading slopes of force-distance curves for various materials pairs examined (gold/nickel, diamond/graphite, diamond/diamond) were consistent with expected relative reduced moduli (Fig. 4) *(24)*. However, because of the difficulty in determining indenter penetration relative to the sample surface for these relatively stiff materials, only qualitative results could be obtained. Semi-quantitative measurements may be possible under certain circumstances (e.g. compliant elastomers) *(22)* where tip penetration into the sample is significant. However, the indentation geometries involving non-perpendicular tip-sample approach result in significant lateral force
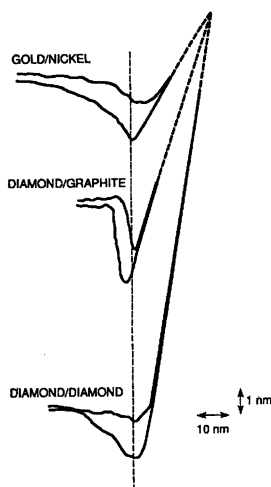
Figure 4. AFM force curves showing slope differences for different material pairs Reprinted with permission from reference (24). Copyright 1994 Institute of Physics.

contributions during indentation (evidenced by asymmetrical indents) *(20)*. Additionally, the compliant materials systems accessible with this approach often have significant time-dependent materials properties (e.g. creep relaxation and viscoelastic behavior) that complicate (and even prevent) analyses of mechanical properties from simple force-displacement curves *(25)*.

AC Modulation Techniques

Depth-Sensing Nanoindentation

By adding a small AC modulation to the force during experiments, and monitoring displacement with a lock-in amplifier, Pethica and Oliver *(3)* demonstrated they could obtain contact stiffness ($\partial F/\partial x$) continuously throughout the indentation. Hardness and modulus vs. depth information, as well as tip characterization, previously obtained by performing multiple indents and analyzing unloading slopes at many different depths, could be performed in one single experiment. Quantification of the data depends on obtaining accurate dynamic characterization of the instrument (dynamic response vs. frequency), and applying an appropriate dynamic mechanical model *(3)*.

The addition of AC force modulation to the nanoindentation measurements increases sensitivity to elasto-plastic deformation and creep, as well as enables examination of damping or loss properties of materials, critical for determining mechanical properties of polymers *(8)*.

AFM-Based Nanoindentation

AC modulation techniques have become commonplace in AFM instrumentation over the last few years, in many cases for the enhanced imaging capabilities it affords. All but one of these modulation techniques involve displacement modulation, either of the sample (z-modulation) *(26-29)* or of the tip holder - depending on frequency of modulation, so-called "tapping mode" near cantilever resonance but above feedback frequency *(30)*. The appropriate dynamic mechanical models and responses for these systems are reviewed by Burnham et al. *(31)*. Quantitative analysis of mechanical properties from these techniques has been attempted *(29,32,33)*, but is complicated due to displacement (not force) modulation and difficulty of knowing contact area. Jarvis et al. *(34,35)* demonstrated force modulation with AFM using a current carrying coil and permanent magnet affixed to the end of a cantilever; therefore the models described above for depth-sensing nanoindentation are applicable, although cantilever calibration and approach angle may be problematic. This is the only technique using AFM cantilevers that truly involves *force* modulation; all the other methods involve displacement modulation *(31)*, but are often misrepresented as force modulation in the literature.

Experimental Procedures and Equipment

Our recent work at the Naval Research Laboratory (NRL) has focused on developing quantitative mechanical properties measurements using hybrid nanoindentation techniques that couple depth sensing nanoindentation with AFM sample positioning and imaging capabilities. Hybrid indentation provides significant advantages over traditional (force controlled) and AFM-based (displacement controlled) nanoindentation instrumentation, eliminating many of the weaknesses of either technique. Specifically, depth-sensing nanoindentation provides accurate load control, high displacement accuracy, and normal (perpendicular) sample loading, while the AFM scanner electronics provide high lateral resolution and imaging. The experiments described in this work have been performed with a Hysitron, Inc. Triboscope nanoindenter coupled with a Digital Instruments Nanoscope IIIa AFM. We have modified the instrumentation to enable AC force modulation by adding a lock-in amplifier, voltage summing electronics, amplifier and break-out boxes (Fig. 5) *(12)*.
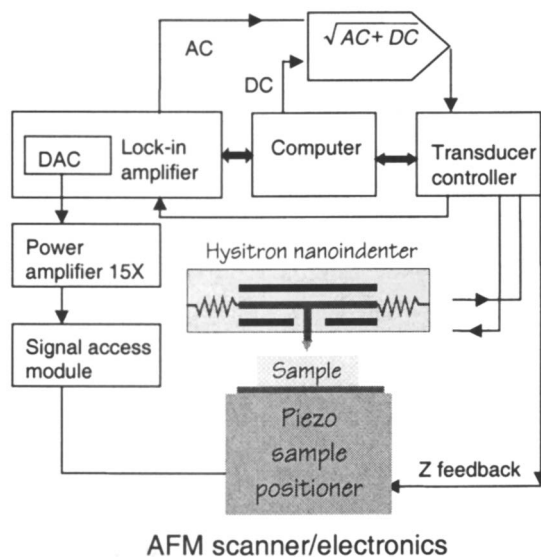
Figure 5. Schematic diagram of hybrid nanoindenter apparatus.

Detailed explanations of AC force modulation techniques and analyses can be found in the literature *(3,8,12)*. Briefly, for a superimposed force $F = F_o \sin \omega t$, there is a corresponding steady-state displacement oscillation at the same frequency given by $x = X_o \sin (\omega t - \phi)$. Using the dynamic model shown in Fig. 6a, an analytical solution for the resulting displacement amplitude, X_o, and phase shift, ϕ, can be found

if the machine frame stiffness is assumed to be infinite. The solution for displacement amplitude is

$$X_O = \frac{F_O}{\sqrt{\left(k - m\omega^2\right)^2 + \left[\left(C_i + C_s\right)\omega\right]^2}} \qquad (2)$$

and phase shift between the applied force and measured displacement is

$$\phi = \tan^{-1}\frac{\left(C_i + C_s\right)\omega}{k - m\omega^2} \qquad (3)$$

where ω is the frequency in rad/s, C_i is the damping coefficient of the air gap in the displacement transducer, m is the indenter mass, and C_s is the damping coefficient of the sample. The combined stiffness of the sample and indenter, k, is given by

$$k = K_s + K_i \qquad (4)$$

where K_s is the sample stiffness and K_i is the indenter spring stiffness. The contact stiffness, $k = (\partial F/\partial x) = F_o/X_o$, at any point in an indentation experiment is given by equation (1), where *slope* is replaced by stiffness k. Thus if either the sample's modulus, E, or contact area, A, is known, the other can be determined from this relationship *(14)*; if the modulus is known the hardness can also be measured. Viscoelastic materials that can damp the AC force have both storage K_s' (in phase) and loss $K_s'' = \omega C_s$ (90° out of phase) components of stiffness; if both are known then storage and loss moduli can be obtained from eq. (1).
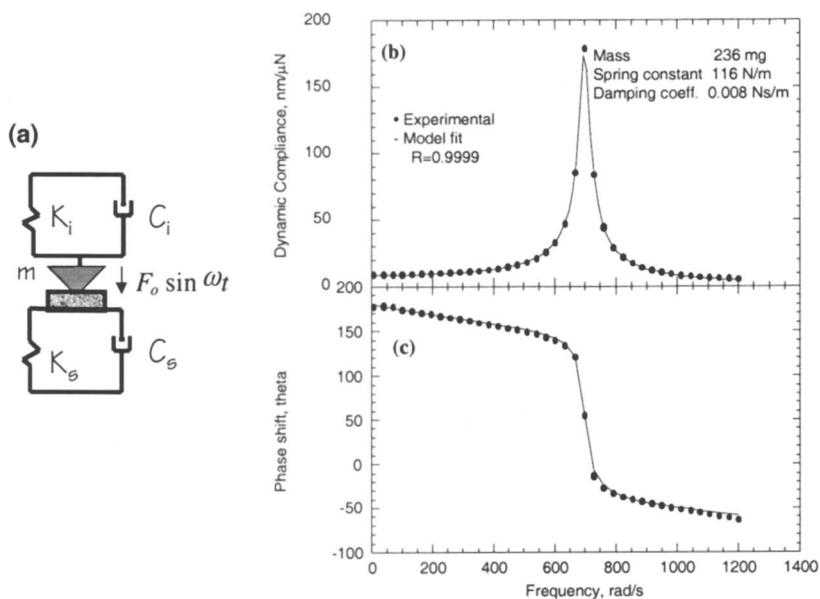
Figure 6. (a) Dynamic model (see accompanying text), (b) dynamic compliance and (c) phase response of the freely suspended indenter. Reprinted with permission from reference (12). Copyright 1999 American Institute of Physics.

Figure 6b and c shows the dynamic compliance and corresponding phase shift of the indenter (uncorrected for electronics). The response was fit to the model in Fig. 6a; for this indenter the damping coefficient, C_i is 0.008 Ns/m, resonance frequency, ω_0 is 110 Hz, indenter mass, m is 236 mg, and spring constant, K_i is 116 N/m. A Berkovich diamond indenter with a tip radius of ~200 nm was used for all experiments. Tip shape calibration and machine compliance were determined by standard techniques *(14)* using electropolished indium and quartz.

Results and Discussion

DC vs. AC Measurements

There are often several methods for measuring the same mechanical properties. As mentioned previously, AC techniques provide the added advantages of enabling time-dependent measurements like damping loss and creep as well as enhancing sensitivity. Here we provide two examples of how AC force modulation contributes information not available through more standard DC experiments.

Spring Stiffness and Damping Loss
Spring stiffness measurements are a good example to illustrate and compare the DC and AC measurement techniques described above. Figure 7 shows a force-displacement curve for the indenter against the end of a small Ta cantilever attached
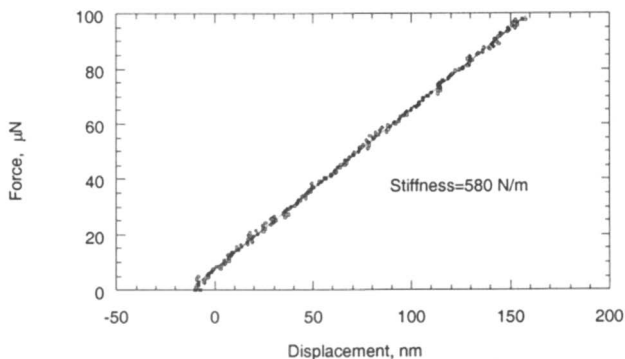
Figure 7. Load-displacement data for tantalum cantilever. The slope is the combined stiffness of the cantilever and indenter; lever stiffness was measured as 580 N/m. Reprinted with permission from reference (12). Copyright 1999 American Institute of Physics.
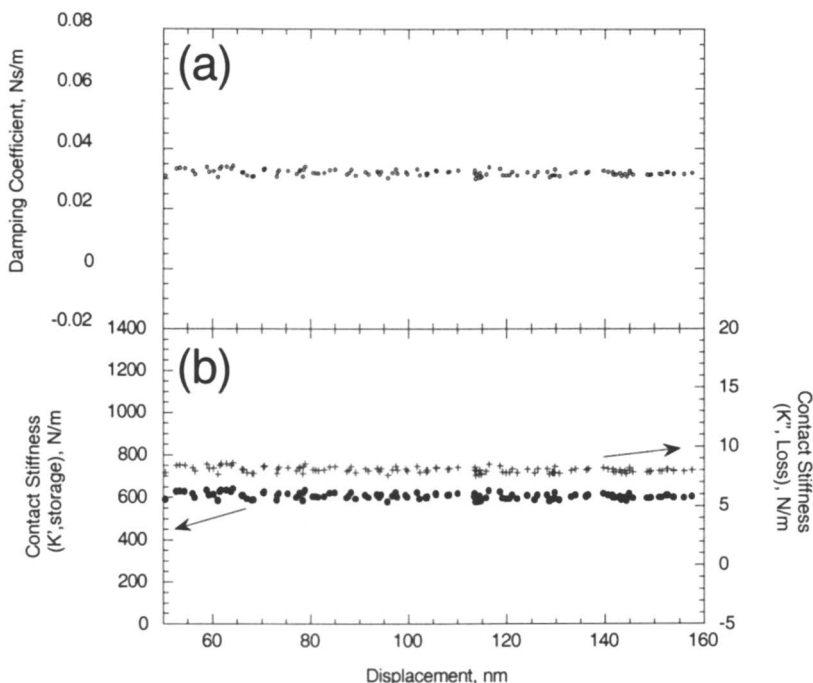
Figure 8. (a) Damping coefficient and (b) stiffness (storage and loss components) of tantalum cantilever glued to glass substrate. Reprinted with permission from reference (12). Copyright 1999 American Institute of Physics.

to a glass substrate via superglue *(12)*. The stiffness of the Ta cantilever was determined by subtracting the indenter spring stiffness (116 N/m) from the slope of the force-displacement curve, and found to be 580 N/m (r=0.98).

For comparison, AC measurements were made using an AC force of 300 nN at 40 Hz during loading and unloading. Interestingly, the measured phase shift and amplitude of the AC displacement response revealed that the cantilever, which was expected to behave like an ideal spring, was actually damped. Figure 8a shows the damping coefficient as a function of displacement using Eq. (3); the main source of damping was likely the glue used to mount the lever on the substrate. Storage and loss components of stiffness were also calculated from the data, and are shown in Fig. 8b. The storage component of the stiffness was 600 ± 10 N/m, in agreement with that measured by the DC technique. The loss component was about 8 ± 1 N/m, demonstrating the importance of rigidly mounting samples for nanoindentation experiments so as not to influence the mechanical response of the system under investigation. The sensitivity of the AC technique is about 0.1 N/m, enabling spring constant determination of small levers used by the AFM and micro-electromechanical systems (MEMS) communities.

Low Modulus Polymer Mechanical Properties

Measuring the mechanical properties of very compliant materials by indentation is difficult because the indenter springs are generally several orders of magnitude stiffer than the contact stiffness. Larger contact areas (e.g. spherical indenters) can be used, but that may defeat the purpose by reducing lateral resolution significantly. The upper plot in Fig. 9 shows the DC load-displacement curve for an indentation against poly-isoprene. The data are linear, demonstrating elastic behavior of the contact, with a slope of 117 ± 1 N/m. However, the stiffness of the indenter itself is 116 N/m, and subtracting this value to obtain the contact stiffness (Eq. 4) leaves a value within the uncertainty of the measurement. By making the same measurement, but adding AC force modulation (AC force of 300 nN at 40 Hz), the contact stiffness throughout the load-displacement curve was obtained (Fig. 9, lower plot). Using experimentally determined tip shape data and a literature value for Poisson's ratio *(36)*, the elastic modulus of the poly-isoprene sample was found to be 1.1 ± 0.4 MPa. This compares favorably with other values found in the literature *(36,37)*.
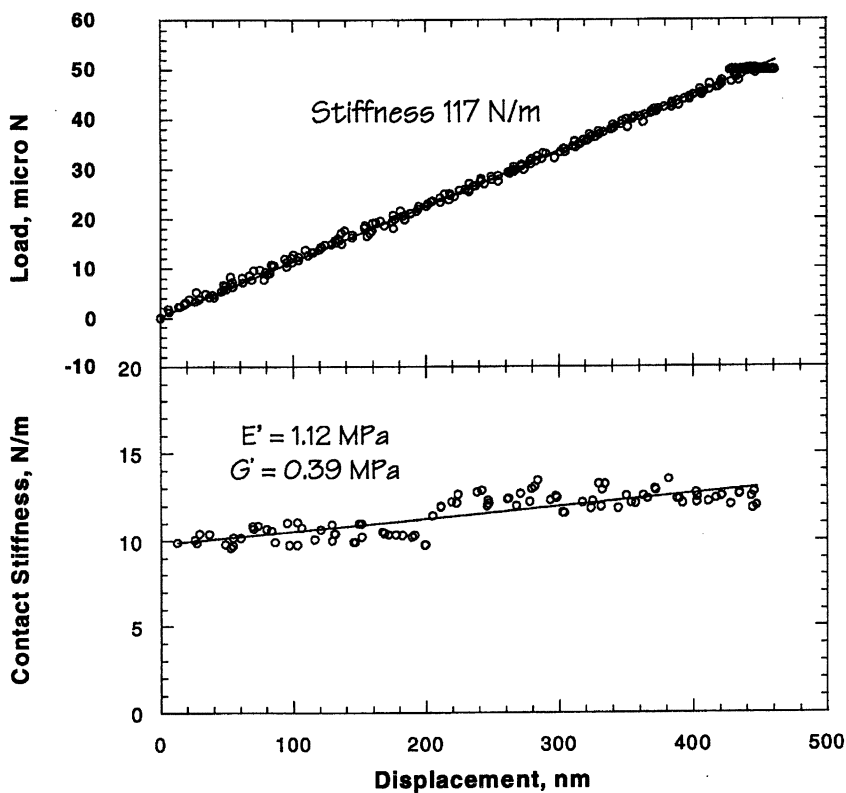
Figure 9. Load-displacement data and contact stiffness for poly-isoprene.

Surface Spectroscopy – Force/Stiffness Measurements and Imaging

Surface Sensitivity and Finding the Surface

One of the challenges in nanoindentation involves detecting the sample surface (before indentation): specimens may undergo damage on approach, and very compliant samples might not be sensed at all (as in the case shown in Fig. 9). Monitoring the dynamic response of the nanoindenter during tip-sample approach provides a very sensitive way to determine the location of the surface prior to indentation and provides a mode of force-distance curve acquisition *(12,38)*. Due to the large phase shift at resonance (Fig. 6), any change in dynamic compliance due to tip-surface interaction results in a large phase shift. For example, if the indenter driving (AC force modulation) frequency is slightly less than the resonance frequency (110 Hz) during the tip-specimen approach, an increasing attractive force (positive force gradient) shifts the resonance frequency to lower frequency. The attractive force results in increased dynamic compliance (decreased stiffness) and decrease in phase (Fig. 6). If the tip-sample distance is decreased further, repulsive interactions can also be sensed by increased interaction stiffness and increased phase shift.
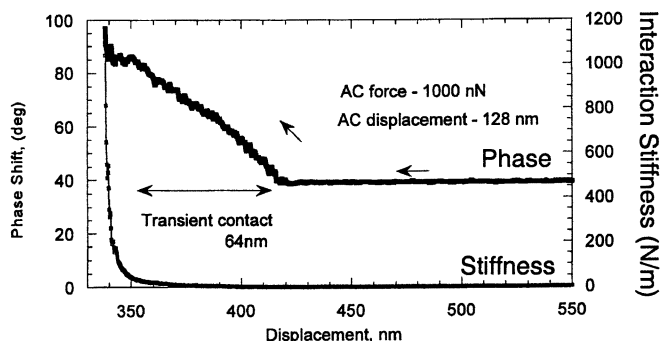
Figure 10. Tip-sample approach curve showing phase response and calculated interaction stiffness.

An example of this approach to finding a sample surface is shown in Fig. 10 above. In this case, a large AC force of 1000 nN was applied to the indenter spring, and the tip-surface separation controlled by the AFM piezo. When the tip and sample begin to interact, significant shifts in the phase are observed, and eventually a sharp increase in phase is observed. Interaction stiffness was calculated from the amplitude and phase response and is shown in the same plot. From this it can be seen that the sharp increase in phase occurs after the sharp increase in contact stiffness. There is a large region of "transient contact" (~64 nm) due to the large AC force used which resulted in a 64 nm displacement amplitude (128 nm total displacement) of the tip. Using much smaller AC forces results in more sensitive surface detection and reduced transient contact. By monitoring the phase shift during the force-distance approach,

one can choose to retract the tip at any point, producing a force-curve and interaction stiffness curve. This allows adhesive and repulsive interactions to be examined more directly.

We have used the above approach to examine pre-contact and apparent contact regimes for various ceramic, metallic and polymer surfaces. An example of stiffness interaction and force curves for a Si surface with a native oxide at ~56% relative humidity (RH) is shown in Fig. 11. The AC force is ~20 nN. The stiffness data initially show a downward deflection (negative with respect to the cantilever stiffness, which has been subtracted) indicating an adhesive interaction between the tip and substrate. The stiffness soon turns positive, and upon retraction shows significant hysteresis; the hysteresis is due to a real change in contact area from surface deformation and is not an experimental artifact. The corresponding force-displacement curve shows that the maximum force during indentation was 300 nN, and confirms that even at this low load that the unloading was not reversible and the deformation not elastic. The negative stiffness and adhesive force observed during retraction is consistent with capillary condensation *(39)*. Estimation of surface energy from this data set and others gave results between 60 and 80 mJ/m *(38)*, consistent with the surface energy of water (72 mJ/m) *(39)*.
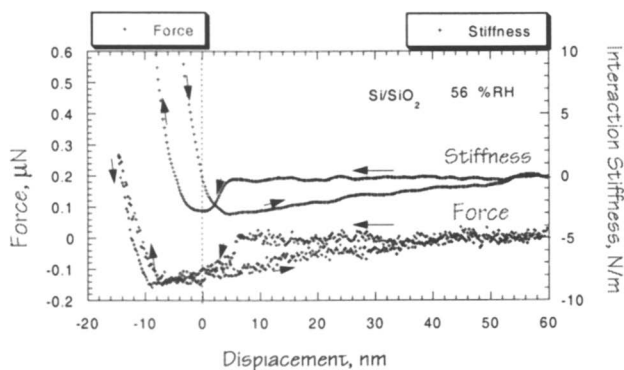
Figure 11. Force and interaction stiffness curves during approach (←) and retraction (→) (38).

The data in Fig. 11 show an offset between the force and stiffness minima in the approach and retraction curves. The explanation for this is shown in Fig. 12, which illustrates the relationship between potential, force and interaction stiffness. These curves provide a basis for determining where the contact point with the surface is located. One definition of contact is the position on the curve where the repulsive force can first be detected *(see 24)*, typically identified by a change in curvature of the force-displacement data *(3)*. Therefore, the force gradient (stiffness-displacement data) reveals more clearly the attractive to repulsive transition. The initiation of repulsive contact is thus found from the minimum of the stiffness approach curve (marked at 0 nm), which marks the maximum attractive interaction stiffness. The stiffness data represent a convolution of force gradient and contact stiffness and is

therefore not as narrow as expected for a true evaluation of surface potential; sharper tips and better force resolution are needed for such a measurement.

Finally, for most surfaces we have examined, the maximum interaction stiffness is not greater than the nanoindenter spring stiffness. This allows the attractive part of the
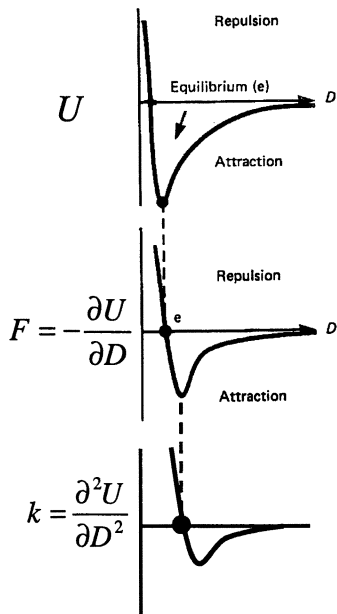
Figure 12. (a) Surface potential, (b) potential gradient (force), and (c) force gradient (stiffness). Adapted with permission from reference (40). Copyright 1991 Academic Press, Inc.
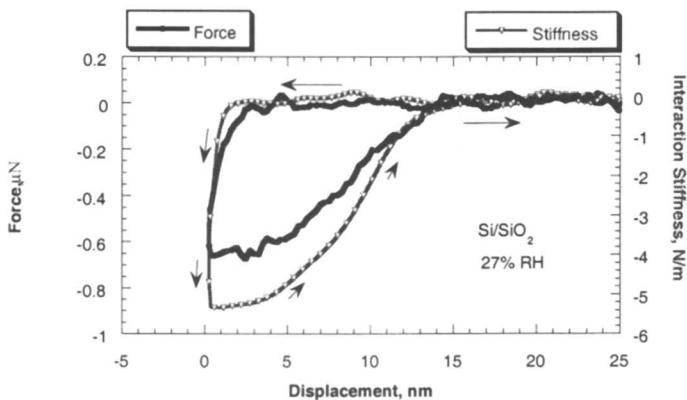
Figure 13. Force-displacement and stiffness-displacement curves showing only attractive interaction.

interaction to be probed while avoiding the problem called "jump-to-contact" experienced in AFM when cantilevers with low stiffness are used. Fig. 13 shows force and stiffness vs. displacement curves for a Si surface with native oxide in 27% RH environment. Both force and stiffness data are consistent with a purely attractive interaction.

Hydrophobic/Hydrophilic Si Surfaces and Humidity

The above spectroscopic techniques were used to examine tip-surface interactions between the diamond indenter and hydrophobic and hydrophilic Si surfaces *(38)*. Surfaces were prepared as hydrophobic using a HF etch and hydrophilic by pirhana etch; oxide film thickness of the treatments were measured by ellipsometry to be 1 nm and 5 nm, respectively. Numerous stiffness-displacement curves were obtained for the as prepared surfaces in dry (<2% RH) conditions, and as the humidity was increased, then decreased. Adhesion interaction lengths (pull-off lengths) were determined from the stiffness-displacement curves by evaluating the distance between the point of contact (0 nm displacement in Fig. 11) and the distance where the interaction stiffness returned to 0 N/m during retraction of the tip from the surface (50 nm in Fig. 11). The top two plots shown in Fig. 14 show the measured pull-off lengths for both surface treatments at various humidities. The pull-off lengths varied considerably depending on surface treatment and humidity, and can be attributed to meniscus formation. The effects of humidity were much greater for the hydrophilic surface, where pull-off lengths were an order of magnitude larger above 60% RH. An estimate of changes occurring in the mechanical properties of the surfaces during these experiments was obtained by examining the ratio of the stiffness (K) vs. the penetration depth (h) (obtained from the repulsive regime, to the left of 0 nm as in Fig 11); this ratio, K/h, is proportional to the reduced modulus of the surface/indenter and is plotted in Fig. 14
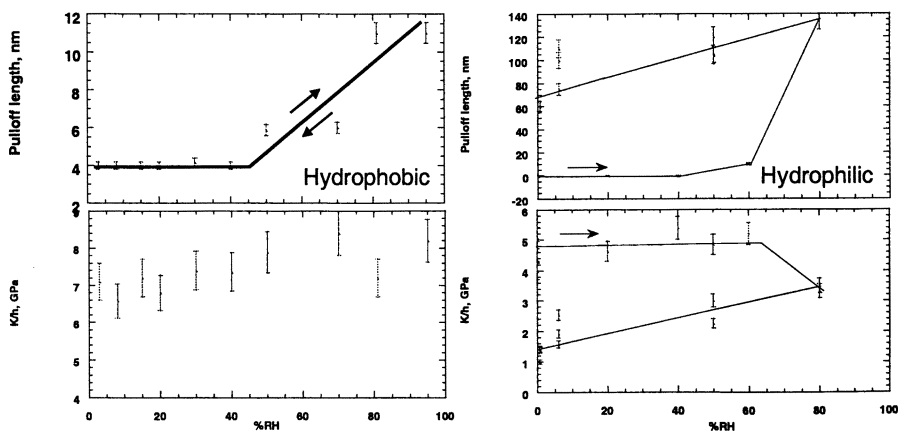
Figure 14. Influence of humidity on pull-off length and ratio of stiffness/penetration depth for hydrophobic (left) and hydrophilic (right) Si/SiO₂ surfaces.

(lower left and right plots) for hydrophobic and hydrophilic surfaces. The stiffness-penetration ratio for the hydrophobic surface did not change appreciably with exposure to humidity, while the hydrophilic surface showed a clear, irreversible reduction in K/h ratio.

For both pull-off length and K/h ratio, the behavior of the hydrophobic surface was fully reversible when humidity was removed. On the other hand, the irreversibility of the hydrophilic surfaces pull-off lengths suggests that water remained on these surfaces. The reduced K/h ratio for the hydrophilic surfaces indicates a lower reduced modulus, suggesting that the surface oxide film has been modified by the exposure to water vapor. Whether the oxide layer became thicker or could be returned to the initial state by heating to drive off adsorbed water was not examined. Low-load indentation experiments demonstrated that these 1-5 nm oxide films altered the indentation behavior of Si surfaces (38).

Mapping the Surface: Stiffness Imaging

The examples presented above are all single point measurements and do not fully take advantage of the scanning capabilities provided by the AFM base. Ideally, one would like to produce an image of sample properties (e.g. map modulus and loss properties) quantitatively and quickly, in an image format. One approach would be to collect multiple force-distance curves over the sample area. This technique of force-curve mapping (41) is very time consuming (a separate force-distance curve is made for each data point in an image) even if the force curves are made rapidly; additionally, materials with time dependent behavior would prove difficult to study.
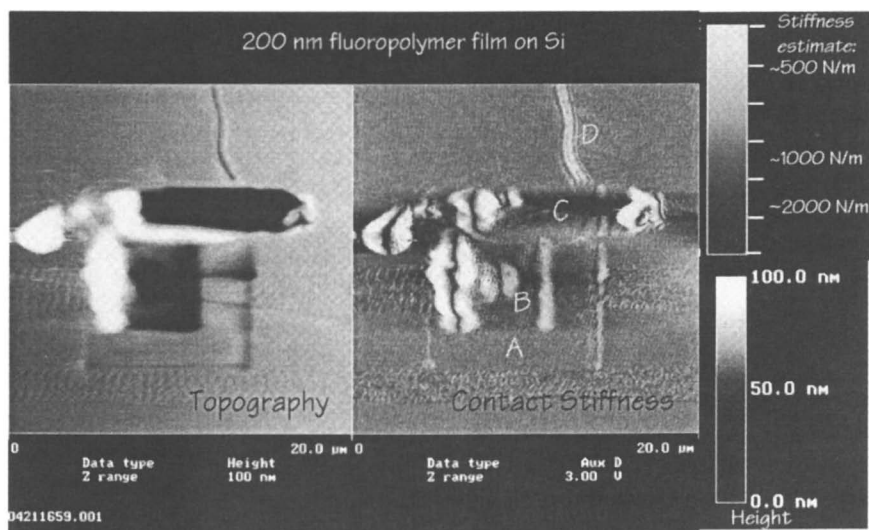
Figure 15. Topography (left) and contact stiffness (right) images obtained of 200 nm thick fluoropolymer film on Si using 300 nN AC force modulation at 200 Hz.

Applying the force modulation technique discussed in this paper with the nanoindenter is possible, but would be particularly inefficient as the force-distance curve acquisition is slow due to the low modulation frequency applied (~100 Hz). Instead, we have chosen to apply the modulated force during contact mode imaging *(42)*. Specifically, during contact mode imaging a ~ 1μN force is applied to the sample. On top of that force, we superimpose a small AC modulated force (10-300 nN). By monitoring amplitude response (Δx), the stiffness of the contact (ΔF/Δx) can be obtained in an image format, alongside topographic data.

An example is shown in Fig. 15. The image is of a thin (200 nm thick) fluoropolymer film deposited on Si via plasma enhanced chemical vapor deposition (PECVD) *(43)*. On the left side of the image is topography data and on the right, the corresponding displacement response of the contact. Contrast in the stiffness image is due to displacement response to the modulated force and is therefore inverted (dark features are higher stiffness and bright features are lower in stiffness). The features in the image were generated by damaging the film, which was uniform and featureless before scanning. The topography image shows regions of thinned film (A) and heavily damaged film (B,C), and a scratch (D). The contact stiffness image reveals all of these features. For example, topography effects on contact area are seen in the edge effects in the image. The stiffness image contrast in and out of the slightly worn area (A) are similar, indicating similar materials properties. Bright regions in the image reveal debris pile up and delamination of the film, and the dark region in the center of the image is consistent with thinning or removal of the film.

The quantitative stiffness image above provides a first step towards quantitative mapping of modulus and loss properties of surfaces. Difficulties to overcome in converting the stiffness data to elastic modulus arise from the need to know the tip-sample penetration at each point in the image, and to mask the low frequency AC modulation from the scanning feedback electronics. Despite these difficulties, such scanning techniques provide great promise towards the goal of quantitative mechanical properties measurements of surfaces.

Summary

This paper summarizes work in nanomechanics using AC force modulation conducted at NRL. It represents recent progress on the way to a goal of *quantitative, dynamic* measurements of surface mechanical properties and nanoscale sliding contacts. Through the examples given, we have demonstrated quantitative, surface sensitive nanomechanics of thin films and compliant polymers, and the ability to examine damping losses and the effects of water vapor. Finally, new, more powerful techniques such as stiffness imaging hold the promise of quantitative mechanical properties mapping at the nanoscale.

Acknowledgements

References

1. Pethica, J. B.; Hutchings, R.; Oliver, W. C. *Philos. Mag. A* **1983**, 48, 593.
2. Binnig, G.; Quate, C. F.; Gerber, Ch. H. *Phys. Rev. Lett.* **1986**, 56, 930.
3. Pethica, J. B.; Oliver, W. B. *Phys. Scr.* **1987**, T19, 61.
4. Tonck, A.; George, J. M.; Loubet, J.-L. *J. Coll. Int. Sci.* **1988**, 126, 150.
5. Carpick, R. W.; Ogletree, D. F.; Salmeron, M. *Appl. Phys. Lett.* **1997**, 70, 1548.
6. Lantz, M. A.; O'Shea, S. J.; Hoole, A. C. F.; Welland, M. E.; Johnson, K. L. *Phys. Rev. B* **1997**, 55, 10776.
7. Zhong, Q.; Innis, D.; Kjoller, K.; Elings, V.B. *Surf. Sci. Lett.* **1993**, 290, L688.
8. Asif, S. A. S., Thesis, 1997 (Oxford, UK).
9. Wahl, K. J.; Stepnowski, S. V.; Unertl, W.N. *Tribol. Lett.* **1998**, 5, 103.
10. Bhushan, B.; Kulkarni, A. V.; Bonin, W.; Wyrobek, J. T. *Philos. Mag. A* **1996**, 74,1117.
11. Stephen, A. J.; Houston, J. E. *Rev. Sci. Instrum.* **1990**, 62, 710.
12. Asif, S. A. S.; Wahl, K. J.; Colton, R. J. *Rev. Sci. Instrum.* **1999**, 70, 2408.
13. Tabor, D. *The Hardness of Metals*, Oxford: London, 1951.
14. Oliver, W. C.; Pharr, G. M. *J. Mater. Res.* **1992**, 7, 1564.
15. Asif, S. A. S.; Pethica, J. B. *Phil. Mag. A* **1997**, 76, 1105.
16. Asif, S. A. S.; Pethica, J. B. *J. Adhesion* **1998**, 67, 153.
17. Doerner, M. F.; Nix, W. D. *J. Mater. Res.* **1986**, 1, 601.
18. Burnham, N. A.; Colton, R.J. *Scanning Tunneling Microscopy and Spectroscopy: Theory, Techniques and Applications;* Ed. D. A. Bonnell; VCH Publishers, Inc., New York, NY, 1993, Chapter 7, p.232.
19. Burnham, N. A.; Colton, R.J. *J. Vac. Sci. Technol. A* **1989**, 7, 2906.
20. VanLandingham, M. R.; McKnight, S. H.; Palmese, G. R.; Eduljee, R. F.; Gillespie, J. W., Jr.; McCulough, R. L. *J. Mater. Sci. Lett.* **1997**, 16, 117.
21. VanLandingham, M. *Microscopy Today* **1997**, 97, 12.
22. VanLandingham, M. R.; McKnight, S.H.; Palmese, G.R.; Elings, J. R.; Huang, X.; Bogetti, T. A.; Eduljee, R. F.; Gillespie, J. W., Jr. *J. Adhesion* **1997**, 64, 31.
23. Hues, S. M.; Draper, C. F.; Lee, K. P.; Colton, R. J. *Rev. Sci. Instrum.* **1994**, 65, 1561.
24. Burnham, N. A.; Colton, R. J.; Pollock, H. M. *Nanotechnology* **1993**, 4, 64.
25. Briscoe, B. J.; Fiori, L.; Pelillo, E. *J. Phys. D: Appl. Phys.* **1998**, 31, 2395.
26. Kolosov, O.; Yamanaka, K. *Jpn. J. Appl. Phys.* **1993**, 32, L1095.

27. Kajiyama, T.; Tanaka, K.; Ohki, I.; Ge, S.-R.; Yoon, J.-S.; Takahara, A. *Macromolecules* **1994**, 27, 7932.
28. Overney, R. M.; Meyer, E.; Frommer, J.; Güntherodt, H.-J.; Fujihira, M.; Takano, H.; Gotoh, Y. *Langmuir* **1994**, 10, 1281.
29. Burnham, N. A.; Kulik, A. J.; Gremaud, G.; Gallo, P.-J.; Oulevey, F. *J. Vac. Sci. Technol. B* **1996**, 14, 794.
30. Maivald, P.; Butt, H. J.; Gould, S. A. C.; Prater, C. B.; Drake, B.; Gurley, J. A.; Elings, V. B.; Hansma, P. K. *Nanotechnol.* **1991**, 2, 103.
31. Burnham, N. A.; Gremaud, G.; Kulik, A. J.; Gallo, P.-J.; Oulevey, F. *J. Vac. Sci. Technol. B* **1996**, 14, 1308.
32. Tanaka, K.; Taura, A.; Ge, S.-R.; Takahara, A.; Kajiyama, T. *Macromolecules* **1996**, 29, 3040.
33. Overney, R.M.; Leta, D.P.; Pictroski, C.F.; Rafailovich, M.H.; Liu, Y.; Quinn, J.; Sokolov, J.; Eisenberg, A.; and Overney, G. *Phys. Rev. Lett.* **1996**, 76, 1272.
34. Jarvis, S.P.; Weihs, T.P.; Oral, A.; Pethica, J. B. *Thin Films: Stresses and Mechanical Properties IV*, MRS Symposium Proceedings; MRS: Pittsburgh, PA, 1993, Vol. 308; pp127-132.
35. Jarvis, S.P.; Weihs, T.P.; Oral, A.; Pethica, J. B. *Rev. Sci. Instrum.* **1993**, 64, 3155.
36. Pyne, A. R.; *Rheology of Elastomers*; Pergamon Press: London, 1958.
37. Loubet, J. L.; Lucas, B. N.; Oliver, W. C. *NIST Special Publication No. 896*; National Institute of Standards and Technology, Gaithersburg, MD, 1996.
38. Asif, S. A. S.; Wahl, K. J.; Colton, R. J. *J. Mater. Res.* **2000**, 15, 546.
39. Israelachvili, J.N.; Tabor, D. *Proc. R. Soc. London Ser. A* **1972**, 331, 19.
40. Israelachvili, J.N. *Intermolecular and Surface Forces;* Academic Press: New York, NY, 1991; p.164.
41. Koleske, D.D.; Lee, G. U; Gans, B. I.; Lee, K. P.; DiLella, D. P.; Wahl, K. J.; Barger, W. R.; Whitman, L. J.; Colton, R. J. *Rev. Sci. Instrum.* **1995**, 66, 4566.
42. Asif, S. A. S.; Wahl, K. J.; Colton, R. J., *Thin Films: Stresses and Mechanical Properties VIII*, MRS Symposium Proceedings; MRS: Pittsburgh, PA, 2000, Vol. 594, in press.
43. Labelle, C. B.; Gleason, K. K. *J. Vac. Sci. Technol. A* **1999**, 17, 445.

Chapter 14

A New, Reactive Potential Energy Function to Study the Indentation and Friction of *n*-Alkane C$_{13}$ Monolayers

Judith A. Harrison[1,3], Steven J. Stuart[2], and Alan B. Tutein[1]

[1]Department of Chemistry, U.S. Naval Academy, Annapolis, MD 21402
[2]Department of Chemistry, Clemson University, Clemson, SC 29634

The indentation and friction properties of *n*-alkane C$_{13}$ chains chemically bound to a diamond (111) surface have been examined using molecular dynamics simulations and a newly developed potential energy function. Both a *flexible* and a *rigid* single-wall, capped (10,10) nanotube were used in the indentation and friction simulations. Gauche defects were formed during indentation of the C$_{13}$ monolayer with both nanotubes. The flexibility of the nanotube, the depth of penetration, and the speed of indentation all affected the number of defects formed. Sliding simulations demonstrate that flexible single-wall nanotubes may not be suitable as scanning probe microscope tips for the study of tribology. Rupture of chemical bonds within the monolayer was possible during indentation and sliding under certain conditions.

Scanning probe microscopies have proven invaluable for the examination of the molecular structure, mechanical properties, and tribological properties of self-assembled monolayer (SAM) systems (1-9). Interest in these organic films has grown recently due to their potential application as boundary layer lubricants in microelectromechanical systems (10-11) and magnetic storage devices (12-14). Adhesion of these films to a given substrate is important in applications that involve solid surfaces in sliding contact. In addition, because the thickness of these lubricating films is in the monolayer regime, adhesion to the substrate is also critical. Thus, molecules that are covalently bonded to the substrate such as those formed from self-assembly, are better candidates for boundary layer lubricants than Langmuir-Blodgett (LB) films.

[3]Corresponding author (jah@nadn.navy.mil).

Salmeron and coworkers examined C_{18} *n*-alkanethiols on Au using atomic force microscopy (AFM) (2). Low-load images of the alkanethiol monolayer have the periodicity of the thiol layers observed in other AFM experiments (($\sqrt{3}$ x $\sqrt{3}$) R30°) (7,8). The AFM images of the thiol lattice became increasingly disordered as the pressure increased. At a well-defined critical pressure the (1 x 1) periodicity of the Au(111) substrate was observed. Reducing the pressure and imaging resulted in the reappearance of the thiol lattice.

Friction and wear properties of alkanethiols on Au and alkylsilane monolayers on both Si and mica using AFM have been examined by a number of groups (1, 3, 6, 9). Short-chain alkanethiols with less than ~8 carbon atoms, are less densely packed than the longer chains and thus are likely to have more defects. For both types of monolayers, these studies have shown that the friction decreases as the length of the alkyl portion of the chain increases. Adhesion between the AFM tip and the monolayer decreased as the chain length increased (1), presumably due to the decreased contact area that arises from the decreased compressibility of the films.

Motivated by this recent interest in monolayer lubricants, molecular dynamics (MD) simulations have been used to examine monolayers of *n*-alkanes that are chemically bound or anchored to diamond substrates. A new empirical-potential energy function, which is capable of modeling chemical reactions in hydrocarbons of all phases, has been developed for this work (15). A single-wall, capped armchair nanotube is used to indent these hydrocarbon monolayers and to investigate friction. The effects of tip flexibility and tip speed on indentation and friction are examined. Particular attention will be paid to the formation of defects and bond rupture (and formation) during the course of the simulations. Previous MD simulations have examined the structure (16-18) and compression of *n*-alkanethiols on Au (19,20). The major difference between those studies and the work discussed here is that *irreversible* chemical changes (or changes in hybridization associated with bond rupture and formation) are possible in these studies.

Methodology

Molecular dynamics simulations involve tracking the motion of atoms and molecules as a function of time (21). This motion is calculated by the numerical solution of a set of coupled differential equations. The force experienced by each atom is governed by a potential energy function. If chemical reactions are to be studied, a potential energy function that has the ability to model chemical reactions must be used. One successful method for treating covalent bonding interactions in molecular dynamics potentials is the Tersoff-type potential (22,23). Unlike traditional molecular mechanics force fields (24,25), the Tersoff model allows for the dissociation and formation of covalent chemical bonds during a simulation. Many-body terms reflecting the local coordination environment of each atom are used to modify the strength of more conventional pairwise terms. With this approach,

individual atoms are not constrained to remain attached to specific neighbors, or to maintain a particular hybridization state or coordination number.

One particularly successful example of a Tersoff potential is the reactive empirical bond-order (REBO) potential developed by Brenner (26-29) to describe the covalent bonding interactions in carbon and hydrocarbon systems. Originally developed for use in simulating the chemical vapor deposition of diamond (26), the REBO potential has recently been extended to provide more accurate treatment of the energetic, elastic, and vibrational properties of solid carbon and small hydrocarbons (29).

While the REBO potential has been used to model small hydrocarbon molecules or functional groups in the past (30), it is poorly suited for modeling liquid and monolayer systems that have significant intermolecular interactions because it lacks dispersion and non-bonded repulsion terms. With this in mind, a new potential energy function that introduces non-bonded interactions while preserving the ability of the original REBO potential to model chemical reactions has been developed (15). The majority of the covalent bonding parameters of the REBO potential were preserved in the new potential due to their success when applied to problems ranging from the initial stages of diamond growth (31) to the tribochemistry that occurs when chemically modified diamond surfaces are in sliding contact (30,32). Because the new potential introduces non-bonded interactions through an adaptive treatment of intermolecular interactions, it is referred to as the adaptive intermolecular REBO potential (AIREBO). Various attempts have been made previously to combine non-bonded interactions with the REBO potentials while preserving chemical reactivity (33,34). The AIREBO potential adds non-bonded interactions to the REBO potential in ways that improve upon earlier extensions to the REBO model.

The AIREBO potential has two significant enhancements compared to the REBO potential, namely, long-range or intermolecular interactions and torsional interactions. Thus, the entire system energy is given by

$$E = \tfrac{1}{2} \sum_i \sum_{j \neq i} \left[E_{ij}^{REBO} + E_{ij}^{LJ} + \sum_{k \neq i,j} \sum_{l \neq i,j,k} E_{kijl}^{tors} \right]. \tag{1}$$

The form of the REBO potential E_{ij}^{REBO}, and its parameters, has been given elsewhere (26,28). The intermolecular contribution to the pair energy is given by

$$E_{ij}^{LJ} = S(t_r(r_{ij})) S(t_b(b_{ij}^*)) C_{ij} V_{ij}^{LJ}(r_{ij}) + [1 - S(t_r(r_{ij})] C_{ij} V_{ij}^{LJ}(r_{ij}), \tag{2}$$

which includes the traditional Lennard-Jones (LJ) potential

$$V_{ij}^{LJ} = 4\varepsilon_{ij} \left[\left(\frac{\sigma_{ij}}{r_{ij}} \right)^{12} + \left(\frac{\sigma_{ij}}{r_{ij}} \right)^{6} \right] \tag{3}$$

modified by several sets of switching functions. The switching function $S(t)$ has the form

$$S(t) = \Theta(-t) + \Theta(t)\Theta(1-t)\left[1 - t^2(3-2t)\right] \qquad (4)$$

with $\Theta(t)$ representing the Heaviside step function. The function $S(t)$ is unity for $t < 0$ and zero for $t > 1$, switching smoothly between these two values at intermediate t with a cubic spline. The function and its first derivative are continuous at the switching region boundaries. The distance between a pair of atoms affects the strength of their LJ interaction through the switching function $S(t_r(r_{ij}))$. Beyond a certain distance $r_{ij}^{LJ\,max}$ the LJ term is included unconditionally. The gradual inclusion of LJ interactions as r_{ij} changes is controlled by the t_r scaling function,

$$t_r(r_{ij}) = \frac{r_{ij} - r_{ij}^{LJ\,min}}{r_{ij}^{LJ\,max} - r_{ij}^{LJ\,min}} . \qquad (5)$$

When r_{ij} is greater than $r_{ij}^{LJ\,max}$, $S(t_r(r_{ij}))$ will be zero and the pair distance has no impact on the LJ interaction. When $r_{ij} < r_{ij}^{LJ\,max}$, the first term in eqn. (2) is nonzero, and the LJ interactions are contingent upon the values of the other two switching functions.

At intramolecular distances, the LJ interaction is included only if there is no significant bonding interaction between the two atoms. This is controlled via $S(t_b(b_{ij}^*))$ switching function and the scaling function t_b, where

$$t_b(b_{ij}) = \frac{b_{ij} - b_{ij}^{min}}{b_{ij}^{max} - b_{ij}^{min}} . \qquad (6)$$

The scaling function converts a REBO bond-order term b_{ij} to a range suitable for use in the cubic-spline switching function. If covalent bonding will occur between two atoms, i.e., the bond order is large, t_b is greater than one and the repulsive LJ interactions will not be present. When covalent bonding is not likely, i.e., the bond order is small, the LJ interactions will be included to a variable degree depending upon the value of b_{ij}. The LJ repulsion will be undiminished for sufficiently low

values of b_{ij}. The adaptive LJ interaction is typically evaluated for pairs of atoms at intermolecular distances where the REBO bond-order term b_{ij} would be zero. Thus, bond-order term b_{ij}^{*} in the non-bonded portions of the AIREBO differs from the REBO bond-order term and represents a hypothetical b_{ij} that is evaluated at r_{ij}^{min}.

Lennard-Jones interactions are disabled for any atom pair that is connected by a series of three or fewer bonds, and partially disabled if the connection is via a series of partially dissociated bonds. This is accomplished using the connectivity switch C_{ij} in eqn. (2), defined as the largest possible product of three or fewer bond weights connecting atoms i and j,

$$C_{ij} = 1 - \max\left\{w_{ij}\left(r_{ij}\right), w_{ik}\left(r_{ik}\right)w_{kj}\left(r_{kj}\right), w_{ik}\left(r_{ik}\right)w_{kl}\left(r_{kl}\right)w_{lj}\left(r_{lj}\right), \left(\forall k,l\right)\right\}. \quad (7)$$

The bond weights w_{ij} are the same as those defined in the REBO potential (26, 30).

The torsional potential for the dihedral angle determined by atoms i, j, k, and l is controlled by the term

$$E_{kijl}^{tors} = w_{ki}\left(r_{ki}\right)w_{ij}\left(r_{ij}\right)w_{jl}\left(r_{jl}\right) \, V^{tors}\left(w_{kijl}\right), \quad (8)$$

where

$$V^{tors}\left(w_{kijl}\right) = \tfrac{256}{405}\,\varepsilon_{kijl}\,\cos^{10}\left(w_{kijl}/2\right) - \tfrac{1}{10}\,\varepsilon_{kijl} \quad (9)$$

and the dihedral angle w_{kijl} is given by

$$\cos(w_{kijl}) = \frac{\vec{r}_{ji} \times \vec{r}_{ik}}{\left|\vec{r}_{ji} \times \vec{r}_{ik}\right|} \bullet \frac{\vec{r}_{ij} \times \vec{r}_{jl}}{\left|\vec{r}_{ij} \times \vec{r}_{jl}\right|}. \quad (10)$$

The values for all the LJ and torsional parameters are given below in Table I.

The AIREBO potential has been validated against structural and energetic properties of both gaseous and liquid hydrocarbons (15). Pair-correlation functions and densities were calculated and compared to experimental values. In general, the model does a good job reproducing these quantities for a range of saturated and unsaturated hydrocarbons with the agreement being much better for saturated hydrocarbons.

Simulation systems are constructed by chemically binding (or anchoring) a monolayer of C_{13} n-alkane hydrocarbon chains to the (111) face of a diamond substrate. Each layer of the diamond substrate contains 480 carbon atoms and the

substrates normally contain 11 layers. The computational cell in the plane that contains the monolayer is approximately 50.8 Å by 52.8 Å (or 22.4 Å² / monomer). A total of 120 hydrocarbon chains, with all of the dihedral angles of the carbon backbone in their *anti* configuration, are attached in a (2 x 2) arrangement to the diamond substrate. (This arrangement of chains was selected because it yields approximately the same packing density and cant as monolayers of alkanethiols on Au (111) (1)).

The suitability of capped nanotubes as scanning probe microscope (SPM) tips was first investigated using computer simulations by Harrison *et al.* (35) after Smalley and coworkers proposed that they might constitute well-defined tips (36). With those things in mind, a single-wall, (10,10) nanotube capped with a C_{5v} hemifullerene dome was used as the probe tip for all the simulations discussed here. (For a more detailed explanation of the cap structure see Harrison *et al.* (35).) The nanotube contains 870 carbon atoms, has a diameter of approximately 14 Å, and has a length from base to the end of the cap of approximately 53 Å. To satisfy the valence requirements of carbon, the carbon atoms at the open end of the tube are hydrogen terminated. A total of 11040 atoms were used to simulate the C_{13} monolayer and the diamond substrate.

Table I. AIREBO torsional and LJ parameters.

	CC	CH	HH
$r_{ij}^{LJ\ max}$ (Å)	$2^{1/6}\sigma_{CC}$	$2^{1/6}\sigma_{CH}$	$2^{1/6}\sigma_{HH}$
$r_{ij}^{LJ\ min}$ (Å)	σ_{CC}	σ_{CH}	σ_{HH}
b_{ij}^{max}	0.81	0.90	0.42
b_{ij}^{min}	0.77	0.75	0.32
ε_{ij} (eV)	0.00284	$\sqrt{\varepsilon_{CC}\varepsilon_{HH}}$	0.00150
σ_{ij} (Å)	3.40	$\frac{1}{2}(\sigma_{CC}+\sigma_{HH})$	2.65
ε_{iCCj} (eV)	0.3079	0.1787	0.1250

Each system is equilibrated for a sufficient time to allow all energies and temperatures to reach their steady-state values prior to indentation. Simulations are performed by holding the bottom (outer) two layers of the diamond substrate rigid. Moving toward the center from the bottom, the next two layers of the diamond are maintained at a constant temperature of 300 K using generalized Langevin dynamics to simulate coupling with an external heat bath (37). The remaining diamond layers

and the hydrocarbon chains are free to move according to classical dynamics. The equations of motion for all non-rigid atoms are integrated using the velocity Verlet algorithm with a constant step size of 0.25 fs (38). Periodic boundary conditions are used in the plane containing the monolayer to simulate an infinite interface.

Two separate sets of simulations are performed: one where the nanotube is *flexible* and one where the nanotube is kept *rigid*. The atoms in the flexible nanotube are partitioned in much the same way as the atoms in the substrate (39). In both cases, indentation (extraction) is accomplished by moving all rigid atoms at a constant velocity toward (away from) the monolayer surface. The load on the probe tip is taken to be the total force on the rigid-layer atoms of the nanotube. Moving the rigid-layer atoms of the nanotube parallel to the monolayer surface at a constant velocity simulates friction. Unless otherwise indicated, all indentation and sliding velocities are 100 m/s. . (See Ref. (39) for a discussion of how these speeds compare to those used in AFM experiments.)

Results
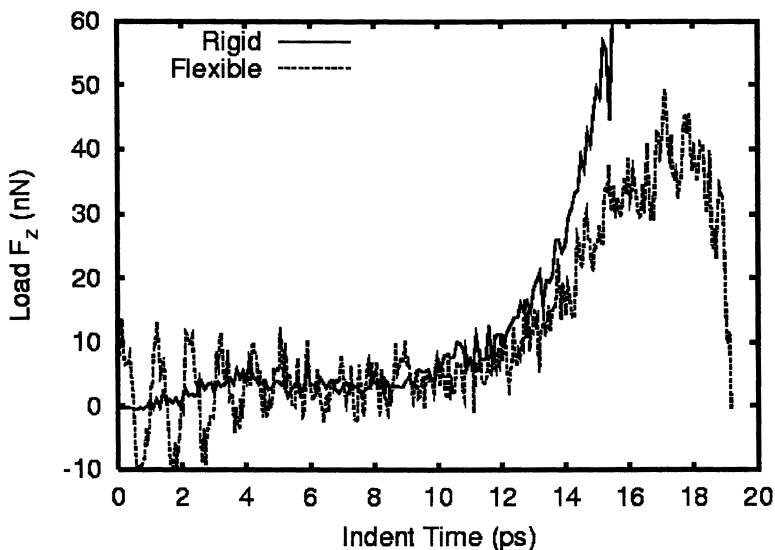
Figure 1. Load on a flexible and a rigid single-wall (10,10) nanotube as a function of simulation time when it is used to indent a C$_{13}$ hydrocarbon monolayer. The same starting configuration was used for both simulations.

Load as a function of time for the indentation of a C$_{13}$ monolayer using both a flexible and a rigid (10,10) nanotube is shown in Figure 1. In the case of the flexible nanotube, the load fluctuates a small amount prior to surface contact, then it increases monotonically until the stress is relieved after approximately 18 ps. The fluctuations

in the load prior to tip contact are the result of longitudinal vibrations of the tip induced by the available thermal energy (41). During indentation the nanotube is gradually tilted away from perpendicular due to its interaction with the monolayer. When it encounters the hard diamond substrate the force on the nanotube is sufficient to cause it to buckle (Figure 2). This stress-relieving deformation has been observed previously (35). In addition, material beneath the nanotube, such as "pinned" alkane chains, causes the nanotube cap to invert. Once buckling occurs, the majority of the stress on the nanotube is relieved, which is apparent from the decrease in force at long times in Figure 1.
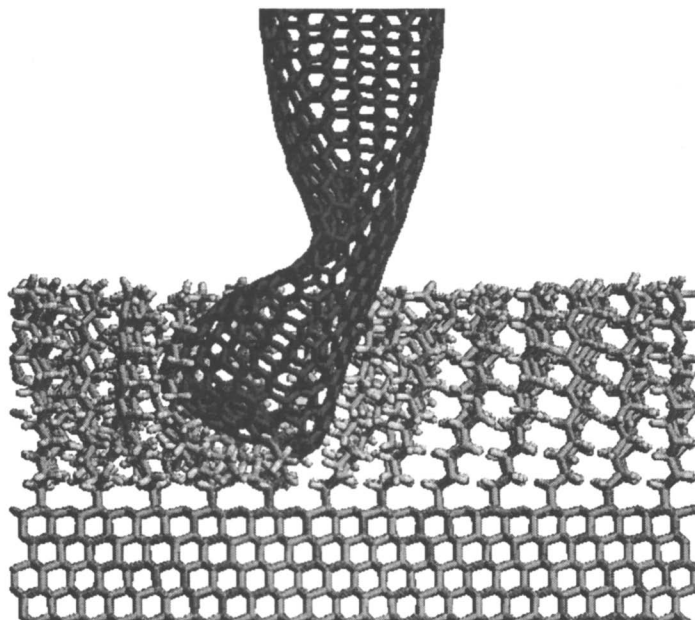
Figure 2. Snapshot from the MD simulation of the interaction of a flexible, capped (10,10) single-wall nanotube (shown in dark gray) with a monolayer composed of C_{13} chains. (The monolayer and diamond substrate are shown in light gray.) The simulation time (load on the nanotube) is 18.0 ps (39.7 nN).

Prior to the buckling of the nanotube the force curves obtained using the rigid and the flexible nanotube are similar, but not identical (Figure 1). At approximately 12 ps the curves begin to diverge. The flexible nanotube is able to reduce the force exerted by the monolayer by deforming while the rigid nanotube is not. Both the rigid and flexible nanotubes deform a small number of the chains within the monolayer during indentation. Eventually, these chains become "pinned" under the nanotube. When a rigid nanotube is used, however, it does not tilt (as the flexible tube does) as it penetrates the monolayer, it does not buckle when it encounters the diamond substrate, and irreversible disruption of the monolayer occurs for extreme indentations. For example, a single chain can become trapped under the nanotube.

Severe indentation causes the chain to be squeezed against the hard diamond substrate. Eventually, an intrachain carbon-carbon bond ruptures (Figure 3).
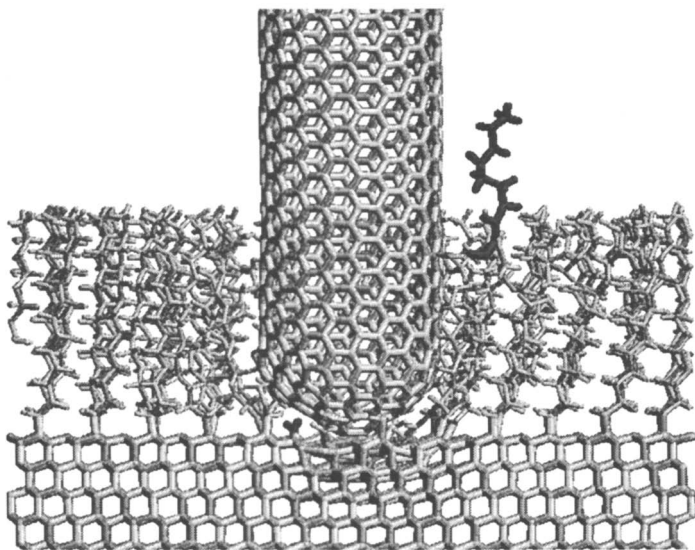
Figure 3. Snapshot from the MD simulation of the interaction of a rigid, capped (10,10) nanotube with a monolayer composed of C$_{13}$ chains. The simulation time (load on the nanotube) is 18.5 ps (240 nN). The alkane chain that has been ruptured is colored dark gray. For clarity, atoms in front of the nanotube are not shown.

Salmeron and coworkers have suggested that gauche defects are introduced into monolayers by an AFM tip during indentation (4). These defects, along with those generated during sliding, may affect the monolayer's tribological properties. The calculated values of intrachain C-C-C-C dihedral angles ϕ are all centered about ~180° (corresponding to the anti conformation) after equilibration. (This conformation has also been referred to as the all-trans arrangement in the literature (40).) The number of gauche-like defects ($\phi > 270°$ or $\phi < 90°$) within the monolayer is plotted as a function of simulation time for the indentation of a C$_{13}$ monolayer using both a rigid and a flexible nanotube in Figure 4. In both cases, the number of defects begins to increase when the nanotube contacts the monolayer and continues to increase during the indentation. For a given simulation time, the rigid nanotube generates more defects in the monolayer than the flexible tube. Because the rigid nanotube does not deform as the indentation proceeds, it penetrates deeper into the monolayer. For example, at 14 ps in Figure 4 the rigid nanotube has penetrated approximately 1 Å deeper into the monolayer than the rigid tube. These observations agree with previous studies that have examined the indentation of *n*-alkane monolayers composed of C$_8$, C$_{13}$, and C$_{22}$ chains using a rigid nanotube (39). Those studies show that the number of defects generated upon indentation depends on the depth of penetration when a small probe tip, such as the nanotube, is used.

When the nanotube is withdrawn from the monolayer, the defects remain in the monolayer for some time after the load on the nanotube has returned to zero. Similar memory effects have been observed in surface force apparatus experiments (42).
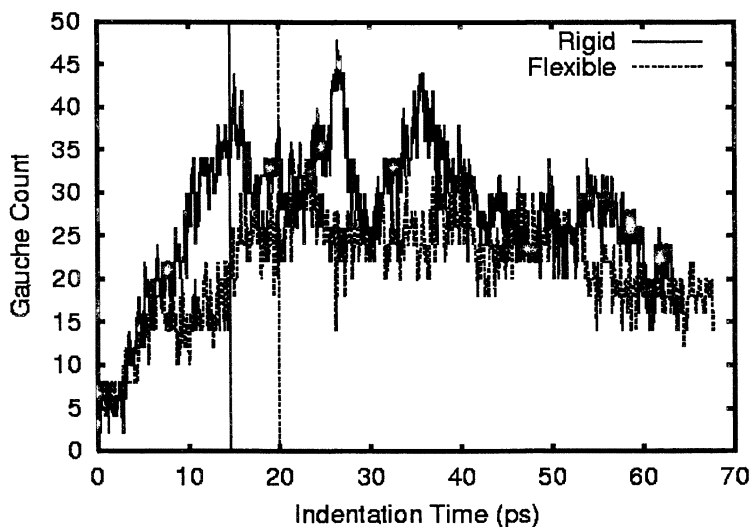
Figure 4. Number of gauche defects formed as a function of simulation time when a flexible and a rigid single-wall nanotube are used to indent (and extracted from) a C₁₃ monolayer. Vertical lines represent the time when tip motion is reversed.
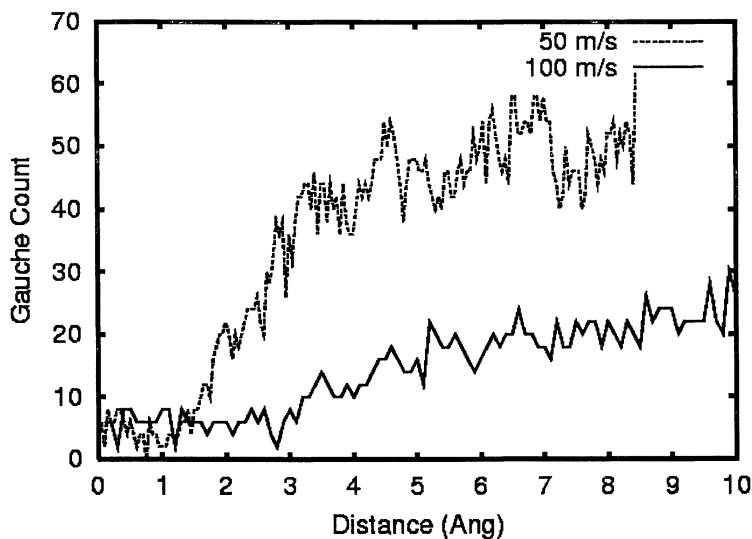
Figure 5. Number of gauche defects formed as a function of distance traveled by the rigid nanotube when indenting a C₁₃ monolayer at two different indentation speeds. The same starting configuration was used in each simulation

The number of gauche defects formed is also profoundly affected by the speed of the indentation. Figure 5 shows the number of defects as a function of distance traveled by the rigid nanotube for two different indentation speeds (100 m/s and 50m/s). These data clearly show that slower indentation speeds lead to the formation of more defects in this system.
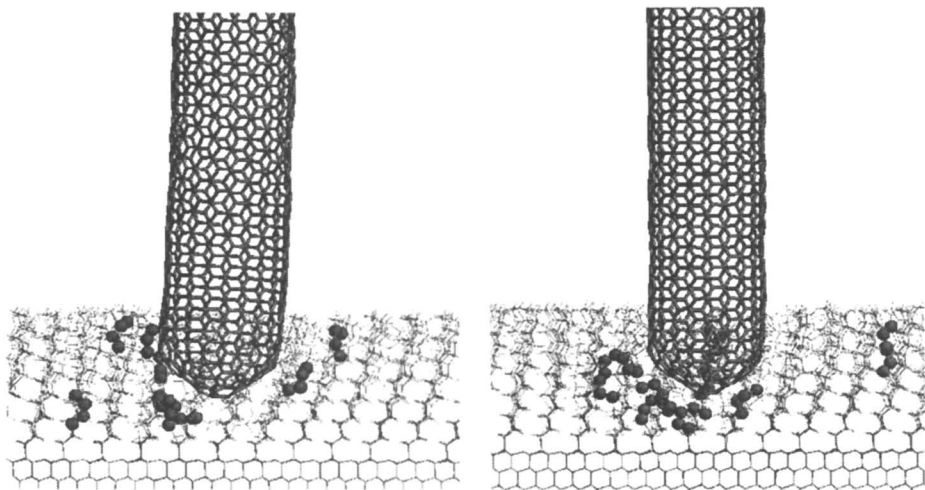
Figure 6. Snapshots from MD simulations where a flexible (left-hand side) and a rigid (right-hand side) nanotube indented a C_{13} monolayer. Sets of carbon atoms within alkane chains whose dihedral angles are in the gauche conformation are represented as large gray spheres. The simulations time is 12.0 ps in both panels. The load is 7.0 nN and 11.2 nN on the flexible and rigid tubes, respectively. For clarity, majority of the atoms in the diamond substrate are not shown.

For both nanotubes, the majority of the gauche defects are localized to the region of the monolayer adjacent to and under the nanotube (Figure 6). The small radius of the nanotube allows it to "slice" into the monolayer, interacting with a small number of hydrocarbon chains. Thus, the defects are localized near the tip. (This is true irrespective of the length of the *n*-alkane chains within the monolayer being indented (39)). The shape of the tip is intimately linked to the location of the defects. When the tip is extended to an infinite hydrogen-terminated diamond lattice, the defects were localized to the ends of the alkane chains (43).

In addition to affecting the number of defects formed during indentation, the flexibility of the tube has a profound effect on the friction. Because the flexible nanotube is embedded in the monolayer (Figure 2), movement of the tube parallel to the monolayer causes the tube to buckle (Figure 7). When the nanotube buckles, it is pulled out of the film slightly, altering the normal load on the tube. Continued sliding causes the end of the now floppy nanotube move from side-to-side and to be pulled farther out of the monolayer. Thus, single-wall nanotubes may not be ideally suited for use as SPM probes in all instances, particularly if the aim of the experiment is to study tribological properties.

Discussion

The nature of molecular dynamics simulations allows for the quantification of the number of defects formed and the determination of their exact location. These simulations show that gauche defects are formed as a result of the indentation process, as predicted by Salmeron and coworkers (4). Due to the geometry of the nanotube, these defects are localized to the region below and surrounding the tube. In addition, due to the small contact area of the nanotube used in these simulations, the number of defects formed is a function of penetration depth into the monolayer (39). Because the flexible nanotube compresses slightly as it interacts with the C_{13} monolayer, it does not penetrate the monolayer as deeply as a rigid nanotube. As a result, the flexible tube generates fewer defects as it indents the monolayer.
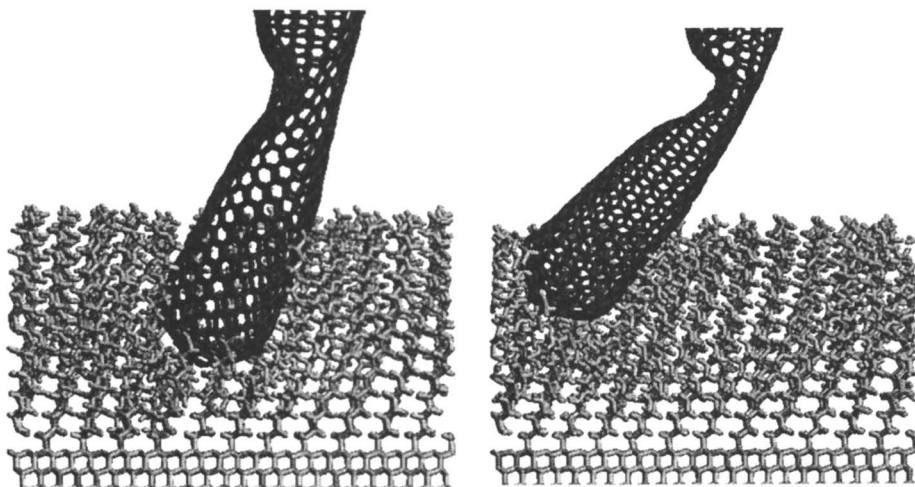
Figure 7. Snapshots from a MD simulation where a flexible nanotube is being moved parallel to the C_{13} monolayer (from left to right) to simulate a friction experiment. The nanotube has been sliding for 10.0 ps (left-hand side) and 31.1 ps (right-hand side).

The number of defects present in the monolayers is important in light of recent quartz crystal microbalance experiments on C_9 alkanethiols on Au that suggest that the number of defects present in these monolayers affects energy dissipation within the films, thus affecting the measured friction (44). The simulations show that the indentation speed has a dramatic effect on the number of gauche defects formed. The origin of this behavior is not fully understood. It appears to be linked to both the time the tip is in contact with the monolayer and the geometry of the tip. Because the computational indentation speeds are orders of magnitude faster than speeds used in AFM experiments, it is difficult to ascertain whether or not this effect is present in AFM experiments. However, one can perhaps infer that comparative AFM

measurements of friction on SAMs should be performed with all experimental parameters, even approach speed, being equal to those from previous studies.

The number of defects formed during indentation (compression) has a marked dependence on the speed of the tip motion and the tip geometry. The origin of this behavior is not fully understood. Future simulations will examine the dependence of defect formation on indentation speed and tip geometry.

Simulations reported here demonstrate that it is possible to initiate irreversible chemical changes within monolayers via severe indentation with a rigid nanotube. Carbon-carbon bonds within a chain pinned by the tip are severed. Chain rupture has also been observed in simulations that examine the friction of hydrocarbon monolayers (46). Alkane chains can be severed from the diamond substrate at their attachment point or ruptured along the chain as the tip slides over them during sliding. This is akin to the irreversible damage of alkylsilane films caused by scanning with AFM (4, 45). In this case, the damage is attributed to a disruption of the cross-linked siloxane network.

Finally, because nanotubes are easy to bend (35, 36), when used as a tip to investigate friction, the nanotubes buckle and "pull" out of the monolayer. This raises some concern with regard to the applicability of single-wall nanotubes for the study of tribology.

References

1. Lio, A.; Charych, D. H.; Salmeron, M. *J. Phys. Chem. B* **1997**, *101*, 3800.
2. Lio, A.; Morant, C.; Ogletree, D.; Salmeron, M. *J. Phys. Chem. B* **1997**, *101*, 4767.
3. Kim, H. I.; Graupe, M.; Oloba, O.; Doini, T.; Imaduddin, S.; Lee, T. R.; Perry, S. S. *Langmuir* **1999**, *15*, 3179.
4. Carpick, R. W.; Salmeron, M. *Chem. Rev.* **1997**, *97*, 1163 and references therein.
5. Kim, H. I.; Koini, T.; Lee, T. R.; Perry, S. S. *Langmuir* **1997**, *13*, 7192.
6. Xiao, X.; Hu, J.; Charych, D. H.; Salmeron, M. *Langmuir* **1996**, *12*, 235.
7. Fenter, P. F. *et al Phys. Rev. Lett.* **1993**, *70*, 2447.
8. Fenter, P. F. *et al. Science* **1994**, *266*, 1216.
9. Harrison, J. A.; Perry, S. S. *MRS Bulletin* **1998**, *23*, 27.
10. Tsukruk, V. V. *et al.* In *Tribology Issues and Opportunities in MEMS*; Ed. Bhushan, B.; Kluwer Academic Publishers: Dordrecht, Boston, London, 1998; Chapter "Tribological Properties of Modified MEMS Surfaces", pages 607-614.
11. Deng, K.; Collins, R. J.; Mehregany, M.; Sukenik, C. N. *J. Electrochem. Soc.* **1995**, *142*, 1278.
12. Homola, A. M.; Mate, C. M.; Street, G. B. *MRS Bulletin* **1990**, *15*, 45.
13. Perry, S. S.; Somorjai, G. A.; Mate, C. M.; White, R. L. *Trib. Lett.* **1995**, *1*, 233.
14. Perry, S. S.; Somorjai, G. A.; Mate, C. M.; White, R. *Trib. Lett.* **1995**, *1*, 47.
15. Stuart, S. J.; Tutein, A. B.; Harrison, J. A. *J. Chem. Phys.* in press.
16. Mar, W.; Klein, M. L. *Langmuir* **1994**, *10*, 188.
17. Bhatia, R.; Garrison, B. J. *Langmuir* **1997**, *13*, 765.

18. Luedtke, W. D.; Landman, U. *J. Phys. Chem.* **1998**, *102*, 6566.
19. Tupper, K. J.; Colton, R. J.; Brenner, D. W. *Langmuir* **1994**, *10*, 2041.
20. Tupper, K. J.; Brenner, D. W. **1994**, *10*, 2335.
21. Harrison, J. A.; Stuart, S. J.; Brenner, D. W. In *Handbook of Micro/Nanotribology, 2nd edition*; Ed. Bhushan, B.; CRC Press: Boca Raton, FL, 1999; Chapter 11 "Atomic-Scale Simulation of Tribological and Related Phenomena", pp. 525-594 and references therein.
22. Tersoff, J. *Phys. Rev. B* **1988**, *37*, 6991.
23. Tersoff, J. *Phys. Rev. B* **1988**, *39*, 5566.
24. Allinger, N. L.; Chen, K.; and Lii, J.-H. *J. Comp. Chem.* **1996**, *17*, 642.
25. Jorgensen, W. L.; Maxwell, D. S.; and Tirado-Rives, J. *J. Am. Chem. Soc.* **1996**, *118*, 11225.
26. Brenner, D. W. *Phys. Rev. B* **1990**, *42*, 9458.
27. Brenner, D. W. *Phys. Rev. B* **1992**, *46*, 1948.
28. Brenner, D. W.; Harrison, J. A.; White, C. T.; Colton, R. J. *Thin Solid Films* **1991**, *206*, 220.
29. Brenner, D. W.; Sinnott, S. B.; Harrison, J. A. (in preparation)(unpublished).
30. Harrison, J. A.; Brenner, D. W. *J. Am. Chem. Soc.* **1994**, *116*, 10399.
31. Garrison, B. J.; Dawnkaski, E. J.; Srivastava, D.; Brenner, D. W. *Science* **1992**, *255*, 835.
32. Harrison, J. A.; Stuart, S. J.; Perry, M. D. In *Tribology Issues and Opportunities in MEMS*; Ed. Bhushan, B.; Kluwer Academic Publishers: Dordrecht, Boston, London, 1998; Chapter "The Tribology of Hydrocarbon Surfaces Investigated using Molecular Dynamics", pages 285--299.
33. Nyden, M. R.; Coley, T. R.; Mumby, S. Polym. Eng. Sci. **1997**, *37*, 1496.
34. Che, J.; Cagin, T.; Goddard III, W. A. Theor. Chem. Acc. **1999**, *102*, 346.
35. Harrison, J. A.; Stuart, S. J.; Robertson, D. H.; White, C. T. *J. Phys. Chem. B* **1997**, *101*, 9682.
36. Dai, H.; Hafner, J. H.; Rinzler, A. G.; Colbert, D. T.; Smalley, R. *Nature* **1996**, *384*, 147.
37. Adelman, S. A.; Doll, J. D. *J. Chem. Phys.* **1976**, *64*, 2375.
38. Swope, W. C.; Andersen, H. C.; Berens, P. H.; Wilson, K. R. *J. Chem. Phys.* **1982**, *76*, 637.
39. Tutein, A. B.; Stuart, S. J.; Harrison, J. A. *J. Phys. Chem. B.* **1999**, *103*, 11357.
40. Dubois, L. H.; Zegarski, B. R.; Nuzzo, R. G. *J. Chem. Phys.* **1993**, *98*, 678.
41. Harrison, J. A.; Tutein, A. B.; Stuart, S. J.; Robertson, D. H.; White, C. T. *in preparation*.
42. Berman, A.; Israelachvilli, J. N. In *Handbook of Micro/Nanotribology, 2nd edition*; Ed. Bhushan, B.; CRC Press: Boca Raton, FL, 1999; Chapter 9 "Surface Forces and Microrheology of Moleculary Thin Films", pp. 371-432.
43. Tutein, A. B.; Stuart, S. J.; Harrison, J. A. *Langmuir* **2000**, *16*, 291.
44. Shinn, N. D.; Mayer, T. M.; Michalske, T. A. *Trib. Lett.*, in press.
45. Xiao, X.; y.-Lui, G.; Charych, D. H.; Salmeron, M. Langmuir **1995**, *11*, 1600.
46. Tutein, A. B.; Stuart, S. J.; Harrison, J. A. *in preparation*.

Chapter 15

Viscoelasticity in Nanoscale Friction on Thin Polymer Films

Greg Haugstad[1], Jon A. Hammerschmidt[2], and Wayne L. Gladfelter[3]

[1]Center for Interfacial Engineering, University of Minnesota, 187 Shepherd Labs, Minneapolis, MN 55455
[2]Eastman Kodak Company, Rochester, NY 14650
[3]Department of Chemistry, University of Minnesota, 207 Pleasant Street, SE, Minneapolis, MN 55455

Friction force microscopy is employed to investigate sliding friction at nanometer-scale contacts on thin polymer films, as a function of relative humidity, scan velocity and temperature. Strong humidity and rate dependence is observed on amorphous regions of two water-soluble polymers, polyvinyl alcohol (PVOH) and gelatin. Crystalline regions of the same polymers exhibit relatively flat frictional response with respect to these variables. Friction on polymethyl methacrylate (PMMA), polystyrene (PS) and polyethylene terephthalate (PET) varies strongly with temperature, similar to the variations in *tanδ* observed in bulk dynamic mechanical measurements. Together these findings reveal the inherently viscoelastic nature of friction on amorphous polymers. The positions of peaks in friction data, associated with the glass transition, indicate enhanced molecular freedom relative to the bulk polymers. A time-temperature analysis of friction on PMMA related to secondary (β) relaxations produces a measurement of the activation energy of the hindered rotation of the $-COOCH_3$ group. This energy also is reduced relative to values tabulated for bulk polymers. A model of energy dissipation throughout the deformed volume of polymer is developed to explain the observed dependence of friction force on *tanδ*. Dissipation due to interfacial "bond" shearing apparently is of minor importance, as is the related role of contact area.

The importance of polymeric films as protective coatings, adhesives, and lubricants has brought increasing attention to polymer surface and thin-film properties.[1,2] In particular, friction on thin organic films has become a topic of extreme scientific and technological interest.[3] The performance of ultrathin lubricants and coatings is critical in magnetic storage media devices, as well as new technologies like microelectromechanical systems. As device sizes shrink, the properties of thin polymer films are expected to vary from those of the bulk polymer.[2] This may be the result of confinement effects,[4] and/or the increasing role of interfaces (substrate/polymer, moving asperity/polymer, and polymer free surface) in affecting film behavior.[5-7] Differences in free volume due to surface chain-end concentration also can impact the near-surface properties of polymers.[7,8]

For several decades the phenomenology of friction on polymers suggested the importance of viscoelastic energy dissipation near deforming microasperities, within multiasperity (macroscopic) contacts.[9,10] For example, rolling friction on polymeric materials exhibited a temperature and rate dependence similar to bulk viscoelastic loss tangent (*tan* δ) data.[11,12] Lacking in early studies was the ability to carefully control the loading conditions at individual microasperities, and to identify the locus of plastic deformation (wear). Scanning force microscopy with lateral force sensitivity ("friction force microscopy") provides not only a measurement of frictional forces at a single asperity contact, but also the ability to image nanoscale morphology and thereby assess the onset of wear.[13] Because the probe has a radius of curvature of tens of nanometers, and applied loads are on the nanonewton scale, ultrathin polymer films indeed can be studied under wearless sliding contact. The recent addition of temperature control,[14-16] plus the ability to explore several decades of scan velocity[14,16-20] (or scan repetition rate[15,17] or observation lag time[13,21]), has initiated rigorous investigations of viscoelasticity at nanoscale sliding contacts. Humidity further impacts viscoelastic dissipation in the case of hydrophilic polymers, because of plasticizing by absorbed water.[22] Its impact on the nanotribology of thin polymer films has been reported in several studies.[19,21,23,24]

In the present study we employ scanning force microscopy to measure the dependence of nanoscale sliding friction on humidity, scan velocity and temperature, for several polymers cast as thin films. The humidity and rate dependence of friction is compared on crystalline and amorphous surface regions of two water-soluble polymers, polyvinyl alcohol (PVOH) and gelatin, to examine the plasticizing effects of water. The temperature dependence of friction is measured on polymethyl methacrylate (PMMA), polystyrene (PS) and polyethylene terephthalate (PET). In the case of PMMA, friction is analyzed in the context of time-temperature superposition. The proximity of energy dissipation to the tip-sample interface is discussed. Dissipation localized at the immediate tip-polymer interface, i.e. the commonly-invoked model of interfacial "bond" shearing and implicitly important contact area,[25] is compared to a model of viscoelastic dissipation throughout the contact deformation volume.[14]

EXPERIMENTAL DETAILS

Materials. Aqueous PVOH solution was prepared by heating 1 wt% mixture of PVOH (Aldrich, 99% hydrolyzed, M_W = 85,000-146,000) in distilled/deionized water (DW) to 90°C. Freshly cleaved muscovite mica (New York Mica Co.) substrates were rinsed with DW, immersed in the PVOH solution, immediately removed as to leave a residual puddle of PVOH solution, and dried slowly overnight at 20°C in a moderate relative humidity (RH) (30% < RH < 60%). Gelatin (Kind and Knox) films were prepared similarly, except a solution temperature of 45°C was reached. Such films are on the order of 100-1000 nm thick as measured by Rutherford backscattering spectrometry. In one case, as noted in the results, the initial 1 wt% solution was diluted to 10^{-3} wt% and cast on cleaved mica. Such films are approximately 3 nm thick as imaged directly with SFM following high-force scratching down to the substrate. PMMA (Polysciences, MW=60,000, Mw/Mn=1.10), PS (Aldrich, MW=44,000, Mw/Mn=1.10), and PET (Aldrich) films were prepared by spin coating (2000 rpm) 0.25 wt % polymer/solvent solutions onto silicon (100) wafers, which had a native oxide layer. Toluene was used as the solvent for PMMA and PS, and 2-chlorophenol was used for PET. PMMA, PS and PET films were annealed at 100°C under vacuum (≈0.01 torr) for 2 hours and allowed to cool under vacuum. PMMA, PS and PET film thicknesses were measured using ellipsometry (Sopra) and found to be approximately 21, 12, and 20 nm (±5nm), for PMMA, PET, and PS, respectively. As-prepared film surfaces had rms roughness ≤ 1 nm. Experiments were performed within days of film coating, and 1 day or less after annealing.

Instrumentation. All film characterization was performed with a PicoSPM (Molecular Imaging) scanning probe microscope with an M-scanner (lateral range = 30 μm, vertical range = 7 μm) in conjunction with a Nanoscope III controller (Digital Instruments). The design of the PicoSPM isolates the sample stage from the piezoelectric scanner and associated electronics with an o-ring-sealed glass chamber, allowing for a wide variation in temperature and gaseous atmosphere. Temperature variation is accomplished via a resistive heating stage (temperature range: ambient to 170°C). The temperature stage was calibrated using a k-type micro-thermocouple attached to a bare Si(100) wafer. The stage temperature response was linear throughout its range, and reached each set temperature within approximately 5 minutes. A CaSO$_4$ column and humidifier in conjunction with a hygrometer and feedback-controlled airflow were used to control the relative humidity (RH) (range = 2-98%). Polymer films were equilibrated at < 5% RH for several hours before beginning an experiment. For variable humidity studies, the RH was equilibrated for approximately 15 minutes before imaging; images/measurements were performed at ambient temperatures of ≈20-22°C using commercial gold-coated 100-μm Si$_3$N$_4$ cantilevers (spring constant ≈ 0.58 N/m) with integrated tips (Digital Instruments). For variable temperature studies, all measurements were performed at 2-8% RH using commercial uncoated 85-μm silicon cantilevers (spring constant≈0.5 N/m) with integrated sharpened tips (Park Scientific Instruments). Reflective coatings were precluded in order to eliminate cantilever bending due to the difference in thermal

expansivity of the cantilever and coating material. The probe tip radius of curvature was characterized through the use of a calibration grating (NTMDT).[14] The grating is composed of silicon needles with a radius of curvature of <10 nm.

Procedures. The frictional force was determined from (one half) the difference of the lateral force measured during left-to-right and right-to-left scans ("friction loops"). Each reported value of friction was the average over at least several friction loops, and as many as 512 loops captured as images (512^2 difference values). All friction loops were collected as raw data, thereby retaining the zero of lateral force. Friction loops captured as images, except those used for the velocity/frequency variation study, employed a scan size of 5x5 μm and scan frequency of 5 Hz, giving a scan velocity (2 × (scan width) × (scan frequency)) of 50 μm/sec. Where reported, absolute friction forces were determined utilizing the coefficient of friction for SiO_2 on SiO_2 as a standard.[14] Force versus Z displacement ("force curve") measurements were collected several micrometers away from the imaged region prior to image collection. This procedure was repeated at each humidity, temperature, scan size, or scan frequency in order to maintain a constant applied load and detect any changes in the state of the tip. "Force volume" mode was used to capture force versus distance data at 32x32=1024 locations arranged in a square grid. Reported pull-off forces are averaged over these 1024 locations, calculated with custom software.

Checks were routinely performed to identify scanning-induced surface modifications. Surface regions were repeatedly raster scanned and subsequently imaged over larger scan sizes, in order to identify modifications. All reported friction force and pull-off force values derive from data acquired without producing significant surface modifications on the nanometer scale. Temperatures and humidities higher than those of reported data indeed yield scan-induced surface modifications.

RESULTS AND DISCUSSION

1. Humidity Dependence of Friction on Water-Soluble Semicrystalline Polymers

PVOH and gelatin films as prepared in this study undergo intriguing morphological transformations upon exposure to high humidity. Representative PVOH film morphology is shown in 5x5-μm topography/friction images in Figure 1: (a) as prepared and (b) after exposure to 95-98% RH for a period of ≈12 hours followed by desiccation to 2-5% RH. Brighter regions correspond to greater height and friction forces. The relative humidity during imaging was (a) 50% and (b) 2-5%. In (a) the topography is granular well below the 1-μm scale, as is the friction (lateral force) image. Apart from this small-scale granularity, the film is homogeneous; images collected at other locations showed similar homogeneity. In (b) the images reveal long fibrous strands largely covering the film surface, confirmed at other locations. The strands have relatively low frictional signature and are 2-3 nm thick.
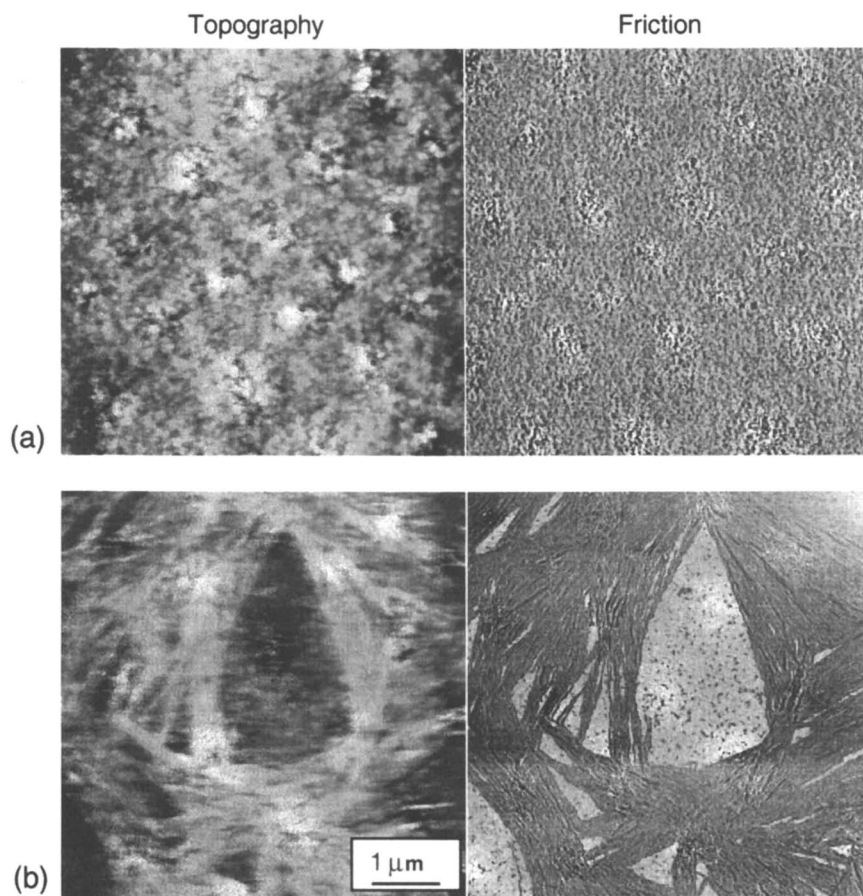
Figure 1. Representative PVOH film morphology in a 5x5-mm region: (a) as prepared and (b) after exposure to 95-98% RH for a period of ≈12 hours followed by desiccation to 2-5% RH. Brighter regions correspond to greater height and friction forces.

The higher friction component seen in gaps between the strands has topographic and friction signatures identical to the single component in (a).

The strands in Figure 1b are interpreted as highly crystalline domains. PVOH is a hydrophilic polymer comprised of atactic hydroxyl groups extending from the polymer backbone. It is known that PVOH can crystallize in atactic form due to strong hydrogen bonding.[22] Because of the large amount of water, on the order of 30% moisture content, that is absorbed by PVOH at 95-98% RH, the polymer molecules will have enhanced mobility. Given that the underlying, more amorphous component remains partially visible, crystallization apparently is confined to the surface. Presumably the mobility near the surface is especially large, allowing entropic barriers to be overcome to enable crystallization. As the sample is dried, strong hydrogen bonding affinity reorients the polymer into the preferred, lower energy crystalline state.

Representative gelatin film morphologies are shown in 3x3-μm topography/friction images in Figure 2: (a) as prepared and (b) after exposure to high humidity followed by desiccation, as in the case of PVOH. To a lesser extent than PVOH, gelatin forms a second low-friction component seen as two submicron islands on top of an unmodified granular phase (Figure 2). Similar low-friction domains have been studied previously on gelatin film surfaces.[13,17,18,23,24] It was proposed that such low-friction moieties contain intramolecularly-folded, triple-helical gelatin, due to collagen-fold renaturation. The results implied that such folding could be induced in gelatin when an adequate amount of water is present. Collagen-fold "crystallization" involves hydrogen bonding between CO and NH groups, both directly and via interstitial water molecules. The present observations following high humidity treatment are assigned therefore to incorporation of free water molecules as needed at interstitial sites within the triple helix, producing low-friction moieties of high crystallinity.

The frictional response of PVOH and gelatin film morphologies as in Figures 1b and 2b were measured as a function of relative humidity up to 75% and 55%, respectively (above which scan-induced wear was problematic). The results are shown in Figure 3. The plots in (a) and (b) compare friction on the highly crystalline regions of PVOH or gelatin with the more amorphous regions, i.e. the underlying unmodified polymer.[26] Essentially no RH dependence is observed on the crystalline regions of PVOH or gelatin films, whereas dramatic increases in friction are observed on the amorphous regions of PVOH (above 60% RH) and gelatin (above 40% RH). In Figure 3c the RH dependence of friction on amorphous PVOH is further examined at four scan velocities. The onset of rising friction shifts to lower RH at slower scan velocities; a shift of about 20% RH results from a velocity decrease of three decades.

We assign the sharp rise in friction at elevated RH to the glass-to-rubber transition. It is well known that both PVOH and gelatin are plasticized by absorbed water.[27,28] At approximately 60% RH a moisture content of $\approx$8% is expected in PVOH. This would shift the glass transition from around 80°C in anhydrous PVOH to 20-22°C,[27] i.e. room temperature, as used in the present experiment. Thus above 60% RH, large-scale molecular motions in response to shear and compressive stresses (tip) will dissipate strain energy. Enhanced energy dissipation is measurable as an abrupt

Topography

Friction

(a)

(b)

500 nm
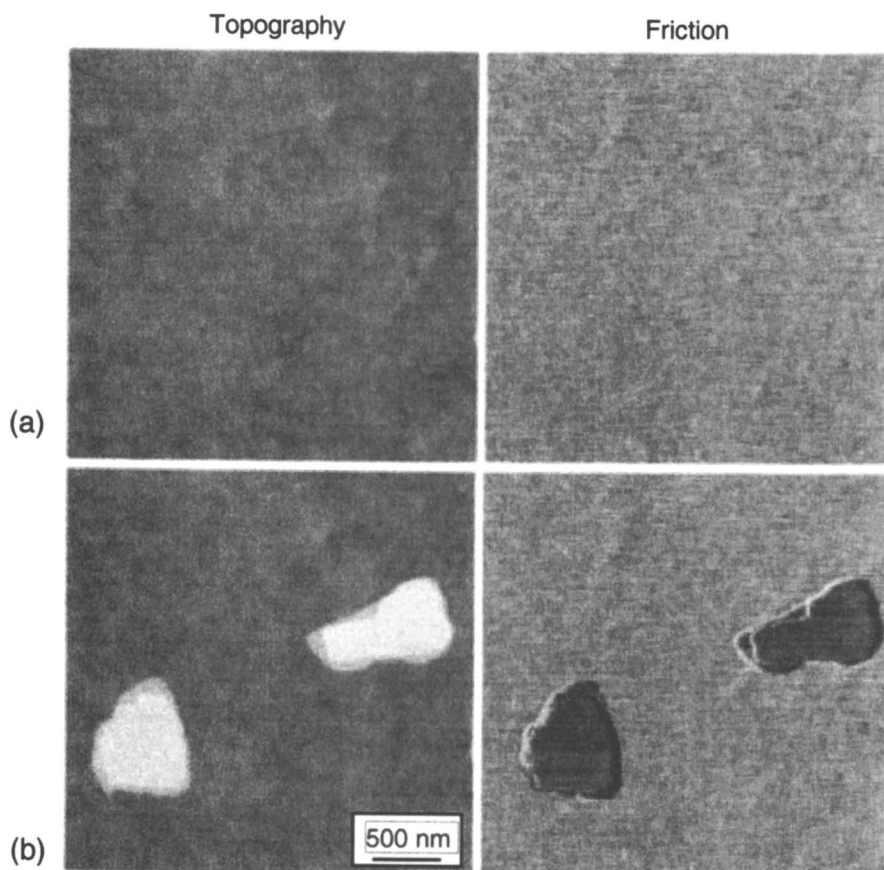
Figure 2. Representative gelatin film morphologies in 3x3-mm region: (a) as prepared and (b) after exposure to high humidity followed by desiccation
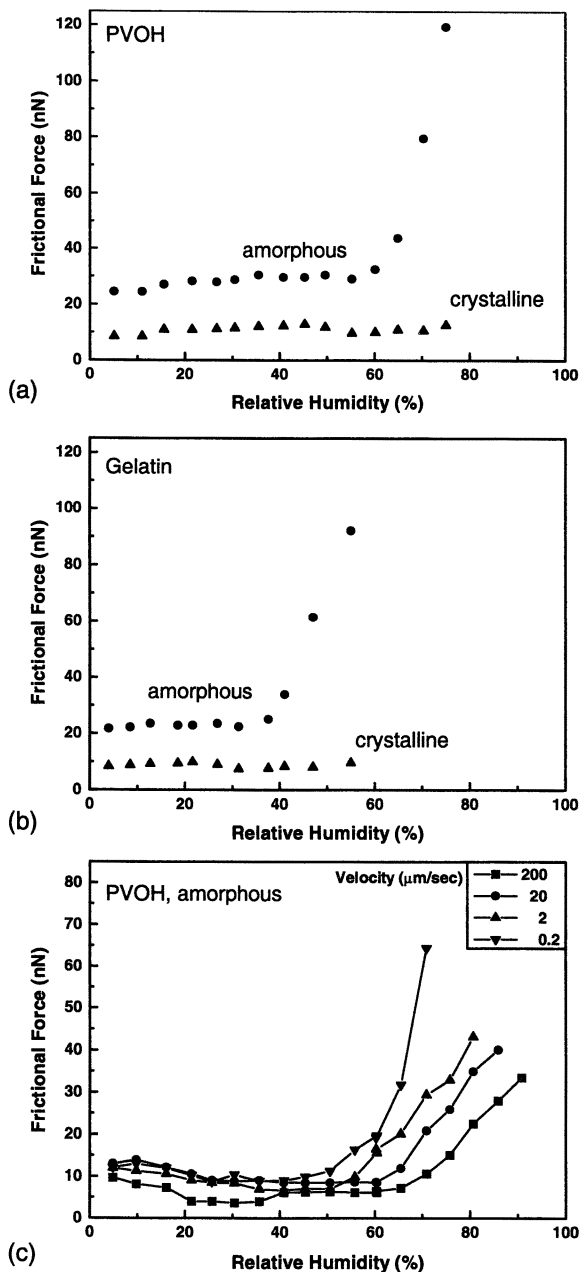
Figure 3. Humidity dependence of friction on crystalline and amorphous components of (a,c) PVOH and (b) gelatin films like those in Figures 1b and 2b. In (c) the humidity-dependence of friction on amorphous PVOH is further contrasted at four scan velocities.

rise in frictional force. Similarly, at approximately 55-60% RH, water content of $\approx$20% is expected in gelatin.[28] This would shift the glass transition from more than 200°C in anhydrous gelatin to around room temperature.[29] These numbers on gelatin and PVOH are consistent with the observed sharp rise in friction force at the high end of the investigated RH range. The 20% difference between the locations of the sharp rise, on PVOH compared to gelatin, could result from a number of variables (e.g. polymer dispersity, aging) which have not been investigated systematically thus far.

The results in Figure 3c illustrate the viscoelastic nature of friction on PVOH, i.e. its rate dependence. Not only is the degree of molecular freedom (via water plasticization) important, but also the amount of time available for molecular relaxations. Faster scan rates allow less time for stress to be maintained on a particular conformer, and thus less time for molecular relaxation of strain energy. Upon increasing the scan rate by three decades, one would have to raise the relative humidity by $\approx$20% to attain the same amount of energy dissipation. Figure 4 addresses explicitly the importance of rate, by plotting friction at a large number of scan velocities and at discrete humidities of (a) 5% and 75 % on PVOH, and (b) 5%, 24% and 58% on gelatin. At the highest humidities on both PVOH and gelatin, friction increases as scan rate is decreased from several hundred microns per second to 1 μm/sec, indicating more rubbery behavior. At scan velocities less than 1 μm/sec, friction continues to increase on PVOH but decreases on gelatin. Peaking friction as a function of rate (or temperature, Section 2), is analogous to peaking loss modulus and loss tangent in conventional dynamic mechanical measurements,[16,17,19,20] and thus locates the glass transition with respect to the relevant variable (scan velocity in this case). At 5% RH, glass transitions of PVOH and gelatin apparently are located at velocities below our measurement window. Instead, in the case of gelatin, much faster secondary relaxations are manifest as rising friction above 100 μm/sec.[17] At intermediate (24%) relative humidities on gelatin, a glass transition "tail" extends from low velocities up to $\approx$1 μm/sec, whereas secondary relaxations apparently are at velocities above our measurement window.

On ultrathin (ca. 3 nm) gelatin films with high water content, outward film deformations can be induced by attractive tip-sample forces during the approach of the tip to contact with sample.[21] This is demonstrated in the 2x2-μm topography/friction images in Figure 5, collected at relative humidities (RH) of (a) 4% and (b) 42%, following multiple approach-withdrawal cycles. In (b) the film is sufficiently rubbery such that weak attractive forces raise a circular region of polymer by several nanometers. Fully elastic behavior is not attained, however, because the deformation is not immediately reversible; instead it remains long enough to be imaged, relaxing on a scale of tens of minutes. (Elastic response would be expected at operating rates well below the glass transition peak.) Reduced friction is observed on the deformed region, apparently reflecting changes in molecular conformation due to the strain of deformation.[21]
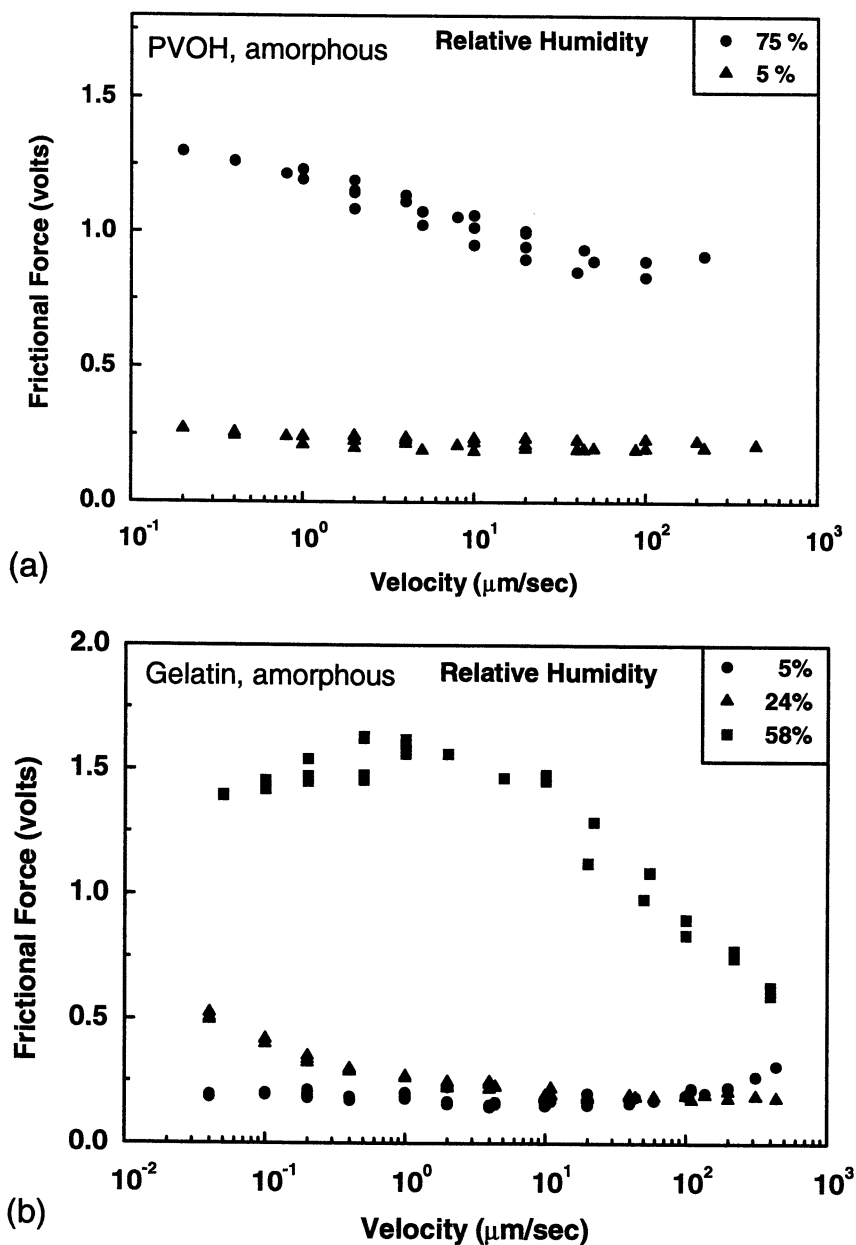
Figure 4. Scan velocity dependence of friction at discrete humidities on amorphous (a) PVOH and (b) gelatin.

Topography   Friction

(a)

(b)   1 μm
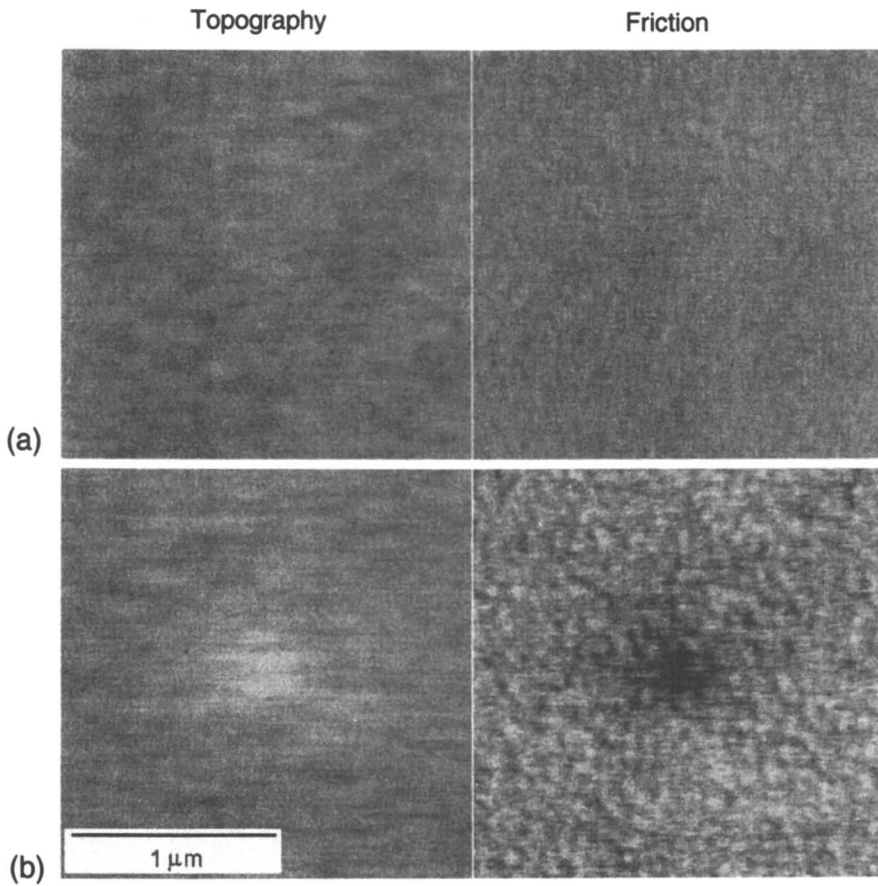
Figure 5. Images of ultrathin (ca. 3 nm) gelatin films, collected at relative humidities (RH) of (a) 4% and (b) 42%, following multiple approach-withdrawal cycles near the center of the imaged region.

2. Temperature Dependence of Friction

Variable-temperature friction measurements were conducted in order to expand the range of relaxations accessible to our experiment, and moreover to examine time-temperature superposition. In Figure 6, friction on thin films of PMMA, PET, and PS is plotted as a function of temperature. For each polymer there is a characteristic, reproducible dependence on temperature. Friction data for PMMA displays a broad peak centered at $\approx 50°C$ and another smaller peak is centered at $\approx 90°C,$. In bulk *tan δ* data a maximum corresponding to secondary β molecular relaxations occurs at $50°C$ at ≈ 2000 Hz.[22] The β mechanism is assigned to the hindered rotation of the $-COOCH_3$ group about the C–C bond linking it to the main polymer chain.[22] The glass to rubber transition (T_g), measured from bulk studies, for PMMA, PET, and PS at 2000Hz are approximately $125°C$, $95°C$, and $125°C$ respectively.[22] In Figure 6, literature *tan δ* data at 2000Hz are included for comparison and are shown as solid lines.[22] For each polymer there is good agreement with the overall shape of the friction and *tan δ* curves. In particular, the breadth of the relaxation peaks are well correlated, except in the case of PS where the explored temperature interval includes only a monotonic rise of friction. There appear to be gross differences, however, in the position of T_g peaks on PMMA and PET.

It is important to consider possible errors in the comparison of time scales for *tan δ* and friction measurements. The measurement rate used for comparison to our data, 2000 Hz, is based on an analysis of tip radius and loading conditions. Briefly, an estimate of tip radius, 20 nm, was obtained by imaging a grating of Si needles. Invoking JKR contact mechanics,[30] a contact diameter was calculated; dividing the scan velocity by this diameter yielded an equivalent frequency of the measurement, 2000 Hz.[14] A potential difficulty of this conversion is its reliance on the estimate of the tip-sample contact diameter. If the radius measured is under/over-estimated by a factor of 2 the frequency calculated changes by the same amount, or $\approx 10^{0.3}$Hz. For the polymers studied herein, a change of one order of magnitude in frequency would correspond to a T_g peak shift of 5°C. Thus our methodology should be within $\approx 1°C$ of measured dynamic experiments, if no differences in surface and bulk properties existed. Furthermore, to account for 35°C and 50°C differences between measurement types, our rate conversion would have to produce 7- and 10-decade frequency errors for PMMA and PET, respectively (5°C per decade of frequency shift).[22] Approximations certainly yield some error in our rate conversion, but clearly they alone cannot account for such gross differences in T_g.

Apparently the differences between T_g determined from our data and from bulk dynamic mechanical measurements are real. This result may reflect confinement, i.e. the presence of substrate and surface separated by a distance (≈ 20 nm) on the order of the radius of gyration of the polymer random coils. In an attempt to identify the relative importance of substrate and surface, we have preliminarily measured the temperature dependence of friction on a PMMA film ≈ 250 nm thick, Figure 7. The shape and position of both the secondary and glass transition peak are approximately the same as on the ≈ 20-nm film, Figure 6. This supports the concept that excess free
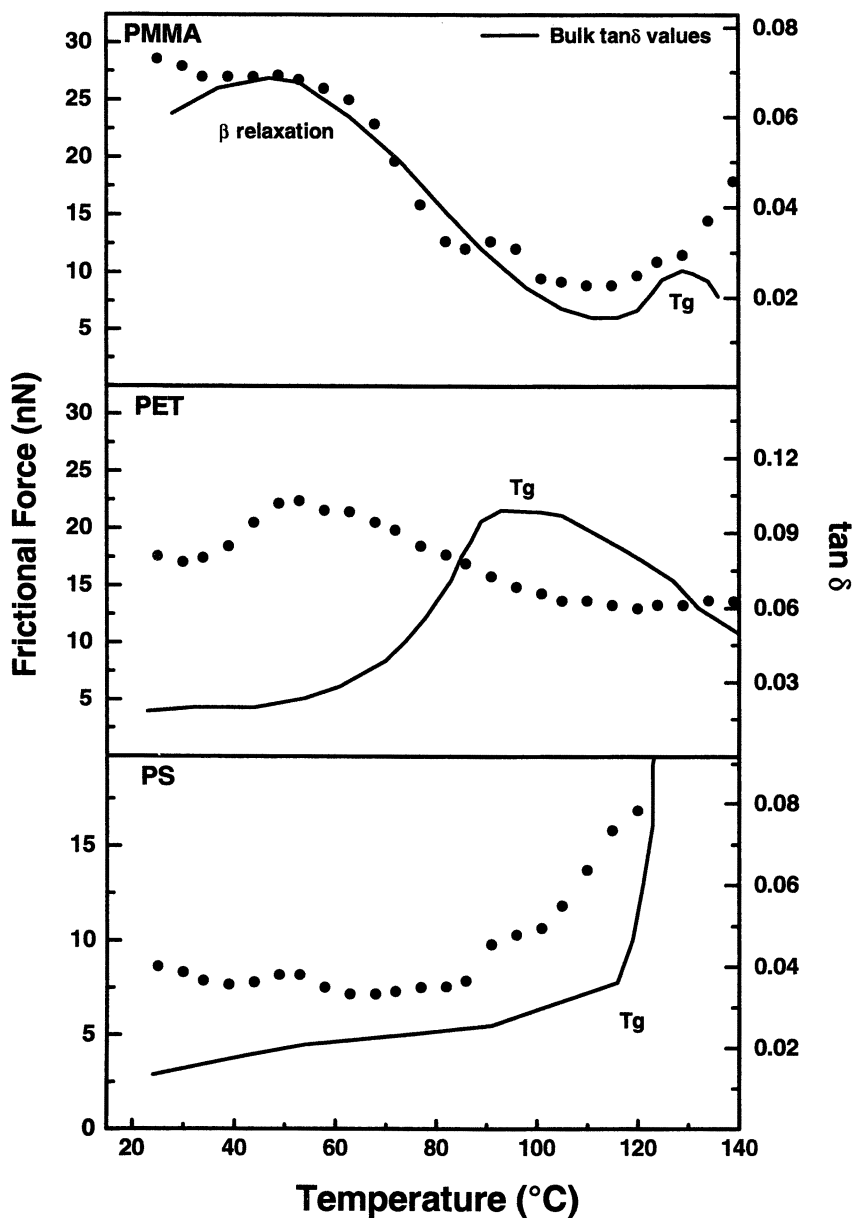
Figure 6. Temperature dependence of friction on ≈20-nm films of PMMA, PET, and PS.
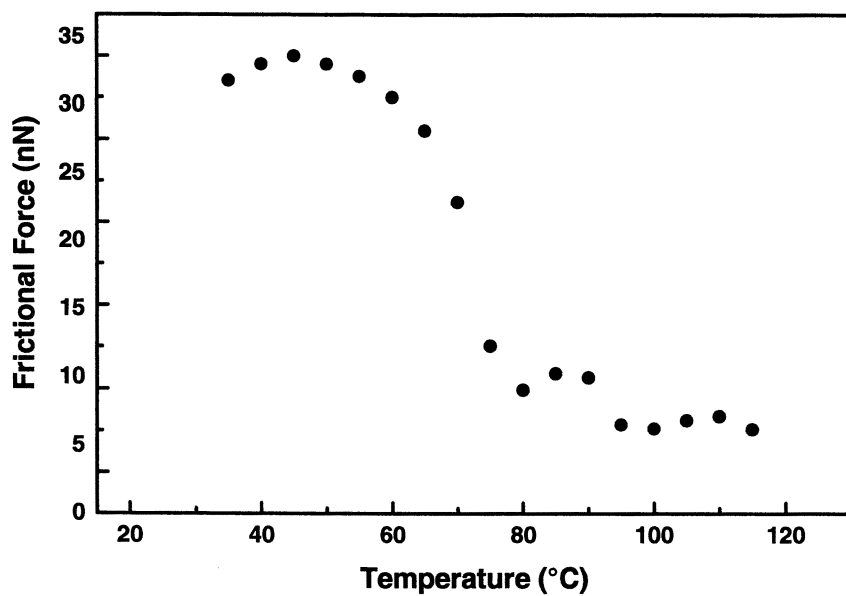
Figure 7. Temperature dependence of friction on a ≈250-nm film of PMMA.

volume at the surface may be induced by segregation of chain ends to the surface, and thus our result is more of a surface effect than a film-thickness effect.

To examine time-temperature superposition we focus upon PMMA and examine the scan-velocity and temperature dependence of friction, Figure 8. In Figure 8a the temperature dependence of friction is plotted with different symbols at four discrete scanning velocities ranging from 2 to 220 μm/sec as indicated. Velocities of 220, 50, 20, and 2 μm/sec are achieved via different scan frequencies and scan sizes. Data were acquired at all four velocities prior to ramping to the next temperature of interest. As rate decreases, the β relaxation peak (at 40°C for 220 μm/sec) apparently shifts to lower temperatures. This is consistent with the idea that the same molecular relaxation requires longer time at lower temperatures. Figure 8b contains the same data as Figure 8a, but plotted as a function of velocity at discrete temperatures. Figure 8c shows a "master curve" constructed from the velocity-dependent data in (b). Here each set of data (at a given temperature) is multiplied by a shift factor a_T, such that the data sets overlie each other. The data were shifted to a reference temperature of 60°C. A plot of shift factors a_T versus 1/T is shown in Figure 8d. The Arrhenius relationship

$$\ln a_T = \frac{E_a}{R}\left(\frac{1}{T} - \frac{1}{T_0}\right)$$

between shift factor a_T and temperature T, with T_0 the reference temperature and E_a the activation energy, is commonly used to analyze secondary relaxation phenomena.[22] From the slope of the Arrhenius plot in Figure 8d, an activation energy of ≈12 kcal/mole was calculated for the hindered rotation of the $-COOCH_3$ group in PMMA, lower than values measured using bulk mechanical and dielectric methods (17-23 kcal/mole). This is consistent with greater free volume at the polymer surface, as discussed above.

3. Volume Deformation Model

The rate dependence of friction on amorphous PVOH and gelatin films and its dependence on water content, the temperature dependence of friction on PMMA, PET and PS films, and time-temperature superposition on PMMA, consistently reveal the viscoelastic nature of energy dissipation in a nanoscale sliding contact. These findings imply that internal molecular relaxation, rather than the shearing of interfacial "bonds",[25] is the dominant mechanism of friction on amorphous polymers. This suggests that the locus of energy dissipation penetrates farther into polymers than on many materials. As a result one expects friction to scale with the volume of the deformation region, rather than the area of tip-sample contact.

This concept is illustrated schematically in Figure 9a. In contact mechanics models like the Hertzian or JKR, a spherical indentor is assumed. There is no way to access the exact shape of the contact zone between tip and sample surface during a SFM experiment. Our assumption of spherical geometry is justified by images of

silicon needles, wherein the tip apex appeared to be spherical.[14] In this case the contact radius should scale with the 1/3 power of load. Friction proportional to contact area thus scales as the 2/3 power of load, whereas friction proportional to deformation volume would scale as the 3/3 power of load (linearly). To test this prediction, we have measured the load dependence of friction on a PMMA film, shown in Figure 9b. The trend of the data was compared to two functional forms: a form with a single term proportional to the 2/3 power of load (dashed line), and a form with two terms, one linear with load and one proportional to the 2/3 power of load (solid line). Notwithstanding slight curvature of the data at low loads, the dominant data trend is linear. This is consistent with the concept of friction force proportional to deformation volume under a spherical indentor.

Studies of stiffer and/or more ordered materials, in which friction force is proportional to contact area, typically find that the magnitudes of friction and pull-off forces track each other, e.g. as a function of interfacial energy.[31] We tested for this in the temperature dependence of pull-off force on PMMA, PET, and PS, shown in Figure 10. The data were collected at each temperature prior to the friction data plotted in Figure 6. No temperature dependence in the pull-off force is observed on PMMA until a discontinuity at 80°C, most likely reflecting a change in tip state; then a steady increase in pull-off force results as the temperature increases into the rubbery regime. On PET no temperature dependence is seen in pull-off force throughout the temperature range explored. On PS the temperature dependence is flat up to nearly 120°C. Thus the temperature dependence of pull-off force on PMMA, PET and PS films does not track, even qualitatively, the friction force.

Figure 10 shows no increase in pull-off force (adhesion) except on PMMA and PS when the temperature was sufficiently high, into the rubbery regime. Above T_g the contact area will increase because of a decrease in storage modulus. Thus one anticipates an increase in pull-off force, as observed on PMMA and PS. (PET does not soften dramatically above T_g at levels of crystallinity above 40%. We have not performed independent measurements of crystallinity on our PET films.) Our frictional data exhibit a temperature dependence similar to *tan*δ, which equals the loss modulus divided by storage modulus. Thus we expect that observed changes in friction below 100°C arise from changes in loss modulus.

To understand this observation, an expression for friction including loss modulus must be developed. When a spherical tip slides across a compliant sample it induces a trench-shaped deformation region, as illustrated in Figure 11. The amount of energy dissipated (δU) per sliding distance (δx) is the frictional force. The energy dissipated per unit volume of deformed polymer is given by the loss modulus E''.[10] Energy dissipation due to the breaking of interfacial adhesive "bonds" is ignored here, based on the above discussion. For a spherical tip with radius of curvature R, contact radius a, and spherical-cap cross section of area A, we obtain

$$F_f = \frac{\delta U}{\delta x} = \frac{E'' A \delta x}{\delta x} = E'' R^2 \left[\sin^{-1}\left(\frac{a}{R}\right) - \frac{a}{R}\sqrt{1 - \left(\frac{a}{R}\right)^2} \right]$$
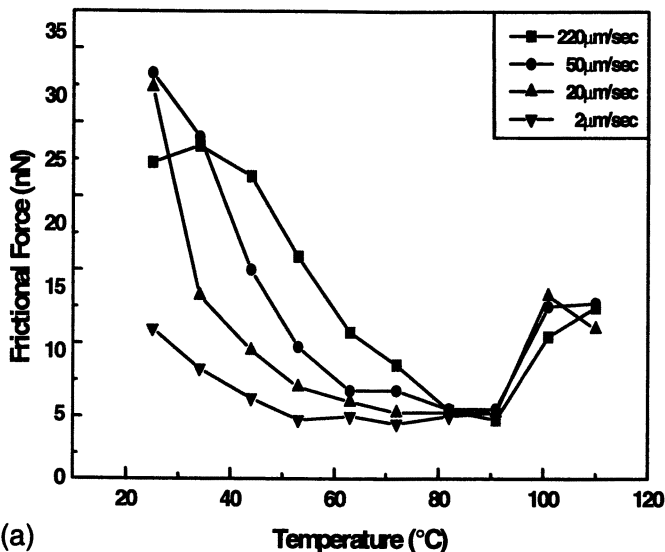
(a)
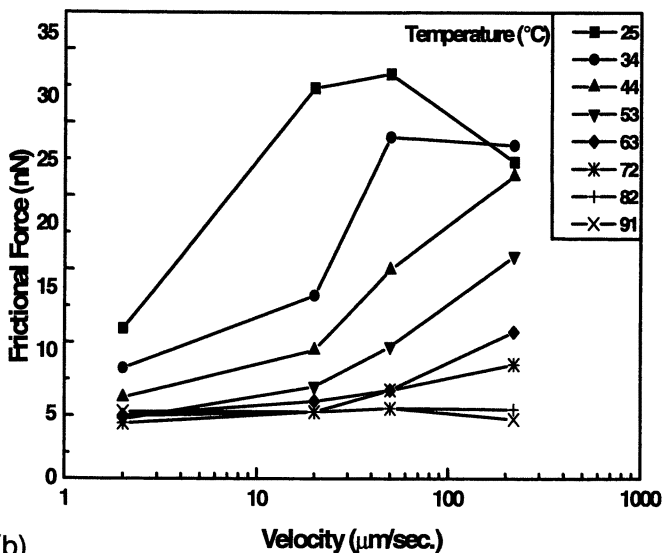
(b)

Figure 8. Time-temperature superposition analysis of frictional data collected on thin PMMA. (a) Temperature dependence of friction at four scan velocities; (b) same data inverted, i.e. scan-velocity dependence of friction at multiple temperatures; (c) "master curve" of same data sets as in (b), but shifted by variable multiplicative factors a_T; (d) plot of shift factors a_T versus inverse temperature, with linear fit.

(c)

(d)
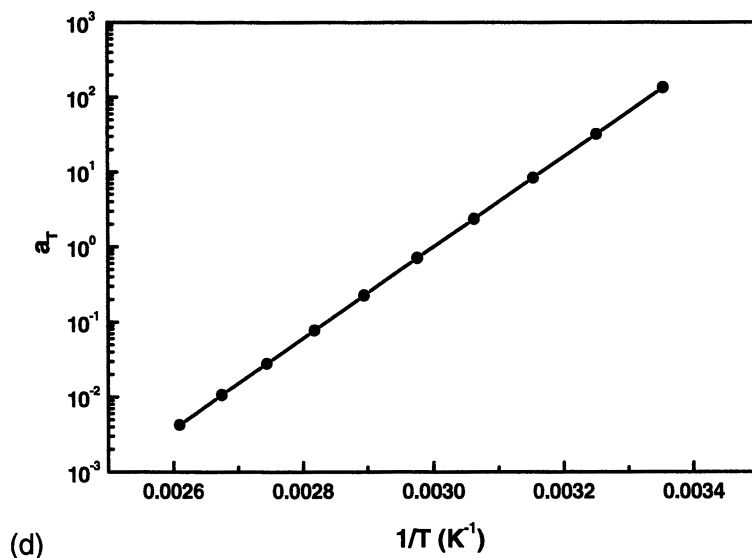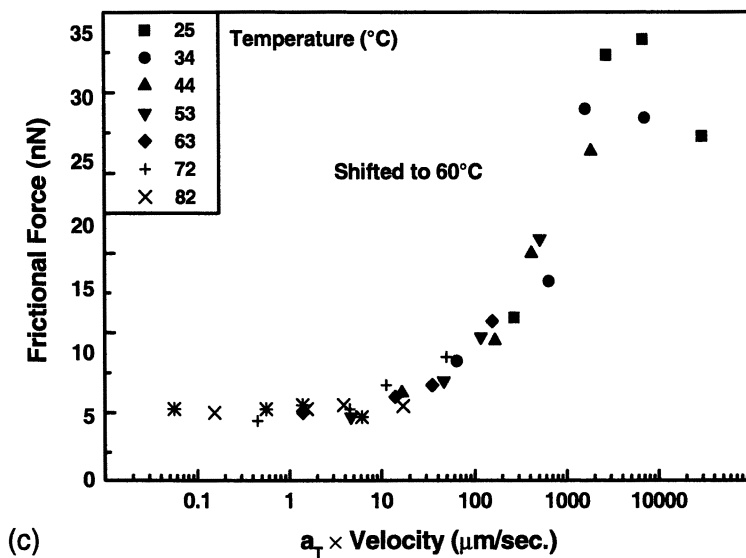
Figure 8. Continued.
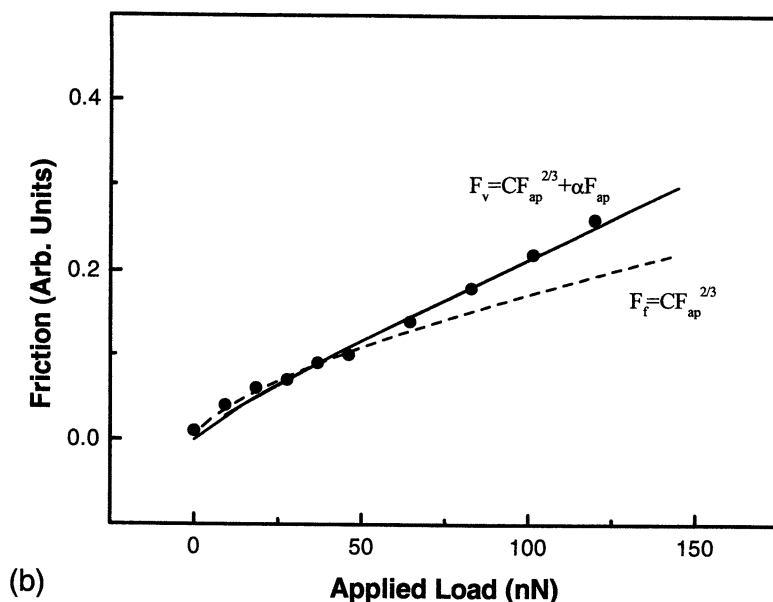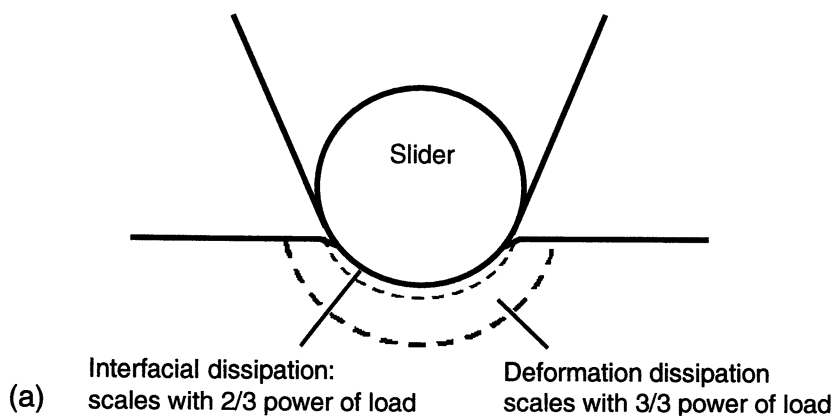
Figure 9. (a) Schematic illustration of the locus of energy dissipation in the case of "interfacial" dissipation, which scales as the 2/3 power of load, and "deformation" dissipation, which scales linearly with load. (b) Load dependence of friction on a thin PMMA film. Plots of two-term (solid line) and one-term (dashed line) models containing 2/3-power and linear load dependences as indicated.
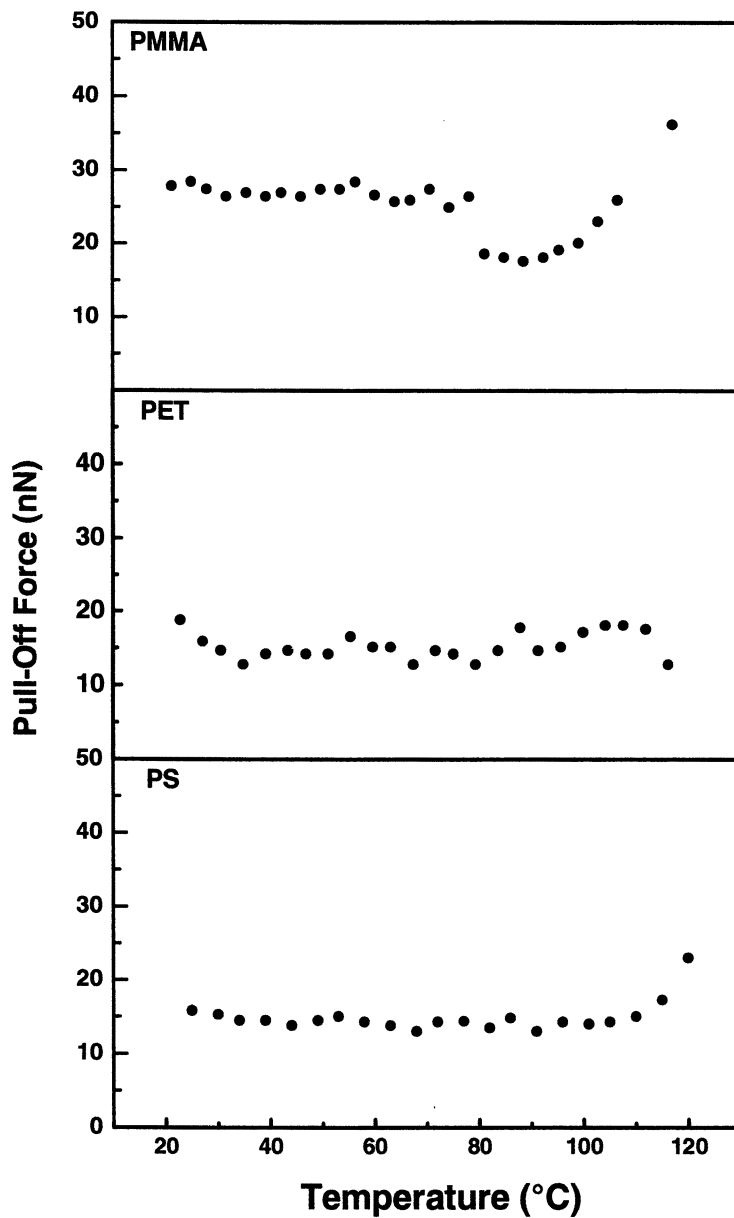
Figure 10. Temperature dependence of pull-off force on ≈20-nm films of PMMA,
PET, and PS.

(a)

(b)

$$Area = R^2 \left[sin^{-1}\left(\frac{a}{R}\right) - \frac{a}{R}\sqrt{1 - \left(\frac{a}{R}\right)^2} \right]$$
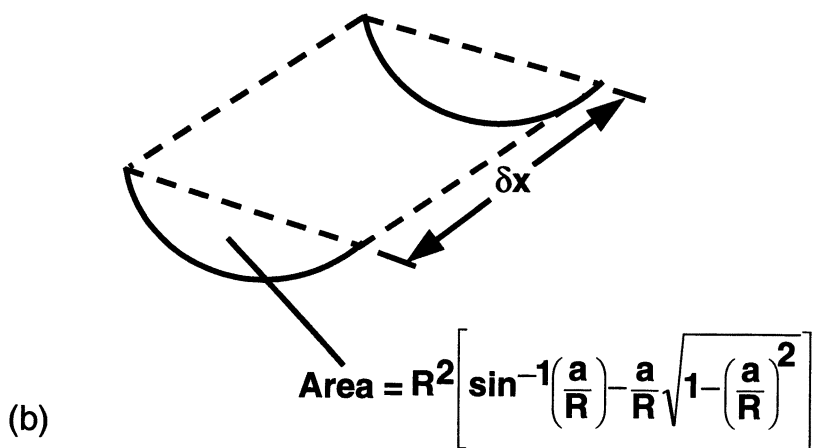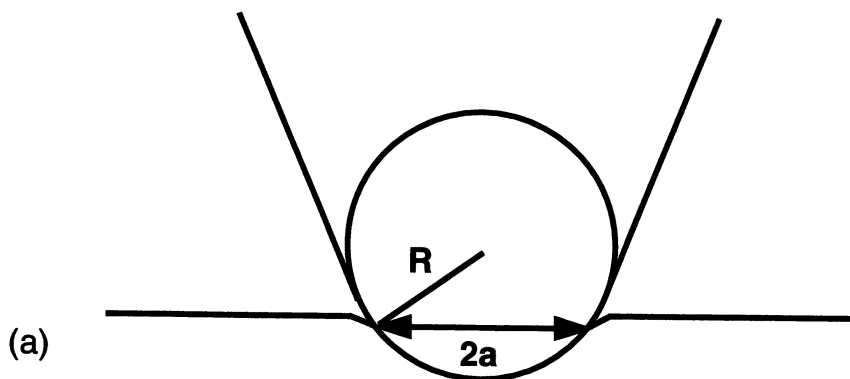
Figure 11. (a) Illustration of polymer indentation by spherical tip with radius of curvature R and contact diameter 2a. (b) Illustration of trench-shaped deformation region swept out by sliding spherical indentor.

Expanding F_f in a power series of (a/R), using the first 3 terms of the expansion we obtain:

$$F_f = E''R^2 \left[\frac{2}{3}\left(\frac{a}{R}\right)^3 + \frac{1}{5}\left(\frac{a}{R}\right)^5 - \frac{3}{28}\left(\frac{a}{R}\right)^7 + ... \right]$$

Assuming JKR contact mechanics,[30] it can be shown that the first term accounts for about 90% of the friction.[14] The cube of contact radius scales as E^{-1}; thus friction is proportional to E''/E', i.e. $tan\delta$.

The largest source of error in this model is the assumption that the volume element for dissipation only includes the amount of polymer traced out by the probe. In actuality, additional energy will be dissipated by creation of a strain field that extends farther into the polymer. A detailed, quantitative application of the above model has indicated that the total energy dissipation is approximately a factor of five greater than given by the volume traced by the tip in Figure 11.[14] This suggests that the radius of the strained volume is larger by perhaps a factor of two, corresponding to a distance into the material of order 10 nm. The strain field of course will not disappear abruptly at a particular distance, but instead diminish continuously. One may assume that energy dissipation is strongest in regions most severely strained. Finite element calculations are needed to determine accurately the depth to which the material is appreciably strained to account more precisely for this "excess" dissipation.

One might attempt to attribute some fraction of the dissipation to purely interfacial shear. It is difficult to postulate a "shear strength" of interactions between tip and sample. A more detailed study of load dependence (Figure 9b) might estimate the fractional energy dissipation at the interface, scaling with contact area as opposed to deformation volume. From our results, the best gauge of interfacial dissipation probably derives from the relative values of friction on highly crystalline PVA and gelatin compared to the more amorphous components (Figures 3a-b). For an upper bound estimate of interfacial dissipation on the more amorphous regions, we first assume that the highly crystalline moieties have *no* internal degrees of molecular freedom (e.g. rotational), and thus *all* dissipation derives from interface shearing. We further assume that extra dissipation on the more amorphous regions derives entirely from internal degrees of freedom. At temperatures and humidities within the glassy regime, we generally measure friction at least 2.5 times larger on the more amorphous regions. Thus we estimate an upper bound of 40% shear dissipation on these regions. At higher humidities (and temperatures) on more amorphous regions, the volume deformation dissipation strongly increases with the onset of rubbery behavior, and thus interfacial shear becomes even less significant (10% or less). The concept that energy dissipated via *internal* degrees of freedom of a polymer, in making and breaking a polymer-inorganic interface, exceeds the energy dissipated *at* the interface by an order of magnitude or more, is well established in polymer adhesive research (i.e. work of adhesion two or three orders of magnitude greater than thermodynamic interfacial energy).[32]

CONCLUSIONS

Nanoscale sliding friction on highly amorphous thin polymer films is dominated by viscoelastic energy dissipation throughout a strained volume of material. Viscoelastic processes are clearly evident in the rate and temperature dependence of friction. In hydrophilic polymers, varying degrees of water plasticization in crystalline versus amorphous regions, and lower friction on crystalline regions in general, are further evidence that viscoelastic dissipation in amorphous regions dominates nanoscale friction. Purely interfacial dissipation, due to irreversible making and breaking of "bonds" between probe and sample, is of lesser importance. Analysis of friction due to both large-scale (glass to-rubber transition) and small-scale (secondary) relaxations suggests enhanced molecular freedom relative to dynamic mechanical measurements in the bulk. We attribute this to surface segregation of chain ends in the polymer films examined. Notwithstanding this finding, the sensitivity of nanoscale friction to molecular relaxations down to depths of order 10 nm into the material implies the ability to probe changes in molecular conformation throughout ultrathin organic films.

REFERENCES AND NOTES

1   Garbassi, F.; Morra, M.; Occhiello, E. Polymer Surfaces; John Wiley and Sons: West Sussex, 1994.

2   Jones, R. A. L.; Richards, R. W. Polymers at Surfaces and Interfaces; Cambridge University Press: Cambridge, 1999.

3   Bhushan, B. Handbook of Micro/Nanotribology; 2nd ed.; Bhushan, B., Ed.; CRC Press: Boca Raton, FL, 1999.

4   Forrest, J. A.; Dalnoki-Veress, K.; Dutcher, J. R. Phys. Rev. E 1997, 56, 5705-5716.

5   Forrest, J. A.; Dalnoki-Veress, K.; Stevens, J. R.; Dutcher, J. R. Phys. Rev. Lett. 1996, 77, 2002-2005.

6   Keddie, J. L.; Jones, R. A. L.; Cory, R. A. Europhys. Lett. 1994, 27, 59-64.

7   DeMaggio, G. B.; Frieze, W. E.; Gidley, D. W.; Zhu, M.; Hristov, H. A.; Yee, A. F. Phys. Rev. Lett. 1997, 78, 1524-1527.

8   Mayes, A. M. Macromolecules 1994, 27, 3114.

9   Lee, L.-H. Advances in Polymer Friction and Wear; Lee, L.-H., Ed.; Plenum Press: New York, 1974; Vol. 5, pp 405.

10   Moore, D. F. The Friction and Lubrication of Elastomers; Pergamon Press, Ltd.: Oxford, 1972.

11 Grosch, K. A. Proc. R. Soc. London 1963, 274, 21.

12 Ludema, K. C.; Tabor, D. Wear 1966, 9, 329.

13 Haugstad, G.; Gladfelter, W. L.; Weberg, E. B.; Weberg, R. T.; Weatherill, T. D. Langmuir 1994, 10, 4295-4306.

14 Hammerschmidt, J. A.; Gladfelter, W. L.; Haugstad, G. Macromolecules 1999, 32, 3360-3367.

15 Schmidt, R. H.; Haugstad, G.; Gladfelter, W. L. Langmuir 1999, 15, 317-321.

16 Kajiyama, T.; Tanaka, K.; Satomi, N.; Takahara, A. Macromolecules 1998, 31, 5150-5151.

17 Haugstad, G.; Gladfelter, W. L.; Weberg, E. B.; Weberg, R. T.; Jones, R. R. Langmuir 1995, 11, 3473-3482.

18 Haugstad, G.; Gladfelter, W. L.; Jones, R. R. J. Vac. Sci. Technol. A 1996, 14, 1864-1869.

19 Hammerschmidt, J. A.; Moasser, B.; Gladfelter, W. L.; Haugstad, G.; Jones, R. R. Macromolecules 1996, 29, 8996-8998.

20 Kajiyama, T.; Tanaka, K.; Takahara, A. Macromolecules 1997, 30, 280-285.

21 Haugstad, G.; Gladfelter, W. L.; Jones, R. R. Langmuir 1998, 14, 3944-3953.

22 McCrum, N. G.; Read, B. E.; Williams, G. Anelastic and Dielectric Effects in Polymeric Solids; Wiley: London, 1967.

23 Haugstad, G.; Gladfelter, W. G.; Weberg, E. B.; Weberg, R. T.; Weatherill, T. D.; Jones, R. R. Mat. Sci. Eng. C 1995, 3, 85-88.

24 Haugstad, G.; Gladfelter, W. L.; Weberg, E. B.; Weberg, R. T.; Weatherill, T. D. Mat. Res. Soc. Symp. Proc. 1995, 355, 253-258.

25 Bowden, F. P.; Tabor, D. The Friction and Lubrication of Solids, Part 2; Clarendon: Oxford, 1964.

26 The more amorphous component is strictly understood to be semicrystalline, containing nanoscale crystalline domains or fibrils embedded in a lossy amorphous matrix.

27 Finch, C. A. Polyvinyl Alcohol: Properties and Applications; Wiley: London, 1973.

28 Curme, H. G. Gelatin; 4th ed.; Curme, H. G., Ed.; MacMillan Publishing Co.: New York, 1966, pp 45-71.

29 Marshall, A. S.; Petrie, S. E. B. J. Photogr. Sci. 1980, 28, 128-134.

30 Johnson, K. L.; Kendall, K.; Roberts, A. D. Proc. R. Soc. London A 1971, 324, 301-313.

31 Noy, A.; Frisbie, C. D.; Rozsnyai, L. F.; Wrighton, M. S.; Leiber, C. M. J. Am. Chem. Soc. 1995, 117, 7943-7951.

32 See, for example, Jones, R.A.; Richards, R.W. in Polymers at Surfaces and Interfaces, Cambridge University Press, 1999, and references therein.

Chapter 16

Microthermomechanical Probing of Thin Composite Polymer Films

Vladimir V. Tsukruk, Valery Gorbunov, Igor Luzinov, Zheng Huang, and Nobi Fuchigami

Department of Materials Science and Engineering, Iowa State University, Ames, IA 50011

Surface distribution of micromechanical properties of polystyrene-polybutadiene (PS/PB) thin films is probed in the range of temperatures. We demonstrate that for heterogeneous polymer films, the micromapping of surface properties can be obtained *concurrently* for glassy and rubber phases as well as across the interface. The histogram of the surface distribution of elastic modulus display two very distinctive maxima for glassy and rubber phases at 2.5 GPa and 6 MPa, respectively. The depth profile measurements demonstrate consistent changes of the rubber phase thickness with distance from the PS/PB interface. Glass transition temperature of glassy matrix, flow temperature of rubber phase, and difference in thermal conductivities all can be collected for heterogeneous polymer films on a microscopic scale.

Introduction

First attempts to record the micro/nanomechanical surface properties with atomic force microscopy/scanning probe microscopy (AFM/SPM) probing were conducted by using the classical Sneddon's approach [1-3]. Further development lead to the micromapping of the surface mechanical properties with a force modulation mode [4-8]. Several studies were focused on the development of dc force-displacement probing of the micromechanical properties [9-15]. In this communication, we report on studies of the micromechanical properties of composite films of polystyrene/polybutadiene (PS/PB) and grafted PS layers and prove the feasibility of

of force-displacement data collection/analysis approach to obtain reliable micromechanical data for composite materials.

Experimental

Samples for investigation were prepared by spin-coating of polystyrene (M_w = 250, 000, Janssen Chemical Co.) / polybutadiene (M_w = 420, 000, Aldrich) blends on a silicon wafer with PS as a glassy matrix and PB as a dispersed rubber phase. The film thickness was kept within 2 - 5 μm. Composite films were probed with a Dimension 3000 microscope (Digital Instruments) in a Force Volume mode with 2 Hz probing frequency and a lateral resolution 32 x 32 or 64 x 64 pixels. Scan sizes varied from 2 x 2 m to 30 x 30 m. The DI thermal stage was used for data collection in the range of temperatures up to 120°C. The SPM tips were silicon tips with a spring constant determined by a combination of resonant frequency measurements and spring-against-spring techniques (16-18). We measured the cantilever resonance frequency and estimated normal and torsional spring constants from calibration plots proposed earlier (17). Tip radius was measured by scanning gold nanoparticles chemically attached to self-assembled monolayers and using a spherical approximation to extract parameters from cross-sections (19).

For data processing, we used the protocol for the microprobing of the adhesive forces and elastic modulus based on the contact model of elastic deformation modified for SPM measurements (12, 13, 15). We analyzed repulsive part of approaching force-distance curves and used the Hertzian contact mechanics model (sphere against plane) combined with the two-spring model to evaluate elastic modulus from these force-distance data. No viscoelastic contribution was taken into account in current analysis. This approach was proved reliable for the probing the range of polymeric materials with elastic modulus as low as 1 MPa and as high as 3 GPa (12-15). The focus of this study was on finding optimal parameters for *concurrent* collection of micromechanical data for two phases (rubber and glassy) with very different elastic properties. Scanning thermal imaging was performed according to the procedure discussed before (20, 21) on an Explorer microscope (Thermomicroscopes).

Results and discussion

As was observed, all PS/PB films are highly heterogeneous with well-developed microphase separation of rubber and glassy phases (Figure 1). The lateral size of the dispersed rubber phase varies from 20 μm to less than 1 μm. Rubber inclusions form either depleted or elevated round-shaped droplets. Cracks are occasionally observed to originate at the rubber-glass interface and propagate through the glassy matrix between large rubber droplets (Figure 1).
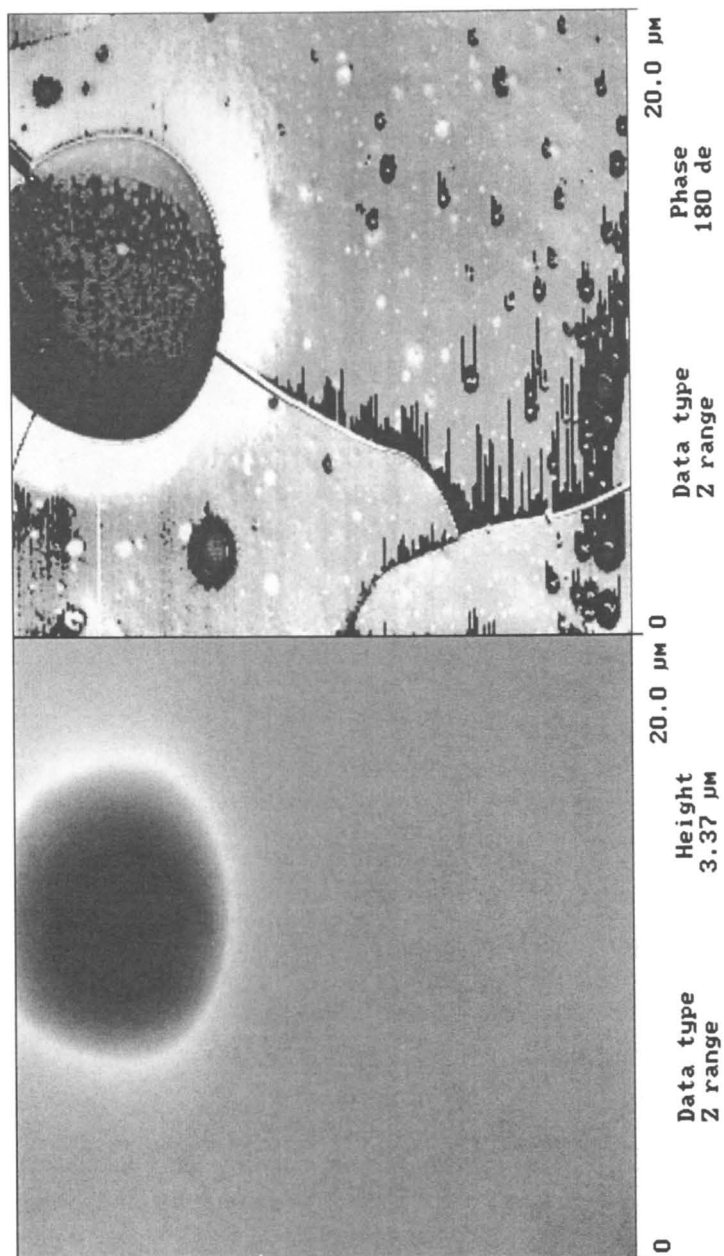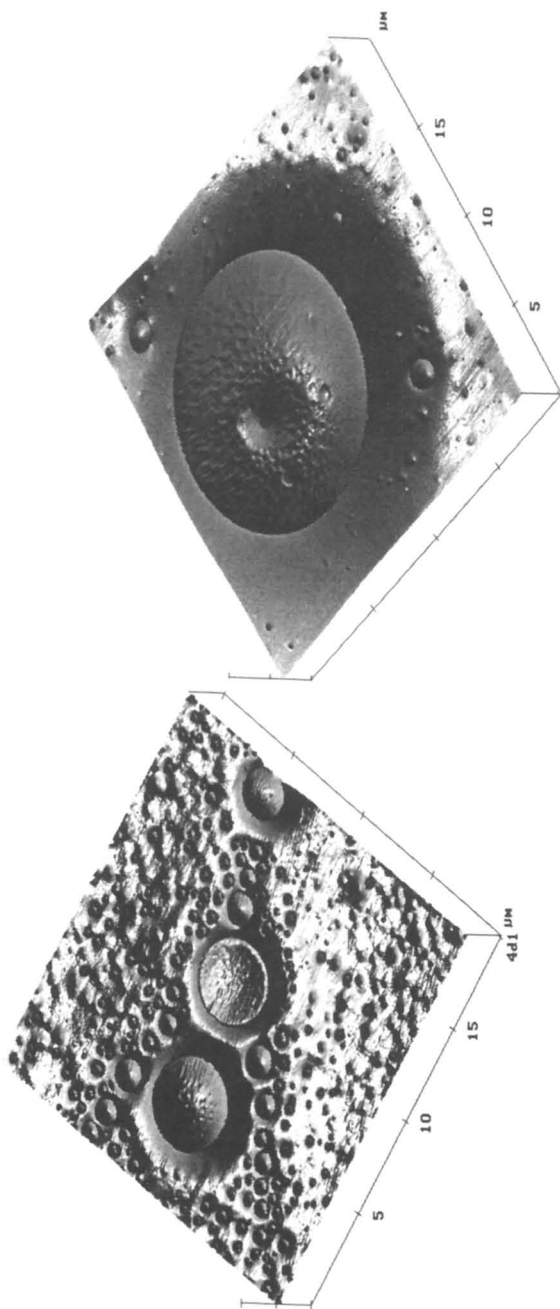
Figure 1. Topography of the PS/PB film with PB as the dispersed rubber phase. Pay attention to the dimensional variation of the PB droplets and the presence of the PS microinclusions inside a large rubber droplet. Top: topography (left) and phase (right) images of the same surface area. Bottom: 3-D representation of the polymer surface at two different locations.

Figure 2 demonstrates the micromapping data (topography, elastic modulus, and adhesive forces) obtained concurrently for the same surface area of the composite film. It shows that, for the rubber phase, the adhesive forces are much higher and elastic modulus is much lower as compared to the glassy matrix. The histogram of the surface distribution of elastic moduli displays two very distinctive peaks (Figure 2). The first, very sharp peak is located in the range 3 - 10 MPa and corresponds to the rubber phase. The broad distribution of elastic moduli between 2 - 4 GPa corresponds to the PS matrix.

Absolute values obtained by the SPM probing are very close to those expected for the bulk material (2-3 MPa for PB and 2-3 GPa for PS) [8]. The higher average value of elastic modulus observed for rubber phase within microscopic droplets can be related to its confined state in the form of thin layers and droplets, a relatively short probing time, as well as the presence of some PS microinclusions inside large rubber droplets (Figure 1). On the other hand, a broad distribution and lower value of elastic modulus for the PS matrix are caused by multiple defects in the form microcracks and small inclusions of rubber phases. A cross-section of the PB phase allows observing close correlation among surface properties as shown in Figure 3. As clear from this data, adhesion and elasticity follow closely topography with sharp changes across the rubber-glass interface, which occupies a fraction of a micrometer in a lateral direction.

Microprobing technique applied here is sensitive to the depth distribution of the elastic properties and can provide insight on buried details of the surface distribution of different polymer phases. As demonstrated in Figure 4, elastic modulus for the rubber phase shows the presence of hard PS surface underneath of compliant material. The elastic modulus depth profile shows a large variation at a very low indentation depth (below 20 nm) caused, mainly, by the instability of the first mechanical contact as discussed in our previous papers [12-14]. In the range of indentation depths from 20 to 150 nm, a gradual decrease of elastic modulus is observed that can be related to either surface hardening phenomena or rate dependent (viscoelastic) contribution. At intermediate indentation depth, a stable, virtually constant value of the elastic modulus is recorded.

For various rubber droplets, a sharp increase of elastic modulus takes place at a very high indentation depth, far exceeding the limitations of the Hertzian model (Figure 4). Therefore, absolute values in this indentation range should be treated with care and here we discuss only qualitative behavior. A sharp increase of "apparent" elastic modulus at higher indentation depths can be associated with the tip approaching a hard PS surface below the rubber phase. Indeed, we observed a significant variation of this depth from 100 nm in the vicinity of the rubber-matrix interface and within very small (less than a micrometer diameter) rubber droplets to as large as >800 nm in the central part of large rubber particles (Figures 4, 5). This depth approximately corresponds to the expected thickness of rubber droplets of different lateral sizes as illustrated in Figure 5 and indicates that rubber material is virtually completely compressed under the SPM tip. Therefore, we conclude that the sharp increase of elastic response at high indentation depth detected by the SPM tip indicates the thickness of the rubber layer on a top of the glassy matrix at a particular location.

At the elevated temperature, the micromapping of composite films shows distinctive rubber and glassy phases up to 100°C. At even higher temperatures, adhesion and elastic surface distributions become very homogeneous with no detectable differences in the micromechanical properties detected between PS and PB phases (Figure 6). Sharp deviations observed only along the rim of round inclusions (the width is less than one micrometer) are caused by the geometrical contribution of different elevations at the PB-PS interface.

From the micromapping data obtained at different temperatures, we measured the temperature dependence of elastic modulus separately for glassy and rubber phases (Figure 7). The absolute value of elastic modulus for the PS phase is virtually constant (about 2 GPa) within an interval of temperatures from room temperature to about 100°C. A sharp drop of PS elastic modulus to the value below 10 MPa is observed within a narrow temperature interval from 100 to 120°C. This indicates glass transformation (103°C as measured by DSC for this PS) and the transition of the glassy matrix to the elastic state.

On the other hand, the average elastic modulus of the rubber phase decreases steadily for higher temperatures (up to 100°C) (Figure 7). Then, its value increases sharply around 110°C and decreases again. This behavior can be understood after careful analysis of modulus depth profiles. Indeed, we estimated the elastic modulus by averaging over a complete indentation depth interval. At temperatures higher than the flow temperature of the PB phase (100°C), the SPM tip penetrates through the viscous phase and effectively interacts only with the hard PS surface. This results in sharp increase of the "integrated" elastic modulus value, which is, essentially, PS modulus itself at this temperature. At even higher temperature, the PS matrix goes through transformation to the elastic state that manifests itself in the sharp reduction of integrated elastic modulus to typical rubber level.

Scanning thermal microscopy (SThM) was used to estimate the surface distribution of the microthermal properties (for details see Ref. 21). As can be seen from the images obtained in this mode (Figure 8, substantial thermal contrast for PB and PS phases can be detected at the probe temperature above 50°C. A geometrical contribution is also clearly visible However, taking into account that the effective thermal contact area for polymeric materials is about 1 μm [21], we can refer the major contribution in different thermal response for the polymer film to different thermal conductivities of glassy and rubber phases.

Finally, we tested micromechanical properties of ultrathin, monomolecular PS brushes with the thickness of 8 nm (determined by ellipsometry and AFM) [22]. The polymer layer is chemically tethered to the surface and posses molecularly smooth surface morphology (Figure 9). We performed micromapping around a worn area intentionally produced by the previous scanning with high forces (Figure 10). We observed that the elastic modulus value inside the worn area (a bare silicon surface) and on the intact PS brush layer exceeds the upper measurable limit of our experimental set-up (10 GPa in this case). This indicates that the SPM tip penetrated completely through the compliant polymer brush layer and probed the underlying silicon surface. Elastic modulus of polymer debris around the worn area was measured to be in the range 300 MPa - 1 GPa, which is fairly close to the expected value for low molar mass PS material. This example demonstrates that microprobing
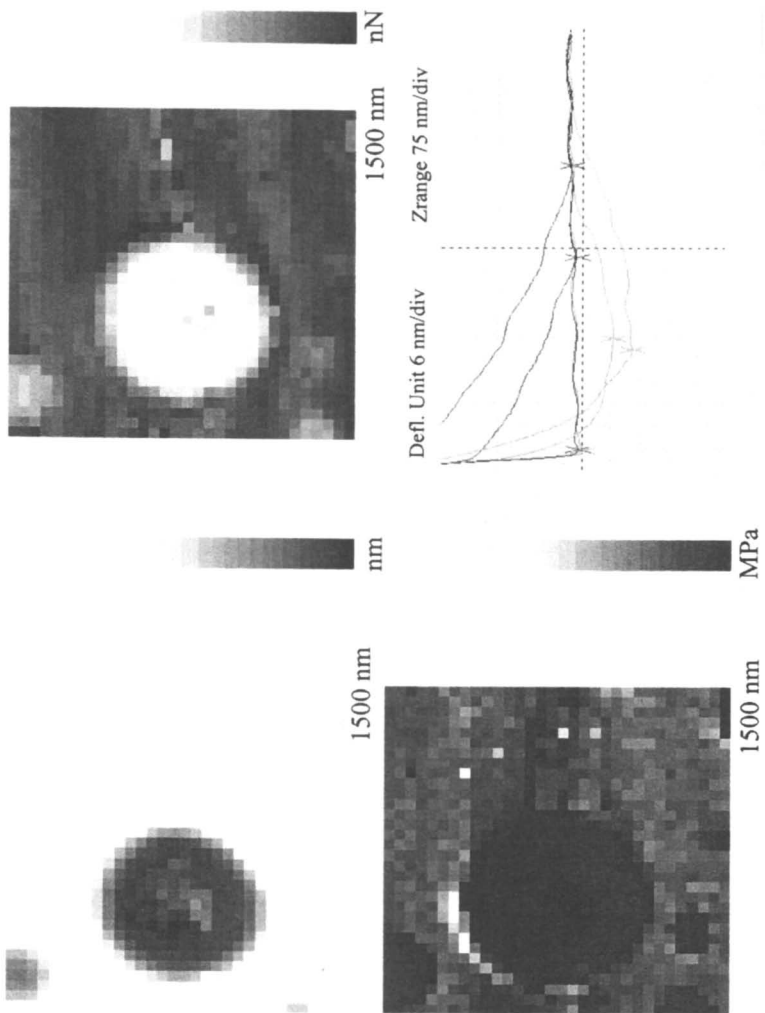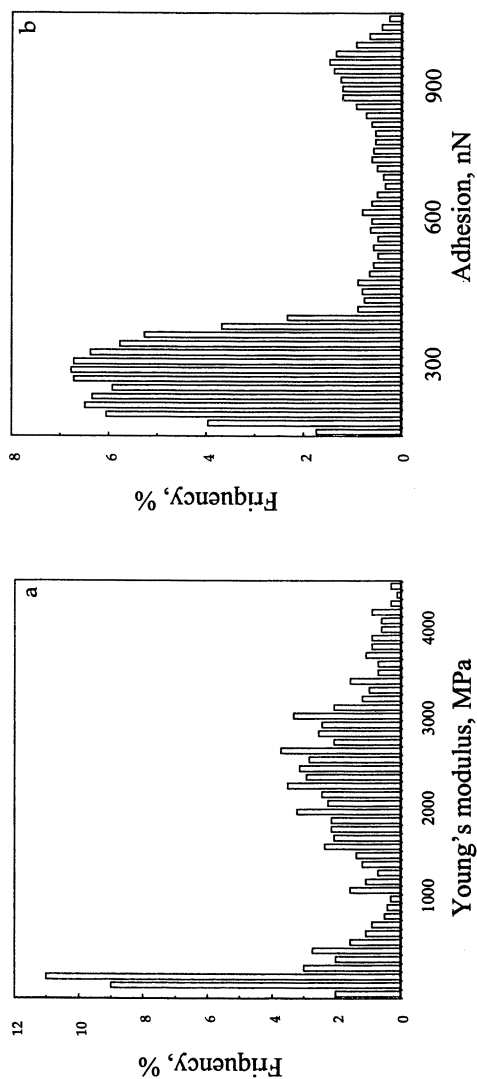
Figure 2. Top: topography (left top), adhesion (right top), and elastic modulus (left bottom) images of the PS/PB blend (15 x 15 μm). Force–distance curves are shown for rubber and glassy phases (right bottom). All mappings are done with the 64 x 64 pixel lateral resolution. Two histograms (bottom) of elastic modulus distribution and adhesive forces show two distinctive peaks for rubber and glassy phases.
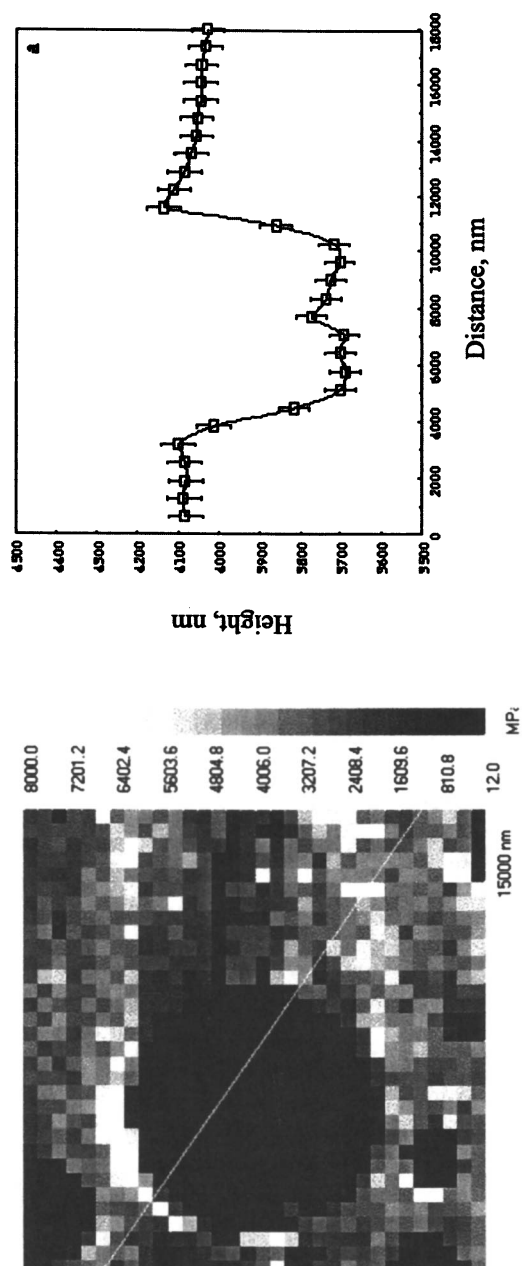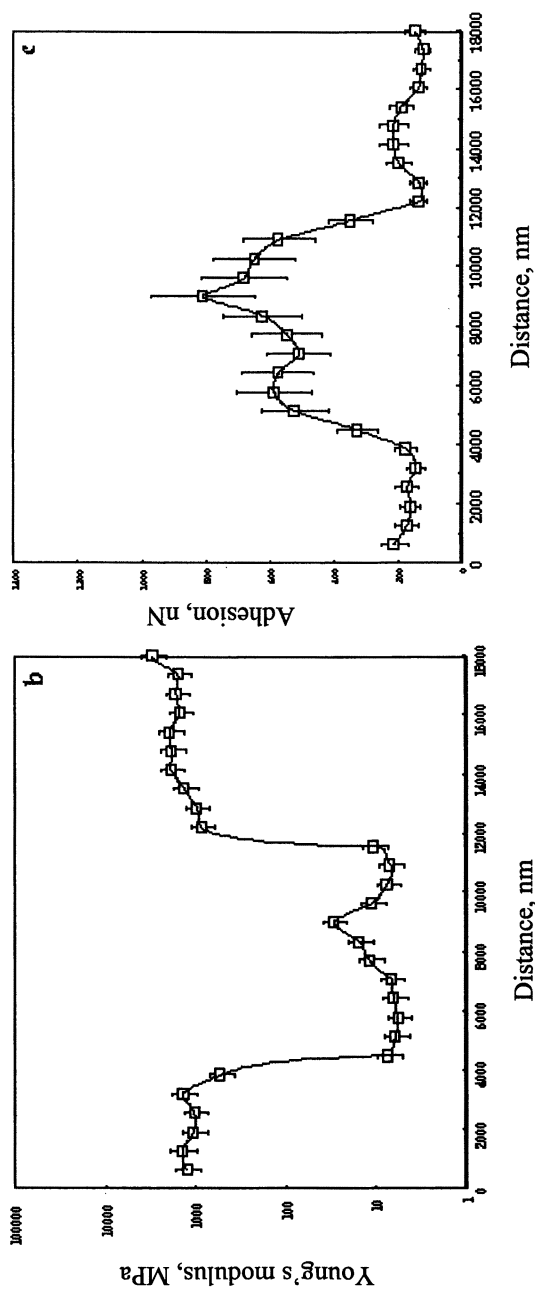
Figure 3. Cross-sections of the rubber phase surface properties within the glassy matrix: elastic modulus, adhesive force, and topography variation are recorded and calculated along the line shown on the image.
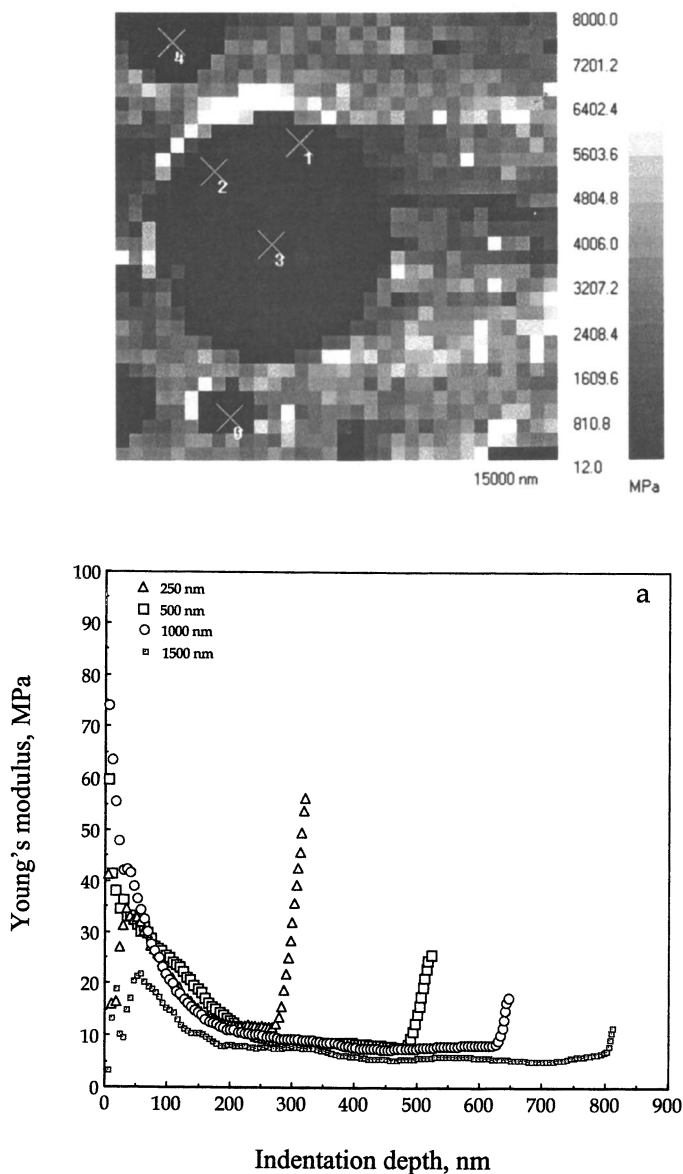
Figure 4. The depth profile of elastic moduli for the rubber phase at different locations within the large rubber droplet and within smaller rubber droplets, numbers indicate the distance from the glassy-rubber interface.
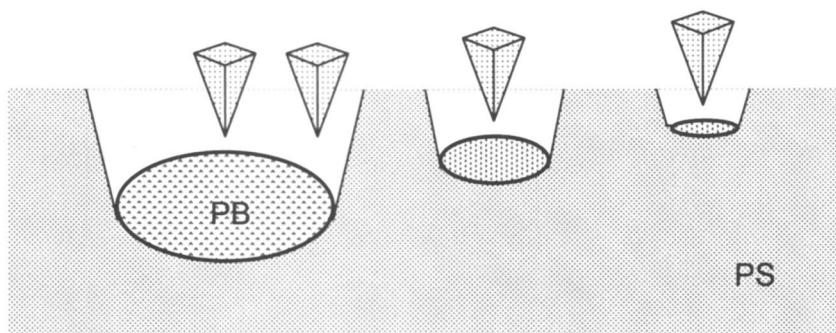
Figure 5. Schematic representation of the micromechanical probing of the rubber droplets with different diameter/thicknesses. Four locations correspond to depth profiles presented in Figure 4.

2771.6
2495.0
2218.4
1941.8
1665.2
1388.6
1112.0
835.4
558.8
282.2

30000 nm   nm

522.4
472.8
423.3
373.7
324.1
274.5
224.9
175.3
125.7
76.1
30000 nm   26.5 MPa

1001.7
915.3
829.0
742.7
656.4
570.0
483.7
397.4
311.0
224.7
30000 nm   138.4 nN
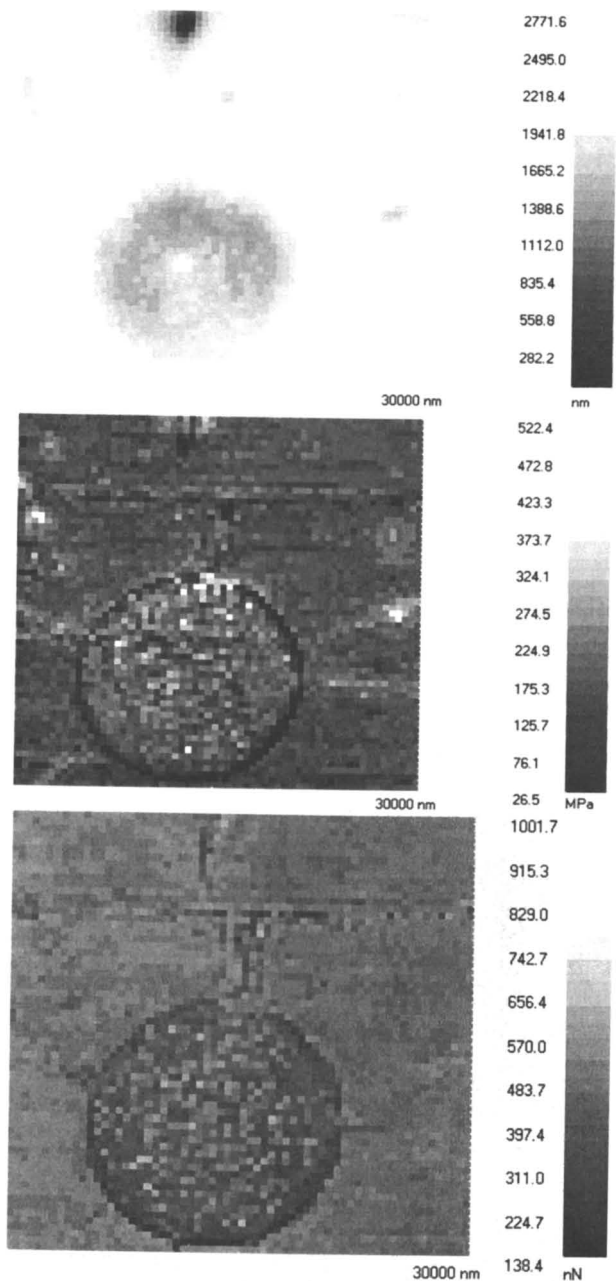
Figure 6. The microprobing of the polymer composite film at elevated temperatures. Topography (top), elastic modulus (middle), and adhesion (bottom), images of PS/PB film (30 x 30 μm) obtained at 120°C. Pay attention to the homogeneous surface distribution of elastic and adhesive properties except the geometrical contribution across the PS/PB interface.

Young's modulus of PS phase in PB/PS spin coated blend film vs. temperature
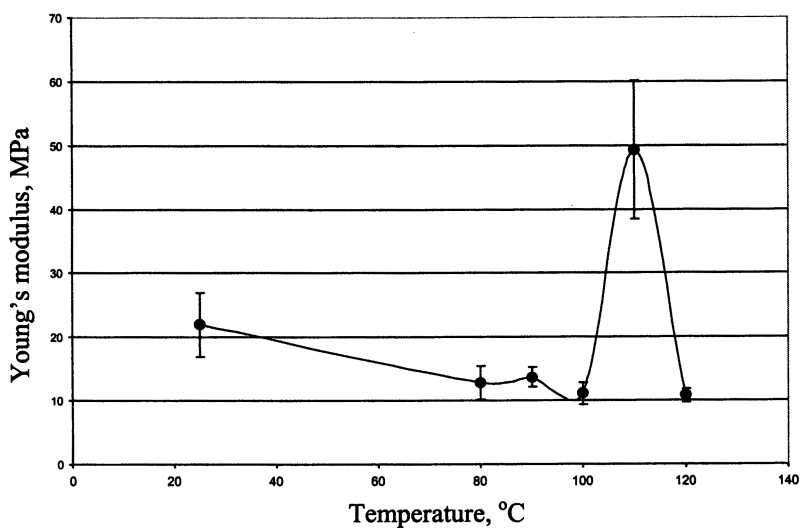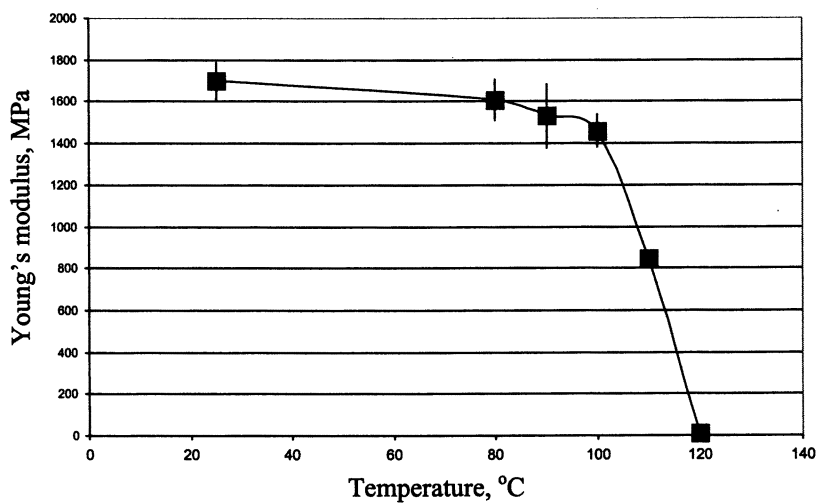
Figure 7. Temperature variation of elastic modulus for the PS matrix (top) and the rubber phase (bottom) as derived from the surface histogram.
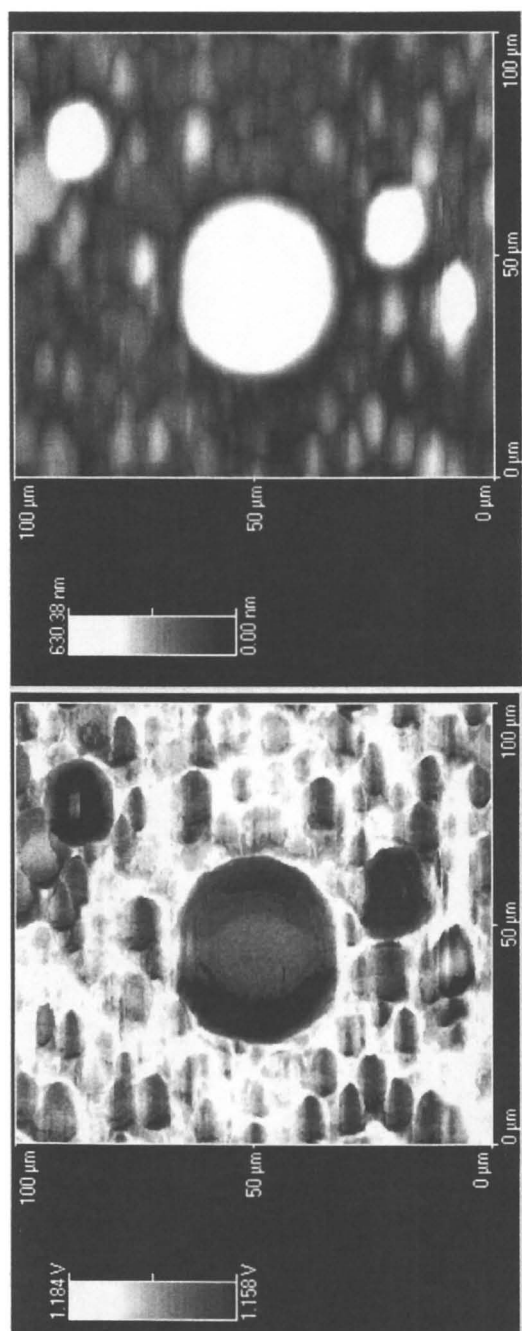
Figure 8. Topography and thermal images of the PS/PB film obtained by the SThM mode at the probe temperature of 60°C.
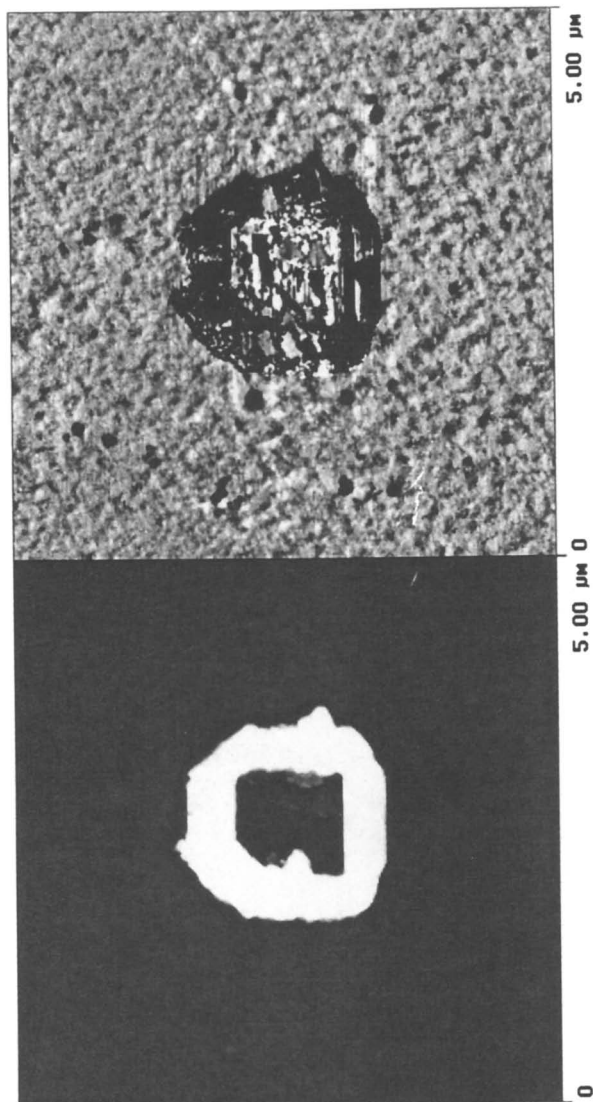
Figure 9. Topography (left) and phase image (right) of PS molecular layer (8 nm thick) tethered to a silicon wafer with the worn area produced by selective scanning with high forces (scan size: 5 x 5 μm).
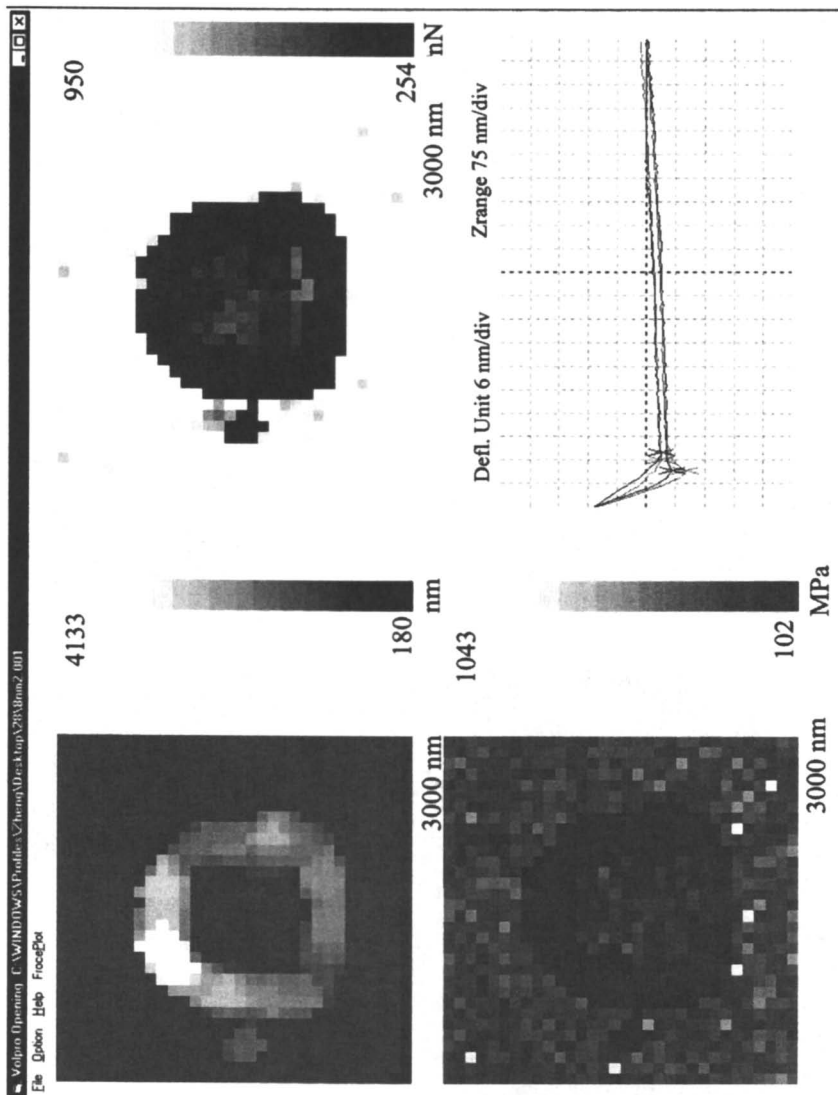
Figure 10. The microprobing of polymer molecular layer chemically tethered to a silicon wafer. Topography (left top), adhesion (right top), and elastic modulus (left bottom) images of the film (3 x 3 μm) with the worn area along with the example of force-distance curves (right bottom). Data shows low adhesion in the debris area and within the worn area and lower elastic modulus for polymer debris.

technique explored in our work can be very informative for extremely thin polymer layers, down to a monomolecular layer.

Acknowledgment

References

1. Binnig, G., Quate, C.F. and Gerber, Ch. *Phys. Rev. Lett.* **1986**, *12*, 930.
2. Landman, U., Luedtke, W. D., Burnham, N. A. and Colton, R. J. *Science,* **1990**, *248*, 454.
3. Burnham, N. A. and Colton, R. J. *J. Vac. Sci. Technol.,* **1989**, *A7*, 2906.
4. Oulevey, F., Gremaud, G., Semoroz, A., Kulik, A. J., Burnham, N. A., Dupas, E. and Gourdon, D. *Rev. Sci. Instr.,* **1998**, *69*, 2085.
5. Marti, O. and Hild. S. in: *Microstructure and Microtribology of Polymer Surfaces,* eds. V. V. Tsukruk, K. Wahl, ACS Symposium Series, v. 741, 2000, p.212.
6. Radmacher, M., Tillmann, R. W. and Gaub, H. E. *Biophys. J.,* **1993**, *64*, 735.
7. Kajiyama, T., Tanaka, K. and Takahara, A. *Macromolecules,* **1997**, *30*, 280.
8. Aklonis, J. J. and MacKnight, W. J. *Introduction to Polymer Viscoelasticity,* J. Wiley & Sons: NY, 1983.
9. Vanlandingham, M. R., McKnight, S. H., Palmese, G. R., Ellings, J. R., Huang, X., Bogetti, T. A., Eduljee, R. F. and Gillespie, J. W. *J. Adhesion,* **1997**, *64*, 31.
10. Overney, R. and Tsukruk, V. V. in: *Scanning Probe Microscopy of Polymers,* eds. B. Ratner and V. V. Tsukruk, ACS Symposium Series, 1998, v. 694, p. 2.
11. Domke, J. and Radmacher, M. *Langmuir,* **1998**, *14*, 3320.
12. Chizhik, S. A., Huang, Z., Gorbunov, V. V., Myshkin, N. K. and Tsukruk, V. V. *Langmuir,* **1998**, *14*, 2606.
13. Tsukruk, V. V., Huang, Z., Chizhik, S. A. and Gorbunov, V. V. *J. Materials Science,* **1998**, *33*, 4905.
14. Huang, Z., Chizhik, S. A., Gorbunov, V. V., Myshkin, N. K. and Tsukruk, V. V. in: *Microstructure and Microtribology of Polymer Surfaces,* Eds. V. V. Tsukruk, K. Wahl, ACS Symposium Series, v. 741, 2000, p. 177.
15. Tsukruk, V. V., Gorbunov, V. V., Huang, Z., Chizhik, S. A. *Polym. Intern.* 1999, accepted
16. Hazel, J. L. and Tsukruk V. V. *J. Tribology,* **1998**, *120*, 814.
17. Hazel, J. L. and Tsukruk, V. V. *Thin Solid Films,* **1999**, *339*, 249.
18. Huang, Z. *MS Thesis*, Western Michigan University, 1999.

19. Bliznyuk, V. N., Hazel, J. H., Wu, J. and Tsukruk, V. V. in: *"Scanning probe Microscopy of Polymers"*, Eds. B. Ratner, V. V. Tsukruk, 1998, v. 694, p. 252

20. Hammiche, A., Hourston, D. J., Pollock H. M., Reading, M., Song, M. *J. Vac. Sci. Techn.,* **1996**, *14(2),* 1486.

21. Gorbunov, V. V., Fuchigami, N., Hazel, J. L., Tsukruk, V. V. *Langmuir,* **1999,** *15,* 8340.

22. Luzinov, I., Julthongpiput, D., Malz, H., Pionteck, J., Tsukruk, V. V. *Macromolecules,* 1999, accepted

Chapter 17

Structural Properties of Self-Assembled Monolayers on Gold Generated from Terminally Fluorinated Alkanethiols

Ramon Colorado, Jr., Michael Graupe, Olga E. Shmakova, Ramon J. Villazana, and T. Randall Lee*

Department of Chemistry, University of Houston, Houston, TX 77204–5641

This research examines the structural effects that accompany systematic alterations in the chemical composition of SAMs on gold prepared from three distinct series of terminally fluorinated alkanethiols having the general formula $F(CF_2)_x(CH_2)_ySH$. In the first series, the length of the fluorocarbon segment is varied (x = 1-10) while the length of the hydrocarbon segment is held constant (y = 11). In the second series, the length of the fluorinated segment is held constant (x = 10) while the length of the hydrocarbon segment is varied (y = 2-6, 11, and 17). In the final series, both the length of the fluorinated segment (x = 1-10) and the length of the hydrocarbon segment (y = 15-6, respectively) of hexadecanethiols are varied. Analyses of the films by ellipsometry and X-ray photoelectron spectroscopy (XPS) reflect the controlled introduction of fluorine within a series. Characterization of the monolayers by polarization modulation infrared reflection absorption spectroscopy (PM-IRRAS) reveals that the conformational order of the hydrocarbon segments in terminally fluorinated films varies systematically with the number of methylene units present, but is unaffected by the length of the overlying perfluorinated terminal segment.

Introduction

Fluorinated organic materials serve as useful coatings in a variety of applications involving computer hard disks, micro-electro-mechanical systems (MEMS), biomaterials, and non-stick coatings [1-4]. The physical properties of these materials (e.g., adhesion, friction, wettability, and thermal stability) are influenced by the

276

structure and composition of the surfaces [5-8]. To better understand this relationship, we evaluated the structural properties of a series of self-assembled monolayers (SAMs) on gold generated from alkanethiols that possess a systematically varied degree of terminal fluorination [9]. The following factors illustrate why the alkanethiolate SAM system is particularly well-suited for studying fluorinated organic interfaces: (1) the films are easy to make, (2) they are densely packed and highly oriented, and (3) their structure and composition can be altered through the use of standard organic synthetic methods [10]. We prepared SAMs on Au(111) from three distinct series of terminally fluorinated alkanethiols having the general formula $F(CF_2)_x(CH_2)_ySH$, in which the length of the fluorocarbon segment (x) and the length of the hydrocarbon segment (y) are varied (Figure 1). In Series 1, we maintain the length of the hydrocarbon segment while increasing the length of the fluorocarbon segment in adsorbates having the formula $F(CF_2)_x(CH_2)_{11}SH$, where x = 1-10. In Series 2, we increase the length of the hydrocarbon spacer while holding the length of the fluorocarbon segment constant in adsorbates having the formula $F(CF_2)_{10}(CH_2)_ySH$, where y = 2-6, and 11. In Series 3, we vary both the length of the hydrocarbon and fluorocarbon segments while holding the total chain length constant at 16 carbon atoms in adsorbates having the formula $F(CF_2)_x(CH_2)_ySH$, where x = 1-10 and y = 16-x, respectively. We characterized the films by ellipsometry, X-ray photoelectron spectroscopy (XPS), and polarization modulation infrared reflection absorption spectroscopy (PM-IRRAS).

Experimental

Ellipsometric Thicknesses. The thicknesses of the monolayers were measured with a Rudolph Research Auto EL III ellipsometer equipped with a He-Ne laser (632.8 nm) at an incident angle of 70° from the surface normal. A refractive index of 1.45 was assumed for all films. For a given sample, the data were averaged over three separate slides using three spots per slide.

Infrared Spectroscopy. Polarization modulation infrared reflection absorption spectroscopy (PM-IRRAS) data were collected using a Nicolet MAGNA-IR 860 Fourier transform spectrometer equipped with a liquid nitrogen-cooled mercury-cadmium-telluride (MCT) detector and a Hinds Instruments PEM-90 photoelastic modulator. The p-polarized light was incident at 80° from the surface normal. The spectra were collected for 1000 scans at a spectral resolution of 4 cm^{-1}.

X-ray Photoelectron Spectroscopy (XPS). A PHI 5700 X-ray photoelectron spectrometer equipped with an monochromatic Al Kα X-ray source (hν = 1486.7 eV) incident at 90° relative to axis of a hemispherical energy analyzer was used to obtain X-ray photoelectron spectra of freshly prepared samples. The spectrometer was configured to operate at high resolution with a pass energy of 23.5 eV, a photoelectron takeoff angle of 45° from the surface, and an analyzer spot diameter of 1.1 mm. Spectra were collected at room temperature and a base pressure of 2 x 10^{-9} torr for the following elements: C 1s (8 scans over 1.67 min) and Au 4f (4 scans over 0.67 min). Standard curve-fitting software using Shirley background subtraction and
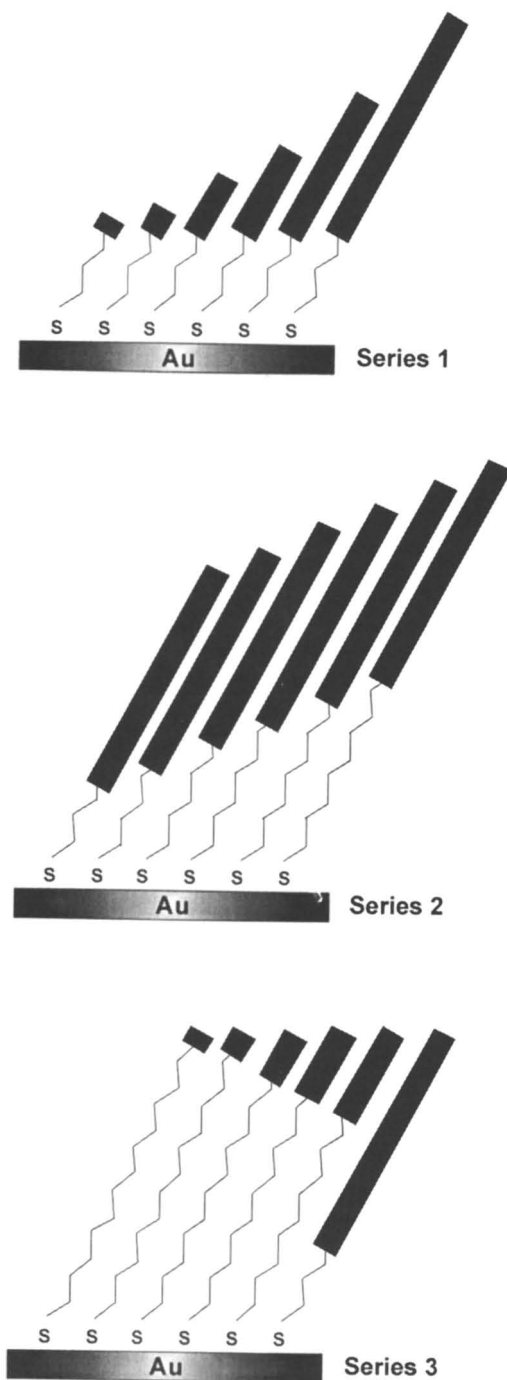
Figure 1. Illustration of SAMs on gold derived from the adsorption three distinct series of terminally fluorinated alkanethiols.

Gaussian-Lorentzian profiles was used to determine the peak intensities. All peaks were fit with respect to spin-orbit splitting. A 100% Gaussian curve was used for the C 1s peaks. Two 65% Gaussian curves in a 3:4 area ratio split by 3.67 eV were used for the Au 4f peaks. The constancy of the F 1s peak intensities for the films indicated that little or no damage occurred to the film during the data acquisition.

Results and Discussion

Ellipsometry

Ellipsometry is commonly used to evaluate the thickness of organic thin films [10]. While considerable experimental uncertainties might often accompany ellipsometric measurements (e.g., $\pm$ 2 Å), the technique is, nevertheless, useful for evaluating changes in film thickness within a series of films in which the structure changes subtly and systematically [11,12]. Figure 2a shows the thicknesses obtained for films from Series 1. The thicknesses increase linearly with an increase in the number of fluorinated carbon atoms (*ca.* 1.23 Å per CF_2 unit) [13]. Errors, however, associated with measurements of ellipsometric thickness preclude a rigorous evaluation of the chain tilt and/or twist in these films. These measurements merely reflect the expected increase in film thickness that accompanies the adsorption of progressively longer molecules.

Figure 2b shows the ellipsometric thicknesses of SAMs from Series 2. In this series, the thicknesses of the films generated from $F(CF_2)_{10}(CH_2)_ySH$ with y = 2-6, 11, and 17 increase linearly as the number of CH_2 groups increases (*ca.* 1.18 Å per CH_2), again reflecting the increase in thickness that accompanies the adsorption of progressively longer molecules [13].

Figure 2c plots the thicknesses of SAMs from Series 3 versus the number of fluorinated carbon atoms. For the entire series, the thickness remains relatively constant (~ 16 Å). Therefore, the results appear to reflect the constant total chain length of the adsorbates. We have recently reported that, within a SAM, the tilt angle with respect to the surface normal of the fluorocarbon segment of constant length increases as the length of the hydrocarbon segment increases [14,15]. Since the changing tilt of the fluorinated segment with the decreasing length of the hydrocarbon segment within SAMs from Series 3 might be expected to influence film thickness, the results also demonstrate that ellipsometry is insensitive to any of these potential changes in thickness.

X-ray Photoelectron Spectroscopy

XPS Intensity of the Au 4f Photoelectrons. The attenuation of gold photoelectrons emitted from a SAM is related to the thickness of the organic overlayer [16,17]. This relationship offers an opportunity to monitor the changes in the monolayer thickness that accompany chemical and structural changes of the adsorbates. Figure 3a shows the natural logarithm of the Au 4f photoelectron intensity as a function of the number
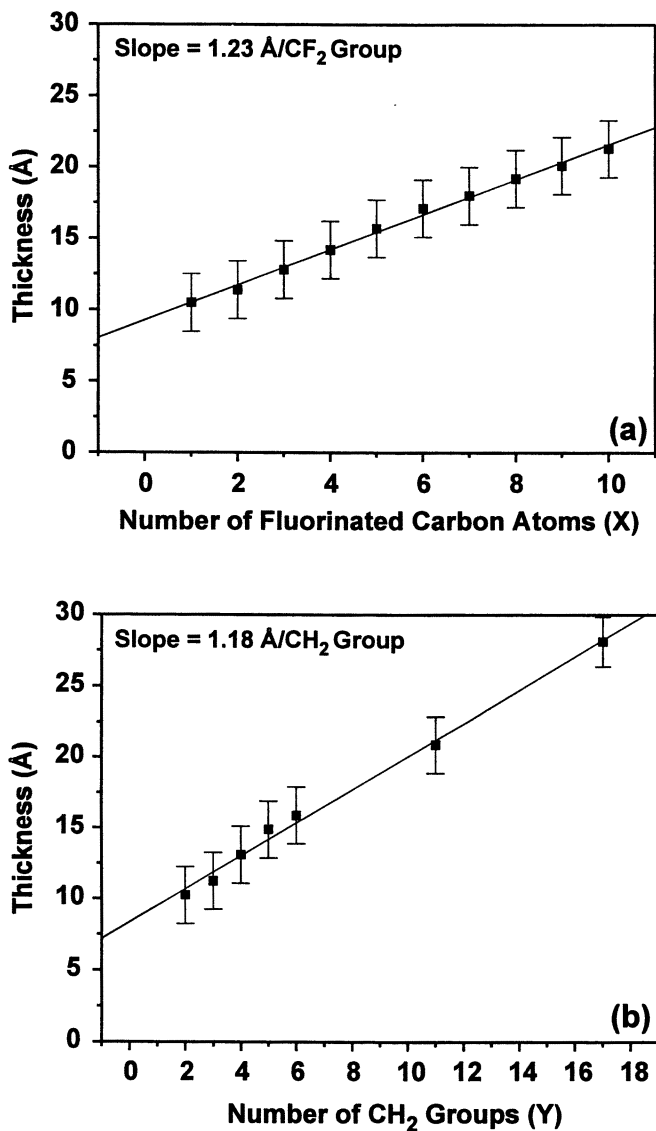
Figure 2. Average ellipsometric thickness of (a) SAMs from Series 1, (b) SAMs from Series 2, and (c) SAMs from Series 3. All measured thicknesses were reproducible within ± 2 Å of the reported average value.
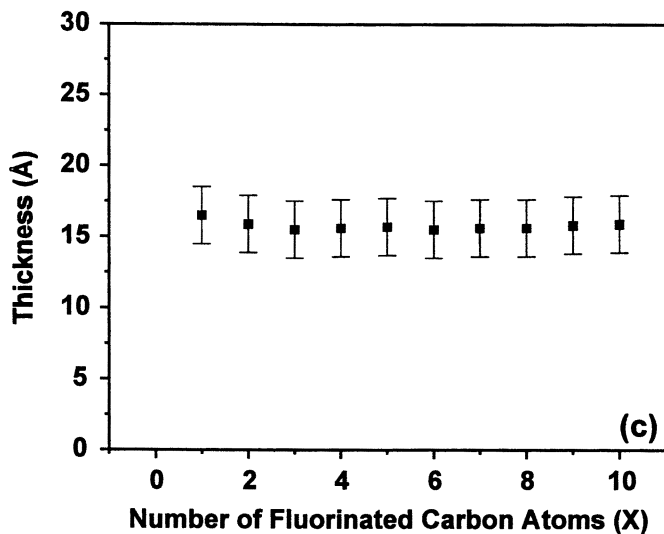
Figure 2. Continued.
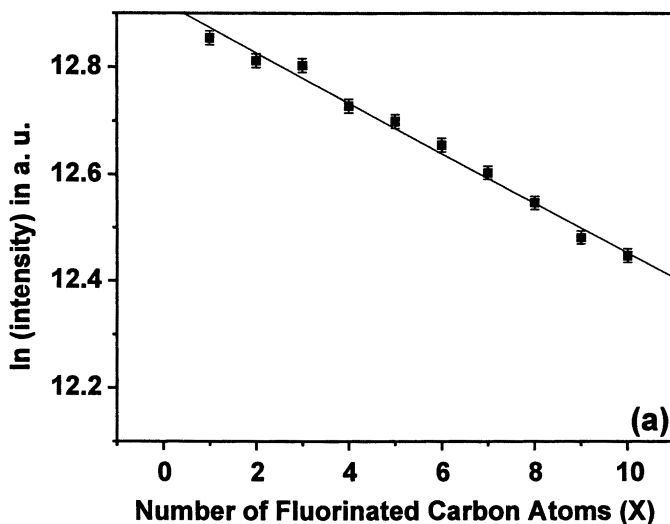
Figure 3. Intensity of Au 4f photoelectrons emitted from (a) SAMs from Series 1, (b) SAMs from Series 2, and (c) SAMs from Series 3. All measured intensities were reproducible within ± 1% of the reported average value, as determined by the standard deviation of four measurements per sample. The lines through the data are intended solely to guide the eye.
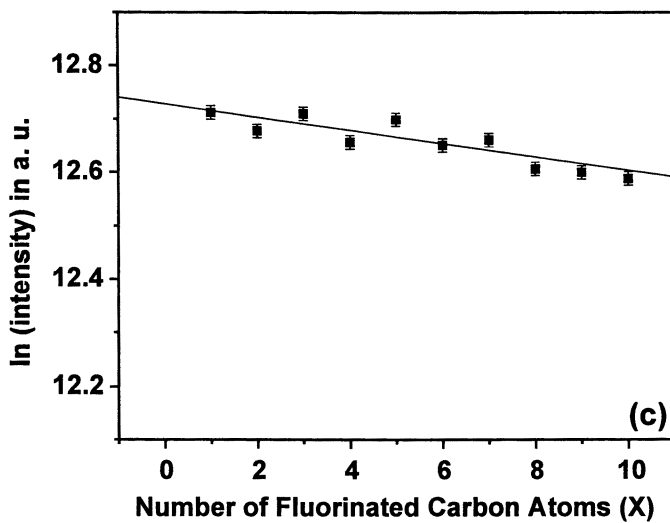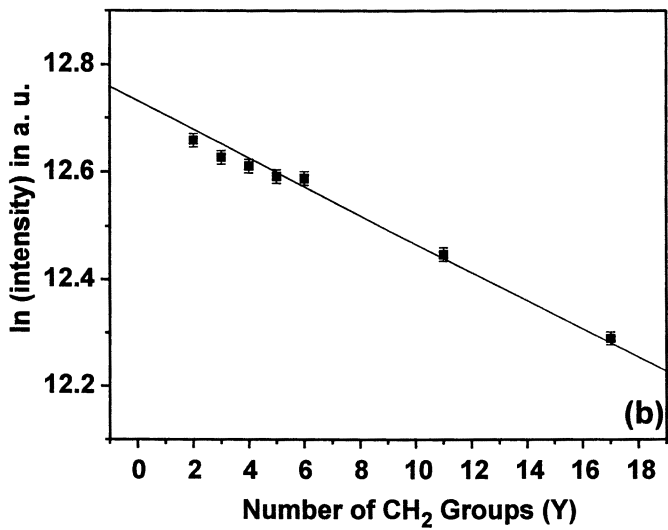
Figure 3. Continued.

of fluorinated carbon atoms in SAMs from Series 1. The natural logarithms of the intensities decrease linearly as the length of the fluorinated segment increases. This trend reflects an increased attenuation of the gold signal as the overall thickness of the monolayers increase. Although similar plots can be used to determine absolute thicknesses in hydrocarbon SAM systems [18], we are unable to calculate the absolute thicknesses of our terminally fluorinated SAMs because both the attenuation length of photoelectrons through fluorocarbons and the twists and tilts of the hydrocarbon and fluorocarbon segments within each film are presently unknown.

Figure 3b shows the attenuation of the gold photoelectrons as a function of the number of CH_2 groups in SAMs from Series 2. The films generated from these adsorbates exhibit a linear decrease in the natural logarithm of intensity as the length of the hydrocarbon segments increase.

Figure 3c plots the natural logarithm of the photoelectron intensity for SAMs from Series 3 versus the number of fluorinated carbons. Like the ellipsometric data for these SAMs, the values remain within a narrow range. The natural logarithm of the intensities, however, appears to decrease as the degree of fluorination increases. If we assume a constant thickness for the SAMs in this series, this trend appears consistent with an enhanced attenuation of Au 4f photoelectrons by CF_2 groups relative to that of CH_2 groups that occurs as the number of fluorinated carbon atoms increases at the expense of the number of CH_2 groups. Changes in the tilt of the fluorocarbon or hydrocarbon segments, however, might also influence the thickness of the films and give rise to the observed trends in attenuation.

XPS Intensity of the C 1s Photoelectrons. The carbon 1s photoelectron spectrum can be used to monitor the relative amounts of fluorocarbon and hydrocarbon in thin films [8]. The peaks arising from CH_2 and CF_2 segments have the following distinct binding energies: 285 eV and 290 eV, respectively. Figure 4a shows the XPS intensities of both the CH_2 and CF_2 C 1s photoelectrons versus the number of fluorinated carbon atoms in SAMs from Series 1. The CF_2 photoelectrons exhibit an expected exponential increase in intensity as the length of the fluorinated segment increases. Although the CH_2 signal for every film in Series 1 arises from an equivalent number of methylene units, the CH_2 photoelectron intensities also exhibit a dependence on the length of the fluorocarbon segment. The intensities of these peaks decrease as the fluorocarbon segment increases in length because the photoelectrons are attenuated more as the number of overlying CF_2 groups increases.

The XPS intensity of the C 1s photoelectrons as a function of the number of CH_2 groups in SAMs from Series 2 is shown in Figure 4b. The CF_2 intensities reflect the constant length of the fluorocarbon segment and remain constant as the length of the hydrocarbon segment increases. As expected, the CH_2 intensities increase exponentially as the length of the hydrocarbon segment increases.

Figure 4c shows the C 1s photoelectron intensities versus the number of fluorinated carbon atoms in SAMs from Series 3. The increase of the CF_2 intensities with increasing length of the fluorocarbon segment is similar to the increase seen for the films from Series 1. In contrast, the CH_2 intensities in the SAMs from Series 3 decrease more than in the films from Series 1 with increasing length of the

fluorocarbon segment. These results suggest that in addition to the increased attenuation by the overlying fluorocarbon segment (which is equivalent in both series), the decreasing number of CH_2 groups in SAMs from Series 3 in comparison to the constant number of CH_2 groups in SAMs from Series 1 serves to lower the methylene photoelectron signal in Series 3.

Polarization Modulation Infrared Reflection Absorption Spectroscopy

Axial Fluorocarbon Band Positions. We obtained spectra of the C-F stretching regions of the SAMs using PM-IRRAS. Two bands that are of particular interest in characterizing the fluorocarbon segments of semifluorinated films are the first and second axial vibrations that occur at 1315-1345 cm^{-1} and 1365-1375 cm^{-1}, respectively [14,19-22]. These bands arise from the helical conformation of the fluorocarbon segment; moreover, the band positions depend on the size of the fluorocarbon helix [20,22]. Figure 5a shows the positions of the axial bands as a function of the number of fluorinated carbon atoms in SAMs from Series 1. As the length of the fluorinated segment increases, both band positions move progressively toward higher wavenumbers. Figure 5b shows the axial band positions versus the number of CH_2 groups in SAMs from Series 2. Since the length of the fluorinated segment remains constant in this series, both band positions remain constant. Figure 5c shows the positions of the axial bands as a function of the number of fluorinated carbon atoms in SAMs from Series 3. Not only do the band positions of these films increase with the length of the fluorocarbon segment as in the films from Series 1, the band positions from a given fluorocarbon length are identical to those in films from Series 1. Since the tilts for fluorocarbon segments of equivalent length in both series are likely to be different [14,15], these results suggest that the absolute position of the axial bands can be used to determine the length of fluorocarbon segments in SAMs without regard to the orientation of the segments within the film.

Antisymmetric CH$_2$ Band Positions. The position of the antisymmetric methylene band in normal alkanethiol SAMs is sensitive to the conformational order of the hydrocarbon chains [10,23-25]. Shifts of these bands to higher wavenumbers are associated with decreases in interchain van der Waals interactions and increases in intrachain gauche defects (i.e., more liquid-like conformational states) [10,23-25]. Figure 6 shows the antisymmetric methylene band position as a function of the total number of carbon atoms in SAMs derived from a series of normal alkanethiols. The results are consistent with a model in which the conformational order (or crystallinity) of the films increases with increasing chain length [10,23].

We examined the antisymmetric methylene band position versus the number of fluorinated carbon atoms in SAMs from Series 1. Figure 7a shows that the band position remains constant as the length of the fluorinated segment increases. These data suggest that the introduction of longer fluorinated segments into the upper portion of the films induces no conformational disordering of the underlying hydrocarbon segments.
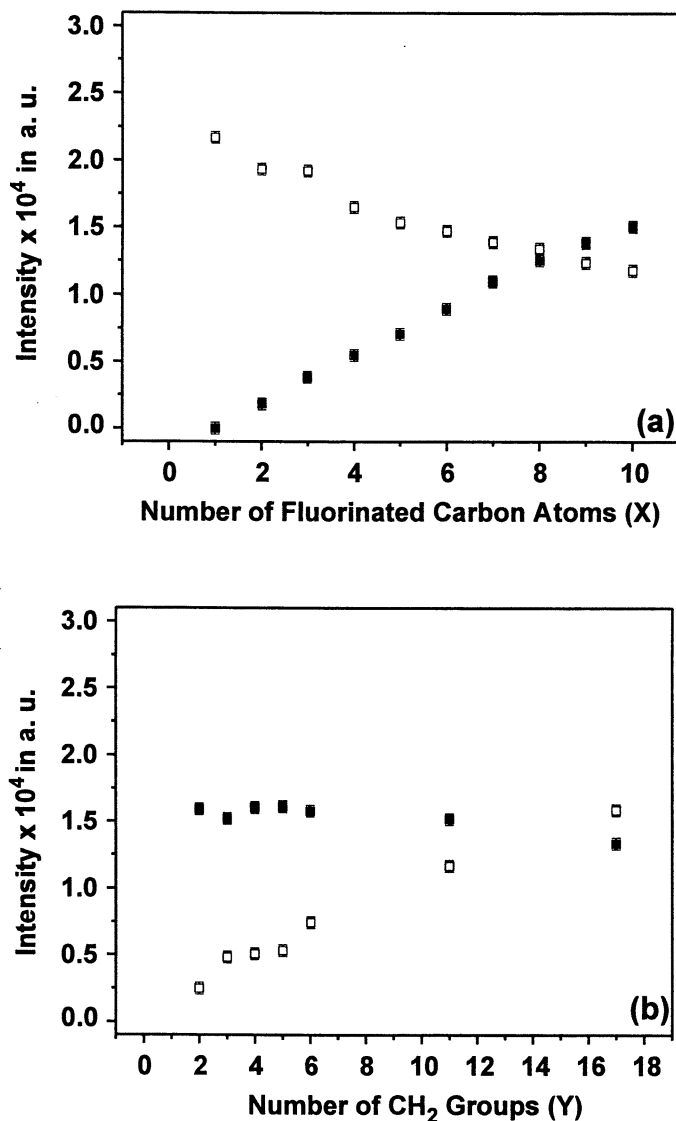
Figure 4. Intensity of fluorocarbon (open squares) and hydrocarbon (filled squares) C 1s photoelectrons emitted from (a) SAMs from Series 1, (b) SAMs from Series 2, and (c) SAMs from Series 3. All measured intensities were reproducible within ± 2% of the reported average value, as determined by the standard deviation of four measurements per sample.
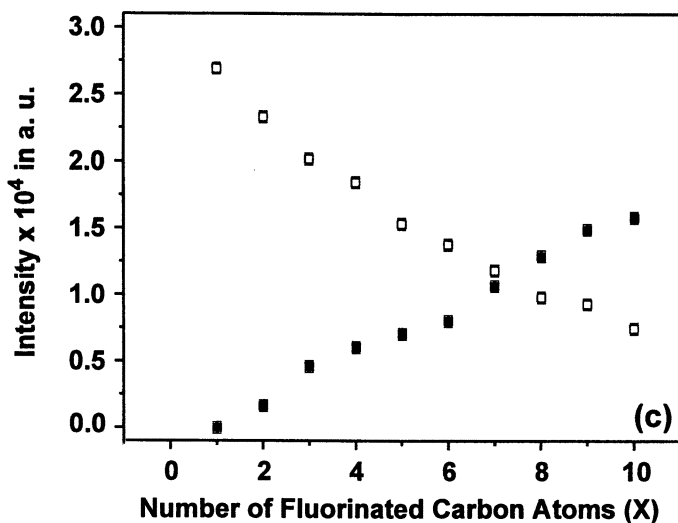
Figure 4. Continued.
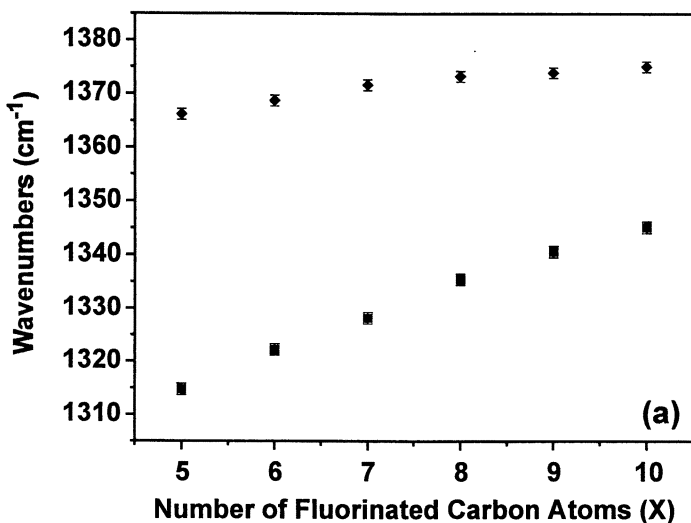
Figure 5. Average band positions of the first (■) and second (◆) axial vibrations of fluorocarbon segments in (a) SAMs from Series 1, (b) SAMs from Series 2, and (c) SAMs from Series 3. All measured band positions were reproducible within ± 0.5 cm^{-1} of the reported average value.
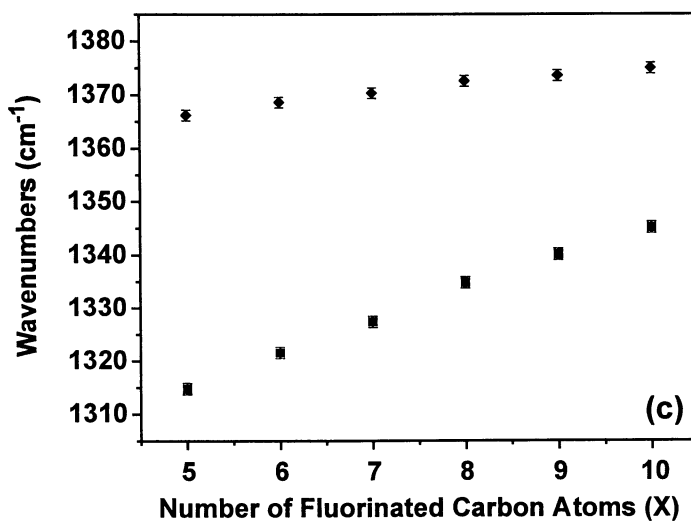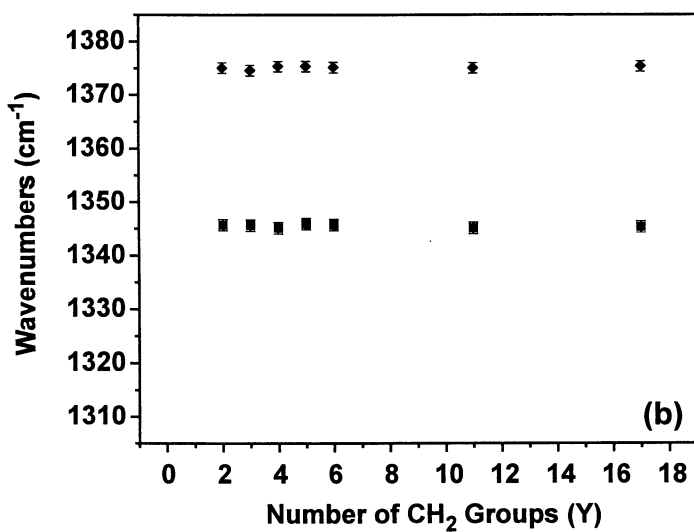
Figure 5. Continued.
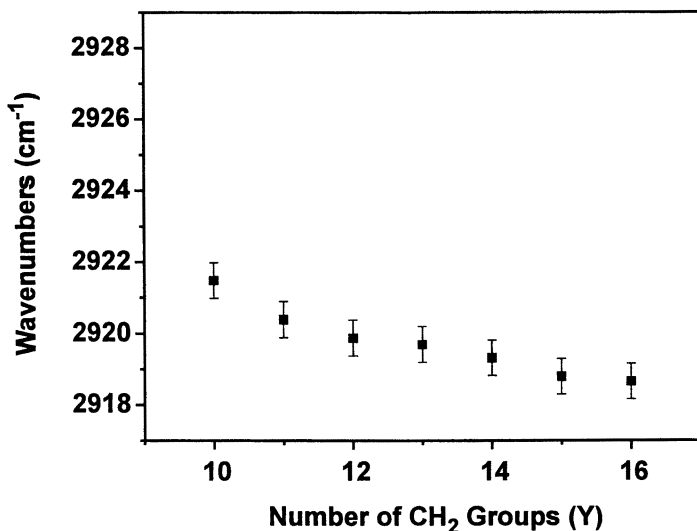
Figure 6. Average antisymmetric methylene band position ($v_a^{CH_2}$) of the hydrocarbon backbone in SAMs from normal alkanethiols. All measured band positions were reproducible within $\pm$ 0.5 cm^{-1} of the reported average value.
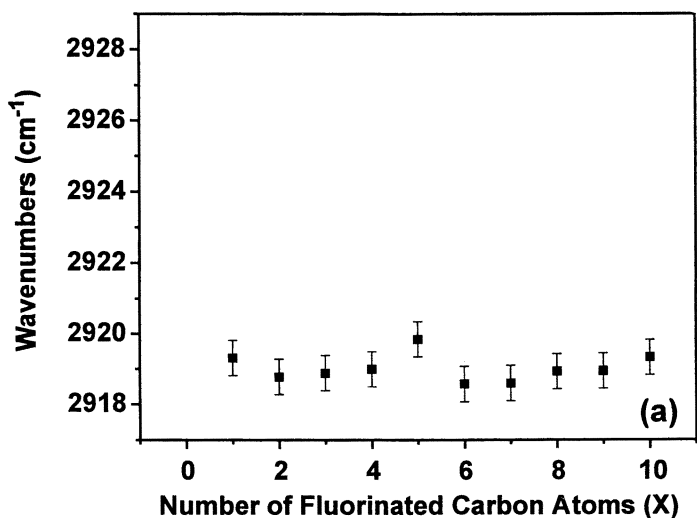
Figure 7. Average antisymmetric methylene band position ($v_a^{CH_2}$) of the hydrocarbon segments in (a) SAMs from Series 1, (b) SAMs from Series 2, and (c) SAMs from Series 3. All measured band positions were reproducible within $\pm$ 0.5 cm^{-1} of the reported average value.
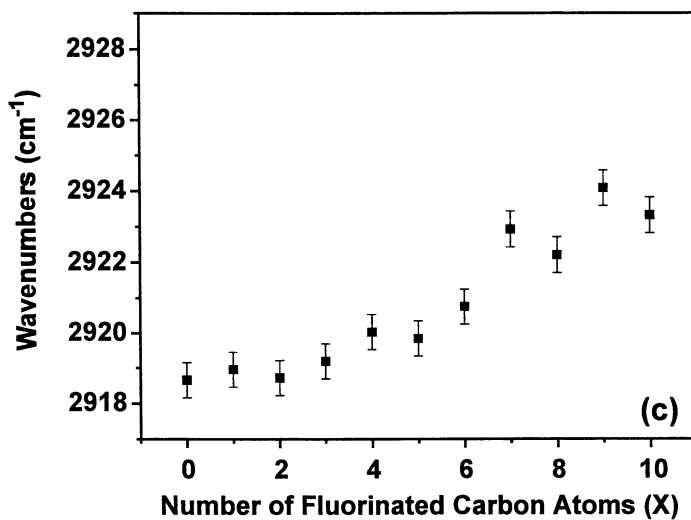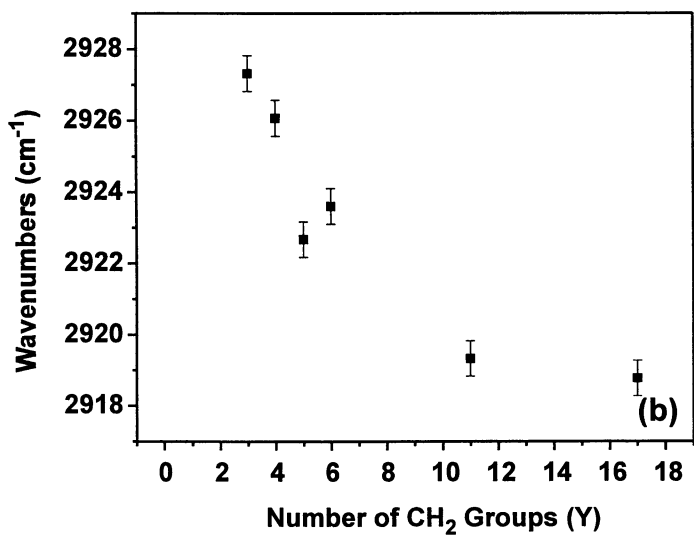
Figure 7. Continued.

Figure 7b shows the antisymmetric methylene band position as a function of the number of CH_2 groups in SAMs from Series 2. As the length of the hydrocarbon segment increases, the band position shifts to lower wavenumber. Consequently, it appears that in films with overlying fluorinated helices of constant size, increasing the number of methylene units leads to more conformationally ordered hydrocarbon underlayers.

Figure 7c plots the antisymmetric methylene band position versus the number of fluorinated carbon atoms in SAMs from Series 3. As the length of the fluorinated segment increases, the band position shifts to higher wavenumber, indicating a decrease in the conformational order of the hydrocarbon backbone [23-25]. Given the aforementioned results for the other two fluorinated series, we believe that the decrease in conformational order arises primarily from decreasing the length of the hydrocarbon segment (loss of strong van der Waals interactions), which reduces the number of stabilizing interchain van der Waals interactions, and is largely unaffected by increasing the length of the fluorinated segment (gain of weaker van der Waals interactions).

Conclusions

We have prepared and characterized SAMs from three distinct series of terminally fluorinated alkanethiols to probe the relationships between the introduction of fluorine and the structure of fluorinated organic thin films. The trends in ellipsometric thickness are consistent with the expected changes in adsorbate length. Characterization of the films by XPS demonstrates that the attenuation of Au 4f photoelectrons follows the expected logarithmic dependence on the total chain length of the adsorbates. Since, however, the attenuation length of photoelectrons through fluorocarbons and the twist and/or tilt angles of the fluorocarbon and hydrocarbon segments in the films are unknown, we are currently unable to calculate absolute film thicknesses from the Au 4f XPS data. Furthermore, as fluorine is systematically introduced into the monolayers, the intensity of the fluorinated C 1s photoelectrons increase exponentially at the expense of the hydrocarbon C 1s photoelectrons. PM-IRRAS studies of the SAMs from Series 1 suggest that the hydrocarbon segments of constant chain length remain ordered upon increasing the length of the fluorinated segment. In SAMs from Series 2 with a constant length of the fluorinated segment, the hydrocarbon segments become more ordered with increasing chain length. In SAMs from Series 3, the hydrocarbon segments become more disordered with decreasing length. This trend appears to arise predominately from the net loss of van der Waals stabilization that accompanies the substitution of CF_2 for CH_2. Taken together, these data suggest that systematic alterations of the adsorbates used to generate SAMs can effect systematic structural changes in the resultant films. Further investigations of the structure of these monolayers by atomic force microscopy (AFM) and near-edge X-ray absorption fine structure spectroscopy (NEXAFS) are ongoing. We are also exploring the influence of these structural changes upon the thermal stabilities of the films.

Acknowledgments

References

1. Homola, A. M.; Mate, C. M.; Street, G. B. *MRS Bull.* **1990**, *15*, 45.
2. Deng, K.; Collins, R. J.; Mehregany, M.; Sukenik, C. N. *J. Electrochem. Soc.* **1995**, *142*, 1278.
3. Ishihara, K. *Biomedical Applications of Polymeric Materials*, CRC Press: Boca Raton, 1993.
4. Kinloch, A. J. *Adhesion and Adhesives*, Chapman and Hall: New York, 1987.
5. Kim, H. I.; Koini, T.; Lee, T. R.; Perry, S. S. *Langmuir* **1997**, *13*, 7192.
6. Kim, H. I.; Graupe, M.; Oloba, O.; Koini, T.; Imaduddin, S.; Lee, T. R.; Perry, S. S. *Langmuir* **1999**, *15*, 3179.
7. Graupe, M.; Takenaga, M.; Koini, T.; Colorado, R., Jr.; Lee, T. R. *J. Am. Chem. Soc.* **1999**, *121*, 3222.
8. Schonherr, H.; Ringsdorf, H.; Jaschke, M.; Butt, H.-J.; Bamberg, E.; Allinson, H.; Evans, S. D. *Langmuir* **1996**, *12*, 3898.
9. Graupe, M.; Koini, T.; Wang, V. Y.; Nassif, G. M.; Colorado, R., Jr.; Villazana, R. J.; Dong, H.; Miura, Y. F.; Shmakova, O. E.; Lee, T. R. *J. Fluorine Chem.* **1993**, *93*, 107.
10. Ulman, A. *An Introduction to Ultrathin Organic Films*, Academic: Boston, 1991.
11. Bain, C. D.; Troughton, E. B.; Tao, Y.-T.; Evall, J.; Whitesides, G. M.; Nuzzo, R. G. *J. Am. Chem. Soc.* **1989**, *111*, 321.
12. Gupta, V. K.; Abbott, N. L. *Langmuir* **1996**, *12*, 2587.
13. The incremental increases in thickness for Figures 2a and 2b are the slopes of lines obtained by fitting the ellipsometric data for Series 1 and 2, respectively, by least-squares linear regression ($R^2 = 0.98$).
14. Tamada, K.; Nagasawa, J.; Nakanishi, F.; Abe, K.; Hara, M.; Knoll, W.; Ishida, T.; Fukushima, H.; Miyashita, S.; Usui, T.; Koini, T.; Lee, T. R. *Thin Solid Films* **1998**, *327-329*, 150.

15. Fukushima, H.; Seki, S.; Nishikawa; Miyashita, S.; Tamada, K.; Nakanishi, F.; Abe, K.; Colorado, R., Jr.; Shmakova, O. E.; Graupe, M.; Lee, T. R., *J. Phys. Chem. B*, submitted.
16. Bain, C. D.; Whitesides, G. M. *J. Phys. Chem.* **1989**, *93*, 1670.
17. Laibinis, P. E.; Bain, C. D.; Whitesides, G. M. *J. Phys. Chem.* **1991**, *95*, 7017
18. Harder, P.; Grunze, M.; Dahint, R.; Whitesides, G. M.; Laibinis, P. E. *J. Phys. Chem. B* **1998**, *102*, 426.
19. Lenk, T. J.; Hallmark, V. M.; Hoffmann, C. L.; Rabolt, J. F.; Castner, D. G.; Erdelen, C.; Ringsdorf, H. *Langmuir* **1994**, *10*, 4610.
20. Tsao, M.-W.; Hoffmann, C. L.; Rabolt, J. F.; Johnson, H. E.; Castner, D. G.; Erdelen, C.; Ringsdorf, H. *Langmuir* **1997**, *13*, 4317.
21. Rabolt, J. F.; Russell, T. P.; Twieg, R. J. *Macromolecules* **1984**, *17*, 2786.
22. Naselli, C.; Swalen, J. D.; Rabolt, J. F. *J. Chem. Phys.* **1989**, *90*, 3855.
23. Porter, M. D.; Bright, T. B.; Allara, D. L.; Chidsey, C. E. D. *J. Am. Chem. Soc.*, **1987**, *109*, 3559.
24. Terrill, R. H.; Tanzer, T. A.; Bohn, P. W. *Langmuir* **1998**, *14*, 845.
25. Synder, R. G.; Strauss, H. L.; Elliger, C. A. *J. Phys. Chem.* **1982**, *86*, 5145.

Chapter 18

Microscopic Structure of Chromatographic Interfaces as Studied by Sum-Frequency Generation Spectroscopy

Lauren K. Wolf, Yarjing J. Yang, Rebecca L. Pizzolatto, and Marie C. Messmer

Department of Chemistry and Zettlemoyer Center for Surface Studies, Lehigh University, 7 Asa Drive, Bethlehem, PA 18015

Model chromatographic interfaces were examined using sum-frequency generation spectroscopy (SFG) in order to study the effect of various solvents on the structure and conformation of the stationary phase. Monolayers formed from mixed alkyltrichlorosilanes on fused silica were examined in contact with air, acetonitrile, isooctane, and water. Results show that monolayers of 100% C_{18} composition show little disorder in the alkyl chains for all the solvents examined, though a very distinct solvent shift is apparent in the methyl symmetric stretch. When mixed composition (C_{18} and C_1) monolayers were examined, significant disorder was induced in the alkyl chains for all the solvents. However, the largest change occurred when the monolayer was in contact with water. These results support a collapsed structure model for the mixed monolayer in contact with water.

Introduction

Chromatographic interfaces are complex systems that require further exploration before a complete description of chromatographic separation can emerge. Stationary

293

phase properties are not always well understood because of contributions from various factors, such as residual surface silanols. In addition, the importance of certain aspects of stationary phase structure such as alkyl chain density, solvent penetration, and stationary phase ordering, are still a broad area of investigation.

Recently, it has been shown that stationary phases composed of long (C_{18}) and short (C_1) alkylsiloxane chains significantly reduce the "tailing" effect in reverse-phase chromatograms (1,2). This "tailing" effect is often caused by the strong acid-base interaction of an analyte with exposed silanol groups on the surface of a silica support. The mixed monolayer stationary phases reduce this interaction by covering excess silanols with methyl spacers (C_1 groups). In addition, the C_{18}:C_1 monolayers provide lower C_{18} chain density at the outer layer of the monolayer surface, which increases the partitioning area of the stationary phase, and improves the chromatographic separation.

Recent theoretical calculations have shown the importance of solvent phase heterogeneity near the interfacial region in mixed solvent systems (3). Thermodynamic measurements have also shown that using an acetonitrile-water mixture changes the entropy of solute "transfer" with a changing acetonitrile mole fraction (4). This change is attributed to the high degree of stationary phase order that forms at high acetonitrile concentrations. It is believed that the ordered stationary phase can reduce the entropy of transfer to an extent that retention becomes enthalpically driven (5). By causing substantial order in the substrate, the entropic cost is equal for adsorption and desorption.

To determine the role of stationary phase structure in the retention process, it is of primary importance to understand its structure in various solvent environments. Studies of the interphase region using deuterium NMR have shown that it is the mobile phase composition that determines the structure of the stationary phase (6). Results have shown that water does not associate strongly with the alkyl chains. However, acetonitrile can associate strongly, even at low mole fractions because of the microheterogeneous environments that exist for the binary mixture. Previous *in situ* studies of the alkyl stationary phases using surface enhanced Raman spectroscopy have also concluded that little conformational change occurs with the addition of a polar solvent to the interface (7).

To further explore the nature of chromatographic interfaces *in situ*, we examine model chromatographic systems composed of 100% C_{18} and mixed (C_{18} and C_1) monolayers in several solvent environments using sum-frequency generation spectroscopy. Sum-frequency generation (SFG) spectroscopy is a powerful surface analysis tool that has proven to be invaluable in the elucidation of molecular structure at many interfaces obscured by adjacent bulk phases. The forbidden nature of the process in isotropic media within the electric dipole approximation permits this technique to be used to examine the structure and properties of the minute interfacial region between two isotropic materials. Interfaces that have been successfully explored include those at gas-liquid, liquid-liquid, liquid-solid, and gas-solid interfaces (8).

Experimental Section

Reagents

Octadecyltrichlorosilane (OTS, purity 95%) and methyltrichlorosilane (MTS, purity 99%) were obtained from Aldrich and were used without further purification. Hexadecane (99+%) and carbon tetrachloride (99.9+%) were also used as received from Aldrich. Sulfuric acid and hydrogen peroxide were analytical grade and obtained from EM Science. Acetone and methanol were HPLC and optima grade, respectively, and obtained from Fisher Scientific.

Substrate Preparation

Fused silica slides (50 x 25 x 1 mm), which were purchased from ChemGlass, Inc., were swabbed and rinsed with methanol followed by distilled water. The slides were then dried under nitrogen and immersed in "piranha solution" (7:3 concentrated H_2SO_4 / 30% H_2O_2) for 1 hour. **WARNING:** *Piranha solution should be kept out of contact with oxidizable organic material. It is a highly reactive mixture and severely exothermic during reaction.* After exposure to the solution for one hour, the slides were rinsed with large amounts of distilled water and dried with nitrogen. The surface morphology of the bare fused silica slide after piranha treatment was measured by atomic force microscopy (AFM). The rms roughness was found to be ~1.67 nm.

Monolayer Formation

Each freshly cleaned slide was placed in a cell in order to expose only one side of the substrate to reagents. In this way, a monolayer forms on only one side of the fused silica slide, which is necessary for the optical experiments. A mixture of 20 mM $C_{18}:C_1$ in hexadecane and carbon tetrachloride (4:1) was then added to the cell. After 30 minutes at room temperature, the slides were rinsed with acetone and methanol, removed from the cell, and rinsed again with copious amounts of the same solvents. Finally, each slide was dried under a stream of nitrogen and stored in sealed vials. Each slide was heated at 70°C for one hour to remove residual solvent prior to sum-frequency generation experiments.

X-ray Photoelectron Spectroscopic Measurements

X-ray photoelectron spectroscopy (XPS) data were acquired with a Scienta ESCA 300 using monochromatic Al Kα X-rays. The analysis area of each sample was approximately 0.8 mm^2, and the pass energy of the detector was 150.0 eV. A 90° take-off angle was employed to measure the spectra. The pressure of the chamber

was approximately 5×10^{-9} Torr. Ten scans of the data were taken for carbon, and 5 scans were taken for silicon. All spectra were fitted using a Voigt function with a linear background correction using the Scienta software. The integrated peak area was divided by atomic sensitivity factors, which were provided by the Scienta software. Monolayer composition was then calculated for each sample using previously described calculations (9).

Sum-Frequency Spectroscopic Measurements

The sum-frequency generation setup is described in detail elsewhere (10). Briefly, a lithium niobate (LiNbO$_3$) optical parametric oscillator is pumped with a Surelite I (Continuum) Nd^{3+}:YAG laser using relay imaging. Tunable infrared light is generated between 2600 - 3200 cm^{-1} (3.1 - 3.8 µm) with a pulse width of 7 ns. The wavelength is calibrated with a polystyrene sample. The visible beam at 532 nm used in the sum-frequency experiment is generated with a potassium dihydrogen phosphate (KDP) crystal. The polarization of the infrared beam is rotated with a Soleil-Babinet compensator. Sum-frequency spectra are obtained by using a total internal reflection geometry as shown in Figure 1 (11-14). The infrared and visible beams are combined through a coupling prism to the fused silica substrate with an index-matching liquid. The generated sum-frequency light is collected and passed through several collimating optics, absorptive, interference and holographic filters, and a Glan-Taylor polarizer. Signal is detected with a photomultiplier tube and then passed to a preamplifier and gated electronics. Each point is the average of 200 laser shots. The sampling size on the surface is determined by the laser spot size which was approximately 200 µm in diameter. Each spectrum represents spectra taken from several places on the sample.

Results and Discussion

To compare the effects of solvent on these model chromatographic interfaces, the sum-frequency (SF) spectra of these systems were collected *in situ*, exposed to one of
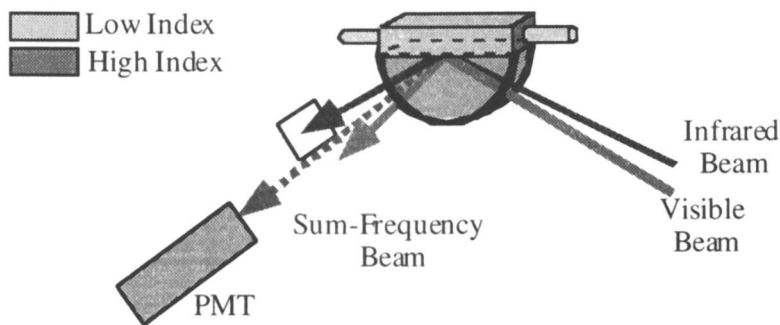
Figure 1: Sum-Frequency Generation Experimental Setup

three solvents or air. Figures 2A and 2B show the SF spectra of complete monolayers of 100% C$_{18}$ on the fused silica surface in contact with water, isooctane, and air (A) and acetonitrile (B). The first important feature to note in these spectra is the lack of a methylene group symmetric stretch (~2850 cm^{-1}). This particular vibrational mode is not SF active when a long alkyl chain achieves an all-*trans* conformation because of the near complete cancellation of the nonlinear polarization on adjacent carbons. As a unique feature of sum-frequency generation spectroscopy, the intensity of this peak has been successfully used to characterize backbone disorder in a variety of systems (*15-17*).
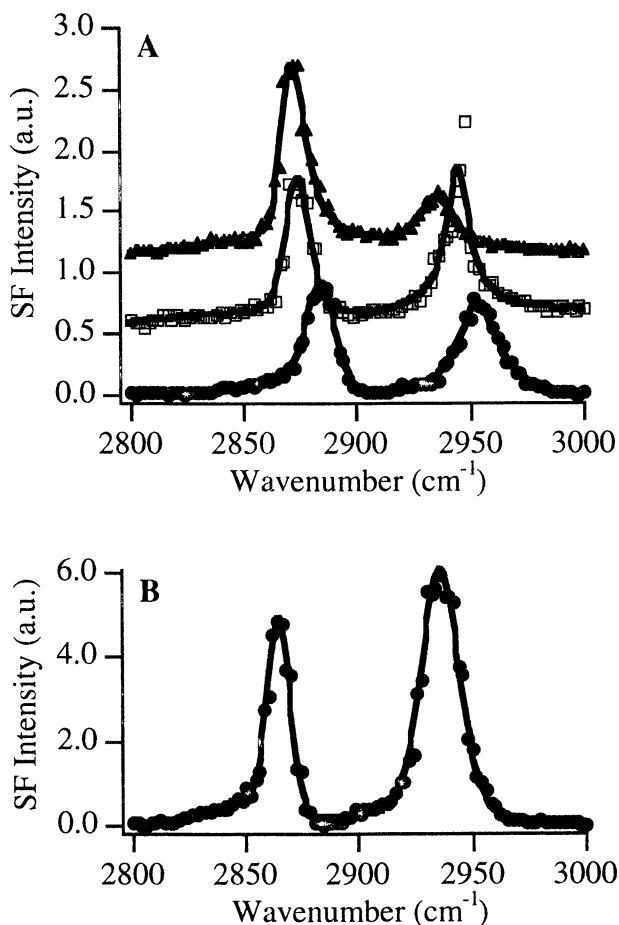
Figure 2: SF intensity spectra of 100% C$_{18}$-modified fused silica surfaces taken with ssp polarization (s-polarized SF, s-polarized visible light and p-polarized infrared light). A: (▲) water, (□) isooctane, and (●) air, B: acetonitrile. The solid lines are fits to the data using Voigt lineshapes.

Figure 2 also shows a spectral shift of the peaks of the methyl symmetric and antisymmetric stretches. This shift corresponds to an approximate 20 cm^{-1} shift going from an air environment to a water environment. Frequently, spectral shifts in infrared spectra of alkyl chains indicate a change in the conformation of the chain backbone (18). This is not the case for these spectra. The observed lack of methylene symmetric stretch in the spectra proves that an all-*trans* conformation dominates for each of these solvent environments. The spectral shift purely indicates the change to a polar solvent environment, which may act to broaden the vibrational potential well. The methyl groups of these systems are obscured by the methylene groups in Raman and IR spectroscopy, making observation of this spectral shift difficult.

This lack of solvent-induced monolayer disorder was also observed by Pemberton and coworkers (7). Pemberton and coworkers used Raman spectroscopy to examine C_{18} alkylsiloxane monolayers on a SiO_2/Ag substrate and found little disruption of the alkyl chains in contact with acetonitrile, as well as water. The results of Carr and Harris (19), however, showed that a C_{18} chromatographic stationary phase assumes a collapsed structure in water. The stationary phase can evolve from this collapsed state with the addition of an organic modifier, such as acetonitrile, to the aqueous solvent. The modifier intercalates into the monolayer, causing an increase in volume, polarity, and alkyl chain order.

The lack of any spectral evidence indicating a collapse in the 100% C_{18}-modified surfaces may result from several differences between our model stationary phases and real chromatographic interphase regions. The first difference may be the lower surface density of alkyl chains due to the irregular surface of the silica gel particles. Although flatter than silica gel surfaces, our fused silica substrates are relatively rough, with an rms roughness of about 1.67 nm. It seems that even with some degree of roughness on the substrate, the packing density may be higher than that found in real systems. This higher packing density prevents sufficient alkyl chain conformational freedom, which is necessary for a chain collapse to occur.

To observe this chain collapse in a model system, it is necessary to compare the SF spectra of mixed C_1 and C_{18} composition monolayers in the different solvent environments. These monolayers, with their higher degree of conformational freedom of the alkyl chains, serve as a more representative model of true chromatographic interfaces. The SF spectra comparing 100% C_{18} monolayers and partial C_{18} monolayers are shown in Figure 3 for air and water and in Figure 4 for isooctane and acetonitrile. These spectra were taken by selecting the *s*-polarized output, and using *s*-polarized visible and *p*-polarized infrared light (*ssp* combination). Examining Figure 3A, a partially formed monolayer displays a significantly different structure than a full monolayer in air. Appearance of the methylene symmetric stretch peak at 2856 cm^{-1} indicates the introduction of *gauche* conformations into the monolayers with the addition of C_1 as "spacers". In addition, the reduction of the methyl symmetric stretch peak at 2884 cm^{-1} for the partial monolayer shows that the methyl group has attained an average orientation that is directed further away from the surface normal than when the surface composition is 100% C_{18}.

The SF spectra obtained with the same polarization combination (*ssp*) and of the same surface compositions in contact with water are shown in Figure 3B. Comparing Figures 3A and 3B, one can see that the water causes a much different structural response in the stationary phase. We see the appearance of the methylene symmetric stretch, as expected, but we see a much larger change in the methyl symmetric stretch intensity than in air, indicating that a larger amount of chain disorder is induced by

contact with water. Albert and coworkers, while examining mixed C_{18} and C_1 monomeric monolayers in contact with high water content solvents, saw a similar reduction of alkyl chain mobility and order with cross-polarization magic angle spinning (CP/MAS) NMR spectroscopy (20).
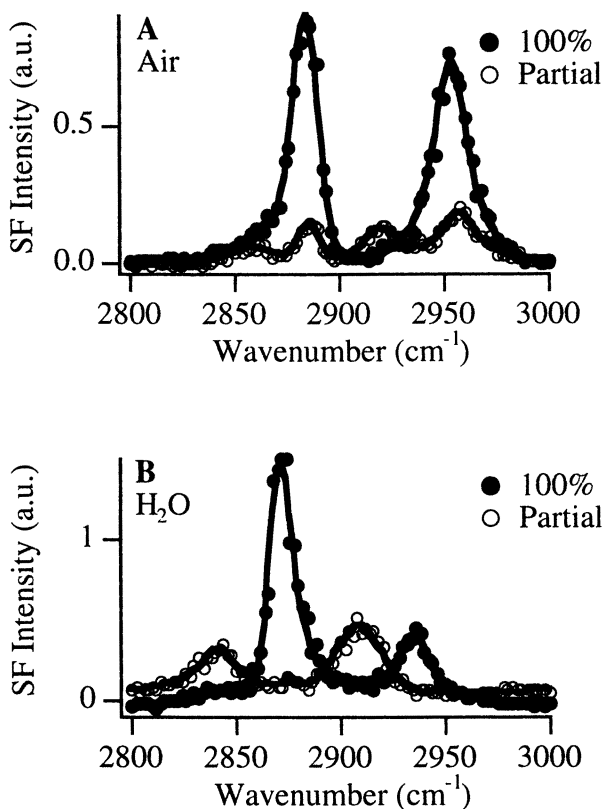
Figure 3: SF spectra for 100% C_{18}-modified and partial (40%) C_{18}-modified fused silica surfaces taken with ssp polarization (s-polarized SF, s-polarized visible light and p-polarized infrared light). A: in contact with air, B: in contact with water. (●) 100% C_{18} and (○) 40% C_{18}- 60% C_1-modified. The solid lines are fits to the data using Voigt lineshapes.

A unique trend emerges as we examine acetonitrile and isooctane in contact with the same monolayers. Figures 4A and 4B show these spectra. By determining the ratio of the intensities of the methyl symmetric stretch (I_{CH_3SS}) to the methylene symmetric stretch (I_{CH_2SS}) with *ssp* polarization, we can get a semi-quantitative comparison of the amounts of *gauche* defects in the alkyl chains. The values for this ratio for 100% C_{18} and partial C_{18} coverages are shown in the first two rows of Table

I. The change in this ratio going from a 100% C_{18}-modified surface to one in which the composition is 40% C_{18} and 60% C_1 is the most interesting feature. For air, we see a change of a factor of 3.9 ± 1.5 on going to a partial C_{18} composition, for isooctane a factor of 11.2 ± 2.5, for acetonitrile a factor of 14.4 ± 1.9 change, and for water we see a factor of approximately 31 ± 7. A larger order of magnitude change for this ratio indicates a significantly higher proportion of *gauche* conformations in the alkyl chain backbone. The measurements for acetonitrile were taken with a 60% C_{18}-modified surface because of sample degradation, but the results still indicate that a significant difference exists for the solvent environments. These results support the theoretical picture of a stationary phase collapse in water.
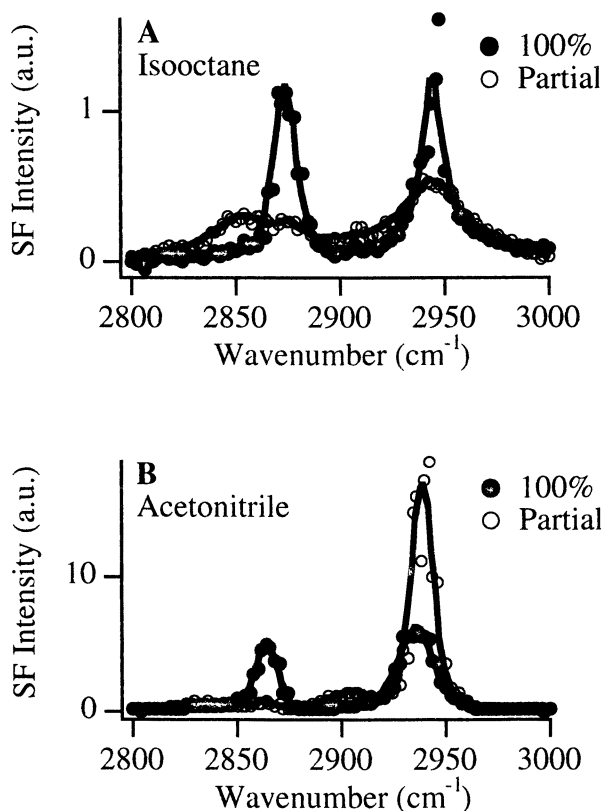
Figure 4: SF spectra for 100% C_{18}-modified and partial C_{18}-modified fused silica surfaces taken with ssp polarization (s-polarized SF, s-polarized visible light and p-polarized infrared light). A: in contact with isooctane, B: in contact with acetonitrile. (●) 100% C_{18} and (○) 40% C_{18}- 60% C_1-modified for isooctane data and 60% C_{18}-40% C_1-modified for acetonitrile data. The solid lines are fits to the data using Voigt lineshapes.

Table I. SF Intensity Ratios for C_{18}- and C_{18}/C_1- Modified Silica Surfaces

	% C_{18} Composition	Air	Isooctane	Acetonitrile	Water
I_{CH3SS}/I_{CH2SS}	100%	10.0 ± 2.1	10.6 ± 1.9	12.4 ± 1.1	12.2 ± 2.1
	40%	2.6 ± 0.9	0.95 ± 0.12	$0.86 \pm 0.08*$	0.40 ± 0.07
$Issp/Isps$	100%	4.8 ± 0.6	-	14.5 ± 1.4	20 ± 5
	40%	0.91 ± 0.18	-	$1.74 \pm 0.19*$	$0.44 \pm .08$

* 60% C_{18} surface composition

Further evidence regarding the structure of the stationary phase in these model systems emerges from polarization studies. In the previous comparison of methyl to methylene symmetric stretch intensities using *ssp* polarization, the decrease in the numerator indicated a general trend of the methyl group to orient at a larger angle from the surface normal. Using *s*-polarized infrared light in a second set of experiments, we can confirm this observation by examining the component of the antisymmetric stretch that lies parallel to the surface. Figures 5 A-D show the SF spectra taken with both *ssp* (*s*-polarized SF, *s*-polarized visible light and *p*-polarized infrared light) and *sps* (*s*-polarized SF, *p*-polarized visible light and *s*-polarized infrared light) polarization combinations.

In Figure 5A, the methyl symmetric stretch is very strong in the *ssp* spectrum, and the methyl antisymmetric stretch, which possesses a transition dipole perpendicular to that of the symmetric stretch, shows a very strong peak with *sps* polarization for the 100% C_{18}-modified surface in air. The lack of these two peaks in the opposite polarization combinations is a very clear indication that the C_{3v} axis of the methyl group lies primarily along the surface normal. This observation is interesting because of the obvious roughness of our silica substrate. Although the average tilt angle for these types of silica surfaces is approximately 15° (*21*), it is likely that the polymerization of the siloxanes forms a much flatter surface, away from which the alkyl chains will be directed (*9*).

In Figure 5B, when methyl groups (methylsiloxanes) are introduced onto the surface as spacers, we see a greater intensity in the methyl symmetric stretch with *sps* polarization and methyl antisymmetric stretch with *ssp* polarization than for 100% C_{18} monolayers. This spectral result indicates that the methyl "spacers" provide additional conformational freedom to the longer C_{18} alkyl chains, allowing the methyl transition dipoles to have an average orientation further from the surface normal. Aside from the spectral shift, the spectra for full monolayers in contact with water and air are very similar (Figure 5C). For partial monolayers (Figure 5D), the change in the methyl symmetric stretch and methyl antisymmetric stretch with changing polarization combinations is much more distinct in water. Therefore, adding the methyl "spacers" to the monolayers seems to allow the alkyl chains enough freedom to change their conformation in response to the contacting solvent.
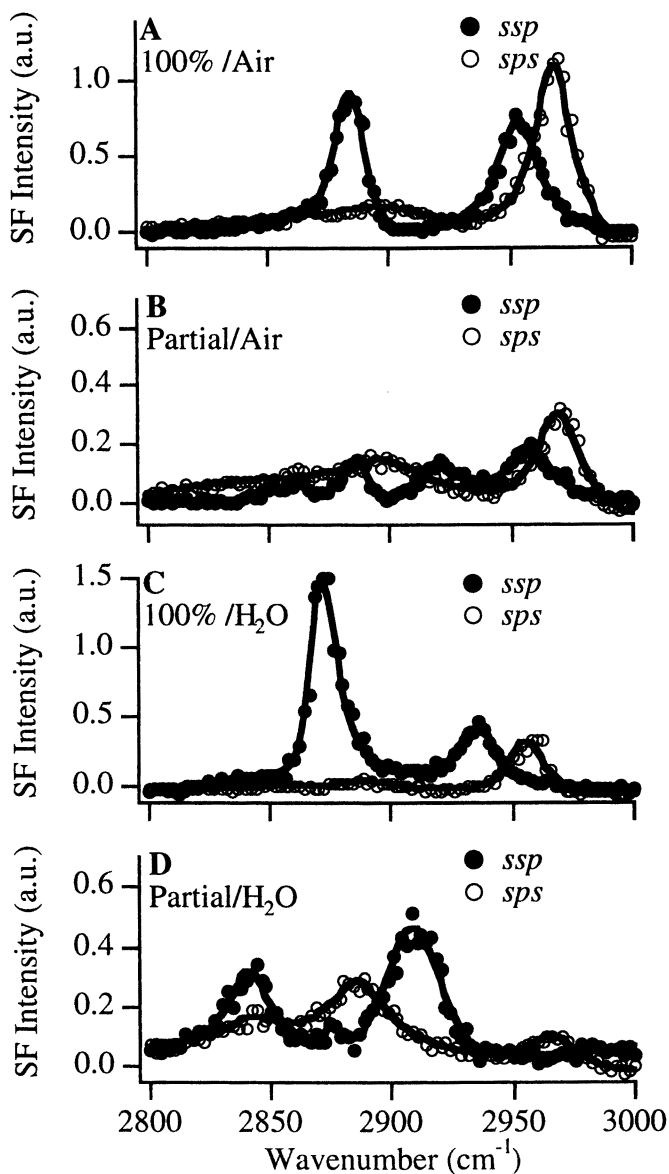
Figure 5: SF spectra for 100% C_{18}-modified and partial (40%) C_{18}-modified fused silica surfaces taken with ssp polarization (s-polarized SF, s-polarized visible light and p-polarized infrared light), and sps polarization (s-polarized SF, p-polarized visible light and s-polarized infrared light). A: 100% in contact with air, B: 40% in contact with air, C: 100% in contact with water, D: 40% in contact with water, using (●) ssp polarization and (O) sps polarization. The solid lines are fits to the data using Voigt lineshapes.

To semi-quantitatively determine the relative change in orientation of the methyl groups on going from a 100% C_{18} to a partially covered C_{18}-monolayer, the ratio of the methyl symmetric stretch intensity with *ssp* polarization ($I ssp$) to that with *sps* polarization ($I sps$) was determined. This ratio is not a direct indication of tilt angle because of the likelihood that a very broad distribution of angles exists. It is a good indicator, however, of the changes that occur with the addition of conformational freedom. This ratio is shown in Table I for two solvents and air. Because of the low refractive index of isooctane, it was not possible to obtain *sps* spectra for the surface in contact with isooctane. Comparing 100% C_{18} surfaces with partial C_{18} surfaces, we see a factor of 5.2 ± 1.2 change for air, a factor of 8.4 ± 1.2 for acetonitrile and a factor of 46 ± 14 change for water. Such a large change in this ratio as caused by the water solvent indicates a very distinct change in the structure of the stationary phase.

Further comparison of these ratios can be made by examining Figures 6A and 6B. These graphs show the change in the methyl symmetric stretch to methylene symmetric stretch intensity ratios with *ssp* light (Figure 6A) and the methyl symmetric stretch with *ssp* and *sps* polarizations (Figure 6B). Although the methyl symmetric stretch to methylene symmetric stretch intensity ratio for the water system is similar to that of the acetonitrile and isooctane, the ratio of methyl symmetric stretch with *ssp* and *sps* polarization is quite different. This ratio indicates that the methyl groups are orienting themselves away from the interface to reduce the high energy interactions with the water.

Summary and Conclusions

Results presented here show that the solvent does influence the structure of the stationary phase of mixed C_{18}-C_1 composition monolayer. Monolayers formed from 100% C_{18} alkylsiloxanes show no discernable conformational differences when placed in contact with different liquids, as found with Raman studies. Only a spectral shift in the methyl symmetric stretch of these monolayers was observed when the solvent was changed. Nevertheless, when methylsiloxane is added to the monolayer, an obvious change in C_{18} alkyl chain conformation occurs. By examining the ratio of the methyl to methylene symmetric stretches, the amount of *gauche* conformations in the alkyl chain backbones is semi-quantitatively characterized. It is found that water, acetonitrile, and isooctane induce similar amounts of *gauche* conformations in the alkyl chains of the stationary phase. By examining the ratio of the methyl symmetric stretch using *ssp* and *sps* polarizations, it is shown that water causes a much larger change in methyl group orientation than does acetonitrile. This reorientation, which is directed away from the surface normal, is consistent with a view of the stationary phase as a collapsed structure when in contact with water.

Acknowledgements
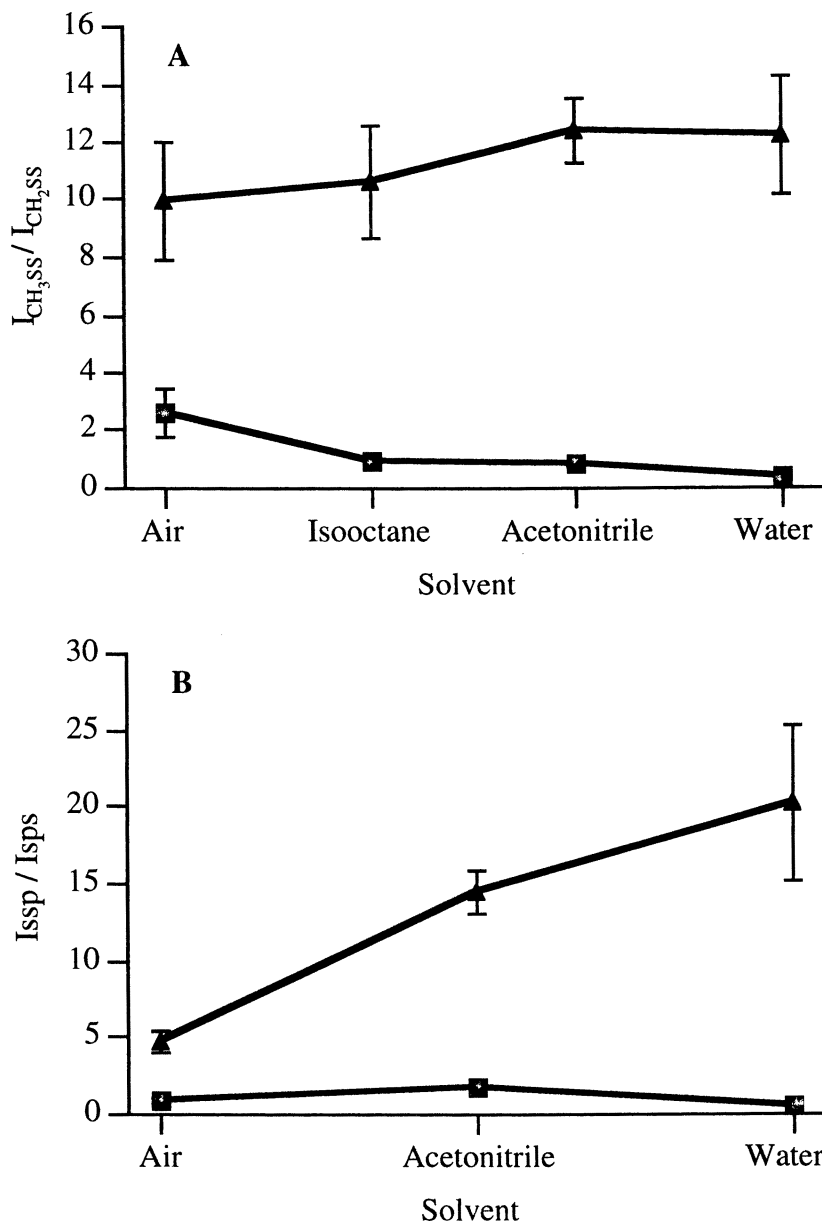
Figure 6: SF intensity ratios for A: methyl symmetric stretch to methylene symmetric stretch intensities for ssp polarization for various solvents, B: methyl symmetric stretch for ssp to the methyl symmetric stretch for sps polarization for (▲) 100% C_{18} and (■) partial C_{18} coverages.

Literature Cited

1. Fairbank, R. W. P.; Xiang, Y.; Wirth, M. J. *Anal. Chem.* **1995**, *67*, 3879-3885.
2. Wirth, M. J.; Fairbank, R. W. P.; Fatunmbi, H. O. *Science* **1997**, *275*, 44-47.
3. Slusher, J. T.; Mountain, R. D. *J. Phys. Chem. B* **1999**, *103*, 1354.
4. Alvarez-Zepeda, A.; Barman, B. N.; Martire, D. E. *Anal. Chem.* **1992**, *64*, 1978.
5. DeVido, D. R.; Dorsey, J. G.; Chan, H. S.; Dill, K. A. *J. Phys. Chem.* **1998**, *102*, 7272.
6. Bliesner, D. M.; Sentell, K. B. *Anal. Chem.* **1993**, *65*, 1819.
7. Thompson, W. R.; Pemberton, J. E. *Anal. Chem.* **1994**, *66*, 3362-3370.
8. Huang, J. Y.; Shen, Y. R. *Sum-Frequency Generation as a Surface Probe*; Dai, H.-L. and Ho, W., Ed.; World Scientific, 1995, pp 5-53.
9. Pizzolatto, R. L.; Yang, Y. J.; Wolf, L. K.; Messmer, M. C. *Anal. Chim. Acta* **1999**, *397*, 81.
10. Yang, Y. J.; Pizzolatto, R. L.; Messmer, M. C. *J. Opt. Soc. Am. B* **1999**, *(accepted)*.
11. Hatch, S. R.; Polizzotti, R. S.; Dougal, S.; Rabinowitz, P. *Chem. Phys. Lett.* **1992**, *196*, 97-102.
12. Hatch, S. R.; Polizzotti, R. S.; Dougal, S.; Rabinowitz, P. *J. Vac. Sci. Tech.* **1993**, *11*, 2232-2238.
13. Conboy, J. C.; Messmer, M. C.; Richmond, G. L. *J. Phys. Chem.* **1996**, *100*, 7617-7622.
14. Messmer, M. C.; Conboy, J. C.; Richmond, G. L. *Resonant Sum Frequency Generation Studies of Surfactant Ordering at the Oil-Water Interface*; Hicks, J. M., Ho, W. and Dai, H.-L., Ed.; SPIE - The International Society for Optical Engineering: San Diego, 1995; Vol. 2547, pp 135-141.
15. Messmer, M. C.; Conboy, J. C.; Richmond, G. L. *J. Am. Chem. Soc.* **1995**, *117*, 8039-8040.
16. Bain, C. D. *Langmuir* **1994**, *10*, 2060.
17. Guyot-Sionnest, P.; Hunt, J. H.; Shen, Y. R. *Phys. Rev. Lett.* **1987**, *59*, 1597-1600.
18. Ulman, A. *Ultrathin Organic Films From Langmuir-Blodgett to Self-Assembly*; Academic Press: San Diego, 1991.
19. Carr, J. W.; Harris, J. M. *Anal. Chem.* **1986**, *58*, 626.
20. Bayer, E.; Paulus, A.; Peters, B.; Laupp, G.; Reiners, J.; Albert, K. *J. Chromatogr.* **1986**, *364*, 25-37.
21. Simpson, G. J.; Rowlen, K. L. *J. Phys. Chem. B* **1999**, *103*, 1525.

Chapter 19

Electrochemical and Infrared Analysis of Alkoxyaniline Derivative Monolayers on Gold

K. Cory Schomburg and Robin L. McCarley

Choppin Laboratories of Chemistry, Louisiana State University, Baton Rouge, LA 70803–1804

Monolayers of 2-(6-mercaptohexan-1-oxy)aniline (AnC6SH) and 2-(7-mercaptoheptan-1-oxy)aniline (AnC7SH) on Au were characterized by reflection-absorption infrared (RAIR) spectroscopy and electrochemistry. Electrochemical oxidation of AnC6SH/Au and AnC7SH/Au in aqueous acidic solution leads to complex voltammetry indicative of oligomerization and degradation reactions of the aniline functionality. Scanning of the potential between 0.0 and +0.9 V vs. SSCE leads to four surface-confined redox waves occurring at +0.2, +0.4, +0.5, and +0.6 V vs. SSCE. The oxidized monolayers were found to display voltammetry equivalent in nature to that observed for poly(o-phenetidine), which exhibits redox waves for the leucoemeraldine/emeraldine (+0.2 V) and emeraldine/pernigraniline (+0.6 V) transformations and the formation of some quinonemonoimine degradation products (+0.4 V) in the polymer. A redox wave attributed to a quinonediimine dimer (+0.5 V) was also found for the oxidized monolayers. Further oxidation of this species leads to increased polymer production and degradation product formation. To reduce degradation product formation, AnC6SH/Au and AnC7SH/Au were oxidized in non-aqueous solution. This method led to production of only surface confined dimers as indicated by electrochemical analysis.

Poly(aniline) and poly(aniline) derivatives are a commercially important class of conducting polymers which have received a great deal of interest in the last twenty years. These polymers can be formed via chemical or electrochemical methods and can be made insulating or conducting by conversion between various electrochemical redox states.[1] Each polymeric state is environmentally stable under ambient conditions and contains its own unique optical and electrical properties.

306

Poly(aniline) and its derivatives have been envisioned for a number of applications such as protective coatings, electrochromic devices, and potentiometric sensors.[2]

Our research interest in poly(aniline) and its derivatives lies in the field of surface modification using self-assembled monolayers (SAMs). SAMs have been well documented in the literature and used for a variety of applications including lubrication, protective coatings, and chemical sensors. Thin films of poly(aniline) have been created using the Langmuir-Blodgett technique and electrochemical methods.[3] We are interested in creating a monolayer containing an aniline tail group tethered to an electrode surface, which could undergo electrochemical polymerization to form a monolayer film of poly(aniline). Such a film could be electrochemically oxidized/reduced to form an insulating or conducting film of molecular thickness.

Attempts to form surface-confined poly(aniline) have previously been made using 4-aminothiophenol on Au.[4,5] After oxidation of the monolayer and successive potential scans, this monolayer was found to produce a surface-confined redox active film. Recently, elucidation of the coupling and degradation pathways of this molecule on Au was reported.[5] Radical-radical coupling was found to occur between adjacent aminothiophenol molecules yielding an electrode surface modified with 4'-mercapto-4-aminodiphenylamine. Upon potential scanning of the surface-confined aniline dimer, an electrochemical-chemical-electrochemical (ECE) reaction was found to occur. Oxidation of the quinonediimine resulted in hydrolysis of the dimer to yield a quinone monoimine species. Further oxidation of this molecule then produced the initial 4-aminothiophenol molecule as well as benzoquinone in solution.

In this paper, we present electrochemical and reflection-absorption infrared spectroscopy (RAIRS) studies on two self-assembled monolayers possessing an alkoxyaniline tail group tethered to a gold electrode surface via an alkyl thiol chain. RAIRS analysis is performed on the self-assembled monolayers and compared to infrared (isotropic) spectra collected for the monomers. These monolayers were also subjected to electrochemical permeability measurements for the determination of the monolayer blocking ability. Cyclic voltammetry was performed on the monolayers in 1 M H_2SO_4 and compared to literature and experimental data collected for poly(o-phenetidine) thin films and dimeric model compounds. The oxidized monolayers are shown to contain some surface-confined polymer and dimeric degradation products. The oxidized monolayers were further analyzed by RAIRS at various potentials for characterization of the polymeric forms. To reduce the formation of degradation products and promote polymer growth, AnC6SH/Au and AnC7SH/Au were oxidized in 0.1 M $LiClO_4/CH_3CN$. Oxidation in this non-aqueous solution produced only surface-confined dimer and no polymer or degradation products.

Experimental

Chemicals

All solvents were of chromatographic grade or better and were used without further purification. Dibromohexane (Aldrich, 96%), dibromoheptane (Aldrich, 97%), KOH (Aldrich, >85%), NaOH (Aldrich, 99%), thiourea (Aldrich, 99+%), o-

phenetidine (Aldrich, 98%), and 2-methoxy-N^4-phenyl-1,4-phenylenediamine (Aldrich, 95%) were used as received. Distilled water was passed through a Barnstead reverse osmosis filter followed by a Nanopure water system to yield water with a resistivity of 18 MΩ cm. All other materials were reagent grade or better.

Synthesis of Aniline-Terminated Alkanethiols

2-(6-Mercaptohexan-1-oxy)aniline (AnC6SH) and 2-(7-Mercaptoheptan-1-oxy)aniline (AnC7SH) were both synthesized using a similar procedure. The potassium salt of o-aminophenol was first made by placing o-aminophenol (1.00 g) and potassium hydroxide (0.52 g) in an argon-purged round bottom flask with dried ethylene glycol dimethyl ether (50 mL). This solution was allowed to stir for 30 min to ensure salt formation. The o-aminophenol salt solution was cannulated to a new round bottom flask containing 25 mL ethylene glycol dimethyl ether and excess dibromoalkane (3.76 g) where a Williamson synthesis was performed under an argon atmosphere. The resulting alkoxybromide compound (0.72 g) was purified by column chromatography using 40 micron silica gel (Alltech Associates, Inc.) and 10% hexanes in ethyl acetate before the next synthetic step. Thiolation of the purified alkoxybromide was achieved by refluxing a mixture of the alkoxybromide (0.50 g) and thiourea (0.14 g) for 8 h to form the thiouronium salt. The thiouronium salt was cleaved by allowing the solution to come to room temperature, adding sodium hydroxide (0.21 g), and refluxing for an additional 8 h to form the thiol. An extraction procedure was used with water and methylene chloride to extract the pure thiol. Methylene chloride extracts were combined and concentrated to yield the pure alkoxyaniline thiol. Purified products were subjected to transmission infrared spectroscopy (IR), gas chromatography-mass spectroscopy (GC-MS), and electron ionization (EI) mass spectroscopy analysis for characterization. Products were found to be >99% pure. The purified products were dissolved in ethanol to create a 0.5 mM alkoxyaniline solution for self-assembled monolayer formation; the monolayer solutions were stored in a drybox or freezer for future use.

Surface Derivatization

Au electrodes were prepared from 99.999% Au wires (Refining Systems, Las Vegas, NV). Electrical contact to the Au wires was made by soldering a copper wire using silver solder. The Au wires were then sealed in a soft glass tube using a methane/oxygen flame. These electrodes were mechanically polished with sandpaper, followed by various grit diamond pastes. After electropolishing in 1 M HClO$_4$, the electrodes were rinsed with copious amounts of 18 MΩ cm water, then blown dry with high-purity N$_2$ gas immediately before further use. Substrates for reflection-absorption infrared spectroscopy were prepared using 99.999% Au (Refining Systems) and 99.999% Cr (Kurt J. Lesker). Glass substrates (1" x 3" microscope slides) were soaked for about 30 min in freshly prepared piranha solution (70/30 (v/v) mixture of 98% H$_2$SO$_4$/30% H$_2$O$_2$). *Caution! Piranha is a very reactive*

material that should be handled with great care. It should be disposed of promptly after use in order to prevent explosions. The assembly was rinsed with 18 MΩ cm water and then dried with N_2 gas. These substrates were immediately placed in an Edwards Auto 306 evaporator system where metal evaporation took place. Pressures during evaporation were never more than 10^{-6} torr. The glass substrates had a 30 Å Cr adhesion layer applied to them, followed by a 2000 Å Au film. Substrates for surface coverage analysis were prepared by placing an aluminum mask over freshly cleaved mica and evaporating ~1000 Å of Au followed by annealing in a muffle furnace at 300°C for 3 hr. The aluminum mask covering the mica was 1" x 3" with five electrode patterns cut equally along the mask. The electrode pattern on the aluminum mask was made by cutting two circles 5 mm in diameter and connecting the circles with a 7 mm long cut 1 mm wide to create a dumbell shape.

Voltammetric Measurements

Electrochemistry was performed in normal three-electrode mode with a PAR 273A potentiostat/galvanostat and a conventional glass electrochemical cell. Potentials were recorded versus a saturated sodium calomel reference electrode (SSCE).

Infrared Spectroscopy

All infrared spectra were obtained with a Nicolet 740 FTIR system using a liquid-nitrogen-cooled, wide-band MCT detector. The analyzing chamber was surrounded with a poly(ethylene) glovebag. The optical bench and sample compartment were purged with house N_2 passed through a home-made water and CO_2 scrubbing system. Reflection spectra were collected using a versatile reflection accessory with retro-mirror attachment (VRA-RMA, Harrick Scientific) using an incidence angle of 86° with respect to the substrate normal. Incident *p*-polarized light produced by a wire grid polarizer (Harrick Scientific) set to 90° was used for the reflection experiments. All reflection-absorption infrared (RAIR) spectra are the result of 2000 scans referenced to a bare Au background. Happ-Genzel apodization was employed throughout this study. All spectra reported here were obtained at 2 cm^{-1} resolution. Reported peak frequencies have errors of ± 1 cm^{-1}. Purge correction to remove residual water vapor bands from the RAIR spectra and baseline correction were performed using the Nicolet SX software.

Results and Discussion

Analysis of AnC6SH and AnC7SH Monolayers

The alkoxyanilines were allowed to self-assemble on gold electrodes for at least eight hours before RAIRS or electrochemical analysis was performed.

Transmission infrared (isotropic) spectra were recorded for both the AnC6SH and AnC7SH molecules; both produced equivalent spectra. Monolayer modified gold slide electrodes were removed from solution, rinsed with ethanol, and dried with N_2 gas before RAIR spectra were recorded. RAIR spectra were collected for AnC6SH/Au and AnC7SH/Au and compared to the AnC6SH isotropic spectrum, Figure 1. Virtually all vibrations present in the RAIR spectra are observed in the
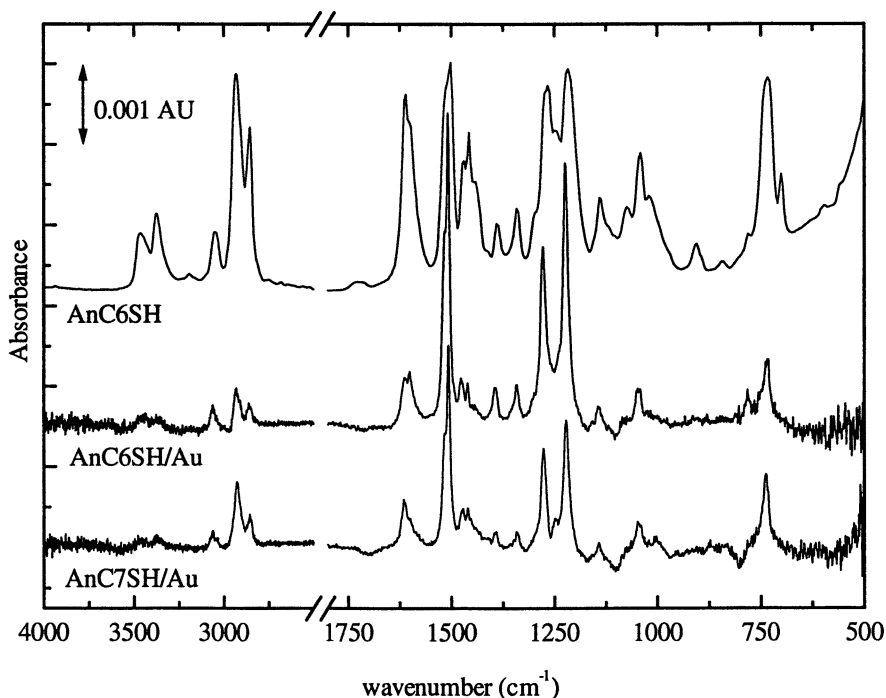
Figure 1. Comparison of the AnC6SH isotropic spectrum with the AnC6SH/Au and AnC7SH/Au RAIR spectra.

isotropic spectrum with a small amount of peak shifting of the RAIR bands in the 1600-500 cm^{-1} region. Band assignments have been made for the major bands in the spectra and are given in Table I. Band intensity ratios for AnC6SH/Au and AnC7SH/Au RAIR spectra versus the respective isotropic spectral bands indicate the aniline tail group has assumed a preferred orientation. The RAIRS data associated with the various aniline ring modes also indicate that the aniline functionality is canted significantly from the surface normal.

       To determine the surface coverage of AnC6SH and AnC7SH monolayers, desorption studies were conducted as described by Porter et al.[6] In this technique, the

Table I. Isotropic and RAIR Vibrational Assignments

AnC6SH IR Monomer (cm⁻¹)	AnC6SH/Au RAIR (cm⁻¹)	AnC7SH/Au RAIR (cm⁻¹)	Assignment
3468	3439	3459	$\nu_a(NH_2)$
3375	3379	3377	$\nu_s(NH_2)$
3047	3063	3063	$\nu(CH)_{Ar}$
2931	2931	2929	$\nu_a(CH_2)$
2855	2862	2857	$\nu_s(CH_2)$
1610	1616	1616	$\delta(NH)/\nu(C=C)_{Ar}$
1502	1508	1507	$\nu(C=C)_{Ar}$
1458	1461	1461	$\nu(C=C)_{Ar}$
1390	1396	1392	??
1342	1343	1343	??
1266	1278	1277	$\nu(ArO)$
1218	1224	1222	$\nu(CN)$
1142	1146	1144	$\omega_{ip}(CH)_{Ar}$
1041	1048	1048	$\nu(CO)$
905	n/o	n/o	$\omega_{oop}(CH)_{Ar}$
733	735	738	$\omega_{oop}(CH)_{Ar}$

n/o indicates not observed

potential of the working electrode is scanned cathodically in 0.5 M KOH/water under a nitrogen atmosphere. Adsorbed thiols produce a voltammetric peak due to thiol desorption from the gold surface. This voltammetric peak is integrated to give the corresponding electrochemical charge for surface coverage (Γ(mol cm⁻²)).

Octadecanethiol/Au was used as a control to compare surface coverages determined for AnC6SH/Au and AnC7SH/Au monolayers. Surface coverage values of 9.3±0.8 x 10⁻¹⁰ (E_p = -1.10±0.02 V), 9.9±1.5 x 10⁻¹⁰ (E_p = -1.06± 0.03 V), and 8.8±0.3 x 10⁻¹⁰ (E_p = -1.24± 0.04 V) mol cm⁻² (5 trials each) were obtained for the AnC6SH/Au, AnC7SH/Au, and octadecanethiol/Au monolayers respectively. Surface coverage values obtained for AnC6SH/Au and AnC7SH/Au were found to be slightly higher from a statistical point of view, than the octadecanethiol/Au. The Γ values obtained in this experiment were not corrected for surface roughness. The desorption potential of AnC7SH/Au suggests that this monolayer is more permeable than AnC6SH/Au and octadecanethiol/Au. This data is further supported by monolayer blocking experiments that are described later.

The blocking ability of AnC6SH/Au and AnC7SH/Au to a solution-phase redox probe was inspected, Figure 2. Blocking experiments provide a measure of the defects and pin-holes that may be present in a monolayer, thus providing a measure of the monolayer packing. Cyclic voltammetry of the monolayers between 0.0 and +0.5 V vs. SSCE (B and C Figure 2) provided a nearly featureless regime to test for monolayer blocking. Dimethylaminomethyl ferrocene in 1 M H_2SO_4 was found to produce a reversible redox wave centered at +0.35 V (Figure 2A) and was used for
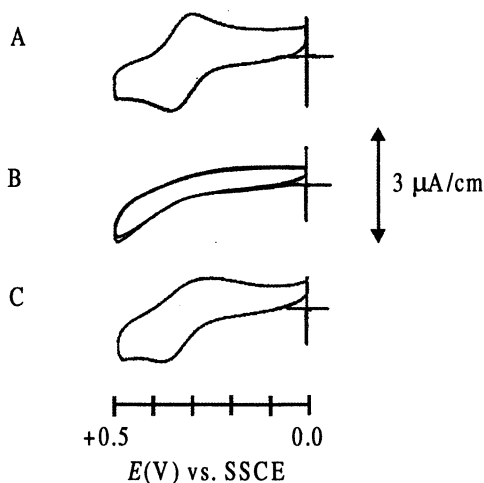
Figure 2. (A) Bare gold electrode in 20 μM dimethylaminomethyl ferrocene/1 M H₂SO₄ with a scan rate of 100 mV/s. (B) AnC6SH/Au and (C) AnC7SH/Au in solution (A).

blocking experiments. AnC6SH/Au yields almost complete blockage of the redox probe to the gold surface (Figure 2B) while AnC7SH/Au provided only partial blocking (Figure 2C).

Electrochemistry of Monolayers in Aqueous Acidic Solution

Electrochemical oxidation of AnC6SH/Au and AnC7SH/Au was performed in 1 M H_2SO_4 using cyclic voltammetry (CV). Upon oxidation, a large irreversible peak was observed at +0.7 V for both monolayers, Figure 3. This peak is attributed to formation of radical-cation aniline tail units. Further cycling of the potential between 0.0 V and +0.9 V reveals a series of complex redox waves for both the *ox*-AnC6SH/Au and *ox*-AnC7SH/Au, Figure 4. Although the RAIR spectra of the pristine AnC6SH/Au and AnC7SH/Au indicate that the films are very similar with respect to molecular orientation, the electrochemistry of the two is quite different.

Four redox waves are present in the voltammograms of *ox*-AnC6SH/Au surfaces. The first wave observed for *ox*-AnC6SH/Au occurs at +0.25 V (I). This wave is small in intensity and is observed to grow and shift negatively in position with increasing cycling time. This wave has no substantial potential difference between the anodic and cathodic redox waves suggesting that the species is surface confined. The second wave at +0.4 V (II) is an intense redox wave that is a shoulder of the +0.5 V wave (III). This wave grows after several potential cycles suggesting an electrochemical-chemical (EC) reaction is occurring and more of this species is being produced with further potential cycling. The third wave observed for *ox*-AnC6SH/Au occurs at +0.5 V (III). This wave is seen to decrease in intensity as the potential is

A

B

3 μA

+0.9   +0.6   +0.3   0.0   +0.9   +0.6   +0.3   0.0

E(V) vs. SSCE   *E*(V) vs. SSCE
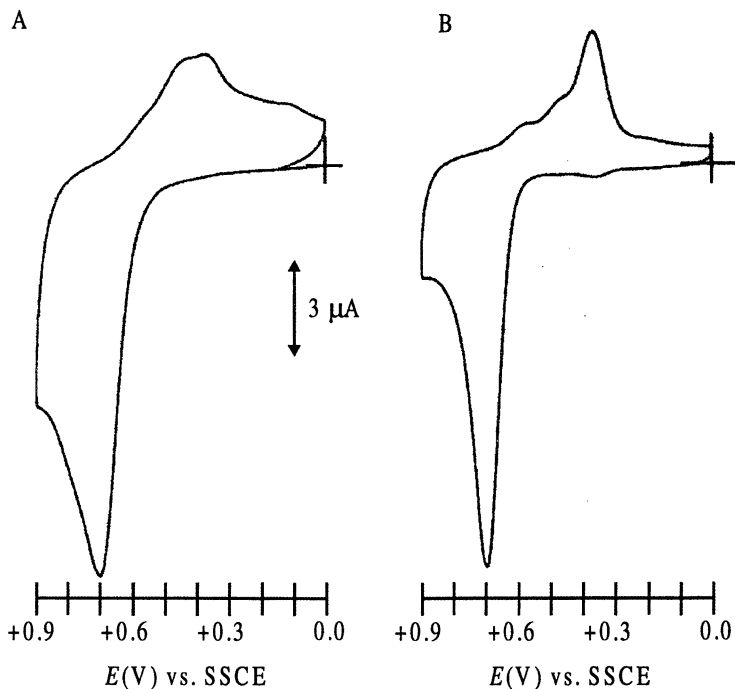
Figure 3. First oxidative scan of (A) AnC6SH/Au and (B) AnC7SH/Au in 1 M H₂SO₄ with a scan rate of 100 mV/s.

cycled, suggesting that this species is being consumed. A fourth redox wave present in *ox*-AnC6SH/Au voltammetry at +0.6 V (IV) becomes present after two potential cycles.

All redox waves present in the *ox*-AnC6SH/Au are present in the *ox*-AnC7SH/Au, but the relative intensities of the waves are different. The second redox wave in *ox*-AnC7SH/Au occurs at the same redox potential (+0.4 V) but is sharper in appearance than that of the *ox*-AnC6SH/Au and does not increase as dramatically upon further potential cycling. Wave III in the *ox*-AnC7SH/Au voltammetry is much smaller in peak intensity than in the *ox*-AnC6SH/Au suggesting that a smaller amount of this species is produced during the initial electrochemical oxidation of the aniline monolayer. The fourth redox wave present in the *ox*-AnC7SH/Au, IV, is also very different than that for *ox*-AnC6SH/Au. The initial presence of this wave is noted after only one scan for *ox*-AnC7SH/Au while it takes two scans to be observed for *ox*-AnC6SH/Au, possibly a result of the difference in chain length or the orientation assumed after potential scanning.

To aid in the characterization of the AnC6SH/Au and AnC7SH/Au voltammetry, poly(*o*-phenetidine) films electrodeposited onto Au were studied. Polymerization of *o*-phenetidine in 1 M H₂SO₄ was achieved by cycling the potential of an Au electrode between 0.0 and +0.9 V vs. SSCE. Once the polymer film had
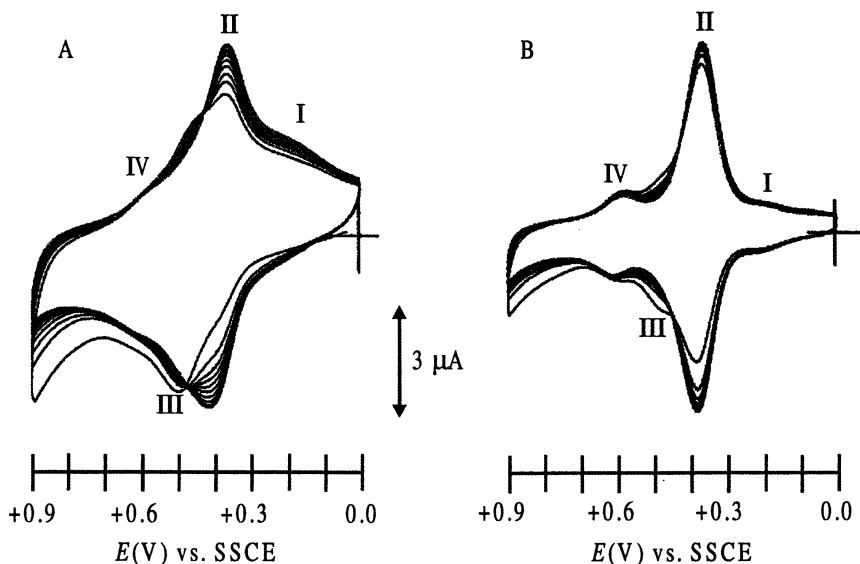
Figure 4. Potential scans 2-10 of (A) ox-AnC6SH/Au and (B) ox-AnC7SH/Au in 1 M
H₂SO₄ with a scan rate of 100 mV/s.

been formed, the electrode was rinsed with water and the voltammetry of the film in 1
M HCl was analyzed and compared to the literature, Figure 5. Three waves are
observed in the voltammetry for the polymer film. The first and third waves
occurring at +0.25 (A) and +0.65 V (C) observed in the poly(o-phenetidine) film are
assigned as the leucoemeraldine/emeraldine and the emeraldine/pernigraniline
transformations respectively. These assignments are based on findings of Park and
co-workers for poly(aniline) thin films and studies by Leclerc and co-workers for
substituted anilines.[7,8] The second wave in the voltammetry at +0.4 V (B) is due to
the formation of degradation products in the polymer film. The oxidation pathway of
aniline polymerization in acidic electrolyte solutions has been shown by Bard and co-
workers to produce a paraamino diphenylamine intermediate in the polymerization
process.[9] This intermediate may undergo an electrochemical-chemical-
electrochemical reaction thus producing quinone and quinoneimine degradation
products throughout the polymer.

The redox transformations observed for the poly(o-phenetidine) film were
used to aid in describing the redox characteristics of ox-AnC6SH/Au and ox-
AnC7SH/Au. The first redox wave I we attribute to the leucoemeraldine/emeraldine
transformation. The second redox wave, II is attributed to degradation products that
are formed upon oxidation of the monolayer in aqueous acidic media. The third
redox wave, III is assigned to the redox reaction of dimers in the monolayer. This
assignment will be discussed in further detail later. Redox wave IV observed in the
ox-AnC7SH/Au voltammetry is attributed to the emeraldine/pernigraniline
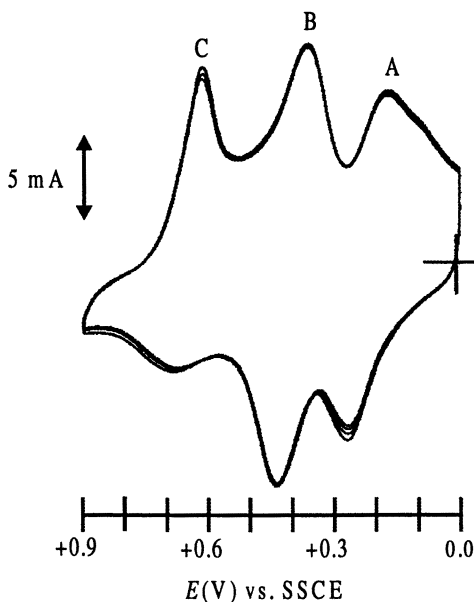
Figure 5. Electrochemistry of electrochemically deposited poly(o-phenetidine) film on a gold electrode in 1 M HCl with a scan rate of 100 mV/s.

transformation, as observed for the poly(*o*-phenetidine) film. The voltammetry observed for *ox*-AnC6SH/Au and *ox*-AnC7SH/Au are also supported by the studies of D'Aprano and co-workers.[10] D'Aprano studied the bulk polymerization of a series of substituted anilines including 2-alkoxyanilines and found voltammetry similar to poly(aniline) and poly(*o*-phenetidine). These studies attributed the redox wave II to irregular couplings, degradation products, dimers, and oligomers.

Assignment of the redox transformations of waves I and IV as leucoemeraldine/emeraldine and emeraldine/pernigraniline are supported by observations associated with the dimer wave at III. As the III wave decreases in intensity, redox waves I and IV in *ox*-AnC6SH/Au and *ox*-AnC7SH/Au increase in magnitude as well as the degradation peak assigned at II. To investigate the possibility of dimer formation, the electrochemistry of 2-methoxy-N^4-phenyl-1,4-phenylenediamine was investigated. This molecule produced one redox wave at +0.45 V in the initial electrochemical scan then a second wave at +0.35 V upon further scanning in 1 M H_2SO_4. The redox wave at +0.45 V is due to a two-electron/two-proton oxidation of the aniline dimer. Upon further potential scanning this dimer was found to hydrolyze forming an electroactive quinoneamine degradation product in bulk solution. Aniline dimer formation and degradation has previously been reported in the oxidation of 4-aminothiophenol on gold electrodes.[5] Radical-radical coupling of the aniline tail group was found to produce a quinonediimine species.[5] This quinonediimine molecule produced a surface-confined

redox wave centered at +0.5 V. The assignment of a dimer wave and its characteristics suggests that dimer formation among AnC6SH/Au monomer units may be the preferred path for coupling of the radical-cation species. Further oxidation of this dimer thus leads to some polymeric film growth and degradation product formation. In AnC7SH/Au, dimer formation is small and the ready formation of polymer is evidenced by the intensity of the IV transformation.

RAIRS of Aniline Monolayers Upon Electrochemical Oxidation

To elucidate the structure of the oxidized aniline monolayers, RAIRS was used to obtain the IR spectra of *ox*-AnC6SH/Au and *ox*-AnC7SH/Au at different electrochemical potentials (following initial oxidation of the monolayers). After initial oxidation of pristine AnC6SH/Au and AnC7SH/Au in 1 M H_2SO_4, the coated Au electrode was removed from solution, rinsed with water, then immersed in 1 M HCl. The potential of the electrode was again cycled through a potential range of 0.0 to +0.65 V vs. SSCE. After several potential cycles, the electrode potential was held at 0.0 V vs. SSCE, rinsed with 1 M HCl, dried with N_2, and evaluated using RAIRS so as to obtain a spectrum of the oxidized film at 0.0 V. HCl is a volatile inorganic acid, thus, we are able to completely dry the surface of the electrode without forming acid films (that form with H_2SO_4) that prevent RAIRS analysis. Once the 0.0 V spectrum was obtained, the electrode was re-immersed in 1 M HCl, and the potential was cycled to +0.65 V, rinsed, dried, and analyzed to obtain a RAIR spectrum of the oxidized monolayer at +0.65 V.

RAIR spectra obtained for the oxidized layers at 0.0 and +0.65 V vs. SSCE are similar between *ox*-AnC6SH/Au and *ox*-AnC7SH/Au but dramatically different than the pristine monolayer spectra, Figure 6 (1800-500 cm^{-1} region). It is observed that the intensities of the bands associated with alkane C-H stretching have now increased, the intensities of vibrations due to the aniline tail group have dramatically decreased, and several spectral shifts are now observed. Comparison of the RAIR spectra for the fully reduced state of the polymer (0.0 V) and the fully oxidized state (+0.65 V) are also different due to oxidation of the phenyl rings to quinoid rings. To ensure the spectral changes observed are reproducible, spectra were recorded at 0.0, +0.65, and then 0.0 V ("0.0 V return") again. Spectra recorded for the 0.0 V and 0.0 V return were nearly identical, indicating electrochemical cycling of the oxidized monolayers was reversible.

To test the environmental stability of the oxidized monolayer, AnC6SH and AnC7SH modified electrodes were oxidized and allowed to sit on the bench top under ambient laboratory conditions. Cyclic voltammetry and RAIRS were performed on the oxidized monolayer every four hours to monitor changes. After 36 hours, no changes were observed for the oxidized film. Oxidized films were also subjected to electrochemical reductive desorption as performed previously with the pristine monolayers, to ensure that electrochemical oxidation does not desorb molecules from the Au surface. Surface coverages calculated for the *ox*-AnC6SH/Au and *ox*-AnC7SH/Au were 8.8±0.8 x 10^{-10} (E_p = -1.12±0.02 V) and 11.8±1.2 x 10^{-10} (E_p = -1.09±0.04 V) mol cm^{-2}, respectively. These values are similar to the values obtained
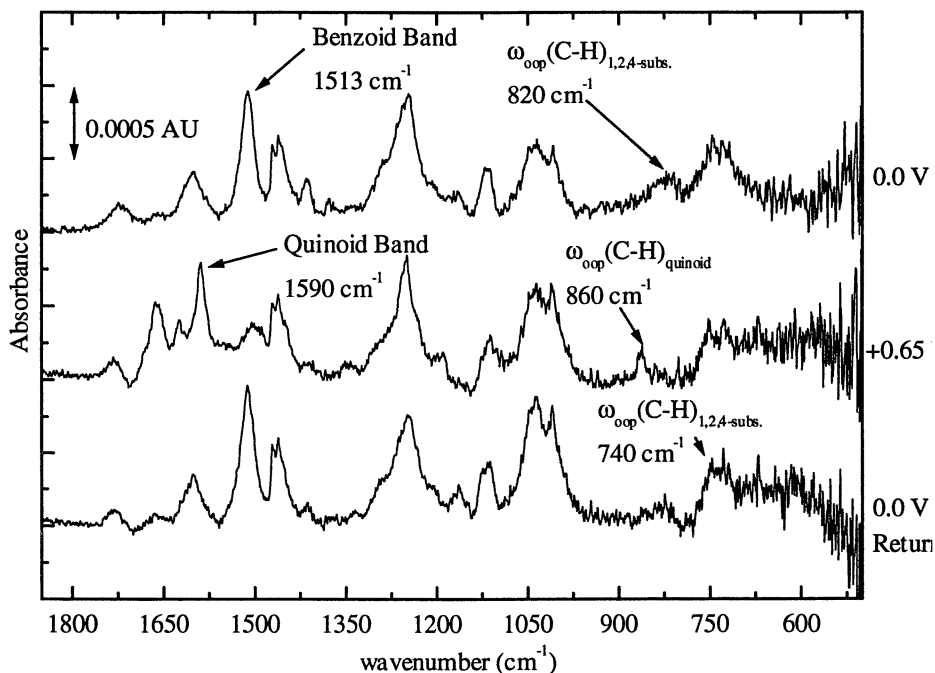
Figure 6. RAIR spectra of ox-AnC7SH/Au at various emmersion potentials.

for pristine AnC6SH/Au and AnC7SH/Au, and show that desorption of molecules from the Au surface does not significantly occur during electrochemical potential cycling.

RAIR spectroscopy of the oxidized monolayers produced complex spectra due to dimers, degradation products, and polymer within the oxidized film. Infrared bands providing spectral information of changes occurring in the polymer films include the 1513, 820, and 740 cm^{-1} bands for the 0.0 V spectra, and 1590 and 860 cm^{-1} bands in the +0.65 V spectra. The 1513 cm^{-1} band observed is assigned to the benzoid vibration for the fully reduced (0.0 V) polymer structure. In the 0.0 V spectra, the 1513 cm^{-1} (benzoid band) band is accompanied by two active out-of-plane deformation vibrations at 820 and 740 cm^{-1} which are due to 1,2,4-ring substitution.[11,12,13]

Transformation of the reduced polymer to the +0.65 V, fully oxidized structure, leads to two characteristic quinoid bands in the infrared spectra, the 1590 and 860 cm^{-1} vibrations. The 1590 cm^{-1} band observed is assigned to the quinoid band formed along the polymer backbone in the fully oxidized (pernigraniline) state. This band is accompanied by another band at 860 cm^{-1} that is due to the out-of-plane deformation of the quinoid ring. Another band that presents support for polymer formation in the *ox*-AnC6SH/Au and *ox*-AnC7SH/Au is a band occurring at 1623 cm^{-1}. This band has been reported by Ping as a –C=C–C=N– asymmetric vibration in

polyaniline films.[13] Similar bands have previously been reported for poly(aniline) films.[11,12]

Degradation products in the oxidized films may also present a source for quinoid and benzoid ring vibrations in the RAIR spectra. In the spectra presented for ox-AnC7SH/Au a small band occurring at 1657 cm^{-1} appears in the +0.65 V spectra. This band does not increase significantly upon further potential scanning. Studies of quinone monolayers attached to Au substrates have shown that the carbonyl band of the quinone occurs at 1660 cm^{-1}.[14] Studies have also shown that quinonemonoimine degradation products are also formed during the electrochemical oxidation of aniline and aniline derivatives. The vibration occurring at 1623 cm^{-1} assigned as an imine vibration of the surface-confined polymer could also be related to the quinonemonoimine species. The 1660 cm^{-1} vibration in conjunction with the electrochemical data provide evidence for the formation of quinonemonoimine degradation products present in the oxidized monolayer.

Electrochemistry of AnC6SH/Au and AnC7SH/Au in Non-aqueous Solution

As an attempt to eliminate the formation of degradation products in the oxidized aniline monolayers, electrochemical oxidation of AnC6SH/Au and AnC7SH/Au was performed in 0.1 M LiClO$_4$/CH$_3$CN from 0.0 to +0.9 V vs SSCE, Figure 7. The first oxidation scan for both monolayers produced an irreversible
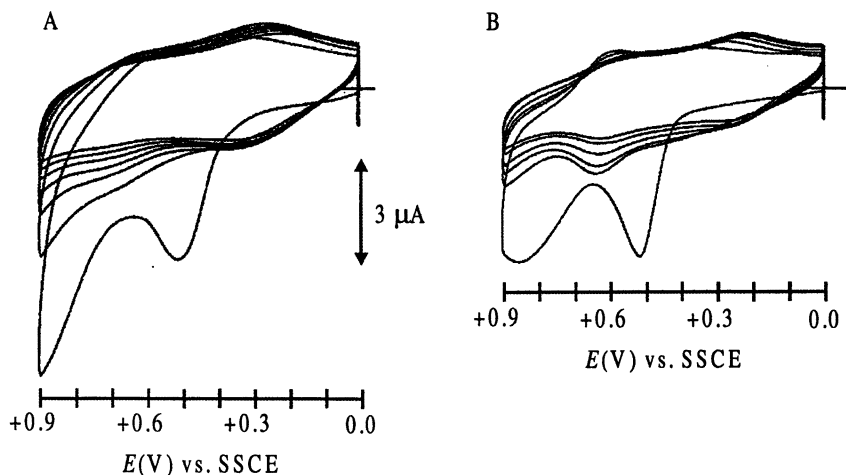
Figure 7. Electrochemical oxidation of (A) AnC6SH/Au and (B) AnC7SH/Au in 0.1 M LiClO$_4$/CH$_3$CN with a scan rate of 100 mV/s.

oxidation wave at +0.5 V, and a second irreversible wave for AnC6SH/Au at +0.9 V and AnC7SH/Au at +0.85 V. Continued scanning in this potential region resulted in the production of two voltammetric waves at +0.25 and +0.65 V (surface-confined in nature) that decreased in intensity after several potential cycles. Each oxidized

monolayer was then rinsed with water, dried with N_2 gas, and immersed in 1 M H_2SO_4 and the voltammetry was again obtained between 0.0 and +0.9 V. It was observed that non-aqueous oxidation produced only dimers throughout the oxidized film as noted by redox waves present at +0.25 and +0.5 V in aqueous acidic solution. The dimer wave at +0.5 V is observed to remain at approximately the same intensity in the *ox*-AnC6SH/Au aqueous voltammetry and decrease after further potential cycling for the *ox*-AnC7SH/Au. Voltammetric scanning of the oxidized films in aqueous solution eventually leads to the formation of small amounts of degradation product, as noted by the growth of the redox wave at +0.45 V for both the *ox*-AnC6SH/Au and *ox*-AnC7SH/Au. A small redox wave due to polymer formation at +0.6 V is also seen to form in the *ox*-AnC7SH/Au; however, no polymer formation is observed for the *ox*-AnC6SH/Au monolayer.

To support our hypothesis that dimer formation has occurred for the monolayers in non-aqueous solution, the electrochemistry of 2-methoxy-N^4-phenyl-1,4-phenylenediamine was investigated in non-aqueous solution between 0.0 and +0.9 V vs. SSCE, Figure 8. As discussed earlier in aqueous acidic solution, this model
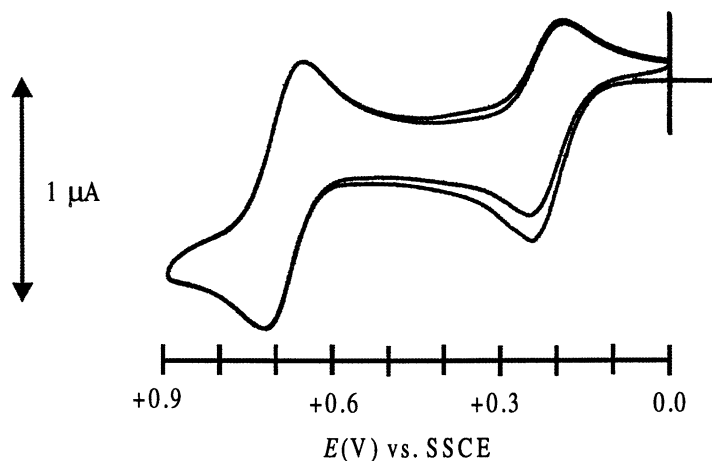
Figure 8. Electrochemistry of 1 mM 2-methoxy-N^4-phenyl-1,4-phenylenediamine in 0.1 M LiClO$_4$/CH$_3$CN with a scan rate of 100 mV/s.

compound produced one redox wave due to the diamine molecule and another redox wave due to the hydrolysis degradation product, the quinoneamine. In non-aqueous solution, this model compound produced two reversible redox waves; the first at approximately +0.25 V and the second at +0.70 V. The first redox wave observed in the model compound voltammetry is attributed to the formation of the radical-cation while the second redox wave is attributed to dication formation. These redox values are very similar to the redox values observed for the *ox*-AnC6SH/Au and *ox*-AnC7SH/Au oxidized monolayers and further support the fact that dimer formation is the preferred method of coupling in non-aqueous media.

Conclusions

AnC6SH and AnC7SH were synthesized and allowed to self-assemble on gold electrodes. Monolayers were examined by RAIR spectroscopy, and it was found that the AnC6SH/Au and AnC7SH/Au have roughly the same surface orientation. Electrochemical blocking analysis of these pristine monolayers was achieved through the use of dimethylaminomethyl ferrocene. AnC6SH/Au was found to effectively block redox activity of dimethylaminomethyl ferrocene while AnC7SH/Au was found to only partially block redox activity. These monolayers were then oxidized in 1 M H_2SO_4 to attempt electrochemical polymerization of the surface-confined aniline groups. The oxidized monolayers produced redox waves indicative of surface-confined poly(aniline), quinonediimine dimers, and quinonemonoimine dimers. The presence of these products was further verified using model compounds and RAIR spectroscopy of the oxidized monolayers. Electrochemical oxidation of the pristine monolayers in 0.1 M $LiClO_4/CH_3CN$ was attempted to reduce the formation of degradation products in the polymer film. Non-aqueous oxidation was found to produce surface-confined aniline dimers only.

Note added in proof: while this manuscript was being reviewed the attempted polymerization of aninobenzenthiol on gold was reported (*Langmuir* 1999, 15, 6807-6812)

References

1.   Kanatzidis, M.G. *C&EN* Dec. 1990, 36-54.
2.   Imisides, M.D., John, R., Wallace, G.G. *Chemtech* May 1996, 19-25.
3.   Dhanabalan, A., Dabke, R.B., Prasanth Kumar, N., Talwar, S.S. , Major, S., Lal, R., Contractor, A.Q. *Langmuir* 1997, 13, 4395-4400.
4.   Hayes, W.A., Shannon, C. *Langmuir* 1996, 12, 3688-3694.
5.   Lukkari, J., Kleemola, K., Meretoja, M., Ollonqvist, T., Kankare, J. *Langmuir* 1998, 14, 1705-1715.
6.   Widrig, C.A., Chung, C., Porter, M.D. *J. Electroanal. Chem.* 1991, 310, 335-359.
7.   Leclerc, M., Guay, J., Dao, L.H. *Macromolecules* 1989, 22, 649-653.
8.   Stilwell, D.E., Park, S.-M. *J. Electrochem. Soc.* 1988, 135, 2491-2496.
9.   Yang, H., Bard, A.J. *J. Electroanal. Chem.* 1992, 339, 423-449.
10.   D'Aprano, G., LeClerc, M. *Chem. Mater.* 1995, 7, 33-42.
11.   Quillard, S., Louarn, G., Lefrant, S., MacDiarmid, A.G. *Physical Review B* 1994, 50, 12496-12508.
12.   Harada, I., Furukawa, Y., Ueda, F. *Synthetic Metals* 1989, 29, E303-E312.
13.   Ping, Z., Nauer, G.E., Neugebauer, H., Theiner, J., Neckel, A. *J. Chem. Soc., Faraday Trans.*, 1997, 93, 121-129.
14.   Ye, S., Yashiro, A., Sato, Y., Uosaki, K. *J. Chem. Soc., Faraday Trans.*, 1996, 92, 3813-3821.

Author Index

321

Subject Index

A

Abbott, Edwin A., concept of multi-dimensional space, 2

AC force modulation. *See* Nanoindentation; Surface spectroscopy

Adaptive intermolecular reactive empirical bond-order (AIREBO) potential
enhancements over REBO potential, 218–220
validation, 220
See also Indentation and friction of *n*-alkane C₁₃ monolayers

Added-mass and two-slope approach, combined. *See* Frictional properties of alkanethiols on gold

Adhesion
calculation for work of, 40
understanding molecular-scale, 168
See also Microthermomechanical probing of composite polymer films; Self-assembled monolayers (SAMs)

n-Alkane C₁₃ monolayers. *See* Indentation and friction of *n*-alkane C₁₃ monolayers

Alkanethiols
friction and wear properties, 217
See also Frictional properties of alkanethiols on gold; Self-assembled monolayers (SAMs)

Alkanethiols, terminally fluorinated. *See* Terminally fluorinated alkanethiols, self-assembled monolayers (SAMs)

Alkanethiols, Ω-substituted. *See* Fluorinated self-assembled monolayer (SAM) film

Alkoxyaniline derivative monolayers on gold
analysis of 2-(6-mercaptohexan-1-oxy)-aniline (AnC6SH) and 2-(7-mercaptoheptan-1-oxy)aniline (AnC7SH) monolayers, 309–312 ·
assignment of redox transformations, 315–316

bare gold electrode in dimethylamino-methyl ferrocene/H₂SO₄, AnC6SH/Au, and AnC7SH/Au, 312f

blocking ability of AnC6SH/Au and AnC7SH/Au to solution-phase redox probe, 311–312, 320

comparison of AnC6SH isotropic spectrum with AnC6SH/Au and AnC7SH/Au RAIR spectra, 310f

electrochemical oxidation of AnC6SH/Au and AnC7SH/Au in LiClO₄/CH₃CN, 318f

electrochemistry of 2-methoxy-N⁴-phenyl-1,4-phenylenediamine in LiClO₄/CH₃CN, 319f

electrochemistry of AnC6SH/Au and AnC7SH/Au in non-aqueous solution, 318–319

electrochemistry of electrochemically deposited poly(o-phenetidine) film on gold electrode in HCl, 315f

electrochemistry of monolayers in aqueous acidic solution, 312–316

experimental chemicals, 307–308

first oxidative scan of AnC6SH/Au and AnC7SH/Au in H₂SO₄, 313f

infrared spectroscopy method, 309

isotropic and reflection-absorption infrared (RAIR) vibrational assignments, 311t

octadecanethiol/Au as control, 311

potential scans of ox-AnC6SH/Au and ox-AnC7SH/Au in H₂SO₄, 314f

RAIR of aniline monolayers upon electrochemical oxidation, 316–318

RAIR spectra of ox-AnC7SH/Au at various emmersion potentials, 317f

redox characteristics of ox-AnC6SH/Au and ox-AnC7SH/Au, 314–315

reflection-absorption infrared spectroscopy, 309

surface derivatization, 308–309

synthesis of aniline-terminated alkanethiols, 308

voltammetric measurements, 309

323

F

Feedback method
  mechanical method for controlling frictional forces, 103–105
  See also Atomic scale friction
Ferrocene moieties. *See* Supramolecular host-guest interactions
Films. *See* Fluorinated self-assembled monolayer (SAM) film
Fixation screws, materials for biomedical implants, 181*f*
Fluid-solid interfaces
  analysis of fluorescence recovery after photobleaching (FRAP) curves for simple liquids, 159–160
  analyzing experimental curves, 160
  boundary condition for flow velocity, 154
  case for investigating polymer fluids, 156–157
  case for investigating simple fluids, 157–158
  case of simple fluids in contact with smooth non-attracting wall, 163–166
  equivalence between wall slip and shear rate for simulated FRAP curves of simple fluids, 159*f*
  evolution of FRAP curves for 1% solution of stearic acid in hexadecane, 164*f*
  flow of hexadecane + 1% stearic acid on bare sapphire surface, 165
  fluorescence recovery time, 159
  FRAP for hexadecane flowing over sapphire surface and dense octadecyltrichlorosilane (OTS) monolayer, 164*f*
  friction and slip at polymer melt-solid interfaces, 160–163
  hexadecane as model non-polar lubricant and sapphire as surface, 163–164
  hexadecane on OTS, 164–165
  molecular mechanism of polymer-wall friction, 162–163
  near field laser velocimetry (NFVL) investigation of polymer melt-solid friction, 161–162
  principle of NFVL technique, 156–160
  schematic representation of correspondence between applied and effective shear rate, 159*f*

schematic representation of no slip or slip boundary condition for fluid velocity at solid wall, 155
schematics of NFLV experimental setup for polymer melts, 156*f*
schematics of NFLV experimental setup for simple fluids, 158*f*
sequence of experiment for polymer melts, 157
sequence of experiment for simple fluids, 158
slip length as function of slip velocity for end grafted chains, 161*f*
surface energy and roughness governing liquid-solid friction, 166
typical results for slip velocity and slip length for poly(dimethylsiloxane) (PDMS) melt flowing against silica surface covered with end grafted PDMS chains, 161*f*
Fluorescence recovery after photobleaching (FRAP)
  analysis of FRAP curves for simple liquids, 159–160
  FRAP for hexadecane flowing over sapphire surface and over dense octadecyltrichlorosilane (OTS) monolayer, 164*f*, 165
  See also Fluid-solid interfaces
Fluorinated self-assembled monolayer (SAM) film
  advancing contact angles of hexadecane, water, glycerol, acetonitrile, dimethyl formamide (DMF), and nitrobenzene on CH_3- and CF_3-terminated SAMs, 65*f*
  AFM (atomic force microscopy) measurements of tip-sample adhesion, 66, 68
  AFM method, 59–60
  chemical composition of terminal groups and frictional response, 60, 64
  contact angle wettability measurement, 59
  differences in adhesion between AFM tip and sample and frictional responses, 64
  evaluating frictional response of SAM terminated with isopropyl (*i*-Pr) groups, 68
  fluorocarbon films, 58–59
  frictional response of CF_3- and CH_3-terminated tridecanethiol SAMs